Ventilation of the oceanic circulation in the Southeast Pacific by mesoscale activity and Rossby waves at interannual to decadal timescales : ENSO teleconnections

Oscar Vergara

THÈSE

En vue de l'obtention du

DOCTORAT DE L'UNIVERSITÉ DE TOULOUSE

Délivré par : *l'Université Toulouse 3 Paul Sabatier (UT3 Paul Sabatier)*

Présentée et soutenue le *07/04/2017* **par :**

Oscar Vergara

Ventilation de la circulation océanique dans le Pacifique Sud-Est par les ondes de Rossby et l'activité méso-échelle : téléconnexions d'ENSO.

JURY

Monsieur Peter Brandt	Professeur d'Université	Rapporteur
Monsieur Thierry Penduff	Chargé de Recherche CNRS	Rapporteur
Monsieur Boris Dewitte	Directeur de Recherche IRD	Directeur de thèse
Monsieur Nicholas Hall	Professeur d'Université	Président du Jury
Madame Angélique Melet	Chargée de Recherche	Examinatrice
Monsieur Oscar Pizarro	Professeur d'Université	Examinateur
Monsieur Marcel Ramos	Directeur de Recherche	Invité

École doctorale et spécialité :
SDU2E : Océan, Atmosphère et Surfaces Continentales

Unité de Recherche :
Laboratoire d'Études en Géophysique et Océanographie Spatiales (UMR 5566)

Directeur de Thèse :
Boris Dewitte

Rapporteurs :
Peter Brandt et *Thierry Penduff*

THÈSE

En vue de l'obtention du

DOCTORAT DE L'UNIVERSITÉ DE TOULOUSE

Délivré par : *l'Université Toulouse 3 Paul Sabatier (UT3 Paul Sabatier)*

Présentée et soutenue le *07/04/2017* **par :**

Oscar Vergara

Ventilation of the oceanic circulation in the Southeast Pacific by mesoscale activity and Rossby waves at interannual to decadal timescales: ENSO teleconnections.

JURY

Monsieur Peter Brandt	Professeur d'Université	Rapporteur
Monsieur Thierry Penduff	Chargé de Recherche CNRS	Rapporteur
Monsieur Boris Dewitte	Directeur de Recherche IRD	Directeur de thèse
Monsieur Nicholas Hall	Professeur d'Université	Président du Jury
Madame Angélique Melet	Chargée de Recherche	Examinatrice
Monsieur Oscar Pizarro	Professeur d'Université	Examinateur
Monsieur Marcel Ramos	Directeur de Recherche	Invité

École doctorale et spécialité :
SDU2E : Océan, Atmosphère et Surfaces Continentales
Unité de Recherche :
Laboratoire d'Études en Géophysique et Océanographie Spatiales (UMR 5566)
Directeur de Thèse :
Boris Dewitte
Rapporteurs :
Peter Brandt et *Thierry Penduff*

Acknowledgements

I gratefully thank my advisor, Dr. Boris Dewitte, for his patience in guiding me through the unveiling of the present research subject, and his confidence in my work. I would also like to thank Dr. Oscar Pizarro, with whom I shared invaluable discussions about ocean dynamics and the challenges of being a researcher. I would also like to thank both rapporteurs, Pr. Peter Brandt and Dr. Thierry Penduff, for their constructive comments and suggestions that contributed to improve this thesis.

My warm thanks to the whole of the LEGOS laboratory personnel, who pulled me through the dreadful amounts of paperwork needed every time I went abroad for a conference or field work, and also assisted me with every detail of the clerical aspects involved in conducting a thesis work.

I couldn't finish this manuscript without acknowledging the support and friendship that I was able to find among the PhD students, postdocs, interns and engineers at LEGOS. I thank you for your good mood and I will always treasure the good times shared along my PhD years.

Last but not least, I would like to thank my family for their priceless support and inspiration which helped me complete this project. Finally, I would like to thank Christelle; without your constant backing and encouragement all of this would have not been possible. Your precious support helped me to endure the harshest moments of this work, and undeniably, part of it is as yours as it is mine.

Contents

A mis padres.

Chapter 1

Introduction

In addition to hosting the most productive upwelling system in the world, the South Eastern Pacific (SEP) is subject to a rich variability at different timescales, due in part to the remote influence of the equatorial Pacific as well as to a prominent ocean-atmosphere interaction. Locally, the circulation in the SEP relates to a nearly year-round equatorward wind field, associated with the eastern rim of the South Pacific Anticyclone (Muñoz and Garreaud, 2005). This alongshore wind field propels the coastal upwelling of colder and nutrient-rich subsurface waters that fertilizes the euphotic zone, and ultimately results in the high productivity found in the SEP (Strub et al., 1998).

The conditions imposed by the local forcing in the SEP are also subject to the remote influence of the equatorial Kelvin waves (EKW) at a variety of timescales (cf. Shaffer et al., 1997; Pizarro et al., 2002; Pizarro and Montecinos, 2004), where the South American coast behaves as an extension of the equatorial waveguide and allows for the poleward propagation of coastally trapped Kelvin-like waves (Spillane et al., 1987), which connect the climate variability in the SEP to the tropical Pacific variability. In this manner, climatic events that take place in the tropical Pacific, such as the ENSO (El Niño Southern Oscillation) events, reflect on the coastal circulation system in the SEP, modulating the local oceanographic and atmospheric conditions. Considering the high productivity of the SEP in terms of fish catch, the occurrence of such events is intertwined with deep socioeconomic repercussions (cf. Cashin et al., 2014), which has motivated several international efforts to improve the current understanding of the SEP dynamics and its teleconnection with the tropical Pacific (e.g. VOCALS-VAMOS[1], CLIVAR[2] and TPOS2020[3] programs).

Although observational efforts to monitor the SEP circulation are currently underway, *in situ* subsurface observations remain sparse, which has prevented a full understanding of the circulation in the region. In this context, the present work focuses on

[1] www.eol.ucar.edu
[2] www.clivar.org
[3] www.tpos2020.org

the problem of the subsurface SEP circulation variability in connection with the variability in tropical Pacific, based on regional oceanic modeling tools. The present chapter introduces the main aspects of the SEP circulation and variability, as well as the processes involved in the oceanic teleconnection between the SEP and the equatorial Pacific. Towards the end of the chapter, a brief description of the ENSO phenomenon and its diversity is made. This introductory chapter concludes with the presentation of the scientific questions and objectives of the present work.

1.1 Wind-driven circulation

In each ocean basin, the large-scale circulation over the first hundreds of meters organizes around a great anticyclonic gyre, and in the case of the Pacific and Atlantic oceans, these features are roughly symmetric about the equator. Researchers in the mid-1800s started to realize that the currents changes in the upper ocean followed a change in the wind field by a matter of hours, and the hypothesis suggesting that the frictional stress of the wind was the responsible of such relationship was first proposed by Croll[4] in 1875. From that period on, the intrinsic turbulent nature of the natural water bodies became known and the concept of turbulent or "eddy" viscosity was developed. Making use of this concept, following works developed the major elements in wind-driven circulation theory (e.g. how the rotation of the earth is responsible for the deflection of wind-driven currents (Ekman, 1902; Nansen, 1898), the equatorial surface currents system and its relationship with the trade winds (Sverdrup, 1947), the solutions of the wind-driven circulation using a realistic wind field (Munk, 1950)).

One of the main particularities of the large-scale ocean circulation is the so-called westward intensification, as shown in figure 1.1, where the flow lines tend to be close together over the western boundary, while they are spaced in the eastern boundary, illustrating that the flow is swift in the west, while it is sluggish on the opposite side of the basin. This feature characterizes all ocean basins and was first explained by Stommel (1948).

In that work, the author based his demonstration in simplified, theoretical models of the ocean and wind pattern, which consisted in a constant-depth rectangular ocean on one hemisphere, and a wind field only varying in the latitudinal direction, as show in figure 1.2. Stommel's work exposed for the first time that the variation of the Coriolis parameter with latitude is responsible for the western intensification of the currents in the ocean, and following works explained this feature in terms of vorticity conservation (e.g. Pond and Pickard, 1983; Rhines, 1986; Lozier and Riser, 1989). In general

[4]James Croll, 19th-century Scottish naturalist mainly known for his works on ice ages periodicity.

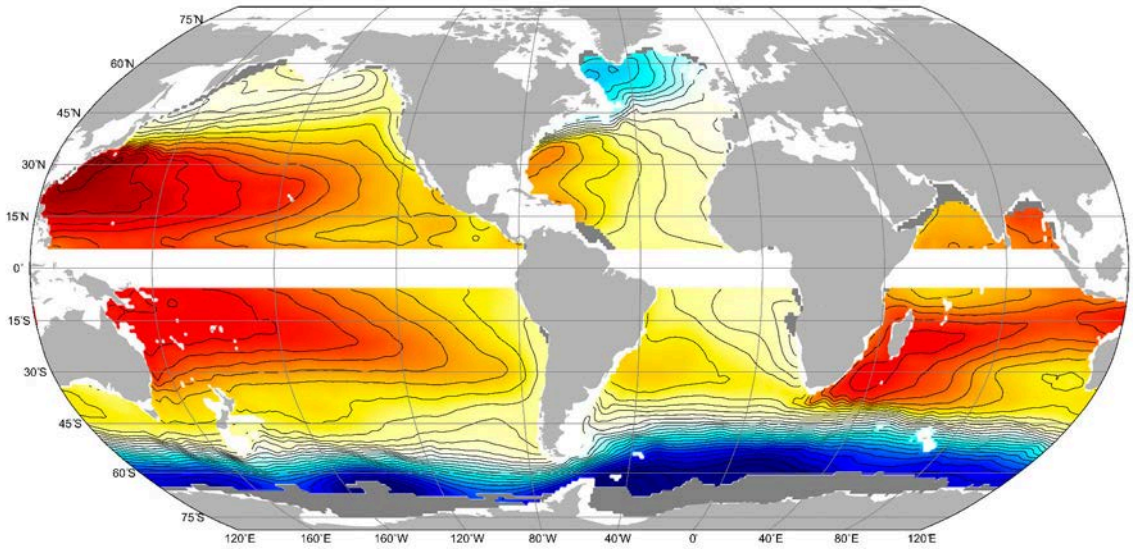

Figure 1.1: *Mean absolute geostrohpic streamfunction at 5db from Argo data (2004-2010). Contour interval is 100 $m^2 s^{-1}$. Dark gray areas were ommited from the analysis. After Gray and Riser (2014).*

terms, the vorticity put into the ocean by the wind stress must be taken out (or balanced) by friction. In the west, a strong friction is needed to balance out the vorticity acquired with the poleward increase in *f*, and for this strong friction to occur strong currents with strong shear are needed. As a result of the western intensification, we find slow currents with low lateral shear in the eastern side of the basin. This induces a poor ventilation of the circulation (Luyten et al., 1983) thus the "age" of the water masses found in the eastern ocean boundaries is higher compared with what is found in the western side (Fig. 1.3), as it is the case when comparing the eastern and western boundaries of the south Pacific.

1.2 The Humboldt Currents system

The south basin of the Pacific Ocean (60°S, 150°E-70°W) accounts for 25% of the total oceans volume, and hosts in its eastern boundary one of the four major coastal upwelling systems of the world. Named after the German naturalist Alexander von Humboldt, the Humboldt Currents System (HCS) extends from southern Chile (near 45°S) to northern Peru (~4°S), and from the coast to ~90°W. This currents system is most notable for its prodigious production of small pelagic fish, which represents 27% of the current annual landing for the fisheries in the Pacific Ocean and has played a key role in the development of several countries for decades.

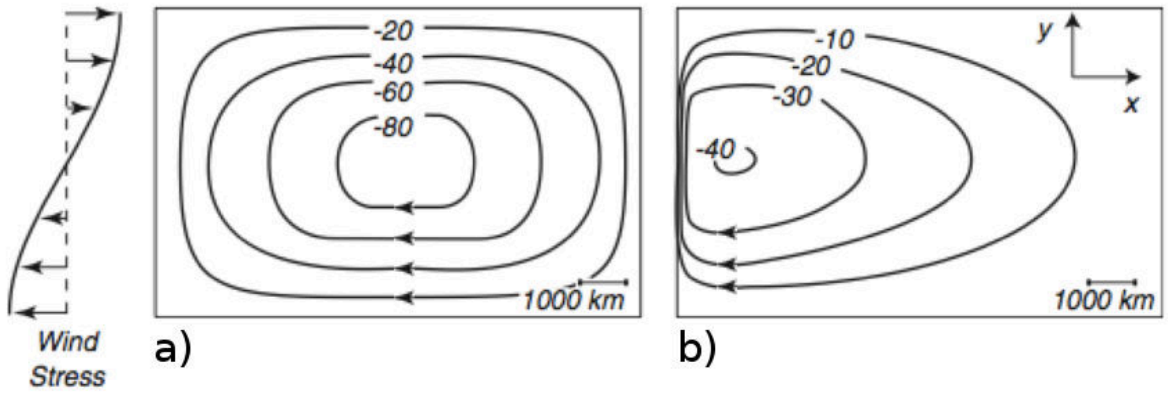

Figure 1.2: *Flow patterns (streamlines) for a simplified wind-driven circulation model in the northern hemisphere with: (a) Constant Coriolis force, (b) Coriolis force increasing linearly with latitude. Idealized wind stress pattern used to force the model is also shown. After Stommel (1948).*

1.2.1 Large scale circulation in the HCS

The large-scale oceanic circulation that shapes the HCS is closely related to the trade winds, which are dynamically set up in both the southern and northern hemispheres by the pressure gradient developed between a low pressure area near the equator and a high pressure region localized around 30°. This pressure gradient induces an air-flow from the mid-latitudes towards the equator, and creates a zonally-narrow wind convergence zone, known as the Intertropical Convergence Zone (ITCZ; Fig. 1.4). In the Pacific, the ITCZ is located on average around 10°N, although its position varies seasonally in connection with the easterlies. Another convection zone characteristic of the tropical Pacific is the South Pacific Convergence Zone (SPCZ), which corresponds to a low-level convection band associated with a subtropical maximum in cloudiness, precipitation and sea surface temperature (Kiladis et al., 1989). It extends from the southeast Pacific (30°S-120°W) to Papua New Guinea, where it merges with the ITCZ (Fig. 1.4). Both the ITCZ and the SPCZ determine the large-scale mean rainfall pattern tropical Pacific band (Takahashi and Battisti, 2007a,b).

The variations of the wind system in the HCS are influenced by the latitudinal shifts of the ITCZ and trade winds in the northern hemisphere, and the latitudinal variations of the SPCZ (Karoly et al., 1998), but they are mainly driven by the shifts of the South Pacific High (SPH) present off central Chile (~30°S). The changes in both the position and the intensity of the SPH impact the wind field in the HCS (Rutllant et al., 2004) and couple to the orographic effect of the Andean mountain range, which results in nearly alongshore equatorward winds close to the coast (Fig. 1.4).

Nevertheless, the wind field exhibits different characteristics along the coast in the

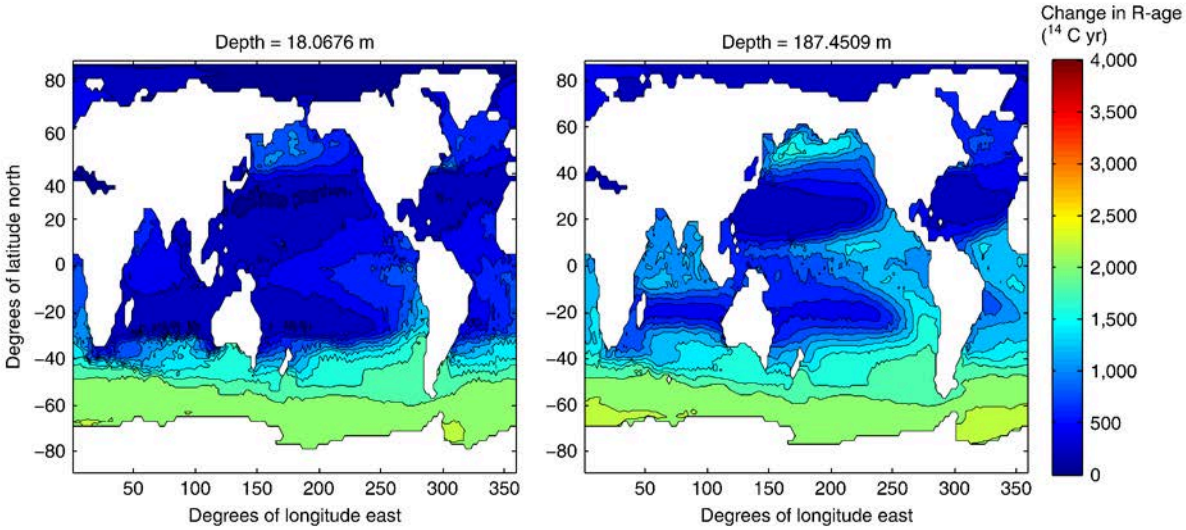

Figure 1.3: *Marine radiocarbon ages (relative to the atmosphere) at 18 and 187 m depth. After Fuente et al. (2015).*

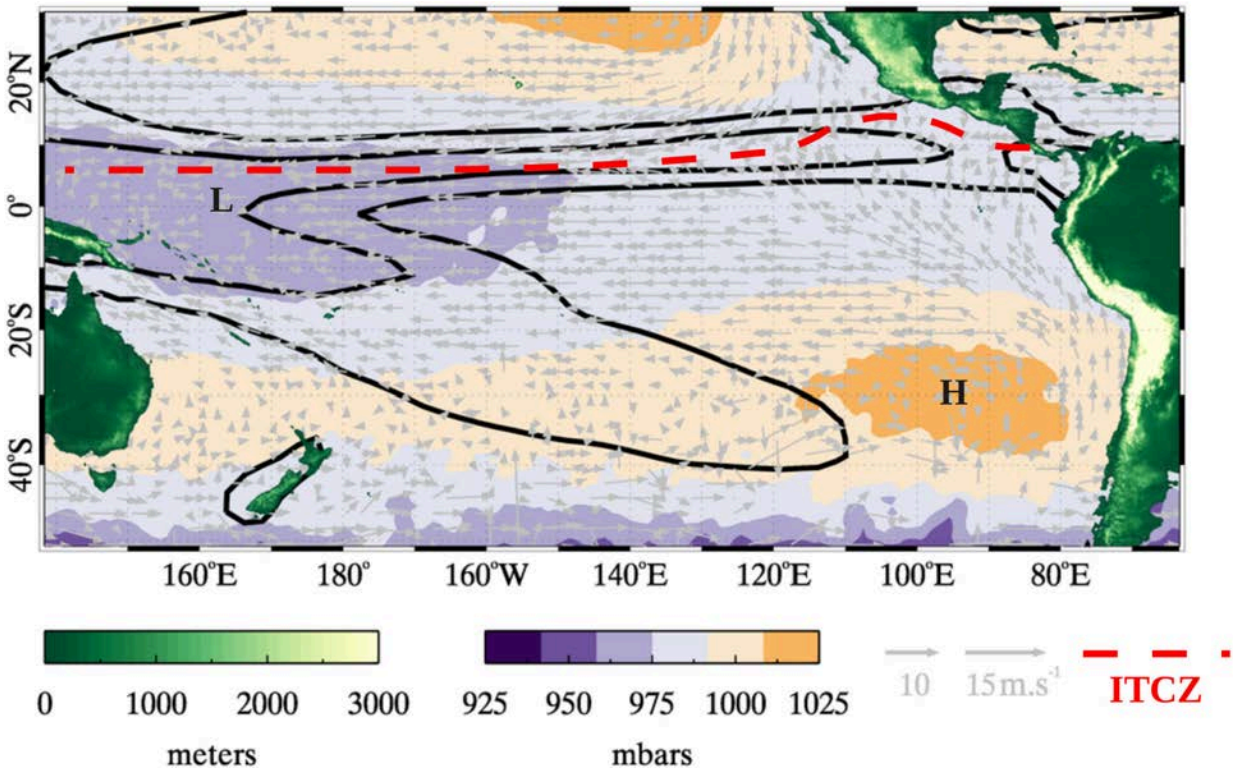

Figure 1.4: *Mean sea level pressure (blue to orange contours) and wind magnitude and direction (arrows) in the south Pacific for the period 2000-2008 (ICOADS dataset). Black contours correspond to mean rainfall values of 3 and 6 $mm\ day^{-1}$, evidencing the low-level convergence bands. Dashed red line qualitatively marks the mean position of the ITCZ.*

HCS. Off Peru, the equatorward winds are intense and almost year-round, with a maximum during austral winter (Bakun and Nelson, 1991; Dewitte et al., 2011). On the

other hand, the wind seasonal cycle off northern Chile peaks during austral spring (Blanco et al., 2002), and during austral summer off central/southern Chile (Garreaud and Muñoz, 2005), which has been related to the seasonal migration of the SPH (Ancapichún and Garcés-Vargas, 2015). Off central Chile, the atmospheric conditions are also subject to the excitation of low atmospheric pressure systems that are trapped to the coast by the pressure gradient between the marine boundary layer and the coastal orography, and propagate polewards (Garreaud et al., 2002).

In the ocean, the circulation in the HCS is composed by several equatorward and poleward alternating currents, with a main surface equatorward flow north of 45°S (Strub et al., 1998) located next to the eastern rim of the SPH (Fig. 1.5). At around 10°S, the main flow turns offshore and flows into the South Equatorial Current (SEC), and a weak ramification continues equatorward and joins the SEC at around 8°S (Wyrtki, 1966). Below the surface, the ramifications of the eastward flowing Equatorial Under Current (EUC) nourish the subsurface poleward components of the HCS: (1) the Peru-Chile Under Current (PCUC), a subsurface poleward flow found over the slope and outer shelf off the Peruvian and Chilean coasts and (2) the Peru-Chile Counter Current (PCCC), located between 150 and 300 Km offshore (Strub et al., 1998; Fig. 1.5). In relationship with its equatorial origins, the PCUC has a distinctive hydrographic signature, characterized as relatively saltier, higher in nutrients and lower in oxygen than the surrounding waters, and these characteristics have allowed to trace it as far south as 48°S (Silva and Neshyba, 1979).

The HCS exhibits an important seasonality in relation to the yearly cycle of the environmental forcing. On a regional scale, the oceanic response to environmental forcing at seasonal timescale is primarily related to the annual net insolation cycle (Takahashi, 2005), although ocean dynamics contribute to make the system heterogeneous and induce distinctive responses to forcing off Peru and Chile, which has been interpreted as the result of a compensation between large-scale dynamical signals (Dewitte et al., 2008a). On the other hand, the oceanic response to environmental forcing next to the coast is closely related to the wind forcing and manifests as coastal upwelling, which is the process responsible for the high primary productivity observed along the coast in the HCS. This coastal upwelling is sustained by the alongshore equatorward wind stress that generates an Ekman divergence of the currents next to the coast, which is in turn compensated by a vertical upward flow of nutrient-rich waters carried by the PCUC (Kelly and Blanco, 1984; Wyrtki, 1963). In addition, the large scale alongshore wind stress decreases over a few hundred kilometers next to the coast, due to the coastal orography, the surface drag gradient between land and sea, and the air-sea interactions over cool seawater (see Capet et al., 2004). It is expected that this

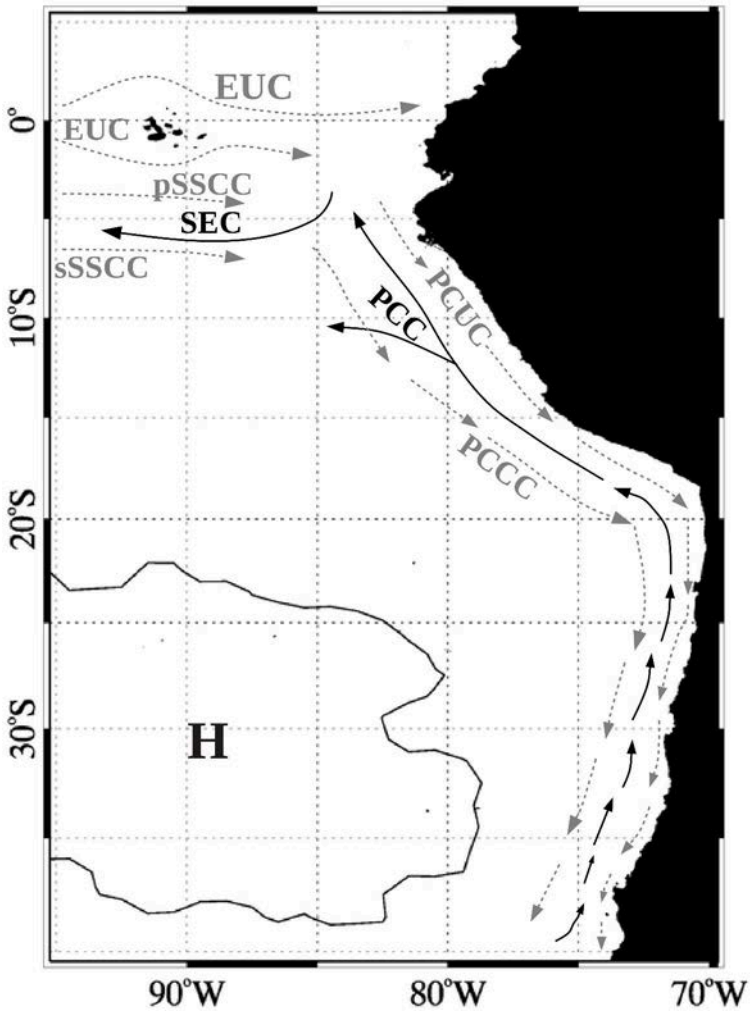

Figure 1.5: *Oceanic circulation scheme in the HCS: Equatorial Undercurrent (EUC), primary and secondary Southern Subsurface Countercurrents (pSSCC and sSSCC), South Equatorial Current (SEC), Peru Coastal Current (PCC), Peru-Chile Undercurrent (PCUC) and Peru-Chile Countercurrent (PCCC). Black lines denote surface currents and gray lines denote subsurface currents. The average position of the 1020 mb sea level pressure contour (used as a proxy for the South Pacific High position) is also represented (H). Currents compiled following Strub et al. (1998), Kessler (2006) and Montes et al. (2010b).*

phenomenon, also known as wind "drop-off", would create an onshore wind stress gradient which would in turn result in a negative wind stress curl and ultimately an Ekman pumping (Bakun and Nelson, 1991) that could also contribute to the vertical upwelling.

Although the mechanisms behind the coastal upwelling in the HCS are related to the large scale wind system present in the region, the small scale variations in the ocean circulation and coastal orography contribute to make the system heterogeneous, encompassing three well-defined upwelling subsystems along the HCS (Montecino and Lange, 2009): (1) the year-round and highly productive upwelling system off Peru,

(2) a low productivity "upwelling shadow zone" in southern Peru and northern Chile, and (3) a productive and seasonal upwelling system in central-southern Chile.

1.2.2 The south Pacific Oxygen Minimum Zone

In addition to a highly productive upwelling system, the SEP encompasses the southern portion of one of the most extensive Oxygen Minimum Zones of the planet (OMZs; Paulmier and Ruiz-Pino, 2009). The OMZs are regions in the ocean characterized by extremely low concentrations of Dissolved Oxygen (DO) in the water column (DO < 60 μM), as a result of complex interactions between the ocean circulation and the biogeochemical cycles (Fig. 1.6; Karstensen et al., 2008). In the HCS, the intense biological production that takes place in the euphotic zone of the water column (first 200m) is accompanied by an important subsurface remineralization of organic matter, which translates as a significant DO demand in the mesopelagic zone (Capone and Hutchins, 2013). This important DO demand couples to poor ventilation, related to a nearly stagnant circulation (Luyten et al., 1983), which allows the OMZ to persist in time. Among the most relevant impacts of the OMZ in the SEP we find the habitat compression of the organisms, given that the OMZ represents a respiratory barrier (Prince and Goodyear, 2006). Additionally, the biogeochemical cycles that take place at extremely low DO concentrations are involved in the local production of climatically-active gases, such as CO_2 (Paulmier et al., 2011) and N_2O (Kock et al., 2016), which are then outgassed to the atmosphere. In this sense, the OMZ has an impact on both the local ecosystems and on the global climate.

Despite its potential implications, several questions remain regarding the OMZ variability and long-term trends (Stramma et al., 2010). Recent light has been shed upon the mechanisms that shape the OMZ (Bettencourt et al., 2015), emphasizing the central role of the mesoscale structures. However, it has not been clarified yet whether or not these structures influence the variability of the OMZ and its long-term evolution, considering that the mesoscale activity appears as a conspicuous feature in the SEP circulation.

1.2.3 Mesoscale features

Over the large-scale circulation pattern found in the HCS, rich mesoscale variability in the form of eddies or vortices, filaments and squirts is superimposed (Fig. 1.7). In the HCS, eddies are characterized by a radius between 50-150 km (Chaigneau et al., 2008; Chaigneau and Pizarro, 2005b) and can persist for months, traveling thousands of kilometers offshore from their genesis region. Eddies are mainly generated

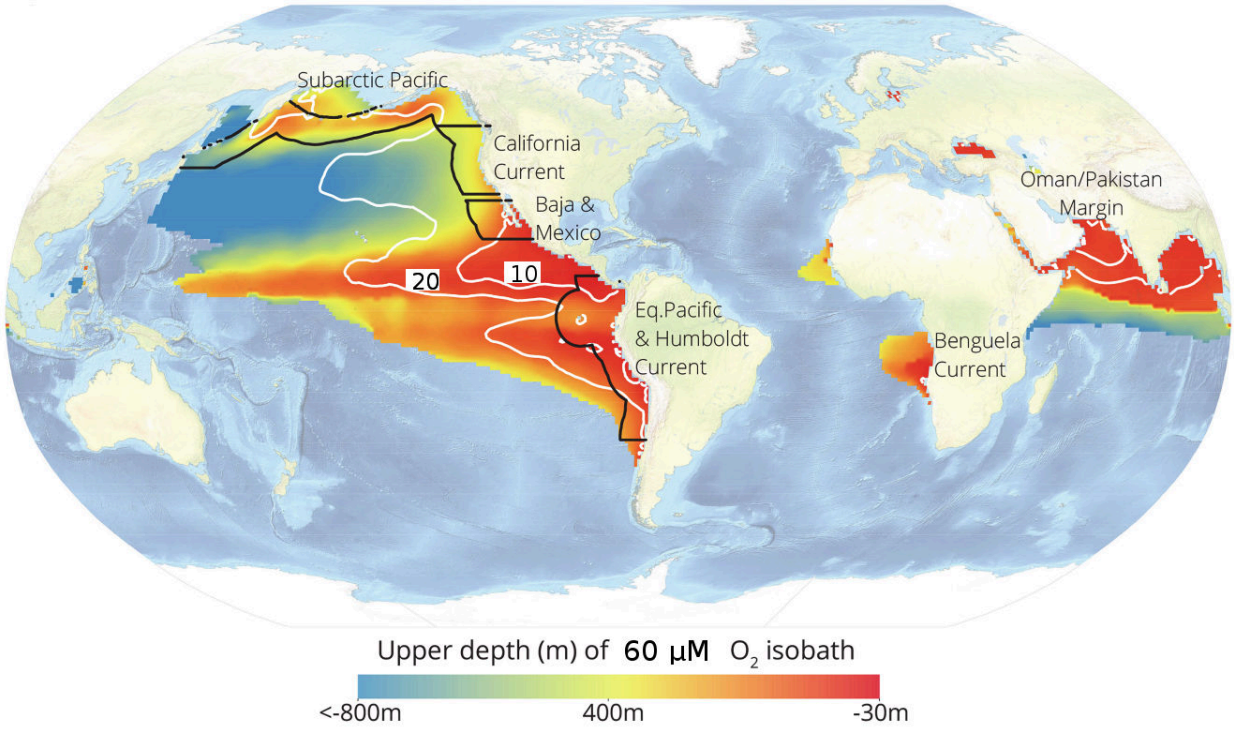

Figure 1.6: *Global Oxygen Minimum Zones (OMZ), including the upper depth of intermediate water hypoxia ($DO < 60\ \mu mol\ L^{-1}$; color shading), and the spatial distribution of severely hypoxic minimums ($DO < 20\ \mu mol\ L^{-1}$) as white lines. After Moffitt et al. (2015).*

from baroclinic instabilities induced by the vertical shear of the currents near the coast (Leth and Shaffer, 2001), and propagate westward with translation velocities between 3-7 $cm\ s^{-1}$ (Chaigneau and Pizarro, 2005b). Observations have shown that the HCS is highly populated by eddies between 9°S and ~36°S, and they participate in the heat (Colas et al., 2012) and salt balance between the offshore and coastal waters through lateral fluxes, even exceeding the mean advective current fluxes in the coastal upwelling region (Chaigneau and Pizarro, 2005a). Despite this evidence, the net contribution of eddies to the SEP's heat budget is still in debate, due to conflicting modeling and observational results (cf. Mechoso et al., 2014). Recent observational analyses even suggest that eddies would not substantially contribute to the surface layer heat budget in the offshore SEP (Holte et al., 2013).

In the SEP, the mesoscale structures also induce a coupling between physical and biogeochemical processes (McGillicuddy et al., 1998), which significantly extends the high primary production zone associated to the coastal upwelling while moving offshore. Observational evidence off central Chile (29°-39°S) indicates that eddies are responsible for more than 50% of the winter chlorophyll-a peak in the offshore coastal transition zone (Correa-Ramirez et al., 2007). In this sense, eddies might represent a pathway that links the highly productive coastal upwelling region with the (essentially

oligotrophic) offshore waters. Nevertheless, this vision is still on debate regarding the highly productive HCS and recent results have established that in fact eddies might contribute to reduce primary productivity as a result of the transport of nutrients from the nearshore to the open ocean (Gruber et al., 2011)

1.3 Teleconnection with the equatorial Pacific

Aside from the local atmospheric and oceanic forcing, the variability in the HCS is intimately related to the variability that takes place in the equatorial Pacific, at timescales ranging from intraseasonal to seasonal (Pizarro et al., 2002; Shaffer et al., 1999), and from interannual (Pizarro et al., 2001, 2002; Vega et al., 2003) to interdecadal (Montecinos et al., 2007). The equatorial region behaves as a waveguide, and allows for the

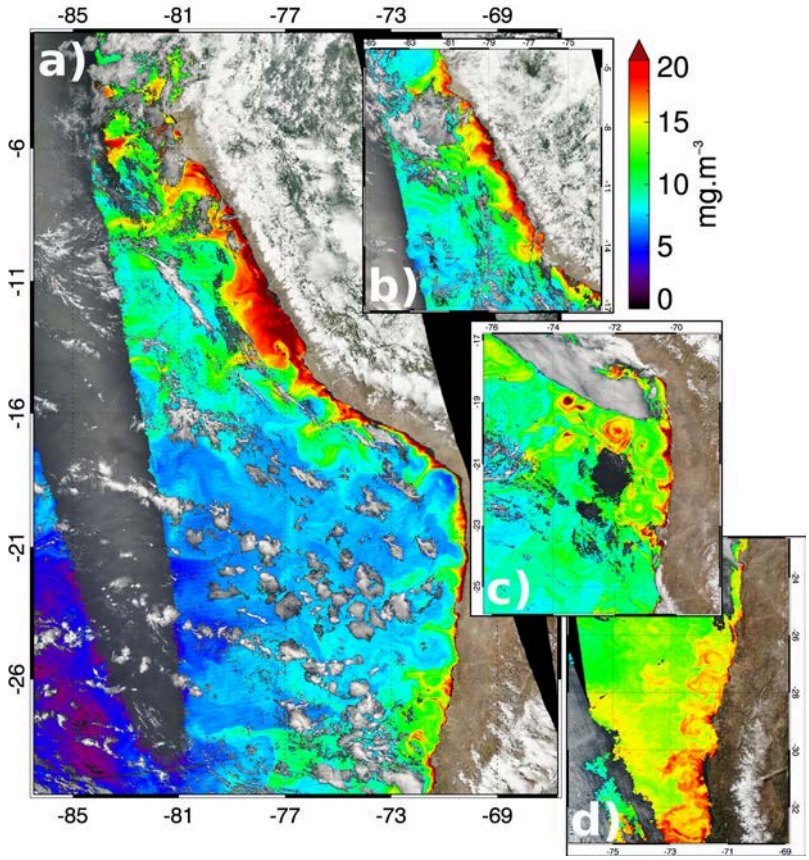

Figure 1.7: *Chlorophyll-a concentration in the Humboldt currents system, illustrating the rich mesoscale variability that is present in the flow. Structures such as eddies, filaments and plumes can be clearly distinguished. The chlorophyll-a data corresponds to snapshots taken by the MODIS spectroradiometer (1 km resolution) at different dates: (a) 18/02/2014, (b) 17/01/2014, (c) 13/09/2014 and (d) 06/07/2014. The coastal orography and clouds correspond to corrected reflectance (true color), also acquired by MODIS. Data source: http://worldview.earthdata.nasa.gov*

zonal propagation of different types of waves. One of the most prominent modes of variability corresponds to the Intraseasonal Equatorial Kelvin Wave (IEKW), generated in the central equatorial Pacific by intraseasonal westerly wind pulses. The IEKW travels to the east and impinges on the American continent. As shown by idealized models, part of the energy is reflected by the eastern boundary and travels to the west as a long Rossby wave, and part is deflected and travels poleward (Cane and Sarachik, 1977; Moore and Philander, 1977) as a free Coastal Trapped Wave (CTW). The South American coast behaves then as an extension of the equatorial waveguide. In contrast to the IEKW, the phase speed of the CTW strongly depends on the shape of the continental slope (Brink, 1982; Clarke and Ahmed, 1999) and stratification (Allen, 1975), and its vertical structure varies with latitude. As the wave travels polewards, the internal Rossby radius of deformation decreases and the bottom topography becomes more important in determining the vertical structure of the gravest baroclinic modes (Brink, 1980). In this manner, at low latitudes the CTW structure is essentially baroclinic, however, as latitude increases, the dominant vertical structure tends to be barotropic (Brink, 1982).

As they travel polewards, the CTWs induce perturbations in the density and pressure field over the continental shelf and slope, which has permitted to observe poleward propagating signals along the South American coast at a wide range of frequencies. Fluctuations of sea level and currents off Peru in the synoptic band (period ~10 days) have been reported to have little relationship with the local wind (Cornejo-Rodriguez and Enfield, 1987; Enfield et al., 1987; R. L. Smith, 1978). Rather, they relate to the poleward propagation of first baroclinic mode CTWs (Brink, 1982; Romea and R. L. Smith, 1983), forced by synoptic-scale mixed Rossby-gravity waves (or Yanai waves), propagating eastward in the equatorial Pacific (Clarke, 1983; Enfield et al., 1987). Further studies unveiled the relationship between the sea level and currents fluctuations observed in the HCS at intraseasonal frequencies (30-90 days) and the remote influence through first baroclinic mode CTWs (Hormazábal et al., 2002; Illig et al., 2014; Shaffer et al., 1997; Spillane et al., 1987), forced by baroclinic IEKWs impinging on the South American coast. Such wind-forced equatorial waves tend to be most prominent during austral summer in the central tropical Pacific (Illig et al., 2014; Kessler et al., 1995), in connection with atmospheric convection events that propagate from the central Indian Ocean into the western Pacific.

The IEKW activity is strongly modulated at interannual timescales reflecting the occurrence of El Niño events (Dewitte et al., 2008a; Kessler et al., 1995) and its diversity (Gushchina and Dewitte, 2012; Mosquera-Vásquez et al., 2014), which corresponds to the most prominent mode of climatic variability in the equatorial Pacific.

1.3.1 A brief description of El Niño

The occurrence of El Niño events entails important disruptions in the tropical Pacific climate system primarily associated with changes in the SST gradients and the ocean-atmosphere feedbacks. Due to the efficient teleconnection that links the tropical Pacific and the SEP, this mode of tropical climatic variability induces significant upheavals in the SEP climate system, which highlights the fact that the influence of these events extends well beyond the equatorial Pacific. In the present section, a brief description of El Niño is made, and the modulation of the SEP variability induced by these events is presented in the following section.

AVERAGE CONDITIONS: in the tropical Pacific, the wind regime dominated by the easterlies induces a flow to the western part of the basin. As the water flows westwards along the equatorial region, the strong insolation induces a surface warming, and a strong zonal SST gradient is developed (around 12°C between the western and eastern Pacific). This zonal gradient reflects as a tongue-shaped cold Sea Surface Temperature (SST) that extends from east to west, and a deeper equatorial thermocline develops in the western Pacific (Fig. 1.8a). The warm water found in the western boundary (known as the "warm pool") generates an important atmospheric thermal convection. The warm and humid air over the warm pool ascends and is driven by the high tropospheric circulation towards the eastern part of the basin, where it loses heat and humidity and settles above the colder sea surface. The air is then driven towards the west by the easterlies, closing the convective loop. This atmospheric circulation cell is known as the Walker circulation (Fig. 1.8a), in honor of Sir Gilbert Walker, who first described the strong inverse correlation between the high and low pressure records obtained at the eastern and western Pacific, and coined the term Southern Oscillation to describe the "seesaw" behavior of the east-west pressure gradient.

EL NIÑO EVENTS: the onset of an El Niño event is characterized by a relaxation of the easterlies, and a consequent reduction of the equatorial and coastal upwelling, which allows the warm pool to grow and expand eastward in the equatorial Pacific (Fig. 1.8b). The shift of the warm pool position induces a zonal displacement of the convective Walker cell which in turns changes the evaporation patterns, generating droughts in the western part of the basin, and strong precipitations in the eastern part (Fig. 1.8b). These events might be followed by cold events in the central equatorial Pacific, known as La Niña events (Fig. 1.8c), which are considered as an enhancement of the average conditions. During a La Niña event, the easterlies are stronger than the average conditions, the

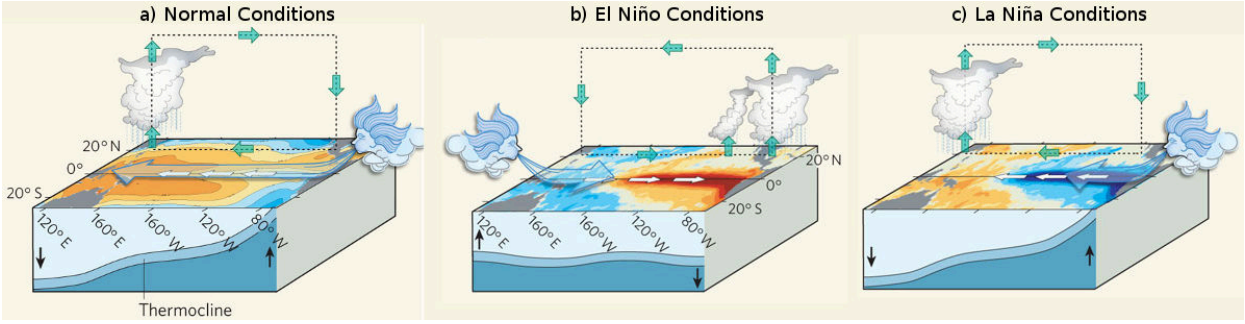

Figure 1.8: *(a) Normal conditions in the tropical Pacific. Conditions during (b) an El Niño event and (c) La Niña event. After Ashok and Yamagata (2009).*

warm pool is warmer than average and the waters in the eastern Pacific are even colder (Fig. 1.8c), which couples to a stronger-than-average Walker circulation. This marked ocean/atmosphere coupling between the anomalies generated by El Niño events and the Southern Oscillation is referred to as El Niño-Southern Oscillation (ENSO).

1.3.2 The ENSO arrival at the Humboldt Currents System

Although the ENSO events peak in the equatorial Pacific, wave dynamics carry the anomalous ENSO signal to the SEP. The equatorial Pacific is heavily disrupted during ENSO events, and this reflects on the IEKW activity. Kessler et al. (1995) showed that during the onset of El Niño events, the eastward extension of the convection cell (associated with a warmer SST) gives the westerlies more fetch to blow upon, generating a more intense IEKW activity. This is coupled to a deepening of the thermocline along the equatorial Pacific, which favors the leading baroclinic mode and enhances the phase speed of the IEKW (Benestad et al., 2002). These changes translate as a modulation of the IEKW at interannual timescale (Dewitte et al., 2008a), which ultimately impacts the CTW activity in the HCS (Enfield et al., 1987). In this sense, Shaffer et al. (1997) documented the intraseasonal currents variations at central Chile (30°S) during the 1991-1992 El Niño event, showing that the most important fluctuations were related to the passage of free CTWs arriving from the north.

Additionally, the CTW activity during the ENSO events severely impacts the coastal thermocline. At the peak of the 1997-1998 El Niño, the thermocline off the coasts of southern Peru and northern Chile showed vertical anomalies in the order of 150m, which were perceived as anomalies in the order of 10 cm in the coastal sea levels observations (Blanco et al., 2002). Several studies evoked the idea that the vertical disruptions of the thermocline depth forced by the intraseasonal CTWs would have an

impact on the source water for the coastal upwelling, such that the upwelled water would be cooler or warmer (and nutrient rich/poorer), in relationship with the upwelling/downwelling phase of the wave (Colas et al., 2008; Huyer et al., 1987; Shaffer et al., 1997). This relationship has been recalled, together with the variations in the alongshore wind intensity (Rutllant et al., 2004), to explain the low productivity observed in the HCS during El Niño events (Barber and Chávez, 1986; Huyer et al., 1987), and the subsequent drop of the fisheries (86% decrease during the 1997/98 El Niño; see Yañez et al. (2001)).

1.3.3 The connection between the equatorial Pacific and the deep eastern Pacific

The oceanic teleconnection between the eastern and equatorial Pacific is not limited to the propagation of CTWs. Theoretical works first showed that, depending on the frequency, the motion might be not only in the form of a Kelvin-like wave trapped along the meridional boundary, but also in the form of long Rossby waves, with a group velocity away from the boundary (Clarke, 1983; Schopf et al., 1981). Further studies demonstrated that for a given frequency, there is a critical latitude (or distance from the equator) such that the energy radiates offshore in the form of baroclinic Extra-Tropical Rossby Waves (ETRW) equatorward of that critical latitude (Clarke and Shi, 1991). The formalism that relates frequency and latitude establishes that lower frequencies favor the untrapped motion, and therefore ETRW can radiate at any latitude along the coast for interannual timescales (Schopf et al., 1981), which has been corroborated by observations as far from the equator as 30°S (Fig. 1.9).

The offshore radiation of energy in subtropical latitudes at interannual timescales was first evidenced for the north Pacific (Kessler, 1990; White and Saur, 1983), using observations of the subsurface thermal structure. Nonetheless, the lack of a well-established observation system (as the one present in the equatorial Pacific) held back a more detailed characterization of the ETRW, as well as their modulation and interactions with the mean circulation. This issue was partly addressed with the first long term observations resulting from the altimetric TOPEX/Poseidon mission, which revealed that the ocean is populated by an ubiquitous Rossby wave field (Chelton and Schlax, 1996), that has the potential to modulate the average circulation in the ocean. In this matter, Qiu (2002) analyzed eight years of the (then) recent altimetric mission to investigate the interannual changes in three subtropical current systems in the north Pacific. This unprecedented work revealed that much of the interannual perturbations observed in the large scale circulation in the mid-latitude system were related to sea

surface height (SSH) anomalies, that propagate from the eastern boundary toward the basin interior as baroclinic long Rossby waves.

First observations also documented a decrease of the ETRW amplitude as they propagate westward (Chelton and Schlax, 1996; Wang et al., 1998), and several mechanisms were evoked to explain it. Qiu et al. (1997) proposed a theoretical framework that evaluated the westward decay of long baroclinic Rossby waves off the equatorial region, related to the effect of eddy dissipation. Later on, using a quasigeostrophic two-layer model, Lacasce and Pedlosky (2004) also recall the nonlinearities of the flow as the source of dissipation, explaining the dissipation process in terms of the baroclinic instability of the Rossby wave itself. In that work, the authors propose that the growth of baroclinic instability of the wave may overcome the stabilizing effect of the planetary vorticity gradient (β effect), and cause the wave to breakdown and transfer energy to a smaller-scale eddy field. Yet, the linear dispersion of Rossby waves associated with the β effect also constitutes a type of dissipation. Schopf et al. (1981) showed that linear dispersion generates a caustic line that originates at the critical latitude and defines a limit for the propagation of boundary forced Rossby waves. Given that linear dispersion becomes increasingly important away from the equator, it is also a potential mechanism that could explain the observed surface decay of the ETRW away from the boundary.

An additional process to consider in the interpretation of the surface signature of long Rossby waves is the vertical propagation of energy that involves the constructive contribution of a certain number of baroclinic modes (Gent and Luyten, 1985; McCreary, 1984). Vertical propagation of long Rossby waves was first investigated in the

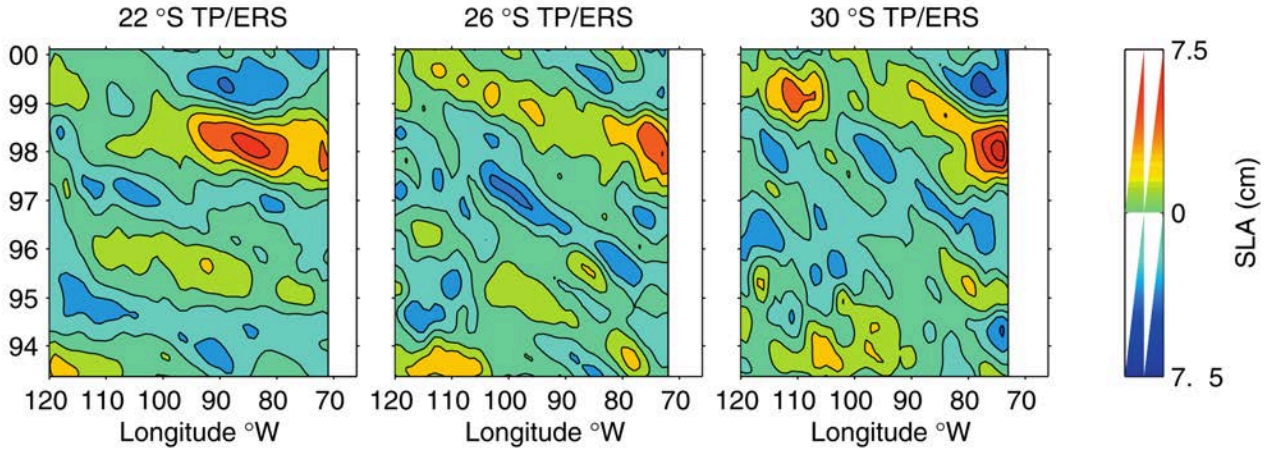

Figure 1.9: *Longitude-time diagrams of interannual sea level anomalies (TOPEX/ERS dataset) for the second half of the 1990s, at three latitudes along the HCS. In particular, the westward propagation a downwelling ETRW, associated with a strong positive sea level anomaly near the coast($> 6cm$), can be distinguished for the 1997/1998 El Niño event. After Vega et al. (2003).*

equatorial region, in order to document and explain the variations of temperature observed below the thermocline at annual period (Kessler and McCreary, 1993). Using an ocean general circulation model (OGCM), Dewitte and Reverdin (2000) successfully reproduced Kessler and McCreary's results in terms of annual subthermocline variability, and reported that the vertical energy propagation in the form of long Rossby waves also takes place at interannual timescale, associated with the reflection of Kelvin waves on the eastern boundary of the equatorial Pacific basin (which are prominent during strong El Niño events).

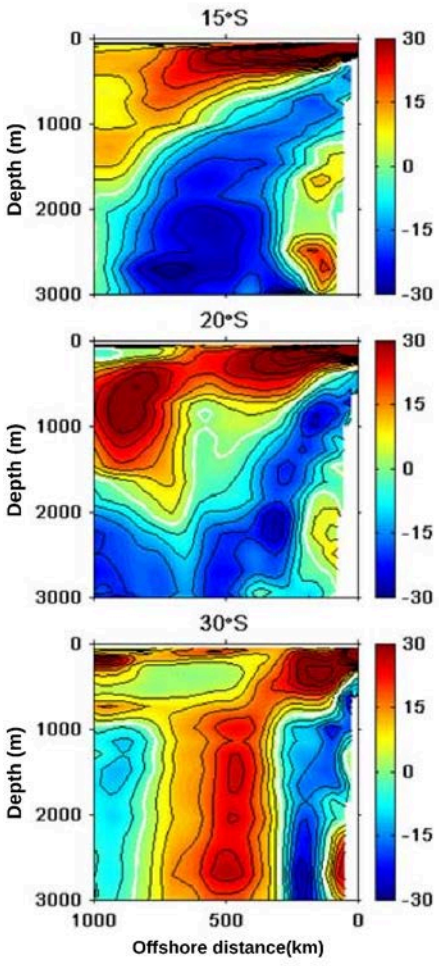

Figure 1.10: *Cross-shore sections of vertical isotherms displacements (in meters) during the peak phase of the 1997/1998 El Niño event at 15°S (top), 20°S (middle) and 30°S (bottom). After Ramos et al. (2008).*

In the SEP, works focusing on the variability of the vertical structure of the circulation later documented the existence of vertical propagation of ETRW at seasonal (Dewitte et al., 2008b) and interannual (Ramos et al., 2008) timescales, evidencing a vertical energy flux associated with the propagation of the ETRW. In particular, Ramos et al. (2008) illustrated the close connection between the subthermocline variability in the SEP and the equatorial variability during the 1997-1998 El Niño event. As the event develops, high-order baroclinic mode contribution to the equatorial Kelvin wave becomes more important, related to a change in the equatorial thermocline depth and vertical temperature gradients (Dewitte et al., 2003). This translates as an increasing dominance of high baroclinic modes along the coast in the SEP throughout the event, which constructively trigger the vertical propagation of ETRW. As shown by Ramos et al. (2008), the signature of the ETRW related to the ENSO events extends several hundreds of Km offshore and penetrates deep into the ocean (Fig. 1.10), which questions about the role that the vertical energy propagation related to the ENSO events could play in the ventilation of the subsurface circulation in the SEP. This acquires particular relevance in the current understanding of the ENSO diversity and its influence out of the tropical Pacific.

1.4 ENSO diversity

Recent studies have reported that over the last five decades, two types of El Niño events have occurred in the equatorial Pacific (Ashok et al., 2007; Kug et al., 2010; Larkin and Harrison, 2005; Yeh et al., 2009), each one having contrasting SST anomaly patterns: *(1)* the Cold Tongue El Niño, or eastern Pacific El Niño (Fig. 1.8b), consisting in a SST anomaly that develops and peaks in the eastern equatorial Pacific (EP), and the *(2)* El Niño Modoki (Ashok et al., 2007) or central Pacific El Niño (CP), that consists of an SST anomaly that develops and persists in the central equatorial Pacific (Fig. 1.11). In addition, both types also differ in the intensity of the SST anomalies developed in the tropical Pacific, with the stronger events occurring in the eastern Pacific (EP). They also exhibit different seasonal evolution patterns (Kao and Yu, 2009; Yeh et al., 2014). During the EP events, the SST anomalies develop in the far eastern Pacific during boreal spring and extend westward over summer and fall, while during the CP events, the SST anomalies extend from the eastern subtropics to the central equatorial Pacific during boreal spring and summer. Despite the phase differences during the development phase, both event types achieve their peak amplitude in boreal winter.

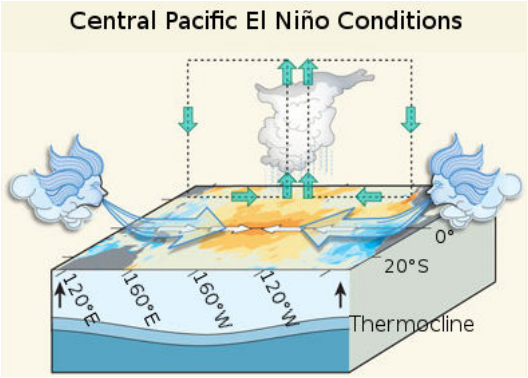

Figure 1.11: *Conditions in the tropical Pacific during a central Pacific El Niño event. After Ashok and Yamagata (2009).*

The contrasting characteristics of both types of El Niño imply different impacts associated with their occurrence. Each type induces a different zonal SST gradient across the equatorial Pacific, and this translates as contrasting atmospheric teleconnections (Ashok et al., 2007; Weng et al., 2009; Yeh et al., 2009). While the convective cell is displaced far to the east during the EP events, the SST anomalies developed during the CP events induce an anomalous twin Walker circulation, with the updraft branch located in the central Pacific (Fig. 1.11; Ashok et al., 2007). Significant differences are also observed in the HCS related to each type of El Niño. While EP events are associated with drastic changes in coastal circulation and hydrographic conditions (Fig. 1.12;

Blanco et al., 2002; Pizarro et al., 2001) and therefore have a profound impact on the local ecosystems (Gutiérrez et al., 2008), the changes imposed by the CP events on the hydrographic characteristics of the HCS are not as severe as during EP events, and are in turn very close to the climatological mean (Fig. 1.13; Dewitte et al., 2012). Recent studies also show that the IEKW activity is distinct between CP and EP El Niño events (Gushchina and Dewitte, 2012; Mosquera-Vásquez et al., 2014).

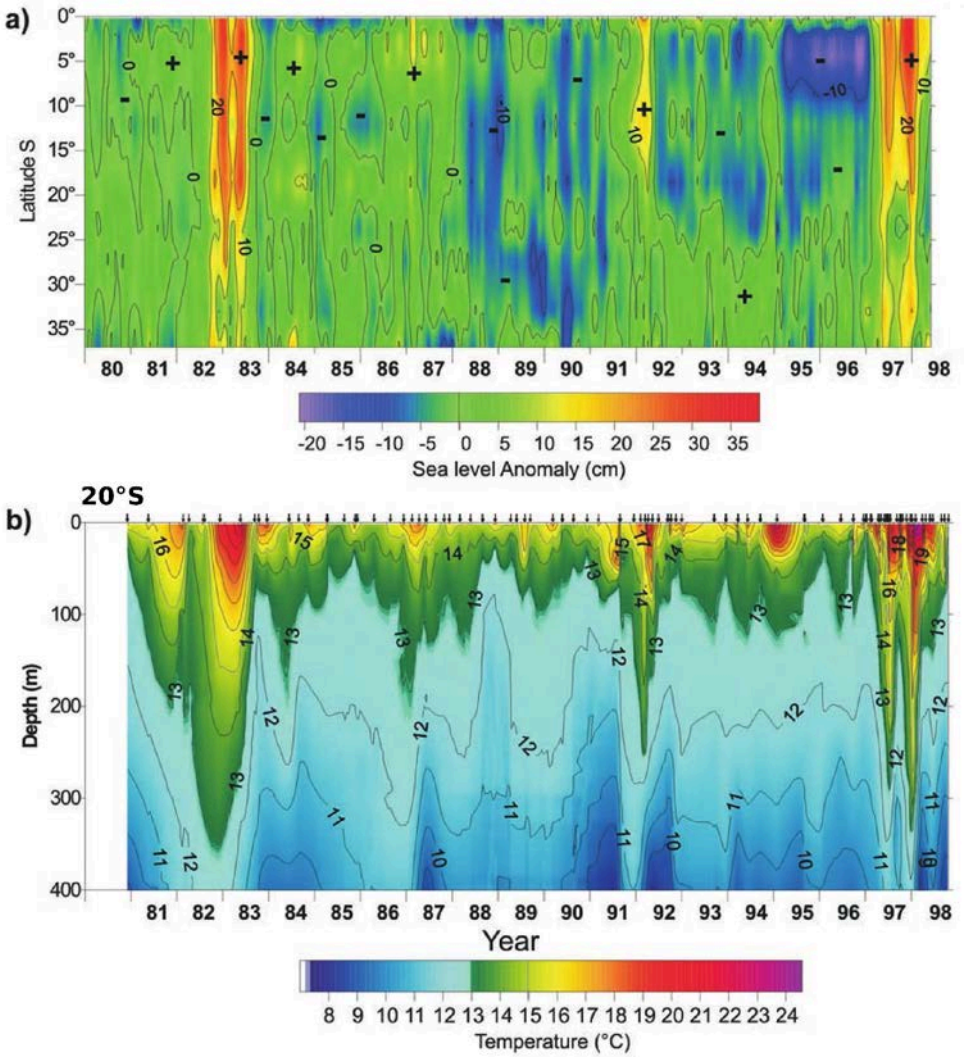

Figure 1.12: *(a) Time-latitude plot of monthly sea level height interannual anomalies from tide gauge data along the coast of the HCS, from 1980 to 1998. (b) time-depth plot of temperatures 10 km offshore of Iquique (20°S). Note the severe thermocline depression during the 1981/1982 and 1997/1998 El Niño events. Sampling is indicated by arrows. After Blanco et al., 2002.*

1.4.1 ENSO diversity trend

Observations point out that the ENSO diversity has accentuated over the last part of the 20th century (Fig. 1.14). CP events have become more frequent (Lee and McPhaden,

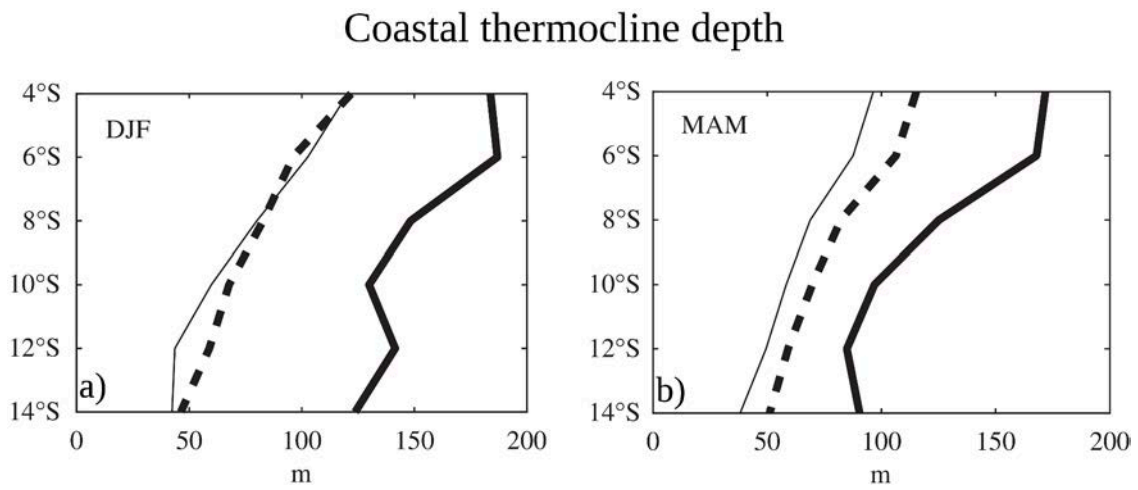

Figure 1.13: *Composites of the mean thermocline depth off the coast of Peru during the peak (DJF) and decaying (MAM) phase of an eastern (thick) and central (thick dotted) Pacific El Niño event. The thin line correponds to the average thermocline depth over the period 1958-2007. After Dewitte et al. (2012).*

2010) as compared to prior decades, which has been interpreted as being related to changes in ENSO characteristics due to global warming (Yeh et al., 2009). Indeed, SST projections in CMIP-class models predict an increase in the ratio of CP type to EP type under different global warming scenarios (Kim and Yu, 2012; Yeh et al., 2009), which is associated with changes in the atmospheric circulation over the tropical Pacific (Vecchi et al., 2006; S.-P. Xie et al., 2010). However, the real impact of global warming on the ENSO diversity is difficult to assess, given that this diversity might also be intrinsically forced by natural variability of the climate system. Using random combinations of spatial structures obtained by a linear stochastic model, Newman et al. (2011) showed that extended epochs dominated by either EP or CP events can be reproduced even when excluding the anthropogenically-induced changes in the background state. Such spontaneous generation of multidecadal epochs of CP and EP events has also been reproduced in coupled GCMs (Kug et al., 2010; Wittenberg et al., 2014), which challenges the interpretation of the ENSO diversity as being a forced mode of variability related to the anthropogenic influence on global warming.

1.5 Thesis motivations and objectives

One of the major concerns in the climatic and oceanographic community is the current earth's energy imbalance (EEI), which arises from an imperfect closure of the

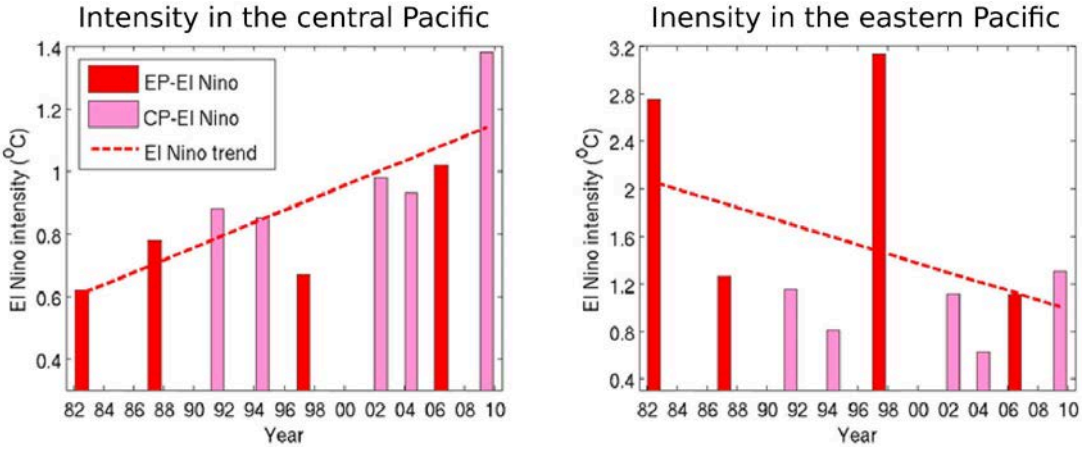

Figure 1.14: *Intensity of El Niño events in the central (left panel) and eastern (right panel) Pacific. Linear trend corresponds to 0.20(±0.18)°C/decade in the central Pacific and 0.39(±0.71)°C/decade in the eastern Pacific. After Lee and McPhaden, 2010.*

planetary radiative budget and manifests as a radiative flux imbalance between the incoming and outgoing radiation in the top of the atmosphere (Hansen et al., 2011). Currently, EEI is positive and is evidenced as a global rise in temperature and sea level, acceleration of the hydrological cycle and increase in the ocean heat content (OHC). Although many aspects of climate are determined by the heat capacity of all the components of the climate system (atmosphere, land, ice and ocean; Trenberth and Stepaniak, 2004), most of the energy accumulation from the EEI manifests as an increased OHC (Abraham et al., 2013; Church et al., 2011), and even though recent evidence shows that the largest fraction of OHC increase has occurred in the upper 700m, both observational and modeling studies indicate that ~25% of OHC increase over the last 45 years took place between 700-2000m depth (Balmaseda et al., 2013; Levitus et al., 2012; Purkey and Johnson, 2010) and indirect estimations for the full-depth OHC are in good agreement with the estimated total EEI (Llovel et al., 2014). This highlights the potential role of the intermediate-deep ocean in buffering the EEI, and calls for a better understanding of the mechanisms that participate in the "ventilation" of the deep oceanic circulation. In this context, the vertical propagation of ETRW that takes place in the SEP, which constitutes a mechanism that links the shallow coastal ocean with the deep offshore and conveys information about the tropical surface variability, has the potential to participate in the oceanic response to the EEI.

While the coastal circulation and its variability in the SEP are relatively well documented, little is known about the variability of the mid-depth and deep circulation components of the system. Observations have shown that currents in the meso and abyssopelagic regions present a marked seasonal cycle, as well as an interannual modulation (Shaffer et al., 2004), which has been interpreted as related to Rossby waves

emanating from the coast in connection with ENSO events. Nevertheless, little has been said about the long-term variations of this mechanism, in connection with the decadal changes observed in the tropical Pacific. No information about a possible impact of the ETRW on the deep ocean other than a modulation of the currents has been brought to light either. This last point is of particular importance, considering the near stagnant nature of the mean circulation in the SEP.

One of the major difficulties in documenting the changes in the SEP circulation is imposed by the lack of a systematic observational system, and particularly in the subsurface, where *in situ* observations are practically nonexistent. International efforts aiming to resolve this issue are currently underway, such as the deployment of floats in the context of the ARGO program, but the spatial and temporal resolution in the SEP is to the present day very low (Fig. 1.15).

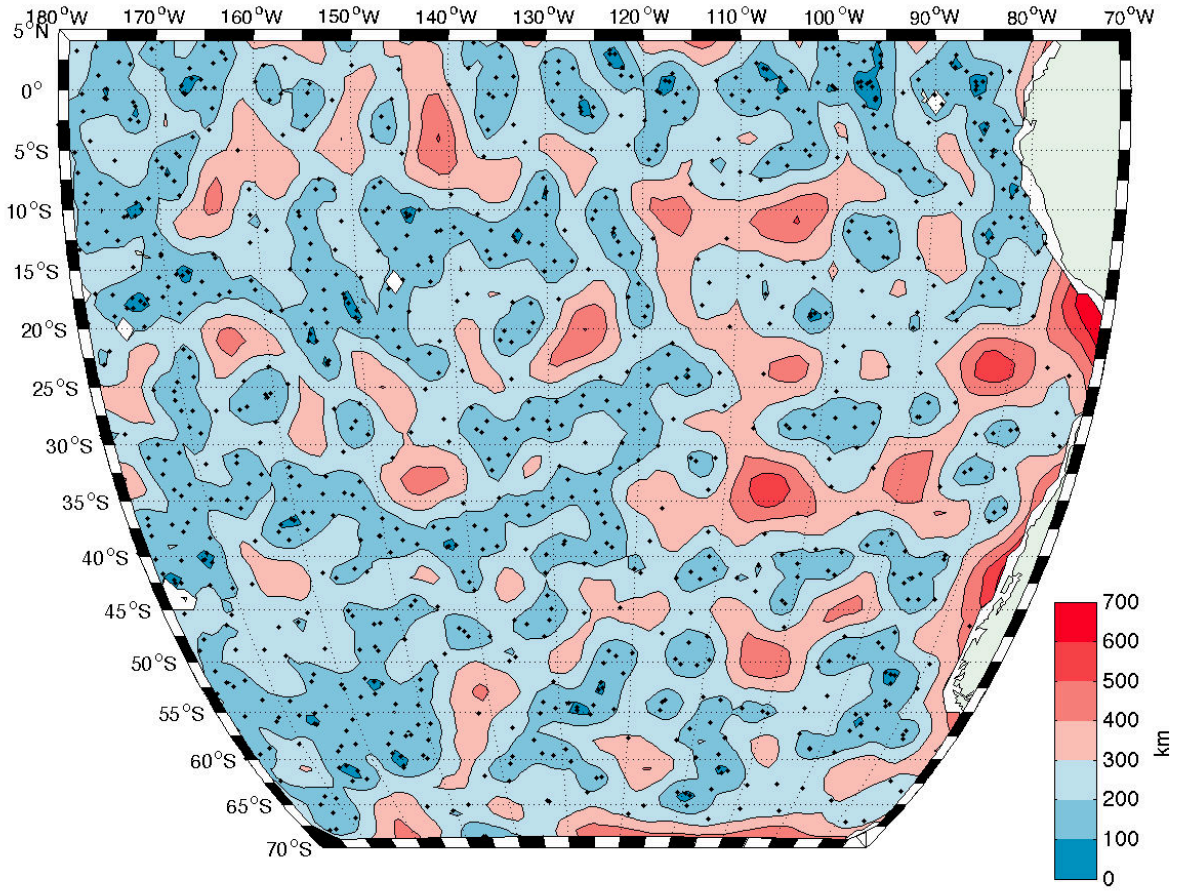

Figure 1.15: *Argo floats sparseness in the south Pacific ocean (as to 21/04/2016). Distance corresponds to the average distance to the 4 nearest floats. Source: http://argo.whoi.edu*

A possible alternative for coping with the lack of in situ observations could come

from the current generation of global general circulation models; however, the spatial resolution that is implemented in the global products generates important misrepresentations of both the oceanic and atmospheric circulation patterns near the coast (Richter, 2015; Zheng et al., 2011), which induces severe biases in the coupled simulations, and particularly in the upwelling regions (Fig. 1.16) where important warm biases are observed. In addition, uncertainties in the atmospheric and oceanic reanalysis products used to force the OGCMs also constitute a source of errors, which has been evoked to interpret the biases observed in forced ocean simulations (e.g. Brodeau et al., 2010). In particular, the accuracy oceanic reanalysis products is penalized by the lack of *in situ* observations available to constrain the assimilation process, which are practically nonexistant in some regions (see Lee and McPhaden (2010) for a review), and atmospheric reanalysis also present errors that are relevant for the dynamics of coastal systems (e.g. wind stress divergence close to the coast (Astudillo et al., 2016); errors in air-sea fluxes (Chaudhuri et al., 2013)). A suitable answer to overcome some of these difficulties could be the use of a regional ocean-modeling platform. The high-resolution capability of this tool greatly improves the biases observed in coastal upwelling systems using global models (e.g. Colas et al., 2012; Dewitte et al., 2012; Penven et al., 2001), and provides with reliable long-term simulations of three-dimensional ocean fields.

In this context, several questions arise regarding the variability of the SEP, which motivates the present work:

- One of the main motivations for the present work is to better understand the seasonal to interannual variability of the deep ocean (subthermocline) in the SEP, with a focus on its forcing mechanisms and how this relates with the elements encompassed by the subthermocline circulation in the SEP. In particular, the implications that the variability of the circulation in this region have for the understanding of the OMZ dynamics is a current concern for the community and remains unaddressed.

- As previously discussed, the ocean plays a central role in the planetary energy budget at climatic scale, which is reflected by the variations in the OHC. The correct interpretation of the current OHC trends (and the EEI trends) therefore requires a sound understanding of the ocean's ability to store and vertically redistribute the excess of energy, which is naturally limited by our knowledge on the processes involved in the deep circulation variability. In this sense, improving the current understanding of a process that could have implications for the ocean's role at climatic scale, such as the vertical propagation of ETRW, is also a motivation for the present work.

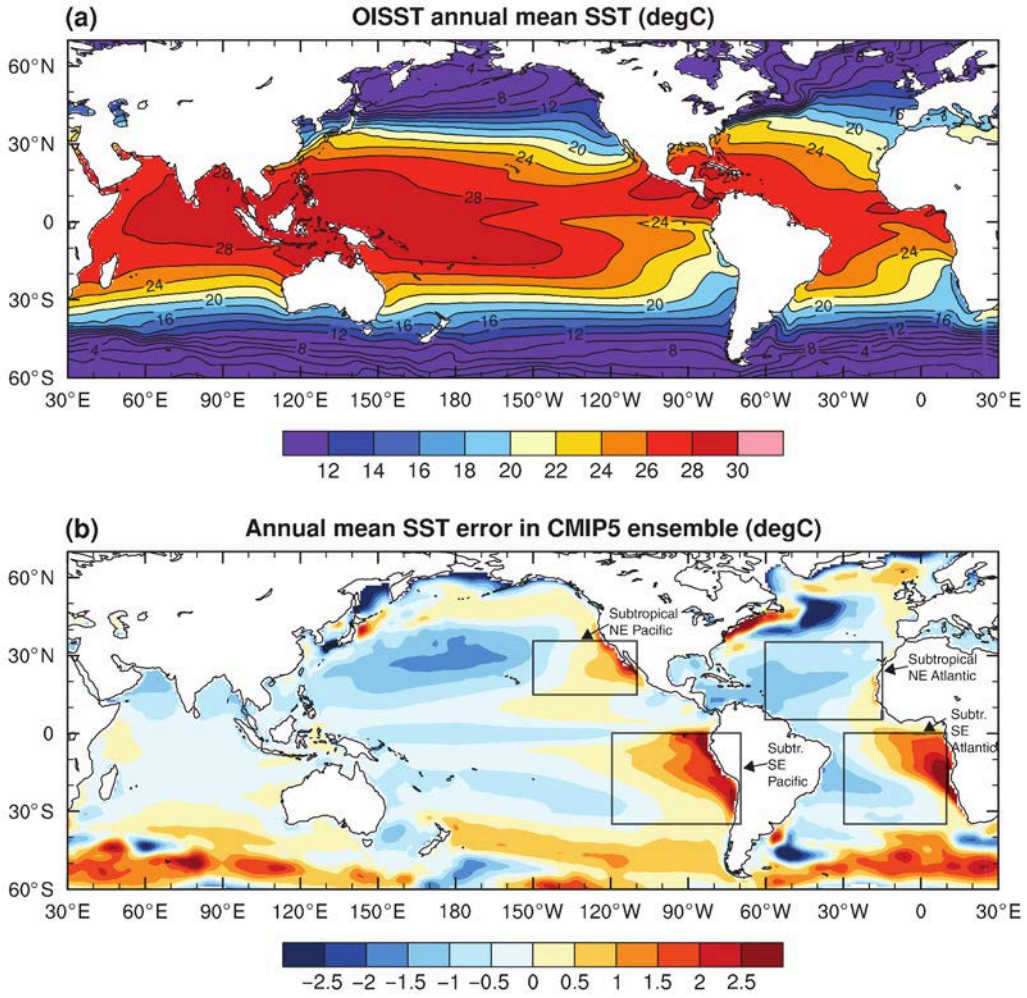

Figure 1.16: *(a) Observed annual mean sea surface temperature (SST) from the optimally interpolated (OI) SST data set. (b) Annual mean bias of the CMIP5 ensemble, relative to OISST. Gray boxes denote the four upwelling regions, where the biases are particularly important. After Richter (2015).*

1.5.1 Scientific objectives and manuscript plan

Although there is substantial evidence that supports the propagation of extra tropical Rossby waves as being a prominent component of the SEP circulation variability at different timescales, this process has not been appropriately diagnosed yet. The main goal of this thesis work is thus to document the connection between the variability that takes place in the equatorial Pacific and the variability of the subsurface circulation along the coasts of Peru and Chile. Within this context, we can summarize the objectives and the approach of the present work as follows:

- To document the vertical energy flux associated with the propagation of the extra-tropical Rossby wave.
- To investigate the influence of the ETRW on the variability of the OMZ.
- The flow fluctuations in the form of mesoscale structures, prominent in the region, should also influence the variability of the circulation in the SEP. To evaluate the influence of the mesoscale activity on the variability of the OMZ, and on the energy flux related to the ETRW are complementary objectives of the present work.

In order to answer to the scientific questions and achieve the objectives previously outlined, the thesis manuscript is organized as follows: *Chapter 2* introduces the tools and methodological approach used to study the variability of the circulation in the SEP and briefly presents the formalism that supports the vertical propagation of extra-tropical Rossby waves. *Chapter 3* focuses on the study of the vertical energy flux related to the propagation of the extra-tropical Rossby wave at interannual to decadal timescales, and how it is impacted by the mesoscale activity. *Chapter 4* addresses the impact that the fluctuations of the circulation in the form of ETRW and mesoscale processes have for the ventilation of the HCS, from the perspective of the OMZ ventilation at seasonal timescale. Finally, *Chapter5* presents the conclusions of the present work and proposes some future perspectives around the study of the subsurface circulation in the region.

Introduction (français)

Situé le long des côtes du Pérou et du Chili, le Système de Courant de Humbolt (HCS[5]) est l'un des plus grand systèmes d'upwelling du monde, reconnu notamment pour sa forte productivité en termes de ressources halieutiques. Ce système de courant est sujet à une riche variabilité induite par les interactions océan-atmosphère ayant lieu tout le long de la côte. Sa variabilité est également modulée par l'influence à distance de la variabilité présente dans le Pacifique équatorial, et qui se propage le long de la côte Sud-Américaine.

La circulation grande échelle du Pacifique s'organise autour d'un système de haute pression, l'Anticyclone du Pacifique Sud (SPA[6]). Cet anticyclone influence les principales caractéristiques de la circulation moyenne dans le Pacifique Sud, dont l'asymétrie Est-Ouest que l'on retrouve dans tous les basins océaniques. Cette asymétrie consiste en des courants très forts vers les pôles coulant le long des façades Ouest des océans, et qui contrastent avec les courants des bords Est, beaucoup moins énergétiques, ce qui entraine de faibles taux de ventilation de la circulation.

Localement, la circulation dans le HCS est fortement liée au vent qui souffle en surface le long des côtes Sud Américaines en direction de l'équateur. Ce vent influence d'une part la circulation moyenne de surface que l'on observe dans la région, dirigée comme le vent vers l'équateur, et d'autre part, le vent parrallèle à la côte induit un transport des eaux de surfaces vers le large, remplacées par des eaux profondes, froides, riches en nutriments et en gaz carbonique. Cette dynamique permet la fertilisation des couches de surfaces sur le plateau continental, ce qui déclenche des maximums locaux de productivité primaire caractéristiques de la région. Bien que l'upwelling soit la principale caractéristique régionale, son intensité varie le long de la côte en fonction de l'orographie locale et de l'intensité du vent. On peut ainsi observer différentes sous-régions : (1) le Pérou, avec un système d'upwelling très productif et quasi-permanent, (2) un système très peu productif entre la frontière Sud du Pérou et le Nord du Chili, et (3) un système très productif et marqué par des variations saisonnières le long des côtes du Chili central et Sud.

En plus de ces systèmes d'upwelling, le HCS abrite la partie sud de la Zone de Minimum d'Oxygène (OMZ[7]) la plus étendue au monde. Cette OMZ résulte de l'interaction entre les forts taux de production primaire ayant lieu dans la couche euphotique, la dégradation de la matière organique produite consommant de l'oxygène, et de la circulation lente et peu énergétique présente sous la surface, ce qui favorise l'accumulation

[5]De l'anglais *Humbolt Currrent System*.
[6]De l'anglais *South Pacific Anticyclone*.
[7]De l'anglais *Oxygen Minimum Zone*.

des eaux pauvres en oxygène.

Malgré leur diversité, les impacts de l'OMZ ont été jusqu'à présent relativement peu étudiés. En effet, l'OMZ du Pacifique Sud est impliquée dans la libération de gaz à effet de serre, notamment le N_2O et le CO_2, qui sont importants à prendre en compte en termes de climat global. De plus, cette zone réduit l'espace habitable par les organismes marins à cause des faibles concentrations en oxygène, ce qui impacte les ressources halieutiques de la région. Ces conséquences peuvent être significatives, et ce à différents niveaux, mais l'étude de la dynamique de l'OMZ en est encore au stade initial. Par exemple, il a récemment été mis en évidence que l'activité méso-échelle régionale serait le facteur principal de la forme et de l'étendue de l'OMZ. Cependant, l'impact de l'activité méso-échelle sur la variabilité de l'OMZ n'a pas encore été étudié. On peut donc s'interroger sur l'effet que la variabilité interne de l'océan pourrait avoir sur les tendances à long terme de l'OMZ.

Les structures de méso-échelle, dominantes dans la région, résultent des instabilités de la circulation, principalement du cisaillement vertical des courants. Les tourbillons de méso-échelle se propagent vers l'Ouest et participent ainsi au bilan de chaleur et de sel entre la zone côtière et le large. Ces structures participent également au couplage physique/biogéochimique qui étend la région fortement productive de la côte vers le large.

En plus du forçage atmosphérique local et de la variabilité interne, la modulation de la circulation du HCS est fortement liée à la variabilité d'origine équatoriale, à des échelles de temps allant de l'intra-saisonnier au décennal. La côte Sud-Américaine agit comme une extension du guide d'ondes équatorial, permettant ainsi la propagation des ondes de type Kelvin piégées à la côte (CTW[8]) vers le pôle. La propagation de ces signaux d'origine équatoriale le long des côtes du HCS entraîne la modulation des caractéristiques océanographiques du plateau continental jusqu'au talus, qui se manifestent sous la forme de perturbations sur les champs de densité et pression, en particulier à l'échelle de temps intra-saisonnière.

L'activité des CTW est particulièrement intense pendant les évènements El Niño (ENSO[9]), qui est relié à une activité plus importante des ondes de Kelvin à l'équateur. Ce mécanisme transmet l'information depuis le Pacifique équatorial vers le HCS, et est responsable des fortes anomalies dans les caractéristiques océanographiques enregistrées le long des côtes Sud-Américaines pendant les évènements ENSO. Par exemple, au cours de la période d'intensité maximale de El Niño 1997-1998, la thermocline s'approfondît de plusieurs dizaines de mètres ($\sim$150 m) du côté Est du Pacifique en réponse au passage des CTW, ce qui était également observé sur le niveau de la mer à

[8]De l'anglais *Coastal Trapped Waves*.
[9]De l'anglais *El Niño Southern Oscillation*.

la côte, avec des anomalies de l'ordre de la dizaine de centimètres. Plusieurs travaux ont évoqués l'idée que les déplacements verticaux de la thermocline, forcés par le passage des CTW au cours de l'ENSO de 1997-1998, pourraient modifier la source des eaux de l'upwelling selon la phase de l'onde ("upwelling" ou "downwelling"). Ce mécanisme, associé aussi aux variations du vent parallèle à la côte, serait à l'origine des chutes des taux de production primaires observés pendant cet évènement, qui ont eu des conséquences catastrophiques sur les ressources halieutiques et leur exploitation dans cette région.

Aux échelles interannuelles, l'influence du Pacifique équatorial sur le HCS n'est pas confinée à la côte, et s'étend également vers le large grâce à la propagation d'ondes de Rossby extratropicales (ETRW[10]). Les premières observations de la propagation de ce type de signal hors des latitudes tropicales ont été apportées par l'altimétrie, avec la mission TOPEX/Poséidon. Ce type d'observations a donné accès, pour la première fois, à un champ quasi simultané du niveau de la mer global, permettant de documenter également la propagation des signaux se dirigeant vers l'Ouest depuis la côte Sud-Américaine, associés à l'évènement El Niño 1997-1998.

Les observations altimétriques mettent aussi en évidence la décroissance significative de l'amplitude de l'ETRW lors de sa propagation vers le large. Ceci peut être lié à différents mécanismes, par exemple, la dissipation turbulente, le "déferlement" de l'onde lié aux instabilités de type barocline, ou encore la dispersion linéaire. La propagation d'énergie verticale induite par la contribution d'un certain nombre de modes baroclines est un autre mécanisme qui peut aussi expliquer l'atténuation de l'onde de Rossby vers le large. Ce type de mécanisme a été étudié dans un premier temps pour expliquer les variations des températures de subsurface observées dans le Pacifique équatorial à l'échelle annuelle, et a été généralisé par la suite pour les variations aux fréquences interannuelles, liées aux variations induites par le phénomène El Niño. Des travaux postérieurs ont mis en évidence que ce processus n'est pas exclusif au Pacifique équatorial, mais que la propagation verticale d'énergie liée à l'onde de Rossby est aussi présente dans le Pacifique Sud-Est. En particulier, Ramos et al. (2008) met en évidence la relation directe qui existe entre la variabilité de la circulation profonde (sous la thermocline) dans le HCS, et la variabilité à l'équateur pendant le fort évènement El Niño de 1997/1998. Ce travail montre également que le signal issu de la propagation d'énergie s'étend sur des centaines de kilomètres vers le large dans l'océan profond depuis les côtes Sud-Américaines, ce qui interroge sur le rôle que ce flux d'énergie pourrait jouer dans la modulation de la circulation profonde dans le HCS. Cette question s'insère dans le contexte actuel où l'on s'interresse aux différents régimes d'ENSO,

[10]De l'anglais *Extra Tropical Rossby Waves*.

et à comment cette diversité pourrait impacter la circulation dans le HCS, sachant que les évènements forts du type 1997-1998 sont plutôt rares.

Les problématiques actuelles liées au déséquilibre radiatif au niveau planétaire, qui sont au centre des recherches dans la communauté climatique, placent l'étude de la circulation profonde et des mécanismes associés à sa variabilité comme l'un de sujets clefs pour comprendre les changements planétaires climatiques. L'océan absorbe et redistribue $\sim$90% de l'excès d'énergie présent dans l'atmosphère sous forme de chaleur, et les études récentes montrent qu'au moins 25% de l'augmentation de température dans l'océan pendant les dernières 45 ans a eu lieu entre 700 et 2000 m de profondeur (Abraham et al., 2013). Cette découverte en particulier permet de s'interroger sur les mécanismes pilotant la redistribution d'énergie au sein de l'océan. Sachant qu'il faut des centaines d'années à la circulation thermohaline pour parcourir un bassin, quels mécanismes sont responsables des changements à l'échelle décennale ? Le but de ce travail est de documenter et de mieux comprendre la connexion entre la variabilité équatoriale et la variabilité de la circulation de subsurface le long des côtes Péruviennes et Chiliennes, à travers la propagation des ondes de Rossby extratropicales. Dans ce contexte, on peut résumer les objectifs et l'approche de ce travail comme suit :

- Documenter le flux d'énergie verticale associé à la propagation des ondes de Rossby extratropicales.
- Estimer l'influence de l'onde de Rossby extratropicale sur la variabilité de l'OMZ.
- Evaluer l'influence de l'activité de méso-échelle sur la variabilité de l'OMZ, et sur le flux d'énergie verticale lié à l'ETRW.

Afin de répondre à ces objectifs, nous avons organisé le manuscrit de thèse de la façon suivante. Le *Chapitre 2* introduit les outils et l'approche méthodologique utilisés pour étudier la variabilité de la circulation dans le Pacifique Sud-Est, et présente aussi de manière succincte le formalisme physique qui justifie la propagation verticale des ondes de Rossby extratropicales. Le *Chapitre 3* est dédié à l'étude du flux d'énergie induit par la propagation de l'ETRW aux échelles de temps interannuelle et décennale, et comment ce flux est impacté par l'activité mésoéchelle. Le *Chapitre 4* étudie l'influence qu'ont les fluctuations de la circulation, sous la forme de l'ETRW et l'activité de méso-échelle, sur la ventilation du HCS, du point de vue de la ventilation de l'OMZ à l'échelle de temps saisonnière. Enfin, le *Chapitre 5* présente les principales conclusions de cette thèse, et propose des perspectives pour l'étude de la circulation de subsurface dans la région.

Chapter 2

Methodology and Observations

In the present chapter we introduce the methodological framework used in the thesis work. During the first part, a concise description of the numerical ocean model used throughout the thesis work is made (a detailed description of the simulations configuration is provided in the *Chapters 3 and 4*). The second part of this chapter pursues with the definition of the physical (Section 4.2) and statistical (Section 4.3) formalisms upon which the diagnostics were built. The chapter concludes with a description of the observational information used in the present work (Section 2.4).

2.1 The regional ocean modeling system: ROMS

The orographic features and the circulation characteristics found in the SEP make this region a challenge for the current generation of geophysical modeling tools. For instance, the coastal upwelling off central Chile is associated with an atmospheric coastal jet 300 km width (Renault et al., 2009), which is comparable to the grid size of a global coupled general circulation models (e.g. CMIP5-class). In this context, several studies have related the global models biases observed in the upwelling regions to misrepresentations of the atmospheric and oceanic processes close to the coast, as a result of an insufficient spatial resolution (e.g. Large and Danabasoglu (2006); S. P. DeSzoeke et al. (2012); Xu et al. (2014); Richter (2015)).

On the other hand, regional models have demonstrated to be an appropriate tool for studying the oceanic and atmospheric processes in the upwelling regions, and particularly in the HCS (e.g. Penven et al. (2005); Montes et al. (2010a, 2011); Colas et al. (2012); Dewitte et al. (2012)). For these reasons, we have chosen the Regional Ocean Modeling System (ROMS; Shchepetkin and McWilliams (2005)) to carry out the present study. The ROMS model solves the Reynolds-averaged Navier-Stokes equations under the hydrostatic and Boussinesq assumptions, which in Cartesian coordinates can be written as:

Momentum conservation:
$$\partial_t u + \vec{u} \cdot \nabla u - fv = -\partial_x \phi + \mathcal{F}^u + \mathcal{D}^u \tag{2.1}$$
$$\partial_t v + \vec{u} \cdot \nabla v + fu = -\partial_y \phi + \mathcal{F}^v + \mathcal{D}^v \tag{2.2}$$

Hydrostatic approximation:
$$\partial_z \phi = -\frac{\rho g}{\rho_0} \tag{2.3}$$

Tracer conservation:
$$\partial_t T + \vec{u} \cdot \nabla T = \mathcal{F}^T + \mathcal{D}^T \tag{2.4}$$
$$\partial_t S + \vec{u} \cdot \nabla S = \mathcal{F}^S + \mathcal{D}^S \tag{2.5}$$

Continuity:
$$\partial_x u + \partial_y v + \partial_z w = 0 \tag{2.6}$$

Equation of state:
$$\rho = \rho(T, S, z) \tag{2.7}$$

with the surface ($z = \xi$) and bottom ($z = -h$) boundary conditions prescribed as:

$$\begin{array}{cc} \boxed{z = \xi} & \boxed{z = -h} \\ A_v \partial_z u = \tau^x{}_s & A_v \partial_z u = \tau^x{}_b \\ A_v \partial_z v = \tau^y{}_s & A_v \partial_z v = \tau^y{}_b \\ K_v^T \partial z T = \frac{Q}{\rho_0 C_p} & K_v^T \partial z T = 0 \\ K_v^S \partial z S = \frac{(E-P)S}{\rho_0} & K_v^S \partial z T = 0 \\ w = \partial_t \eta + u \partial_x \eta + v \partial_y \eta & w = -u \partial_x h - v \partial_y h \end{array} \tag{2.8}$$

where:

- $\vec{u} = (u, v, w)$ is the velocity field, in Cartesian coordinates,
- $f(x, y)$ is the Coriolis acceleration,
- $h(x, y)$ is the depth of sea floor below mean sea level,
- $\eta(x, y, t)$ is the surface elevation,
- g is the gravitational acceleration,
- $\rho_0 + \rho$ is the total density,
- $T(x, y, z, t)$ and $S(x, y, z, t)$ are the potential temperature and salinity fields,
- P is the total pressure ($P \approx -\rho_0 g z$),
- $\phi(x, y, z, t)$ is the dynamic pressure, equal to $\frac{P}{\rho_0}$,

- $\mathcal{F}^u$,$\mathcal{F}^v$,$\mathcal{F}^T$ and $\mathcal{F}^S$ correspond to forcing/source terms,
- $\mathcal{D}^u$,$\mathcal{D}^v$,$\mathcal{D}^T$ and $\mathcal{D}^S$ correspond to the horizontal, diffusion terms,
- ${\tau^x}_s$, ${\tau^y}_s$ are the Cartesian components of the wind stress,
- ${\tau^x}_b$, ${\tau^y}_b$ are the components of the bottom stress,
- Q and $E - P$, represent the surface heat, evaporation and precipitation fluxes respectively,
- A_v, K_v^T and K_v^S are the vertical mixing coefficients (viscous, temperature and salinity).

Please note that there is no river runoff forcing in the simulations used in the present thesis, considering that there are no large rivers north of 37°S.

2.1.1 Coordinate transformation

The search for numerical efficiency, and the need to deal with steep topography and better account for mixing processes incited ROMS developers to apply a spatial coordinate change before actually solving the equations system (Eqs. 2.1 to 2.7). In the vertical, the Cartesian coordinate system is replaced by a stretched-vertical coordinate system that follows the topographic irregularities (σ-coordinate), with the possibility of increasing the vertical resolution close to the upper and lower boundaries. The stretched vertical coordinates (s) are related to the Cartesian z-levels by:

$$z = \eta(1+s) + h_c s + (h - h_c)C(s); s \in [-1, 0] \tag{2.9}$$

where s is a nonlinear vertical transformation function, η represents the free surface (as in Eq. 2.8), $h(x, y)$ is the unperturbed water column thickness, h_c is a positive thickness that controls the stretching, C is a non-dimensional, monotonic, vertical stretching function ranging from $[-1, 0]$ defined as:

$$C(s) = (1-b)\frac{\sinh(\theta s)}{\sinh(\theta)} + b\frac{\tanh(\theta(s+1/2)) - \tanh(\frac{\theta}{2})}{2\tanh(\frac{\theta}{2})} \tag{2.10}$$

In practice, the vertical resolution in the water column is adjusted using the parameter h_c, and the resolution at the bottom and near the surface is adjusted by the parameters θ and b respectively.

In the horizontal direction, the Cartesian coordinates are also replaced by a different basis that copes better with the terrain irregularities. In ROMS this is achieved

by implementing a coordinates change from Cartesian to curvilinear. Let $\eta^\star(x, y)$ and $\xi^\star(x, y)$ be the new coordinate system, which relate to the velocity field as:

$$\begin{aligned} \vec{v} \cdot \hat{\xi}^\star &= u \\ \vec{v} \cdot \hat{\eta}^\star &= v \end{aligned} \tag{2.11}$$

which can be used to re-write equations (2.1) to (2.7) (cf. Arakawa and Lamb (1977)).

2.1.2 Pressure gradient errors

The approach of vertical coordinate change results in an accurate representation of the bottom and surface conditions. However, this approach entails significant errors in the computation of the pressure force gradient. The pressure force gradient is represented by the sum of two terms in the s coordinate system; a pressure gradient along the s-isopleths plus a corrective term that prevents vertical pressure gradients in the first term. This relationship can be expressed, in the x direction, as follows:

$$\begin{aligned} -\frac{1}{\rho_0}\frac{\partial P}{\partial x}\Big|_z &= -\frac{1}{\rho_0}\frac{\partial P}{\partial x}\Big|_s + \frac{1}{\rho_0}\frac{\partial z}{\partial x}\Big|_s \frac{\partial P}{\partial z} \\ &= -\frac{1}{\rho_0}\frac{\partial P}{\partial x}\Big|_s + \frac{1}{H_z}\frac{1}{\rho_0}\frac{\partial z}{\partial x}\Big|_s \frac{\partial P}{\partial s} \end{aligned} \tag{2.12}$$

where

$$H_z \equiv \frac{\partial z}{\partial s} \tag{2.13}$$

The problem arises near steep topographic features, where both terms acquire similar amplitude but with opposing sign, which might translate as important truncation errors when resolving in discrete form (Song, 1998). Over topographic features, this error is the highest near the bottom, where the s-coordinate slopes are very steep. To minimize this error, the implementation of a high-order finite differences scheme and a topography smoothing pre-processing are recommended. The level of smoothing applied to the topography (h) is done following $r = \frac{\triangle h}{h}$. As shown by Haidvogel et al. (1991), $r \leq 0.2$ greatly improves the errors associated with the topographic effect.

2.1.3 Spatial discretization and time stepping

The governing equations (Eqs. 2.1 to 2.7) are discretized over a boundary-fitted, orthogonal-curvilinear coordinates $(\xi^\star, \eta^\star)$ grid. The discretization is made over a second-order scheme, using an Arakawa C-grid (Fig. 2.1a); Arakawa and Lamb (1977)),

which in combination with an adequate spatial resolution allows resolving spatial scales smaller than the local Rossby deformation radius (Hedström, 1997). The model variables are staggered over the Arakawa C-grid so the free surface, density and tracers are located at the center of the cell whereas the horizontal velocity components are located at the west/east and south/north edges of the cell, respectively. That is, the density is evaluated between the grid cell points where the currents are evaluated.

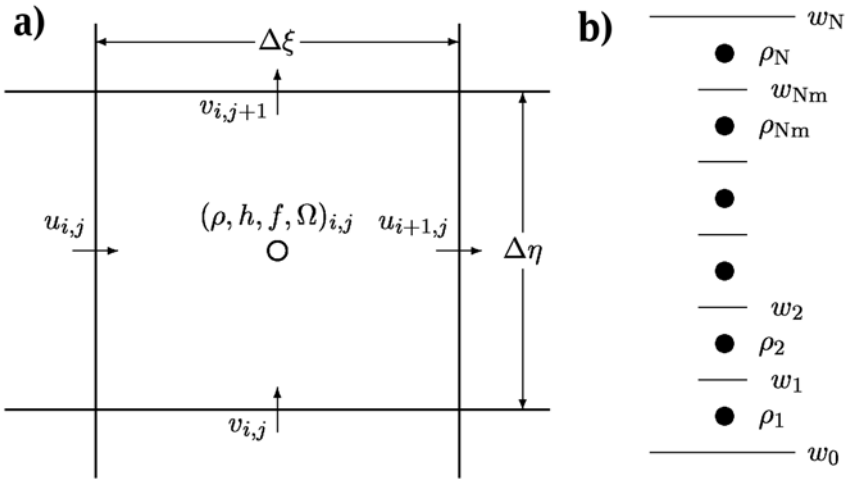

Figure 2.1: *(a) Placement of variables on an Arakawa C-grid. Note the horizontal spacing between the velocity components and the other variables. (b) Placement of variables on the staggered vertical grid.*

In the vertical direction, the discretization is made over the terrain following grid described in section 2.1.1. The model state variables are vertically staggered so that horizontal momentum, density and tracers are located at the center of the grid cell, while vertical velocity and vertical mixing variables are located at the boundaries of each grid cell (Fig. 2.1b).

In order to correctly resolve the variability associated with the barotropic mode (much faster than the one related to the baroclinic modes), a mode-splitting technique is applied to resolve the primitive equations and the continuity equation in the temporal scheme. This consists in separating the baroclinic (3D) flow component from the barotropic (2D) one, before solving the equations, and re-coupling them afterward. The mode splitting is done using a time filter, which ensures that the continuity equation is satisfied on the discrete level, thus removing previous restrictions of small free-surface changes (Marchesiello et al., 2003). Solving the baroclinic flow component is (numerically) more expensive than solving the barotropic component, so the barotropic mode iteration is done a certain number of times for each iteration of the baroclinic mode.

The re-coupling between the modes is done by several subsequent substitutions between the barotropic velocities (2D) and the vertical integral of the baroclinic velocities. To avoid any potential aliasing of the 2D high-frequencies in the 3D model, the barotropic components are averaged over the baroclinic time stepping (Shchepetkin and McWilliams, 2005). The time stepping used corresponds to a third-order leap-frog/Adams-Moulton (predictor-corrector) scheme.

2.1.4 Advection scheme and mixing parametrization

The tracer and momentum advection terms are processed with high order advection schemes, conceived to minimize diffusion and the errors related to dispersion. For the horizontal advection, a third-order upstream-biased scheme is used. This scheme in particular has a velocity-dependent hyper-diffusion dissipation as the dominant truncation error (Shchepetkin and McWilliams, 1998). In the vertical, the advection is found by reconstructing the vertical derivatives using parabolic splines (equivalent to a 8th-order conventional advection scheme).

The vertical mixing parametrization in ROMS can be either by local or non-local closure schemes. The most extensively used is the non-local closure scheme based on the K-profile boundary layer formulation (KPP; Large et al. (1994)), that computes the vertical mixing coefficients (A_v, K_v^T and K_v^S) in the water column. The boundary conditions of the vertical flux provide the momentum and tracer fluxes at the bottom and surface.

The horizontal sub-grid scale mixing is parametrized by a biharmonic Laplacian term, which also smooths the numerical noise related to the advection scheme. However, implementing this smoothing requires the introduction of important diffusion-dissipation terms, which in turn induce a numerical diffusion. By construction, the advective scheme of ROMS limits the dispersion, which means that the dissipation-diffusion is implicitly treated by the advection scheme, depending on the horizontal grid size. In this manner, the horizontal viscosity/diffusion coefficients are optimized by the advection scheme itself. The horizontal diffusion coefficients are therefore defined as:

$$\begin{aligned} D_h^q &= A_h^q \Delta_h q + B_h^q \Delta_h^2 q, \\ \text{where } \; q = u, v, T, S, \;\; &\text{and} \;\; \Delta = \partial_{xx}^2 + \partial_{yy}^2 \\ &\text{and } A_h^q, B_h^q \text{ are determined implicitly.} \end{aligned} \tag{2.14}$$

2.2 Long Rossby waves

As was established in *Chapter 1*, the central objective of the present work is to document the variability of the circulation in the SEP related to the vertical propagation of long Rossby waves. In this sense, it becomes important to recall certain elements that allow to develop the Rossby wave theory.

2.2.1 At the origin of long Rossby waves: the β-plane

The Coriolis parameter is defined as $f = 2\Omega \sin(\theta)$, where Ω is the angular rotation rate of the Earth and θ is the latitude. If we consider a varying latitude, we can expand f (using a Taylor series) around a given latitude θ_0:

$$\begin{aligned} f &= f_0 + \frac{\partial f}{\partial \theta}\Big|_{\theta_0} \Delta\theta + \frac{\partial^2 f}{\partial \theta^2}\Big|_{\theta_0} \frac{\Delta\theta^2}{2} + ... \\ &= 2\Omega \sin(\theta_0) + 2\Omega \cos(\theta_0)(\theta - \theta_0) + \mathcal{O}(\Delta\theta^2) \end{aligned} \tag{2.15}$$

where $f_0 = 2\Omega \sin(\theta_0)$ and $\Delta\theta = \theta - \theta_0$. Retaining the first two terms, we have:

$$f = f_0 + \beta_0 y \tag{2.16}$$

where $\beta_0 = 2(\Omega/a)\cos(\theta_0)$ and $y = a\Delta\theta$, where a is the radius of the Earth. Retaining only the first term in Eq. (2.15) corresponds to a fixed latitude approximation, the so called f-plane. However, we are interested in a framework that allows for variations of the Coriolis parameter values. Equation (2.16) describes the linear change of the Coriolis parameter with latitude, and is known as the β-plane. For more rigorous developments of the β-plane approximation, the reader can refer to the works of Veronis (1963, 1981), Pedlosky (1987), and Verkley (1990). This simple approximation that allows for the variations of the Coriolis parameter is what gives rise to the propagation mechanism of Rossby waves.

Consider two water parcels located at a given latitude θ_0, and move one poleward (Fig. 2.2a) and the other equatorward (Fig. 2.2b). If we assume a constant depth around the latitude θ_0, the conservation of potential vorticity reduces to a conservation of absolute vorticity $\zeta + f$. The parcel that was moved poleward will increase its planetary vorticity (and acquire clockwise relative vorticity), while the one that was displaced towards the equator will decrease its planetary vorticity (and get anti-clockwise relative vorticity). This perturbations introduced in the vorticity field will generate in turn an anomalous circulation. The net effect of the induced circulation on the vorticity distribution is to advect the interface northward, west of the vorticity minimum (Fig.

2.2a), and southward, west of the vorticity maximum (Fig. 2.2b). In this manner, the water parcels oscillate around the equilibrium latitude θ_0, and the perturbation propagates westward. This westward propagation of the anomalies constitutes in principle a Rossby wave.

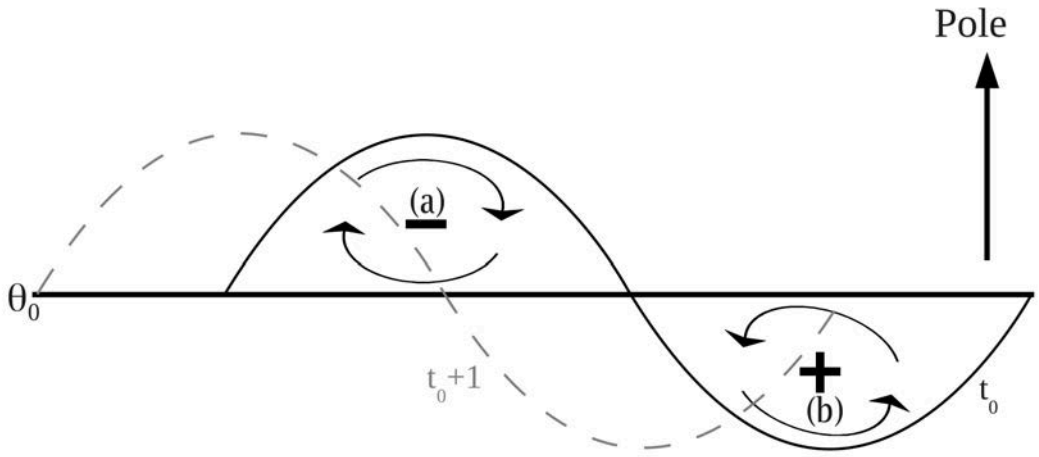

Figure 2.2: *Direction of relative vorticity generated by the meridional (a) poleward and (b) equatorward movement of water parcels. Plus and minus signs indicate the positive/negative relative vorticity acquired due to the meridional displacement.*

Having described the principles for the existence of the long Rossby wave, it is now appropriate to develop its formalism, which will be used to diagnose this phenomenon.

2.2.2 The dispersion relation for long Rossby waves

Consider the horizontal movement equations restricted to homogeneous, inviscid and unforced flows on a β-plane, in the linearized shallow water approximation. The general idea behind the linearization around a state of rest is that all variables involved have infinitesimal small amplitude. This means that terms linearly dependent on these variables have very small amplitude, and the non-linear terms are even smaller (i.e. negligible). With all these assumptions, the horizontal momentum conservation equations (Eq. 2.1 and 2.2) become:

$$\begin{aligned} \frac{\partial u}{\partial t} - (f_0 + \beta y)v &= -g\frac{\partial \eta}{\partial x} \\ \frac{\partial v}{\partial t} + (f_0 + \beta y)u &= -g\frac{\partial \eta}{\partial y} \end{aligned} \tag{2.17}$$

where η corresponds to the anomalies of the surface elevation and f_0 the Coriolis parameter at a given latitude. For this approximation, the vertically integrated continuity equation (Eq. 2.6) becomes:

$$\frac{\partial \eta}{\partial t} + H\left(\frac{\partial u}{\partial x} + \frac{\partial v}{\partial y}\right) = 0 \tag{2.18}$$

The system (2.17) can be rearranged as:

$$\begin{aligned} f_0 v &= g\frac{\partial \eta}{\partial x} + \left(\frac{\partial u}{\partial t} - \beta y v\right) \\ f_0 u &= -g\frac{\partial \eta}{\partial y} - \left(\frac{\partial v}{\partial t} + \beta y v\right) \end{aligned} \tag{2.19}$$

which can be reinjected into Eq. 2.17 to obtain:

$$\begin{aligned} &\frac{1}{f_0}\frac{\partial}{\partial t}\left[-g\frac{\partial \eta}{\partial y} - \left(\frac{\partial v}{\partial t} + \beta y u\right)\right] - f_0 v - \frac{\beta y}{f_0}\left[g\frac{\partial \eta}{\partial x} + \left(\frac{\partial u}{\partial t} - \beta y v\right)\right] = -g\frac{\partial \eta}{\partial x} \\ &\frac{1}{f_0}\frac{\partial}{\partial t}\left[g\frac{\partial \eta}{\partial x} - \left(\frac{\partial u}{\partial t} - \beta y v\right)\right] + f_0 u - \frac{\beta y}{f_0}\left[-g\frac{\partial \eta}{\partial y} - \left(\frac{\partial v}{\partial t} + \beta y u\right)\right] = -g\frac{\partial \eta}{\partial y} \end{aligned} \tag{2.20}$$

In this system, the terms dominated by β are small compared to f_0 and can therefore be dropped. In addition, we are interested in solutions dominated by a frequency much lower than the changes in the flow, so the time derivatives involving the velocity field can also be dismissed. This is equivalent to applying the first order geostrophic approximation in Eq. 2.19, namely $u \simeq -g/f_0 \partial_y \eta$ and $v \simeq g/f_0 \partial_x \eta$. Rearranging Eq. 2.20 in terms of u and v yields:

$$\begin{aligned} v &= \frac{g}{f_0}\frac{\partial \eta}{\partial x} - \frac{g}{f_0^2}\frac{\partial^2 \eta}{\partial y \partial t} - \frac{\beta g}{f_0^2} y \frac{\partial \eta}{\partial x} \\ u &= -\frac{g}{f_0}\frac{\partial \eta}{\partial y} - \frac{g}{f_0^2}\frac{\partial^2 \eta}{\partial x \partial t} - \frac{\beta g}{f_0^2} y \frac{\partial \eta}{\partial y} \end{aligned} \tag{2.21}$$

Injecting Eq. 2.21 into 2.18 leads to:

$$\frac{\partial \eta}{\partial t} + H\left[\frac{\partial}{\partial x}\left(\frac{-g}{f_0}\frac{\partial \eta}{\partial y} - \frac{g}{f_0^2}\frac{\partial^2 \eta}{\partial x \partial t} + \frac{\beta g}{f_0^2} y \frac{\partial \eta}{\partial y}\right) + \frac{\partial}{\partial y}\left(\frac{g}{f_0}\frac{\partial \eta}{\partial x} - \frac{g}{f_0^2}\frac{\partial^2 \eta}{\partial y \partial t} - \frac{\beta g}{f_0^2} y \frac{\partial \eta}{\partial x}\right)\right] = 0 \tag{2.22}$$

which can be expressed as a single equation for the surface displacement:

$$\frac{\partial \eta}{\partial t} - \frac{c^2}{f_0^2}\frac{\partial}{\partial t}\nabla^2\eta - \beta\frac{c^2}{f_0^2}\frac{\partial \eta}{\partial x} = 0 \tag{2.23}$$

where $c^2 = gH$ is the phase speed, and ∇^2 is the two-dimensional Laplace operator. We assume a plane wave-like solution of the form $\eta = \eta_0 e^{[i(kx+ly-\omega t)]}$, where k and l are the zonal and meridional wavenumbers respectively, and ω the angular frequency. We introduce this solution in Eq. 2.23, to obtain:

$$-i\omega - \frac{c^2}{f_0^2}(-i\omega)(-k^2 - l^2) - \beta ik\frac{c^2}{f_0^2} = 0 \tag{2.24}$$

or

$$\boxed{\omega = -\frac{\beta k}{k^2 + l^2 + f_0^2/c^2}} \tag{2.25}$$

which corresponds to the dispersion relation for long Rossby waves[1]. Eq. 2.25 states how the angular frequency ω relates to the two horizontal wavenumbers k and l. From this dispersion relation, we can find the phase speed of the wave, which in the zonal direction is given by $c^{(x)} = \omega/k$. This relations hip gives a negative phase velocity, which in Cartesian coordinates implies a westward propagation direction. The meridional phase velocity is found similarly ($c^{(y)} = \omega/l$), and has no preferred direction.

This approximation for deriving the long Rossby waves dispersion relation (Eq. 2.25) is suitable for latitudes near the equatorial region, where the use of a Cartesian form of the governing equations produces an isometric coordinate system. However, this approximation can be generalized to be used in the extra tropical region, yielding the exact same result. This is achieved by performing a coordinate change from Cartesian to a local Mercator projection. The process requires expanding the coordinate system around a latitude of interest φ_0 and substituting the corresponding variables in the momentum and continuity equations. For the development of the mid-latitude β-plane, the reader is invited to refer to Gill (1982), section 12.2.

Although the assumptions made here are satisfactory for the theoretical development of long Rossby waves, there are serious restrictions for its application to the real ocean. One of the strongest conditions imposed in most studies is the assumption that the ocean reduces to one baroclinic mode (i.e. two homogeneous layers). In reality, stratification (along with f and g) is one of the key steering factors for ocean flows

[1]Please note that if we consider the short wave limit ($k \to \infty$), equation 2.25 can be reduced to $\omega = -\beta/k$, which yields a positive phase velocity in the x-direction. Thus, *short* Rossby waves propagate eastward as opposed to westward propagating long Rossby waves.

and cannot be easily neglected. In particular, the exclusion of a more realistic vertical ocean structure precludes any process that could take place in the vertical dimension, which is actually the focus of the present study. This motivates to complement the present theoretical approach with the appropriate elements for studying the processes associated with long Rossby waves in the vertical.

2.2.3 Theoretical approach for vertically propagating Rossby waves

One approach commonly used involves a simplification of the momentum equations using a variables separation technique, which gives the solution of a system as a sum of normal modes. Each of these modes has a characteristic fixed vertical structure and behaves in the horizontal dimension (and in time) in the same way as a homogeneous fluid with a free surface. In other words, this technique grants access to the vertical dimension while retaining the simplicity of the barotropic approximation.

In this case we look for solutions of the linearized movement equations with a separable vertical structure in the form:

$$[u, v, \eta]\,(x, y, z, t) = \sum_{n=0}^{\infty} [u_n, v_n, \eta_n]\,(x, y, t) \cdot \Psi_n(z) \tag{2.26}$$

This represents the fields $[u, v, \eta]$ as the sum of a barotropic mode ($n = 0$) plus an infinite number of baroclinic modes ($n \in [1, \infty]$), where $\Psi_n(z)$ is the vertical structure associated with the n^{th} mode. The equations 2.17 and 2.18 can be therefore rewritten for the case of a continuously stratified ocean as:

$$\begin{aligned} \frac{\partial u_n}{\partial t} - (f_0 + \beta y) v_n &= -g \frac{\partial \eta_n}{\partial x} \\ \frac{\partial v_n}{\partial t} + (f_0 + \beta y) u_n &= -g \frac{\partial \eta_n}{\partial y} \\ \frac{\partial \eta_n}{\partial t} + \frac{c_n^2}{g} \left(\frac{\partial u_n}{\partial x} + \frac{\partial v_n}{\partial y} \right) &= 0 \end{aligned} \tag{2.27}$$

for the horizontal direction, and:

$$\frac{d}{dz} \left(\frac{1}{N^2} \frac{d\Psi_n(z)}{dz} \right) = -\frac{1}{c_n^2} \Psi_n(z) \tag{2.28}$$

for the vertical, where $N^2 = -\frac{g}{\rho_0} \frac{\partial \rho}{\partial z}$, is the Brunt-Väisälä frequency and c_n is a constant of separation for the homogeneous equation 2.28. This system satisfies the dispersion relation for long Rossby waves (2.25), which becomes:

$$\omega = -\frac{\beta k}{k^2 + l^2 + f_0^2 / c_n^2} \tag{2.29}$$

As shown in Ramos et al. (2008) and Dewitte et al. (2008b), this dispersion relation can be adapted to study the vertical propagation of extratropical Rossby waves in slowly varying media (WKB approximation). The first assumption involves the consideration of very long zonal wavelengths (hence low k), meaning that $k^2+l^2 \approx 0$. This assumption yields a reduced form of Eq. 2.29:

$$\omega = -\frac{\beta k c_n^2}{f_0^2} \tag{2.30}$$

This expression can be differentiated with respect to the local vertical wavenumber m_n, to obtain the vertical group velocity. From the relation $m_n = N/c_n$ (cf. Gill (1982), section 6.11), the vertical group velocity (c_{ng}^z) is:

$$c_{ng}^z = \frac{dz}{dt} = \frac{\partial \omega}{\partial m} = \frac{2\beta k N^2}{f_0^2 m^3} \tag{2.31}$$

similarly, the zonal group velocity can be estimated:

$$c_{ng}^x = \frac{dx}{dt} = \frac{\partial \omega}{\partial k} = -\frac{\beta c_n^2}{f_0^2} \tag{2.32}$$

In general terms, c_{ng}^x and c_{ng}^z define the velocity at which the energy or information is conveyed along the wave, and we can define the trajectory of the wave energy in the (x, z) plane as:

$$\boxed{\frac{dz}{dx} = \frac{c_g^z}{c_g^x} = 2\frac{\omega f_0^2}{\beta c N}} \tag{2.33}$$

Relation 2.33 defines the wave ray-paths under the WKB assumption, and will be used in the following chapters to diagnose the vertical propagation of long Rossby waves. In particular, Eq. 2.33 will be used in *Chapter 3* to investigate the changes of the propagation characteristics of ETRW related to the ENSO diversity.

It should be kept in mind that the solution and application of the relation 2.26 (and subsequent relations) for the study of long Rossby waves under the assumptions made here (known as the Standard Linear Theory (SLT)), relies on a very simplified approximation of the ocean. It therefore does not take into account the impact that several characteristics of the real ocean could have on the structure and phase speed of the normal modes, such as the coupling with bottom topography (Killworth and Blundell, 1999; Tailleux, 2012), mean flow (Fu and Chelton, 2001; Killworth and Blundell, 2003a,b, 2004, 2005; Tailleux, 2012) or vertical vorticity shears (R. A. DeSzoeke and Chelton, 1999). In particular, in a work that evaluated the effect[2] of the baroclinic mean

[2]The theoretical framework that takes into account the effects of the mean flow and bathymetry is known as the Extended Linear Theory (Killworth and Blundell, 2003a,b).

flow and bathymetry on the surface signature of long Rossby waves in the subtropical Pacific (poleward of 17°S) west of ~100°W, Maharaj et al. (2007) evidenced that the first two baroclinic modes from the extended theory explained up to 60% more variance in the observed SLA signal than their SLT equivalents. Moreover, in that work the authors indicate that the impact of the mean flow tends to be the most influential factor in the extended theory, which suggests that the effect of the mean baroclinic flow should be considered in the study of ETRW over the central-western Pacific. Over the SEP however, estimations of the effect of the mean baroclinic flow on the phase speed value and vertical structure of the first two baroclinic modes show that there is little deviation between the standard and the extended linear theories for this region (Ramos et al., 2008), which provides confidence in using the relations derived from the SLT for the study of the ETRW in the SEP. The relevance of our approximation will be assessed *a posteriori*, in the light of the results exposed in *Chapters 3* and *4*.

2.2.4 Rossby wave energy flux

In the ocean, a significant fraction of the wind power is converted to buoyancy power, which in turn causes vertical movements in the isopycnals and affects the rate of change of available potential energy. In the tropics, the mean available potential energy is primarily a measure of the mean thermocline slope along the equator (Brown and Fedorov, 2010). Therefore, in the tropical Pacific, there is a direct connection between the wind power at the ocean surface and the mean thermocline slope. In the mid-latitudes of the SEP, a large fraction of the wind power that originates in the tropics is converted to buoyancy power in the subthermocline, through the propagation of extra-tropical Rossby waves that originate from the coast and propagate westward and downward. Buoyancy power (B) causes vertical movements in the isopycnals and affects the rate of change of available potential energy (dE/dt). For a water parcel of volume V, the buoyancy power can be written as follows: $B = \iiint(\rho' g w) dV$, where ρ' is the anomalous density related to the vertical displacement of the isopycnal and w is the vertical velocity (see equation 5 of Brown and Fedorov (2010)).

This buoyancy power can be related to the vertical energy flux in the ocean associated with the vertical movements of the isopycnals, and has a correspondence with the vertical component of the mechanical energy flux (the so-called Eliassen and Palm flux, (wp)). For the long-wave field, the mechanical energy flux vector can be defined as (up, vp, wp), where (u, v, w) is the velocity field and p is the pressure field (Eliassen and Palm, 1960). This definition will be used in *Chapter 3* to diagnose the vertical energy flux associated with long Rossby waves at interannual to decadal timescales,

and the results of the vertical energy flux will be interpreted in light of the theoretical framework provided by Eq. 2.33.

Dissipation of the Rossby wave energy flux

In principle, the energy flux induced by the vertical propagation of long Rossby waves is an adiabatic (reversible) process, which means that it only acts to conservatively reorganize the energy field. However, as we will see in *Chapter 3*, we observe that the amplitude of the vertical energy flux associated with different timescales decreases (or attenuates) along the propagation trajectory. Invoking the energy conservation principle, this amplitude attenuation implies that the wave energy must be transferred to some other process, and several hypotheses involving the non-linearities in the momentum conservation equations exist in this regard (e.g. baroclinic instability and subsequent breaking of the waves (Lacasce and Pedlosky, 2004), momentum diffusion into the eddy field (Qiu et al., 1997), wave triad instability (Qiu et al., 2013)). Recent theoretical results also indicate that the vertical amplitude attenuation of long Rossby waves in the mid-latitudes could be due to diapycnal diffusion (i.e. non-linearities in the tracer conservation equation; (Marchal, 2009)), which has also been observed in realistic ocean simulations (Furue et al., 2015).

In order to gain further insight on the variations of the vertical energy flux, we develop a formalism based on the anomalous vertical mass flux, which is used in *Chapter 3* to interpret our results.

In conditions of stable stratification, the anomalous vertical mass flux associated with the vertical displacement of a water parcel is given by $m_z = \overline{\rho' w'}$ (Monin and Ozmidov, 1985), where the prime denotes the fluctuating density and vertical velocity. As the water parcel is displaced vertically, a potential energy per unit volume per second is associated with the change in height, which can be written as $\overline{g\rho' w'}$.

Assuming that the density fluctuations in the subthermocline are essentially controlled by variations in temperature (T'), we have:

$$\rho' = -\alpha \rho_0 T' \tag{2.34}$$

where α is the volume expansion coefficient of seawater and ρ_0 is the average density. The expression for the potential energy associated with m_z can then be written as:

$$\overline{g\rho' w'} = -g\alpha\rho_0 \overline{w'T'} \tag{2.35}$$

Before proceeding further, it is convenient to verify how the vertical gradients of w' scale in relationship to the vertical gradients of p', for the scales of interest. This condition will allow us to derive a simplified expression involving $\overline{p'w'}$ (the vertical component of mechanical energy flux vector induced by the anomalous p' and w' fields) from Eq. 2.35.

From the relations that govern small perturbations in an incompressible stratified fluid, we can write the vertical velocities associated with those perturbations in terms of the time derivative of the density perturbations:

$$\frac{\partial \rho'}{\partial t} = w' N^2 \frac{\rho_0}{g} \tag{2.36}$$

where N is the Brunt-Vaisala frequency. Using the hydrostatic relation, we can rearrange Eq. 2.36 in the form:

$$w' = -\frac{1}{\rho_0 N^2} \frac{\partial}{\partial t} \left[\frac{\partial p'}{\partial z} \right] \tag{2.37}$$

For large-scale waves, the rate of change of pressure perturbations (and velocity) is proportional to the wave frequency ($\partial p'/\partial t \propto \omega$), which allows us to write the dimensional analysis of $\partial w/\partial z$ (taking the vertical derivative of Eq. 2.37) as:

$$\frac{\partial w'}{\partial z} = \frac{\Delta w'}{\Delta z} \approx \frac{\omega}{N^2} \frac{p'}{\rho_0 H^2} \tag{2.38}$$

where ω the frequency of interest and H is a vertical scale of variation for w' (which for the first three baroclinic modes is in the order of 10^3 to $10^2 m$, see Ramos et al. (2008)). Considering a period superior to 1 year (interannual), H as 10^3 m, a Brunt-Vaisala frequency of 0.2 cycles per hour (in the range of the lowest measured values in the abyssal Pacific; cf. Wunsch (2013), Levitus (1982)), and a typical ρ_0 value qual to 1027 $kg\ m^{-3}$, Eq. 2.38 scale as:

$$\frac{\Delta w'}{\Delta z} \sim p' \cdot 10^{-9} \tag{2.39}$$

This suggests that over the same vertical scale, the term $\overline{p' \partial w'/\partial z}$ would tend to be smaller than the term $\overline{w' \partial p'/\partial z}$ (See *Chapter 3*). This also implies that the vertical gradient of the heat flux can be interpreted as anomalous nonlinear vertical advection of temperature since $\overline{w' \partial T'/\partial z} \approx \partial \overline{(w'T')}/\partial z$ (assuming Eq. 2.34), which links the energy flux to the rate of temperature change in the deep ocean.

Using the hydrostatic approximation, we can rearrange Eq. 2.35 as:

$$\boxed{\frac{\partial \overline{p'w'}}{\partial z} = g\alpha\rho_0\overline{w'T'}} \tag{2.40}$$

which implies that the vertical gradients of $\overline{p'w'}$ scale as $\overline{w'T'}$.

Introducing a vertical heat flux (Q) defined as:

$$Q = -C_p\rho\overline{w'T'} \tag{2.41}$$

where C_p is the specific heat of seawater at constant pressure, we can then rewrite Eq. 2.40 in terms of Q as:

$$\boxed{\frac{\partial \overline{p'w'}}{\partial z} = -\frac{g\alpha}{C_p}Q} \tag{2.42}$$

The expression 2.42 relates the vertical gradients of the wave energy flux to a vertical heat flux, and can be interpreted as the rate of energy loss to smaller scales by working against the vertical density gradients. Therefore, the dissipation[3] or decrease in the vertical wave energy flux traduces as vertical heat flux. This formalism is used in *Chapter 3* to interpret the results obtained from the analysis of the interannual vertical energy flux.

2.3 ENSO indices

As exposed in the introductory chapter, ENSO is the dominant mode of coupled ocean-atmosphere variability on interannual timescales, and even though the development and peak phases of the events take place in the tropical Pacific, it has an important influence on the extratropical variability. Over the years, several methodological approaches have been developed to document and quantify the ENSO modulation of the oceanographic characteristics and dynamical processes in the SEP. A straightforward approach involves the analysis of the local oceanographic records during the different phases of a particular ENSO event, such as the ocean currents data (e.g. Shaffer et al. (1999); Pizarro et al. (2002)), coastal sea level (Pizarro et al., 2001) or coastal upwelling conditions (Vargas et al., 2007; Aravena et al., 2014), and describe the impact of the event in terms of the amplitude of the anomalies.

[3]Strictly, dissipation corresponds to the effect of molecular friction on kinetic energy. However, in the present work we use this term in a more general sense as the transfer of energy, e.g. from the large-scale wave field to the mesoscale field.

A complementary approach frequently used to document the impact of the events consists in contrasting the local records against indices that quantitatively define the ENSO events. This approach has the advantage of summarizing the complex nature of the ENSO events while retaining information about their duration and intensity. Definition of such indices are diverse, and range from a simple SST-threshold based index restricted to the equatorial Pacific (e.g. Niño 3.4 (Trenberth, 1997), Trans Niño Index (Trenberth and Stepaniak, 2001)), to more complex ones involving several variables measured over the whole tropical Pacific basin (e.g. Multivariate ENSO Index (Wolter and Timlin, 1993)).

Given their simplicity and skill, the use of indices to interpret the variability associated with ENSO is very common, and has been extensively used for understanding the remote influence that the equatorial Pacific variability exerts on the SEP. However, the current understanding of the ENSO diversity has required a reinterpretation of the classical definitions of El Niño in terms of the EP and CP events, which present very different spatial patterns in the tropical Pacific, and strongly differ in the amplitude of the anomalies (Ashok et al., 2007). In this context, Takahashi et al. (2011) proposed two orthonormal indices that account for the evolution of both ENSO regimes. These indices (henceforward E and C indices) are based on a 45° rotation of the leading EOF functions of the SST anomalies in the equatorial Pacific:

$$\begin{aligned} E &= (PC1 - PC2)/\sqrt{2} \\ C &= (PC1 + PC2)/\sqrt{2} \end{aligned} \tag{2.43}$$

where PC1 and PC2 correspond to the principal components of the EOF analysis.

This rotation of the first two dominant EOF modes of SST anomalies allows for deriving two modes than can be more easily interpreted. In particular the E mode account for extreme El Niño events and the C mode accounts for Central Pacific El Niño events. Following the methodology of Takahashi et al. (2011), the E and C indices are estimated. First, an EOF analysis is performed on the SODA data set SST between 10°S and 10°N in the tropical Pacific. The spatial EOF patterns obtained are similar to the ones reported in Ashok et al. (2007), with a positive amplitude maximum along the equatorial Pacific for the first mode (Fig. 2.3a), and a (smaller) positive amplitude located in the central Pacific (near the dateline) for the second (Fig. 2.3b). The dispersion diagram of the principal components evidences the two ENSO regimes, where the PCs from the SST anomalies align following two preferential directions, the E and C indices (Fig. 2.3c). This result illustrates that the $E - C$ axes selection obeys the direction preferred by the system and hence they have a dynamical meaning, rather than a merely statistical one (Takahashi et al., 2011).

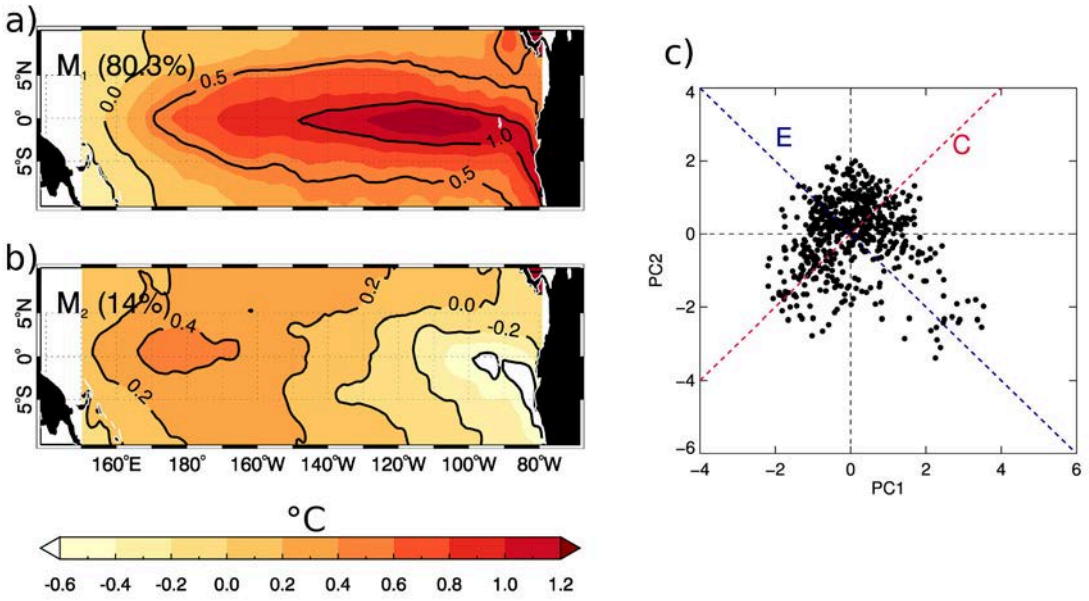

Figure 2.3: *(a) First and (b) second EOF-mode pattern of interannual SST in the tropical Pacific. Percentage of explained variance by each mode is indicated between parentheses. (c) Dispersion diagram of the Principal components (PC) associated with the spatial EOF-mode patterns. The E and C axes are also indicated.*

This methodology captures the salient features of the two El Niño regimes. The spatial SST pattern associated with the E index has its maximum amplitude along the eastern equatorial Pacific (east of 120°W) and along the northern coast of South America (Fig. 2.4a). On the other hand, the C pattern has its maximum amplitude in the central equatorial Pacific, in the Niño 4 region (170°E-100°W; Fig. 2.4b).

In *Chapter 3*, the E and C indices are used as a basis to document the impact of the two ENSO regimes on the extra-tropical long Rossby wave.

2.4 Observations

Although in the present work we implement a modeling approach to study the subsurface ocean variability, this work is still supported by observational data sets, and in the following we introduce the observations used throughout the present study. In some cases, these data sets might be used as the boundary conditions to force the oceanic simulations (e.g. reanalyses and climatological data sets), or as a benchmark to evaluate the realism of the simulations (e.g. *in situ* measurements and remote sensing observations). The application and treatment of the information are detailed directly in *Chapters 3 and 4*.

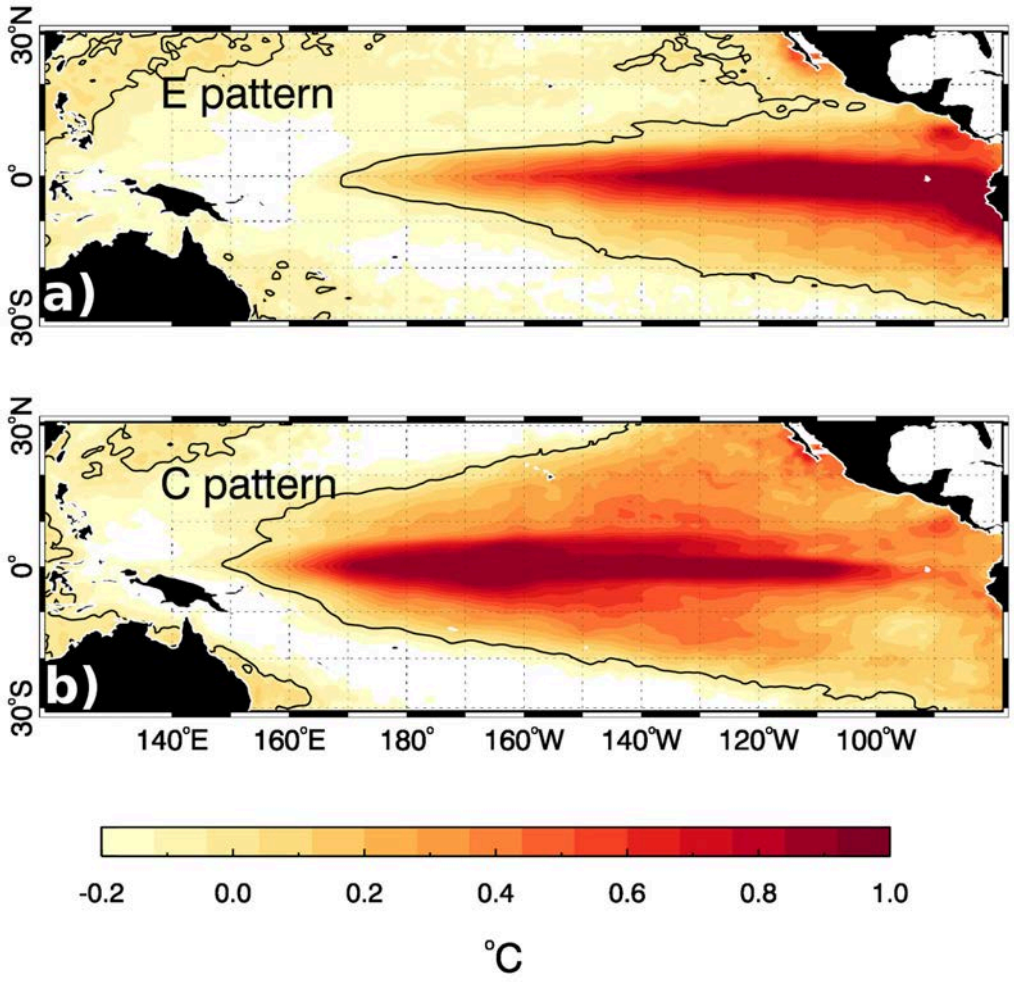

Figure 2.4: *SST projections onto the (a) E and (b) C indices in the tropical Pacific over the period 1958-2008.*

2.4.1 Climatologies and reanalyses

Simple Ocean Data Assimilation (SODA) reanalysis data set

The SODA data set is a reanalysis product that assimilates *in situ* observations from the last six decades in an eddy-permitting global ocean model (Carton et al., 2000a,b), to deliver time series of different ocean fields (velocity, temperature, salinity, sea surface height and sea surface wind stress) over a global $0.5° \times 0.5°$ horizontal grid in 40-vertical levels. The main source of *in situ* observations assimilated in SODA corresponds to the World Ocean Atlas database, extended to include data from the National Oceanographic Data Center (NOAA) and operational profile observations from the Global Temperature-Salinity Profile Program archive (combining observations from the TAO/Triton mooring thermistor array and ARGO floats).

The assimilation algorithm implemented in SODA can be described by the following sequence: (1) a state forecast based on a GCM (POP 2.1; Carton et al., 2000b) is produced for the time t_k. (2) All *in situ* observations available at time t_k are combined with the forecast, providing an estimation of the ocean state referred to as the "true state" for time t_k. (3) The true state estimation is used as the initial condition for the forecast at the time t_{k+1}, and the sequence is repeated. More information on the methodology and the estimation of associated errors can be found in Carton et al. (2000b).

The SODA data set used in the present study covers the period 1958-2008, and is implemented as the oceanic boundary conditions for the simulations (*Chapters 3 and 4*), and for comparison/benchmarking of the model performance.

CSIRO Atlas of Regional Seas (CARS)

The CARS data set is a climatological compilation of ocean observations over the period of modern ocean measurement (1940-2009; Ridgway et al., 2002). The data is derived from a quality controlled archive of historical oceanic measurements (mainly research vessel profiles and autonomous floats), and interpolated on a global $0.5°\times0.5°$ grid, over 79 vertical levels (with increased resolution near the surface). The mapping algorithm is an adapted version of a weighted least-squares quadratic smoother (Ridgway et al., 2002), which fits a quadratic function in the horizontal plane to generate a regular grid. The function fitted in the horizontal plane is scaled to take into account the bottom topography. Further details on the mapping technique employed in the construction of CARS can be found in Dunn and Ridgway (2002) and the CARS website[4].

CARS does not provide information on a given date, but only the time average values plus the annual and semiannual harmonics (Condie and Dunn, 2006). The harmonics are simultaneously fitted to the time series at every grid point, and are progressively damped as depth increases, until the semiannual and then annual fit are extinguished. This means that there will be areas where only the information about the annual harmonic (and time average) will be available. For instance, in the SEP, CARS provides information on the annual harmonic for the first 1000 meters depth, but only for the first 250 m in the case of the semiannual harmonic.

In addition to the sea water state variables (temperature and salinity), CARS includes in its latest versions a set of biogeochemical variables, such as oxygen, nitrate and phosphate. CARS is used as a biogeochemical ocean boundary conditions for the simulation experiment in *Chapter 4*.

[4]http://www.marine.csiro.au/~dunn/cars2009/

ICOADS data set

The International Comprehensive Ocean-Atmosphere Data Set (ICOADS[5], former COADS (Slutz et al., 1985)) consists of a compilation of *in situ* surface marine meteorological and oceanographic observations since the late 1700s to the present day, over a regular $1°\times1°$ global grid (Worley et al., 2005), and corresponds to the most complete and heterogeneous collection of surface marine data in existence. The data processing system that incorporates observations from multiple sources into ICOADS follows a series of redundant quality control steps aiming to remove outliers and duplicates based on spatial and temporal statistical criteria, and detect eventual errors associated with incorrect representation of latitude and longitude in old reports (cf. Woodruff et al. (1987)). The data is then binned into a regular spatial grid. No "analysis" of the data is performed (such as spatial or temporal interpolation or smoothing). The quality control applied to the observations makes the atmospheric variables provided by the ICOADS data set more accurate over coastal upwelling regions, in comparison to the available atmospheric reanalyses (e.g. NCEP/NCAR and ERA-40 reanalyses; Narayan et al. (2010)).

For the present study, monthly ICOADS observations provide the air temperature used to derive the atmospheric fluxes at the air/sea interface (from bulk formulation (Hodur et al., 2002)), in addition to the short and longwave radiation and relative humidity used to force the regional simulations of *Chapters 3 and 4* at the air/sea interface.

MetOffice temperature analyses

The MetOffice Hadley Centre[6] produces and maintains several gridded data sets of ocean temperature. In *Chapter 3* we evaluate the skill of the simulation in reproducing different aspects of the mean circulation in the region and its variability, by contrasting the simulated temperature fields against two different temperature products from the MetOffice Hadley Centre.

We use the EN4[7] temperature product, which corresponds to a compilation of all temperature profiles available since 1900, over a global $0.5°\times0.5°$ grid in 42 vertical levels. The EN4 combines temperature profiles from several sources (see Good et al. (2013) for a comprehensive list), which are subject to a quality control process aiming at removing duplicate profiles, errors in position and faulty profiles (spikes, steps, density inversions, etc.)[8]. After the quality check, the data for each month is combined with

[5]http://icoads.noaa.gov/
[6]http://www.metoffice.gov.uk/hadobs/index.html
[7]http://www.metoffice.gov.uk/hadobs/en4/
[8]see Ingleby and Huddleston (2007) for more details on the quality control process.

a background ocean state (obtained from a forecast of the previous month), using an iterative optimal interpolation method (Lorenc et al., 1991), and recursive horizontal-vertical filters to model the information spreading between observations. For further details on the data processing techniques applied in producing the EN4 data set, please refer to Good et al. (2013).

This data set (version 4.2.0) is used to validate the simulated average thermocline depth in the SEP, which is an essential feature of the regional circulation, and in determining the vertical structure of the baroclinic modes (Dewitte et al., 2008b, 1999).

2.4.2 Remote sensing data

Sea Surface Temperature (SST)

The Optimum Interpolation Sea Surface Temperature (OISST v.2[9]) data is used in *Chapter 4* to assess the simulation skill in reproducing the mean SST pattern and gradients. This data set corresponds to an analysis of SST constructed by merging data from satellite based measurements (Advanced Very High Resolution Radiometer (AVHRR) SST sensor) and *in situ* data from different sources (ships, buoys). The OISST analysis combines the observations over a regular grid using a weighted sum of the data, assuming a Gaussian correlation error (see Reynolds and T. M. Smith (1994) for details). Prior to the data merge, eventual biases in the satellite based measurements (e.g. due to aerosols contamination of imperfect cloud masking) are corrected relative to the *in situ* data using a linear combination of rotated empirical orthogonal functions (Dool et al., 2000). The product used in the present study corresponds to the $0.25° \times 0.25°$ daily OISST v.2 (Reynolds et al., 2007).

Sea Level Height (SLH)

Satellite altimeter observations of SLH obtained by the radar altimeters onboard the TOPEX/Poseidon and Jason1-2 missions, and are used in *Chapters 3 and 4* to validate different aspects of the SEP circulation reproduced by the simulations. The data used corresponds to the $0.25° \times 0.25°$ weekly sea level height TOPEX/Jason1-2 merged product, obtained from the Sea Level Research Group, University of Colorado[10]. The intermission data merging process involves a bias correction treatment, that takes into account the inherent errors of each instrument (related to imperfect atmospheric corrections and lack of accuracy of the altimeters), and inter-mission biases related to differences in the measurement reported by each instrument (associated for example with

[9]https://www.ncdc.noaa.gov/oisst
[10]http://sealevel.colorado.edu/

measurement delay and instrumental drift). The SLH estimations are then validated against a global network of tide gauges (Mitchum, 2000). For details on the principles behind the altimetric SLH estimations, please refer to Fu and Cazenave (2001).

One of the aspects of the circulation that is validated in *Chapters 3 and 4* using the SLH is the mean eddy kinetic energy field, which indirectly reflects the vertical structure of the circulation and also gives information on the realism of the mesoscale activity levels reproduced by the simulation. In *Chapter 3*, we also use SLH to test the simulation skill in reproducing the interannual coastal sea level fluctuations in the SEP.

Chlorophyll-a

Ocean color data acquired by the SeawiFS instrument are used in *Chapter 4* to assess the skill of the simulation in reproducing the surface Chlorophyll-a (Chl-a) concentration pattern and seasonal cycle. These observations are also used as boundary conditions for a coupled physical/biogeochemical simulation in *Chapter 4*.

The SeaWiFS instrument consists of an optical sensor, designed to measure the electromagnetic radiance reflected by the Esarth's surface (vegetation, water, terrigenous materials, etc.) and atmosphere inside the visible band of the electromagnetic spectrum. The central principle for the use of this sensor in the context of ocean observation is the specificity of light absorption by the different sea-water constituents (Hooker et al., 2002). In this manner, it is possible to compute Chl-a concentration from the reflected sunlight, using semi-empirical equations that relate certain bands of the visible spectrum (centered around the blue and green regions) with the Chl-a concentration (cf. O'Reilly et al. (1998) for details on the algorithms). Given that the SeaWiFS measurement principle operates on the visible part of the electromagnetic spectrum, the ocean color measurements are severely handicapped by cloud coverage (Woodward and Gregg, 1998), and it is not uncommon for Chl-a variability studies to use synoptic binned or mapped products, which merge satellite images from several days and thus limit the cloud interference (which is particularly important in the SEP as seen in Fig. 1.6).

The data used in *Chapter 4* of the present study corresponds to the 9km 8-day binned composites of Chl-a product, distributed by the Ocean Biology Processing Group (OBPG) at NASA's Goddard Space Flight Center[11]. The binning process consists in combining all the measurements, spanning 8 days and store them on a global, equal-area grid of 9.2 Km bin size. This process limits to some extent the interference and data loss due to cloud coverage.

[11] http://oceancolor.gsfc.nasa.gov/cms/

2.4.3 *In situ* data

Sea level stations

The University of Hawaii Sea Level Center (UHSLC[12]) is part of an international effort to establish a global *in situ* sea level observing system (Global Sea Level Observing System; IOC (2012)), which maintains the largest network of tide gauge measurements with over 700 hundred active tide gauges around the globe (some of which have been active for over 150 years). As part of this effort, the UHSLC processes and distributes hourly and daily sea level data through its website[13]. The data processing consists of several quality control steps aimed at removing outliers and rectifying measurement errors (e.g. datum inconsistencies, timing errors). Sea level data retrieved from UHSLC is used in *Chapter 3* of the present study to evaluate the simulation skill in reproducing the alongshore sea level variations related to the equatorial Pacific interannual variability. For this purpose, 8 sea level stations along the coast of South America are used: La Libertad (2.2°S), Paita (5.1°S), Lobos de Afuera (7.0°S), Callao (12.0°S), Antofagasta (23.6°S), Caldera (27.0°S), Valparaíso (33.0°S) and Puerto Montt (41.0°S).

ARGO floats data

The ARGO[14] program is an international effort to monitor the ocean, that consists of a global array of lagrangian floats that provide near real-time measurements of temperature and salinity of the ocean, between the surface and 2000m depth. The program initiates in the late 1990s as a response to the lack of *in situ* subsurface ocean observations at a global scale, which limited the interpretation of trends observed in ocean measurements (e.g. Skliris et al. (2014), Durack and Wijffels (2010), Hosoda et al. (2009)), and also prevented the validation and correct interpretation of global climatic models (Roemmich and Owens, 2000). Today, the ARGO program amounts to over 3500 active floats worldwide, which produce over 10^5 profiles per year. In this context, several research groups produce temperature/salinity fields derived from the ARGO profiles, over a regular grid, using different mapping and interpolation methods (cf. ARGO website for a comprehensive list of different products based on ARGO data).

In the present work, we use the ISAS13 product developed and maintained by the LPO (Laboratoire de Physique des Océans[15]), and available upon request[16]. This product consists in monthly temperature/salinity fields over a regular global $0.25° \times 0.25°$

[12] http://uhslc.soest.hawaii.edu
[13] http://uhslc.soest.hawaii.edu/datainfo/
[14] http://www.argo.ucsd.edu
[15] http://wwz.ifremer.fr/lpo/
[16] fabienne.gaillard@ifremer.fr

grid, and 151 vertical levels between 0 and 2000m depth, spanning the period 2002-2012. The ISAS13 data set is used in *Chapter 3* of the present work, in order to investigate the capacity of the ARGO observations to study the vertical propagation of long Rossby waves in the SEP at annual and interannual timescales.

Currents

In *Chapter 3*, *in situ* current measurements are used to validate the velocity field reproduced by the simulation. These currents measurements were collected by three Anderaa RCM7 current meters and an upward looking ADCP (Workhorse Sentinel 300 kHz) moored at ~120m depth (Fig. 2.5), spanning the period between November 1991 and September 2008 (Table 2.1). This mooring is part of an observational system deployed at (71°47'W, 30°21'S) and is maintained by the Center for Oceanographic Research in the Eastern South Pacific (COPAS[17]), University of Concepción, and was made available by Dr. Oscar Pizarro[18].

Table 2.1: *Depth and measuring period for the different current meters in the COSMOS mooring.*

Instrument	Start	End	Depth
ADCP	Apr 2003	Sep 2006	10-110 m (5m bin size)
RCM7	Nov 1991	Sep 2008	220 m
RCM7	Nov 1991	Sep 2008	480 m
RCM7	Nov 1991	Jun 2008	750 m

[17]http://www.sur-austral.cl/
[18]orpa@profc.udec.cl

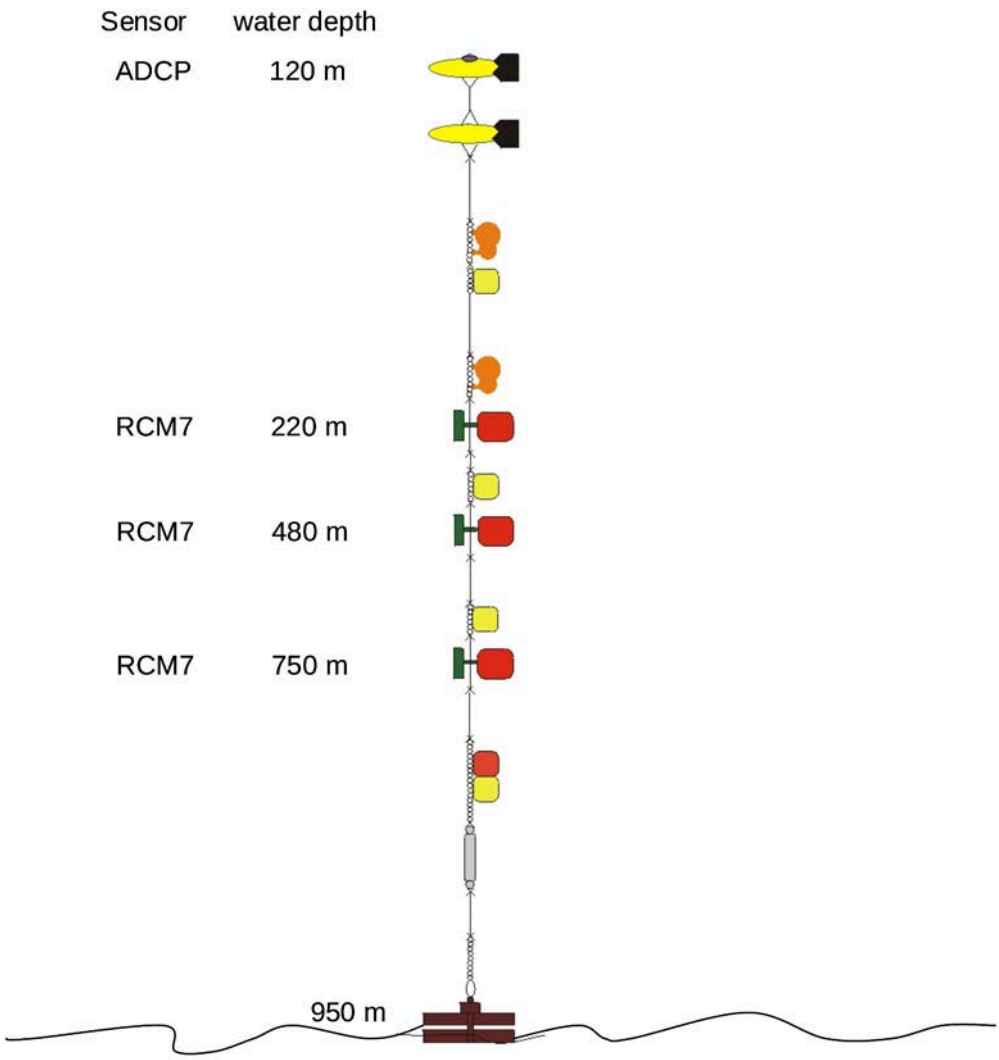

Figure 2.5: *Schema of the COSMOS mooring. Source: http://www.profc.udec.cl*

Chapter 3

Subthermocline variability in the South Eastern Pacific: interannual to decadal timescales

3.1 Overview

As exposed in *Chapter 1*, the coastal waveguide constitutes an oceanic pathway that allows for the discharge of the tropical climatic variability onto the mid-latitudes, which results in the large modulation of the circulation observed in the SEP at ENSO timescales. Information from the equatorial Pacific is conveyed into the SEP by Kelvin-like waves that propagate polewards along the coastal waveguide, and trigger the westward/vertical propagation of interannual extra-tropical Rossby waves. Several works have related the modulation of the circulation and hydrographic characteristics in the SEP during the ENSO events to the westward propagation of Rossby waves (e.g. Pizarro et al. (2002); Vega et al. (2003); Correa-Ramirez et al. (2012); Morales et al. (2013)). Using velocity measurements at different depths over the continental slope at 30°S, Shaffer et al. (2004) observed large anomalies of the alongshore flow in relationship with the 1997/98 El Niño event, in addition with an upward phase propagation (therefore a downward energy propagation) of the velocity anomalies. This was the first observational evidence of a vertical energy flux at interannual timescale in the SEP, in relationship with the equatorial variability. Ramos et al. (2008) would later generalize this result (from 15° to 30°S), and identify the westward/vertical propagation of long Rossby waves (from the coast towards the abyssal ocean), as the mechanism associated with the vertical energy flux during the 1997/98 El Niño event. In this context, the present chapter is dedicated to the study of the energy flux conveyed by the extra-tropical Rossby wave in relationship with the ENSO events that take place in the tropical Pacific, and its fate in the abyssal region off South America. In a global context, documenting the energy fluxes in the ocean can be considered a prerequisite

for interpreting the response of the oceanic circulation to the present Earth's energy imbalance, which is a current concern of the climatic and oceanographic communities. Recent works evidence that the response of the deep ocean (depths > 700m) to changes in Earth's energy balance may have accelerated in recent years (Church et al., 2011; Gleckler et al., 2016), although the mechanisms of energy redistribution in the deep ocean remain uncertain (Liu et al., 2016). Understanding the role of the deep ocean circulation in the planetary energy budget is thus of interest in this matter.

The main objective of this chapter is to document the vertical energy flux associated with the interannual fluctuations of the subthermocline circulation in the SEP, which is entailed by the vertical propagation of long Rossby waves. In the first part of the present chapter we investigate if the signature related to the propagation of long Rossby waves is present in the available subsurface long-term ARGO observations. In the second part of the chapter, we document the vertical energy flux associated with the occurrence of El Niño events and the low-frequency modulation of this flux related to the interdecadal climatic variability in the tropical Pacific.

3.2 Is it possible to use ARGO data to observe the long Rossby wave?

Apart from the coastal observations of sea level, surface temperature, and a few current meter moorings scattered off the Chilean coast, long term *in situ* observations in the SEP are practically nonexistent. This has prevented carrying out a documentation of the vertical/westward propagation of long Rossby waves from observational data in the SEP. However, a possible solution to these difficulties could come from the gridded products derived from ARGO floats currently available. Deployment of ARGO floats date back to the year 2000, and have increased at a rate of ~800 new floats every year since, which offers an unprecedented spatial and temporal coverage of the ocean. In this section, the applicability of the ARGO observations for the study of the vertical propagation of long Rossby waves is evaluated, first in the equatorial Pacific, and then in the southeastern Pacific. The results are contrasted against previous observational and modeling works.

3.2.1 Argo data set

The ARGO product used to complete this diagnosis corresponds to the ISAS13[1] global monthly temperature and salinity fields, spanning the period 2002-2012. In particular, this product was selected among the available data sets due to the length of the record and to its spatial resolution. The horizontal grid corresponds to the isotropic 0.5°x0.5° global Mercator grid (77°S-66.5°N), with a resolution that increases with latitude. The vertical resolution (151 levels) decreases with depth, from 5 m resolution in the upper layers to 20 at 2000m depth. For further details on the product and its mapping, the reader is referred to Gaillard (2012).

3.2.2 The equatorial Rossby wave

A diagnosis of the annual signal in the ARGO temperature records is carried out in order to verify to which extent is possible to use the ARGO data set to document this process. As a first step, the annual signal in the temperature records along the equatorial Pacific is analyzed (Fig. 3.1) in a similar manner as in Kessler and McCreary (1993) and Dewitte and Reverdin (2000), in order to document its main characteristics. The zonal section suggests two different regimes, divided by a slanted line extending roughly from 160°E at 2000m to the eastern boundary at around 300m (Fig. 3.1a). To the west of this line the phase contours are approximately parallel (Fig. 3.1b), with an upward/westward phase propagation. This distribution changes drastically near the thermocline, where the phase lines have a more shallow slope. A linear regression on the phase diagrams of figure 3.1b yields an estimated zonal wavelength λ_x of ~$12200\,km$. The vertical wavelength λ_z is estimated similarly to be ~$4400\,m$. A meridional section at 170°E (region where the phase lines slope steeply downward) reveals that the vertical phase structure is characteristic of the region between 6°S and 6°N, with phase lines roughly horizontal across the equator, and an upward phase propagation below 700m (Fig. 3.1d). The amplitude in this region shows two off-equatorial maxima below 1000 m depth in consistency with the expected off-equatorial amplitude maximum of long Rossby waves.

Estimations of the phase speed of the observed signal were carried out using three different approximations (Note that in order to ease the comparisons against the existing literature, c and m are used in the present chapter to denote the Rossby wave phase speed and vertical wavenumber respectively). Using the dispersion relation for long zonal wavelengths trapped about the equator (Kessler and McCreary, 1993), it follows that the phase speed for a first-meridional ($l = 1$) annual Rossby wave is

[1] http://wwz.ifremer.fr/lpo/content/view/full/71089

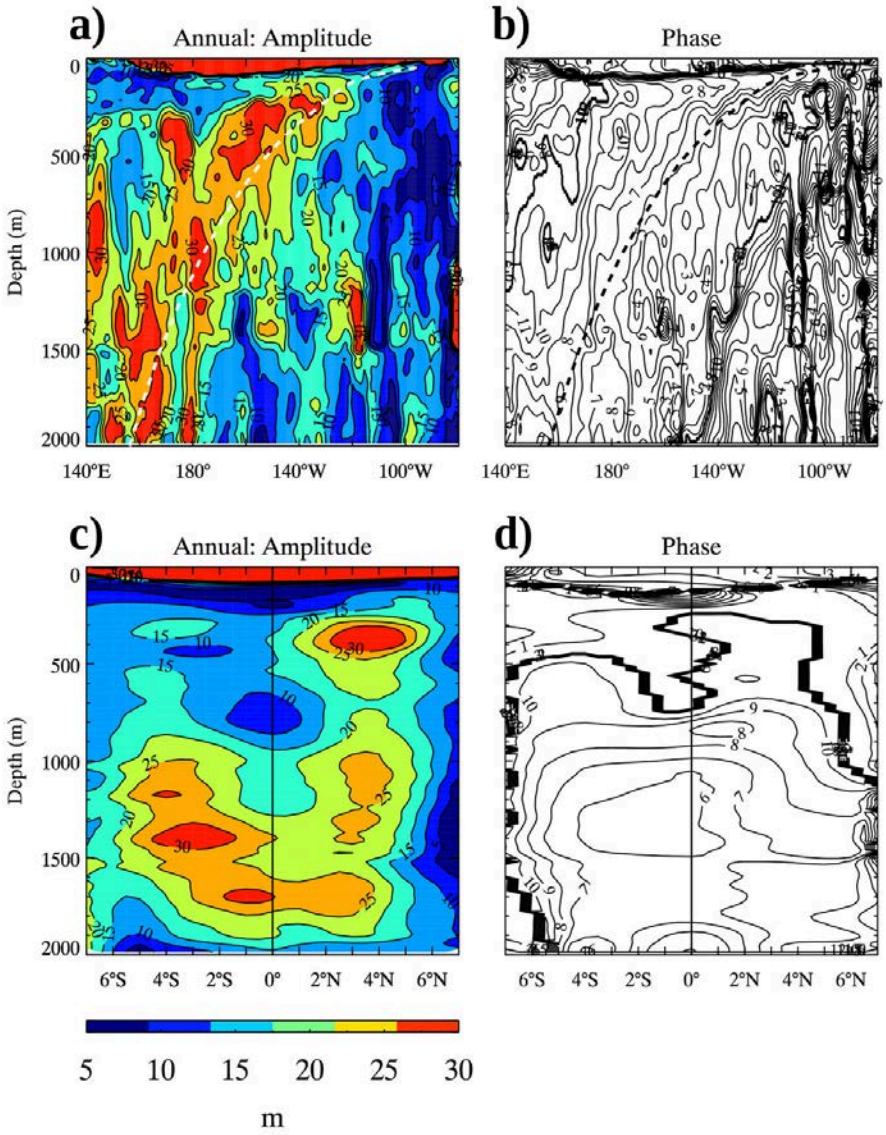

Figure 3.1: *Annual harmonic of vertical isotherm displacements along a zonal section at 4°N (a, b) and a meridional section at 170°E (c,d). (a,c) Amplitude (in meters) and (b,d) phase (with respect of the date of highest amplitude). Phase contours are labeled in months, with the contour at the first day of each month. The dashed lines in (a,b) correspond to the WKB raypath of the* $l = 1$ *annual Rossby wave, computed following* $\frac{dz}{dx} = \frac{(2l+1)\,\omega}{N_b(z)}$ *(Kessler and McCreary, 1993).*

$c \sim 1.16\,m\,s^{-1}$. An estimation of the phase speed using the WKB identity $c = \frac{N}{m}$, considering that average value of $N = 1.6 \cdot 10^{-3}\,s^{-1}$ between 1000 and 2000m, yields $c \sim 1.12\,m\,s^{-1}$ (3% difference from the previous estimation). Finally, a third estimate of c might be obtained form the location of the off-equatorial amplitude maxima (y_m) of the $l = 1$ Rossby wave, using the relation $c = (2/3)\,\beta\,y_m^2$ (Kessler and McCreary, 1993). From figure 3.1c, the location of the off equatorial maxima is roughly 290 km (2.6°), which gives a phase speed $c \sim 1.28\,m\,s^{-1}$ (9% higher than the first estimate and

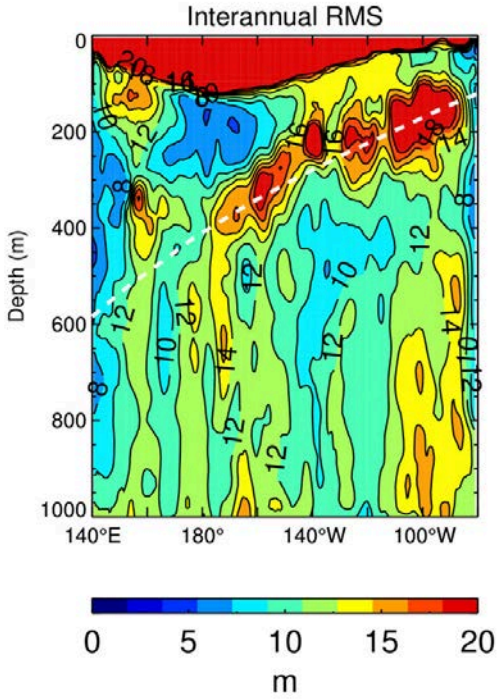

Figure 3.2: *Root mean square of isotherm displacements interannual anomalies (departs from mean seasonal cycle) along a section at 2.5°S. Dashed line correspond to the WKB raypath of the $l = 1$ Rossby wave (3.7 years period).*

13% higher than the second). The consistency of the three estimates of c shows that the observed signal is coherent with an $l = 1$ vertically propagating Rossby wave. An additional consistency check is achieved by comparing the phase lines and the theoretical WKB raypath slope for the $l = 1$ Rossby wave. Below 700m in the western region, the phase lines orientate approximately parallel to the theoretical WKB raypath, which is indicative of vertical/westward phase propagation.

These characteristics of the annual Rossby wave estimated from the annual temperature variations in the equatorial region are consistent with the previous observational (Lukas and Firing, 1985; Kessler and McCreary, 1993) and modeling (Dewitte and Reverdin, 2000) studies.

The relevance of the ARGO data set for studying the vertical structure of the equatorial long Rossby wave at interannual timescales is also evaluated. Figure 3.2 reveals that the subsurface interannual variability maximum extends from the east part of the equatorial basin toward the west, and slopes downward. A spectral analysis along this subsurface maximum reveals a peak at 3.7 yr period, which corresponds to the documented El Niño frequency. An harmonic analysis similar to what is presented for the annual cycle was performed for the $3.7\,years^{-1}$ frequency. Figure 3.3 shows the amplitude and phase of the anomalous isotherm displacements (3.7 yr) harmonic along a

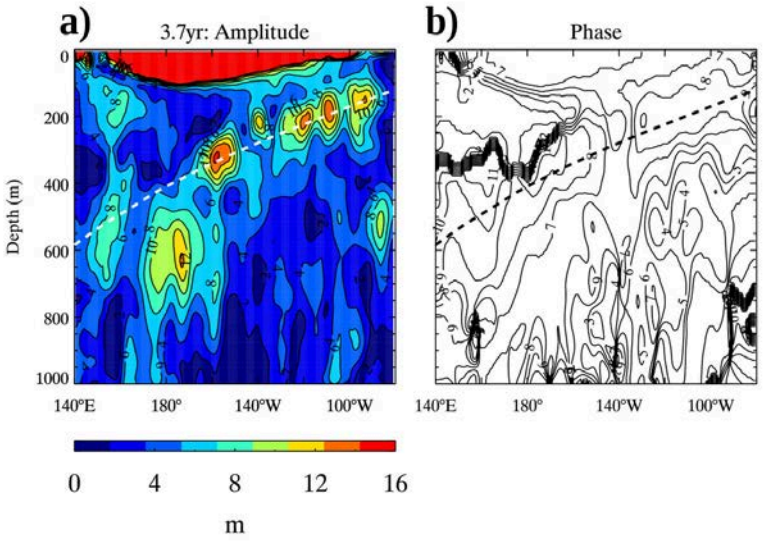

Figure 3.3: *Zonal section of the (3.7 yr period) harmonic of vertical isotherm displacements at 2.5°S. (a) Amplitude (in meters) and (b) phase (date of highest temperature). Phase contours are drawn every 3.7 months (1/12 of the period). Dashed line correspond to the WKB raypath of the $l = 1$ Rossby wave (3.7 years period).*

zonal section across the Pacific at 2.5°S (latitude of highest harmonic amplitude). Maximum subthermocline amplitude is found near the eastern boundary at ~150 m, and slopes westward and downward along a phase isopleth, which agrees with the theoretical WKB raypath for the $l = 1$ Rossby wave (at $3.7\,years^{-1}$). As for the annual timescale, the orientation of the phase lines is suggestive of westward and downward propagation, although this is less evident than for the previous analysis (phase lines are not as organized as in the annual harmonic case). Nevertheless, this analysis qualitatively agrees with the results obtained by Dewitte and Reverdin (2000). From the phase diagram presented in figure 3.3b, the zonal wavelength (estimated similarly as for the annual cycle) is $\lambda_x \sim 20000\,km$ which gives a phase speed of $c \sim 0.51\,m\,s^{-1}$ for a $l = 1$ Rossby wave. The vertical wavelength is estimated to be $\sim 1200\,m$, which results in a phase speed of $c \sim 0.57\,m\,s^{-1}$, considering $N = 3.0 \cdot 10^{-3}\,s^{-1}$ in the central Pacific between 500 and 1000 m.

The analyses carried out show that the current ARGO dataset might be exploited to document the main characteristics of the vertically propagating Rossby wave in the equatorial Pacific at annual timescale. However, the results are less conclusive when investigating for the interannual timescale.

3.2.3 The Extra-Tropical Rossby wave

Previous studies have evidenced the vertical propagation of ETRW in the SEP at annual (Dewitte et al., 2008b) and interannual timescales (Ramos et al., 2008) occurring as far as 30°S. In this section, the relevance of the ARGO dataset for investigating the vertical propagation of ETRW is documented for both the annual and interannual timescales.

Figure 3.4 presents zonal sections of the annual amplitude and phase of the isotherm displacements at three different latitudes (same latitudes analyzed in Dewitte et al. (2008b) for the annual period). At 11°S, the amplitude diagram shows a maximum that extends westward/downward from the coast ($\sim 200\,m$), with a slope to the west. The phase diagram at 11°S shows approximately parallel phase lines sloping offshore, that agree with the theoretical WKB raypaths for the annual ETRW (first three baroclinic modes). However, these characteristics disappear as latitude increases. At 17°S, although the phase diagram could reveal (to some extent) a westward propagation, the amplitude maximum does not follow the same orientation, and is not in agreement with the expected theoretical trajectory. The same results are obtained further south. At 27°S no evidence of vertical/westward propagation is observed in the amplitude diagram (Fig. 3.4e).

A similar analysis to the one performed in the equatorial region was carried out in the SEP, at interannual timescales. Although the RMS of the interannual vertical isotherm displacements could suggest an offshore signal propagation near the tropical band (Fig 3.5a), this trend disappears toward mid latitudes (Fig. 3.5bc). The hamornic analysis (similar to what is shown for the equatorial region) does not show characteristics of vertical/westward phase propagation at interannual timescale.

3.2.4 Conclusion

The relevance of an ARGO product spanning the period 2002-2012 for documenting the vertical propagation of the annual and interannual Rossby wave in the equatorial and south eastern Pacific oceans is evaluated. The results concerning the vertical/westward propagation of long Rossby waves at annual and interannual timescales are satisfying in the equatorial region, and compare well with previous observational and modeling works. On the other hand, the good results do not replicate off the equatorial region. At both annual and interannual timescales, no clear evidence of a vertical/westward propagating signal in the temperature records is observed in the SEP.

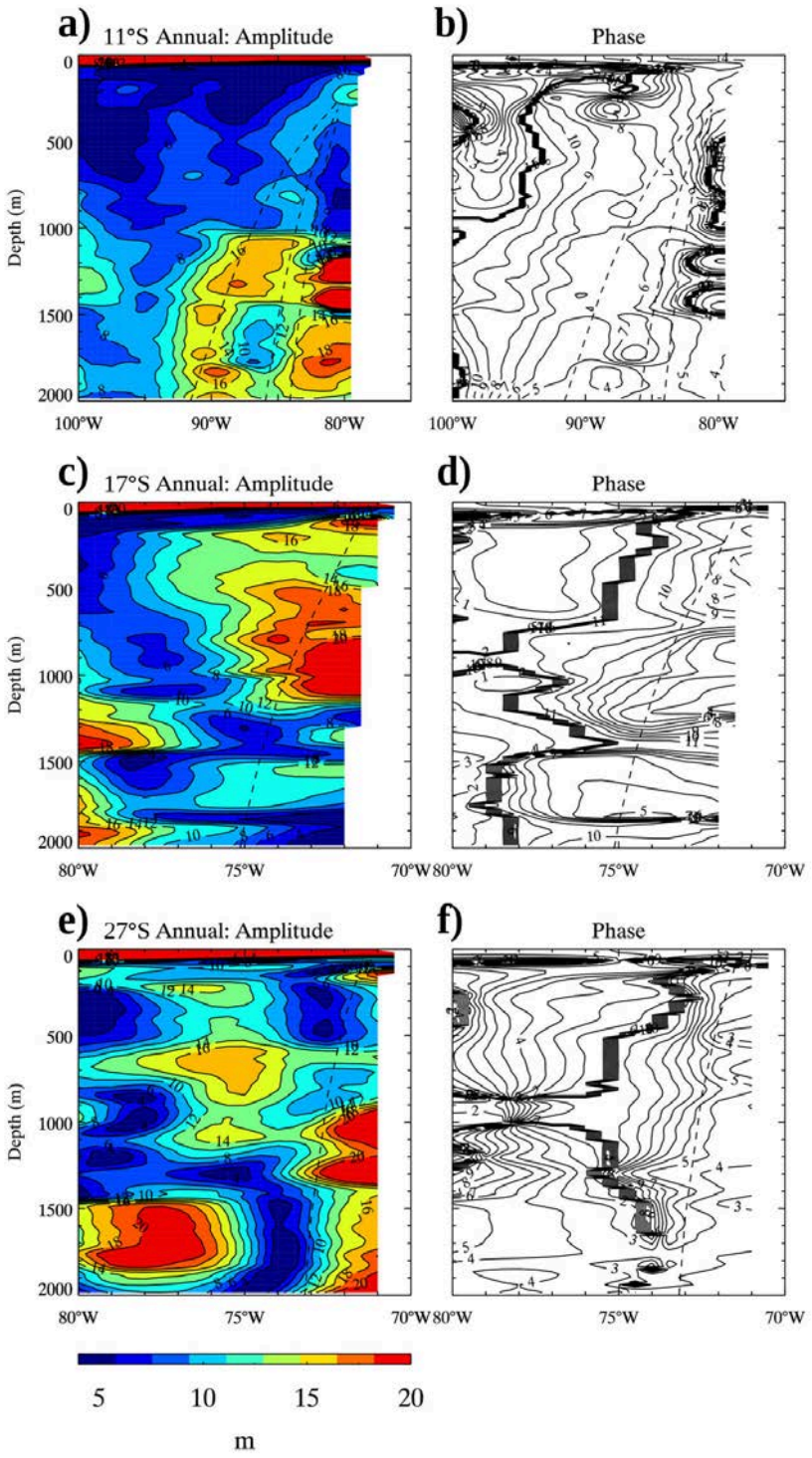

Figure 3.4: *Zonal sections of the annual harmonic of vertical isotherm displacements at three different latitudes. (a,c,e) Amplitude (meters) and (b,d,f) phase (date of highest temperature). Phase contours are labeled in months, with the contour at the first day of each month. The dashed lines correspond to the WKB raypath of the annual Rossby wave (first three baroclinic modes in (a,b) and only first baroclinic mode in (c,d,e,f)).*

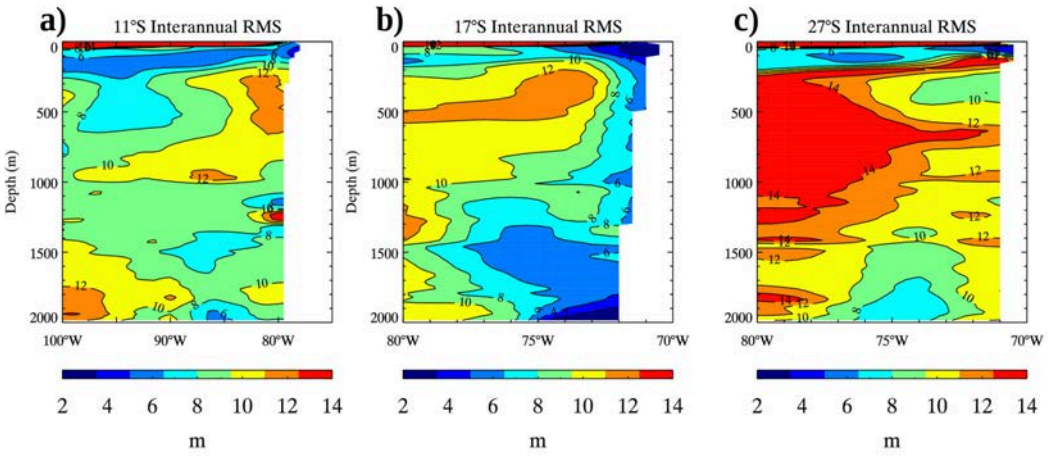

Figure 3.5: *Same as Fig. 3.2 but for zonal sections at (a) 11°S, (b) 17°S and (c) 27°S.*

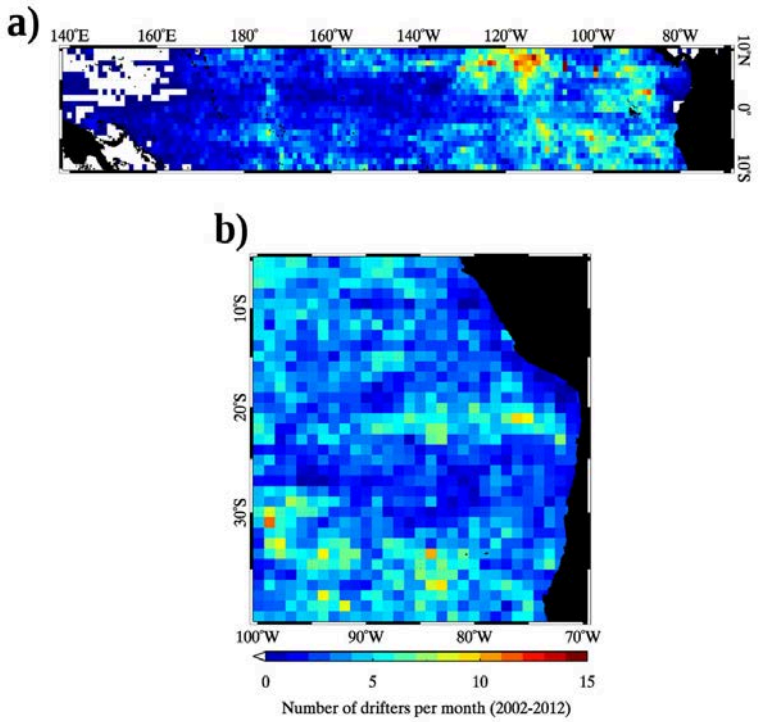

Figure 3.6: *Average monthly density (1° × 1° pixel) for the ARGO profiles in the (a) equatorial and (b) south eastern Pacific. Computed over the period 2002-2012.*

The difficulties to diagnose this process in the SEP could be due to several factors. First is the length of the records, which will impact the timescales that can be accurately resolved. This factor is evidenced in the equatorial region by the loss in definition of the westward propagating signal when analyzing the interannual harmonic (phase lines less organized in comparison to the analysis for the annual harmonic). Secondly, the diagnosis of the vertical propagation of long Rossby waves implemented here relies heavily on the appropriate vertical and horizontal resolution of the temperature product imposed by the spatial coverage of the ARGO floats, which is more important in the equatorial Pacific than in the SEP (Fig. 3.6). In addition to a lower spatial coverage, the phase speed of the long Rossby waves decreases with latitude[2], which difficults even more its observation off the equatorial region. In this sense, it becomes appropriate to take advantage of the current high resolution modeling tools, in order to correctly document this process in the SEP.

3.3 Vertical energy flux at interannual to decadal timescales

This subsection corresponds to the manuscript "Vertical energy flux at ENSO timescales in the subthermocline of the Southeastern Pacific", published in "Journal of Geophysical Research: Oceans".

Citation: Vergara, O., B. Dewitte, M. Ramos, and O. Pizarro, (2017), Vertical energy flux at ENSO time scales in the subthermocline of the Southeastern Pacific, J. Geophys. Res. Oceans, 122, 6011–6038, doi:10.1002/2016JC012614.

[2]Compared to the equatorial region, the phase speed of the first baroclinic mode at interannual timescale is 30% lower at 10°S and 90% at 20°S; see Ramos et al. (2008)

RESEARCH ARTICLE
10.1002/2016JC012614

Key Points:
- Energy propagates vertically in the SEP at interannual time scale, related to the extreme Eastern Pacific El Niño events
- This vertical energy flux is induced by the propagation of long Rossby waves
- The dissipation of the energy beams in the deep ocean is associated with vertical diffusion

Correspondence to:
O. Vergara,
oscar.vergara@legos.obs-mip.fr;
B. Dewitte,
bxd@legos.obs-mip.fr

Citation:
Vergara, O., B. Dewitte, M. Ramos, and O. Pizarro (2017), Vertical energy flux at ENSO time scales in the subthermocline of the Southeastern Pacific, *J. Geophys. Res. Oceans*, *122*, doi:10.1002/2016JC012614.

Received 6 DEC 2016
Accepted 31 MAY 2017
Accepted article online 2 JUN 2017

Vertical energy flux at ENSO time scales in the subthermocline of the Southeastern Pacific

O. Vergara[1], B. Dewitte[1,2,3,4], M. Ramos[2,3,4,5], and O. Pizarro[6,7,8]

[1]Laboratoire d'Études en Géophysique et Océanographie Spatiales, LEGOS, University of Toulouse, IRD, CNES, CNRS, UPS, Toulouse, France, [2]Departamento de Biología, Facultad de Ciencias del Mar, Universidad Católica del Norte, Coquimbo, Chile, [3]Millennium Nucleus for Ecology and Sustainable Management of Oceanic Islands, Coquimbo, Chile, [4]Centro de Estudios Avanzado en Zonas Áridas, Coquimbo, Chile, [5]Centro de Innovacicen Acuócola Aquapacífico, Coquimbo, Chile, [6]Department of Geophysics, University of Concepción, Concepción, Chile, [7]Millennium Institute of Oceanography, University of Concepción, Concepción, Chile, [8]COPAS Sur-Austral, University of Concepción, Chile

Abstract The question of how energy is redistributed in the ocean has renewed the interest for the processes leading to midlatitude subthermocline variability at low frequency. Here we investigate a process that has been disregarded although potentially relevant for climatic studies dealing with the planetary energy budget. The focus is on the Southeastern Pacific where an efficient oceanic teleconnection takes place, linking the remote surface equatorial momentum forcing with the subthermocline through the vertical propagation of low-frequency long-wavelength extratropical Rossby waves (ETRW). A high-resolution model is used to document the vertical energy flux associated with ETRW at interannual to decadal time scales. The analysis of a long-term (1958–2008) simulation reveals that the vertical energy flux can be interpreted to a large extent as resulting from the coastally forced ETRW as far south as 35°S, so that heat content variability can be predicted along theoretical trajectories originating from the coast below the thermocline. It is shown that the vertical energy flux associated with the El Niño Southern Oscillation forms beams below the thermocline that account for a large fraction of the total vertical energy flux at interannual time scales. Extreme El Niño events are the dominant contributor to this flux, which is hardly impacted by mesoscale activity. The energy beams experience a dissipation processes in the ocean below 1000 m that is interpreted as resulting from vertical turbulent diffusion. Our results suggest that the ETRW at ENSO time scales are strongly dissipated at the surface but still can modulate the heat content in the deep ocean of the Southeastern Pacific.

1. Introduction

Due to an extremely weak circulation, the eastern boundary current systems are considered "shadow zones," nonventilated by the mean wind-driven circulation [*Luyten et al.*, 1983], which has widespread implications. For instance, the important subsurface oxygen consumption associated with the highly productive upwelling system found in the Southeastern Pacific (SEP) combines with this sluggish circulation to yield one of the largest and most intense oxygen minimum zones (OMZ) of the world [*Paulmier and Ruiz-Pino*, 2009]. Although this oxygen depleted region is the focus of a growing interest from the scientific community, the interpretation of its long-term trends and low-frequency variability remains ambiguous, partly due to conflicting results from modeling and observational studies [*Stramma et al.*, 2008, 2012], and to the complex biogeochemical-physical processes that govern its variability [*Brandt et al.*, 2015]. Uncertainties in the fate of the OMZ, which has become a societal concern due to its role in the carbon cycle [e.g., *Paulmier et al.*, 2011] and its connection with the coastal ocean along densely populated areas, has contributed to renew the interest for the intermediate to deep circulation in the region.

The mechanisms associated with the variability of the circulation and the ventilation of the subthermocline in the SEP remain unclear. Most studies have proposed that it is related to the variability in the thermohaline circulation (i.e., transport), which has multiples sources [e.g., *Shaffer et al.*, 2004; *Yeager and Large*, 2007], and diffusive processes associated with diapycnal mixing [e.g., *Furue and Endoh*, 2005]. This conceptual view has in particular served as a background approach for investigating the heat uptake by the deep ocean associated with climate change [*Kuhlbrodt and Gregory*, 2012; *Marshall and Zanna*, 2014]. In general, the

However, recent modeling studies have suggested that the vertical propagation of long Rossby waves of equatorial origin could contribute to the ventilation of the subthermocline in the SEP [*Dewitte et al*., 2008; *Ramos et al*., 2008]. Although wave propagation in a well-stratified fluid corresponds to an adiabatic process (hence no diapycnal mixing is expected) [*Winters et al*., 1995], dissipation and mixing could result from the vertical displacement of the isotherms as the wave energy beams form [*McCreary*, 1984], so that energy (in the form of heat) could be accumulated. The question of whether such process takes place at low frequency is therefore also relevant for the interpretation of the deep circulation variability. Although observational evidence of this process has only been established near the equator [*Kessler and McCreary*, 1993], it could also be relevant in the SEP given the efficient oceanic teleconnection that exists between the southeastern and tropical Pacific basins. Previous studies have shown in particular that several aspects of the coastal circulation of the SEP (SST, thermocline, coastal currents) are linked to the remote equatorial forcing for frequencies spanning from intraseasonal [*Shaffer et al*., 1997; *Dewitte et al*., 2011] to seasonal [*Ramos et al*., 2006], and from interannual [*Pizarro et al*., 2002; *Dewitte et al*., 2012] to interdecadal [*Montecinos et al*., 2007]. While at intraseasonal frequencies the pressure and currents variability originating from the equator is trapped along the coast [*Clarke and Shi*, 1991], at lower frequency it radiates in the form of extratropical Rossby waves, with a characteristic signature on sea level anomalies [*Chelton and Schlax*, 1996]. In particular, *Vega et al*. [2003] suggests that altimetric observations off Peru and central Chile during the extraordinary 1997–1998 El Niño event could be interpreted as resulting from a first baroclinic-mode Rossby wave forced along the coast. They also note a significant dissipation at the surface as the wave radiates offshore, which was also reported by subsequent studies [*Challenor et al*., 2004; *Ramos et al*., 2008]. While such dissipation could result from nonlinear processes such as eddy dissipation [*Qiu et al*., 1997] or wave breakdown and subsequent energy transfer to the eddy field [*LaCasce and Pedlosky*, 2004], the observed decrease of the surface Rossby wave signature might also be interpreted as a consequence of the vertical propagation resulting from the constructive contribution of a certain number of baroclinic modes. *Ramos et al*. [2008] evidenced the vertical propagation of long Rossby waves in the SEP based on a medium-resolution (eddy-permitting) ocean simulation, focusing on the 1997–1998 El Niño. In that work the authors evidenced the offshore propagation of long Rossby waves from the region beneath the permanent thermocline next to the slope, toward the deep ocean, several hundred kilometers offshore. While it is likely that the characteristics of such a process are model-dependent, the evidence presented in *Ramos et al*. [2008] questions the extent to which this process can be relevant for interpreting the heat content variability at low frequency in the deep ocean (i.e., below 1000 m), for which estimations from observations remain uncertain, even during the Argo floats era [*von Schuckmann et al*., 2014]. This issue has been a concern in the climatic community, since it is currently thought that the planetary radiative imbalance at the top of the atmosphere could be explained by the heat content absorbed by the intermediate and deep oceanic layers [see *Abraham et al*., 2013, for a review] for which very few observations are available (in particular below 2000 m). The vertical energy flux driven by the propagation of ETRW is thus a relevant mechanism for better understanding how the ocean might take up energy at climatic time scale in the subtropical eastern Pacific. Documenting the circulation variability in this region is also relevant for clarifying the contribution of the natural and forced variability to the changes in ocean heat content under anthropogenic forcing, considering that the Interdecadal Pacific Oscillation (IPO), the internal mode of decadal-to-interdecadal variability in the Pacific, has a strong influence on the SEP circulation [*Montecinos and Pizarro*, 2005; *Vargas et al*., 2007].

The objective of this paper is to document the subthermocline variability at interannual to decadal time scale in the SEP, and evaluate the extent to which it can be interpreted as resulting from the vertical propagation of energy. It can be viewed to some extent as an extension of *Ramos et al*. [2008], which focuses on a single extreme El Niño event. Recent studies report that El Niño variability results from at least two regimes of interannual variability, whose imprints on the SST anomalies are referred to as Eastern Pacific El Niño and Central Pacific El Niño events [see *Capotondi et al*., 2015, for a review]. These two types (or "flavors") of El Niño have distinct teleconnections along the coast of Peru and Chile [*Dewitte et al*., 2012], which questions the extent to which the results of *Ramos et al*. [2008] can be applied to all the ENSO events. The low-frequency change in the frequency of occurrence of the two types of El Niño observed in recent

While previous relevant studies were based on the analysis of medium-resolution oceanic models to address this issue, here we take advantage of a long-term regional eddy-resolving oceanic simulation of the SEP that allows for a realistic representation of the mesoscale activity and mean stratification near the coast (i.e., coastal upwelling). In particular, a realistic simulation of the coastal circulation provides confidence in the simulation of the energy flux of equatorial origin that propagates in the SEP through the radiation of ETRW from the coastal domain. The use of a regional oceanic model is motivated essentially by the limitations of the currently available data sets (e.g., coarse temporal and spatial sampling). The model also allows for addressing aspects of the mesoscale dynamics in the subthermocline and for sensitivity experiments. The present work is structured as follows: section 2 presents the regional simulations and the observational data used for benchmarking the simulation, which, for clarity is synthesized in the Appendix A. Section 2 also provides the details of the methods. In section 3, we document the characteristics of the energy flux at ENSO and decadal time scales, and interpret it as resulting from a vertically propagating ETRW. Section 4 is a discussion focused on the interpretation of the dissipation of the energy beams evidenced in section 3. The concluding remarks are presented in section 5.

2. Data and Methods

2.1. Data

Temperature, sea level height (SLH), currents, and reanalysis products are used for evaluating the model performance:

2.1.1. Sea Level Height

We use the TOPEX-JASON 1 merged SLH data set, distributed by the Sea Level Research Group, University of Colorado. This data set corresponds to a globally gridded $0.5^\circ \times 0.5^\circ$ monthly product. The information used corresponds to the period 1992–2008. Further details on this product may be found in *Nerem et al*. [2010].

2.1.2. SODA Data Set

The Simple Ocean Data Assimilation (SODA) project is a reanalysis data set that provides gridded state variables (temperature and salinity), as well as derived fields for the global ocean. In this study, monthly and 5 day means of the SODA 2.1.6 product version are used. This product covers the time period from January 1958 to December 2008, over a horizontal uniform grid of $0.5^\circ \times 0.5^\circ$ and a 40 levels vertical grid, with 10 m resolution near the surface. Further details on both the assimilation algorithm and the data sources used in the assimilation process may be found in *Carton et al*. [2000] and *Carton and Giese* [2008]. The 5 day means outputs are used as open boundary conditions for the regional model (see section 2.2), while the monthly mean data are used for estimating the vertical energy flux in order to compare with the regional model solution.

2.1.3. COSMOS Mooring Data

In situ current measurements from a long-term mooring deployed 13 km offshore of Coquimbo, Chile (30.4°S, 71.8°W) are contrasted against the simulation in order to evaluate the model skill in reproducing the coastal current field. This mooring was maintained by the Center for Oceanographic Research in the Eastern South Pacific (COPAS) at University of Concepción. This mooring remained operational for about 20 years (since November 1991), and it stands as one of the longest coastal current records in the eastern South Pacific [cf. *Shaffer et al*., 1997, 2004].

The data used were collected by three Anderaa RCM7 current meters at nominal depths of 220, 480, and 750 m, and an upward looking Acoustic Doppler Current Profiler (ADCP, Workhorse Sentinel 300 KHz) moored at $\sim$120 m depth. The time series used covers the period between November 1991 and September 2006. Time means for each current meter were obtained by averaging the hourly values.

2.1.4. Tide Gauge Data

Tide gauge data from eight locations along the west coast of South America (La Libertad (2.2°S, 80.9°W), Paita (5.1°S, 81.1°W), Lobos de Afuera (6.9°S, 80.7°W), Callao (12°S, 77.1°W), Antofagasta (23.7°S, 70.4°W), Caldera (27.1°S, 70.8°W), Valparaiso (33°S, 71.6°W), and Puerto Montt (41.5°S, 72.9°W)) are used to test the simulation skill in reproducing the coastal sea level perturbations. The data are available at web site of the University of Hawaii Sea Level Center.

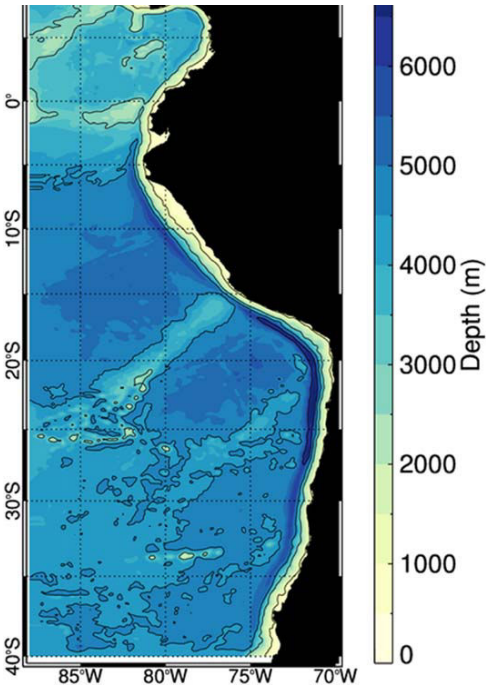

Figure 1. Model domain bathymetry in meters (color shading every 500 m). Black contours correspond to 200, 2000, 4000, and 6000 m depth.

perature profiles from 1900 to 2016, with worldwide coverage over 42 vertical levels [*Good et al.*, 2013]. This data set merges in situ temperature profiles (including Argo), through an objective-mapping analysis and profile quality control algorithms. The data are publicly available at the Met Office website. They are used here to assess the simulation skill in reproducing the mean thermocline depth.

2.2. Methods

2.2.1. Regional Simulations

Our approach is based on numerical experiments with a regional oceanic model. The Regional Ocean Modeling System (ROMS) ocean circulation model [*Shchepetkin and McWilliams*, 2005] at an eddy-resolving resolution (1/12° at the equator) is used over a domain spanning from 10°N to 40°S, and from the coast to 88°W, with lateral open boundaries at its northern, western and southern frontiers (Figure 1). The model resolves the hydrostatic primitive equations with a free-surface explicit scheme, and a stretched terrain-following sigma coordinates with 37 vertical levels. Subgrid vertical scale is parameterized using the KPP boundary layer scheme [*Large et al.*, 1994]. Bottom topography is from the GEBCO 30 arc sec grid data set, interpolated to the model grid and smoothed as in *Penven et al.* [2005] in order to minimize the pressure gradient errors and modified at the boundaries to match the SODA bottom topography. The open boundary conditions are provided by 5 day mean oceanic outputs from SODA for temperature, salinity, horizontal velocity, and sea level for the period 1958–2008. Wind stress and speed forcing at the air-sea interface come from statistical downscaling of NCEP1 [*Kalnay et al.*, 1996]. The statistical model is built from QuikSCAT data [Centre ERS d'Archivage et de Traitement (*CERSAT*), 2002] and was motivated by the need to correct for unrealistic features in the NCEP surface winds. Details on the statistical model can be found in *Goubanova et al.* [2011] while the benefit of using the downscaled product for regional oceanic modeling in this region is documented in *Cambon et al.* [2013]. Atmospheric heat fluxes were derived from the bulk formula using the temperature from COADS $1° \times 1°$ monthly climatology [*daSilva et al.*, 1994]. Precipitation, relative humidity as well as shortwave and longwave radiation are also from COADS. No land runoff is applied in our configuration, considering that there are no large rivers north of 37°S.

Two simulations are considered in this study: (1) A Control Run (CR) that is similar to the one of *Dewitte et al.* [2012] and (2) an experiment that considers the same forcing than CR but with a modified physics, consisting in removing the nonlinear terms in the momentum equations and replacing them by a constant viscosity term with a viscosity coefficient set equal to 100 $m^2\ s^{-1}$. This latter experiment, referred to as LIN, simulates a much damped Eddy Kinetic Energy (EKE), and allows assessing the effect of eddies (nonlinearities) on the characteristics of the vertical energy flux by comparing to estimates from CR.

The CR simulation has been previously contrasted against observations for the Peru region [*Dewitte et al.*, 2012; *Vergara et al.*, 2016], and complementary test are presented here for the whole Peru-Chile region. Since the magnitude of the vertical energy flux in the subthermocline depends on the characteristics of the thermocline, we first compare the model thermocline against observations. The thermocline depth is computed following *Pizarro and Montecinos* [2004] (criteria based on the highest vertical temperature gradient), for the observations and the simulation (Figure A1). For both the CR and the observations, the maximum thermocline depth is found in the region west of 80°W and south of 20°S, with differences of 10 m west of

olution between the simulation and the data set. However, we observe that the zonal gradient of the mean thermocline depth (50 year average) in the simulation is similar to the observations (Figure A1c). In order to assess the realism of the vertical structure variability (i.e., thermocline "shape"), we also perform a vertical mode decomposition of the mean density profiles at each grid point using the local depth for the model and for the observations (SODA), which provides the vertical mode functions (baroclinic modes) and then the wind projection coefficients in the linear formalism (P_n, where n stands for the baroclinic mode order) [see *Dewitte et al*., 1999, for details on the method]. The wind projection coefficients are an integrated measure of the "shape" of the stratification. Note that the results of the vertical mode decomposition are only used at a distance from the coast of at least 50 km and where water depth reaches at least 1000 m, which ensures that there is little influence of friction along the continental slope-shelf. The Figure A2 presents the P_n of the first three baroclinic modes for the model and SODA averaged over two domains. It shows a fair agreement between model and SODA indicating that the mean thermocline in the regional model is realistic. Another indirect measure of how the model simulates the mean circulation is provided by the mean EKE (Figure A3). The levels of mesoscale activity computed from the simulation and satellite altimetry have a similar average pattern (over the 1992–2008 period). Given that in this region, the predominant mechanism for the generation of mesoscale eddies is through baroclinic instabilities [*Belmadani et al*., 2012; *Colas et al*., 2012], the fair agreement between the simulation and the observations in terms of EKE levels indirectly reflects a realistic vertical structure of the current system near the coast from which eddies are generated. However, the simulation presents slightly higher amplitudes than the observations, which might be due to the model setting not taking into account air-sea interactions at mesoscale [*Renault et al*., 2016]. The differences in amplitude could also be due to biases in the equatorial boundary forcing [*Belmadani et al*., 2012].

The realism of the coastal current in the SEP simulated by the model is evaluated through direct comparison against in situ current measurements over the shelf (Figure A4), which indicates that the simulation represents a realistic vertical structure of the different components of the mean circulation. Further analyses evaluate the realism of the interannual variability, complementing the material presented in *Dewitte et al*. [2012] (see Appendix A for details).

2.2.2. Estimation of Vertical Energy Flux

The mean energy flux is estimated as the temporal (50 year) mean of the product between the pressure and velocity anomaly fields. Anomaly is defined as the departure from the mean seasonal cycle (linear trend was removed from each field prior to the anomaly computation). According to linear theory, this flux forms beams that approximately follow the theoretical raypaths of long Rossby waves at a particular frequency [*McCreary*, 1984]. The beams are more likely to form in regions where vertical temperature gradients are weak (Wentzel-Kramers-Brillouin (WKB) approximation; see *Gill* [1982]), that is, below the thermocline.

According to the WKB raypath theory, vertical isotherm displacements ζ should scale as $N^{-1/2}$, where N is the Brunt-Väisälä frequency, and therefore ζ varies smoothly along raypaths below the thermocline. These raypaths correspond to the trajectory of the energy flux vector $(u\ p, v\ p, w\ p)$, where (u, v, w) and p are the velocity components and pressure deviations from the background state [*Eliassen and Palm*, 1960]. The vertical velocity is estimated from the temporal derivative of the vertical isothermal displacements (i.e., $\partial\zeta/\partial t$) instead of using the vertical velocity from the model (w), given that w from the model presents high-frequency variability related to the nonlinearities of the flow. In particular, we compared harmonics (amplitude and phase) from both fields, and the prognostic variable is usually noisier (not shown). The choice of estimating w from temperature also eases the comparison with observations or Reanalysis products, and is consistent with former studies [*Kessler and McCreary*, 1993; *Dewitte and Reverdin*, 2000; *Ramos et al*., 2008]. Note that this assumes that the advection of vertical isotherm displacements is much weaker than $\partial\zeta/\partial t$, which is acceptable given the weak mean circulation in the subthermocline in this region [*Shaffer et al*., 2004] and is consistent with linear approximation. Throughout the paper, we use p in meters (i.e., scaled by an average density equal to 1025 kg m^{-3} and the acceleration due to gravity, 9.8 m s^{-2}) and w in m s^{-1}, which yields m^2 s^{-1} as the units of $\langle p\ w \rangle$. Angled brackets stand for the average over 1958–2008, the time period of our model experiments. The slope of the theoretical trajectories of the beams is given by:

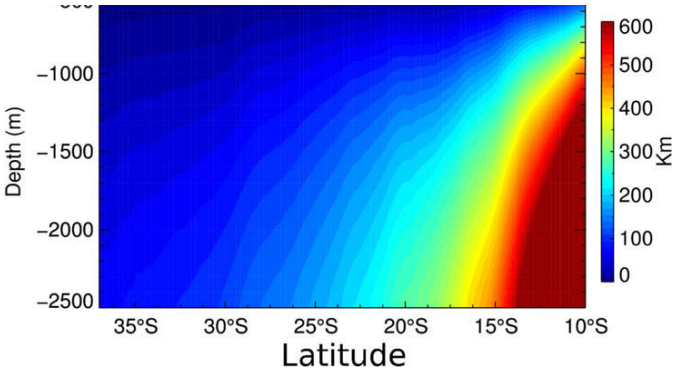

Figure 2. Distance from the coast of the theoretical WKB trajectories originating from the coast below the thermocline (∼100 m). The mean value of the phase speed of first and second baroclinic modes is used for the estimate of the trajectory slope, using a period equal to 3.7 years.

where ω is the wave frequency, f is the local coriolis parameter, β is its local derivative from the β-plane approximation, N is the 50 year mean Brunt-Väisälä frequency and c_n is the phase speed of the nth baroclinic mode (cf. Appendix sections in *Dewitte et al*. [2008] and *Ramos et al*. [2008], for further details). The values of c_n are obtained from the vertical mode decomposition of the mean density profiles of the model at each grid point. Figure 2 presents the distance x (x=0 at the coast) reached by the wave characteristic computed from (1) for a wave period of $2\pi/\omega$=3.7 years (dominant ENSO period) and a phase speed equal to the average of the phase speeds of the first and second baroclinic modes. Note that even though theory of vertically propagating waves assumes a background density structure that is horizontally homogeneous, the formalism can still be applied using a slightly varying background stratification, which is the case below the thermocline in the study region. The method thus assumes that modal dispersion is weak and is validated a posteriori, provided that the energy beams exhibit features that can be interpreted in the light of the "classical" theory. This approach was also used in previous relevant studies [*Dewitte and Reverdin*, 2000; *Dewitte et al*., 2008].

The vertical mode decomposition also yields the vertical structure functions that are used as basis functions for the model variability (pressure) and to estimate the contribution of the baroclinic modes to the sea level anomaly field. The baroclinic modes contribution to the sea level variability allows deriving the energy flux associated with the sum of the contributions of the gravest baroclinic modes (modes 1–3) that are used to interpret the results and for initializing a linear Rossby wave model at the coast (see section 2.2.3).

It should be kept in mind that the WKB theory has some limitations. First, this theory assumes a slowly varying $N(z)$, so the interpretation of the estimated fluxes in the near surface region, where stratification experiences important changes, is not straightforward. Second, this theory could break down in regions of steep topographic features [*Tailleux and McWilliams*, 2002; *Tailleux*, 2004], given the impact that such features have on the local baroclinic modes structure and therefore their phase speed. So, we consider here the WKB ray trajectory starting from the base of the permanent thermocline and far enough from the continental shelf and slope, that is at a distance from the coast of at least 50 km or where water depth reaches at least 1000 m.

A common approach used to study the vertical propagation of Rossby waves is to trace the amplitude-phase diagrams and the theoretical WKB raypaths for the frequency of interest [e.g., *Kessler and McCreary*, 1993; *Dewitte and Reverdin*, 2000; *Thierry et al*., 2004]. However, we are interested here in diagnosing the energy flux associated with the ENSO variability, which spans a wide range of frequencies. In order to encompass the whole spectrum of ENSO variability, the velocity and pressure fields used to compute the interannual vertical energy flux are regressed against two-independent indices that account for the ENSO regimes and that allow grasping a significant amount of the variance associated with ENSO. The E and C indices proposed by *Takahashi et al*. [2011] are used. They are based on the linear combination of the first two EOF modes of the SST in the tropical Pacific and allow for describing two regimes of the ENSO variability, one accounting for extreme Eastern Pacific El Niño events (E) and the other one accounting for the Central Pacific El Niño events and La Niña events (C). The indices are defined as $E=\frac{PC1-PC2}{\sqrt{2}}$ and $C=\frac{PC1+PC2}{\sqrt{2}}$, where the PC1 and PC2 are the principal component (PC) time series of the first two EOF modes of SST

$$p'_{approx}(x,y,z,t) = p_E(x,y,z)E(t) + p_C(x,y,z)C(t) \quad (2)$$

$$w'_{approx}(x,y,z,t) = w_E(x,y,z)E(t) + w_C(x,y,z)C(t) \quad (3)$$

where the primes denote interannual anomalies (i.e., anomalies with respect to the mean seasonal cycle for the period 1958–2008). The approximate p' and w' (p'_{approx} and w'_{approx}, respectively) correspond to the p' and w' fields regressed against the $E(t)$ and $C(t)$ indices. The difference between w' and p' and its approximations (from equations (2) and (3)) will be referred to as residual (Res) and thus correspond to the variability in w' and p' that is not related linearly to ENSO.

Given that the E and C indices are orthogonal, the mean interannual energy flux $\langle p' \cdot w' \rangle$ (average over 1958–2008 at a given location x, y, z) reduces to:

$$\langle p'_{approx} w'_{approx} \rangle = p_E w_E + p_C w_C \quad (4)$$

This approach allows for taking into account a wide range of frequencies relevant for ENSO in the estimate of the energy flux. It assumes that the regression of pressure and vertical velocity against the E and C indices captures the salient features of the ENSO teleconnection in the SEP. The relevance of the method is verified a posteriori, as long as the estimated flux exhibits features consistent with the vertically propagating Rossby wave. The residual also contains interannual variability that could be related to decadal or lower time scales of variability embedded in the E and C indices, and will be also documented and interpreted (cf. section 3).

Therefore, despite the relatively short record (from 1958 to 2008), an attempt is made to document the decadal vertical flux that is defined as $\langle p_D w_D \rangle$, where the subscript D stands for the decadal component, estimated by linearly regressing the interannual anomaly fields p' and w' (estimated as above, including detrending) against an index of the main mode of natural variability in the Pacific, the IPO (Interdecadal Pacific Oscillation) [*Power et al*., 1999]. The Tripole Index (hereafter referred to as TPI, *Henley et al*. [2015]) is used. The TPI index is estimated using sea surface temperature interannual anomalies (SSTA) from the SODA data set, following the methodology described in *Henley et al*. [2015].

2.2.3. Multimode Linear Rossby Wave Model

A multimode linear Rossby wave model is used as a tool for the interpretation of the results. The model is based on a quasi-geostrophic approximation [cf. *Meyers*, 1979; *Kessler*, 1990], and is used to compute the isotherms excursions forced by the Ekman pumping and the boundary conditions at the coast. Based on the linearized momentum equations, the linear model equation is:

$$\sum_{n=1}^{M} (\partial_t h_n(x,y,t) + c_{rn}(y)\ \partial_x h_n(x,y,t) + \epsilon_n(y) h_n(x,y,t)) = -\sum_{n=1}^{M} \left(P_n(x,y)\ \left(\nabla \times \left(\frac{\vec{\tau}(x,y)}{\rho_0 f(y)} \right) \right) \cdot \hat{k} \right) \quad (5)$$

where h_n is the nth baroclinic mode contribution to the thermocline depth variation, c_{rn} is the Rossby wave phase speed associated with the nth baroclinic mode ($c_{rn} = (c_n^2/f^2)\beta$), averaged over a coastal fringe 500 km wide. P_n is the wind projection coefficient associated with the nth baroclinic mode, $\vec{\tau}$ is the surface wind stress vector, ρ_0 is the reference sea water surface density (1025 kg m^{-3}), f is the Coriolis parameter, and ϵ_n is a dissipation coefficient for the nth baroclinic mode, modeled as a Rayleigh-type friction. This coefficient is computed following *Gent et al*. [1983], as $\epsilon_n = \epsilon_1 (c_n/c_1)^q$, with c_1 and c_n the phase speed associated with the first and nth baroclinic modes, respectively (i.e., c_n^2 is the separation constant of the differential equation which solutions are the linear normal modes, *Fjelstad* [1933]), ϵ_1 fixed equal to 300 days^{-1} and q adjusted empirically for each latitude. The value of q is selected based on the comparison between the multimode linear model and the CR simulation. The linear model was run at each latitude (between 5°S and 35°S) for a range of q values (from 0 to 2.5, *Gent et al*. [1983]) and the selected q corresponds to the value for which the correlation between $\sum_{n=1}^{3} h_n(x)$ and $h(x)$ (from CR) is maximum (we verified that for the selected values of q the correlation values were always higher than 0.8).

The solution to equation (5) is found by integrating along the wave characteristic $\int_0^x \frac{dx}{c_n(x)}$ [*Gill and Clarke*, 1974]. A similar model was used by *Vega et al*. [2003] to interpret the altimetric sea level data during the

the thermocline depth anomaly (h_n) of the full-physics model as boundary conditions at the coast. The latter is derived from the vertical mode decomposition of the pressure field (p_n) and using the hydrostatic equation [see *Dewitte*, 2000]:

$$h_n(x_0,y) = \frac{g}{N^2\left(z=\overline{H}(x_0,y)\right)} \sum_{n=1}^{M} p_n(x_0,y,t)\,\frac{d\psi_n}{dz}\left(x_0,y,z=\overline{H}\right) \tag{6}$$

where x_0 corresponds to the distance from the coast equal to 50 km or where water depth reaches at least 1000 m, $\overline{H}(x_0,y)$ is the mean thermocline depth along the coast estimated as described in *Pizarro and Montecinos* [2004], g is the acceleration due to gravity, N is the Brunt-Väisälä frequency, and ψ_n is the vertical structure for the nth baroclinic mode. In order to filter out variability in h_n associated with either coastal-trapped Kelvin waves (that would be related to the intraseasonal time scales) or mesoscale activity not relevant in this linear framework, a 12 month low-pass spectral filter is applied on h_n. The linear model solution consists in the sum of the first three baroclinic modes (i.e., $n=[1,2,3]$).

The result of the multimode linear Rossby wave model is used to compute the contribution of the first three baroclinic modes to the pressure field (p_n) and to the vertical isotherm displacements (ζ_n) following *Dewitte and Reverdin* [2000]:

$$p_n(x,y,z,t) = \sum_{n=1}^{3}\left(\frac{h_n(x,y,t)c_n^2(x_0,y)}{\overline{H}(x,y)g}\;\psi_n(x_0,y,z)\right) \tag{7}$$

$$\zeta_n(\mathrm{x},\mathrm{y},\mathrm{z},\mathrm{t}) = \frac{g}{N^2(x,y,z)}\sum_{n=1}^{3}\left(p_n(x,y,z,t)\;\frac{d\psi_n(x_0,y,z)}{dz}\right) \tag{8}$$

where h_n is given by the solution of equation (5) using (6) as boundary condition at the coast, c_n is the phase speed (i.e., root mean square of the separation constant) of the baroclinic mode n, $\overline{H}$ is the time (50 year) average thermocline depth, g is earth's gravity acceleration, ψ_n is the vertical structure of the nth baroclinic mode for pressure and N is the Brunt-Väisälä frequency. Equations (7) and (8) are used to estimate the contribution of the baroclinic modes to the vertical energy flux (section 4.1).

3. Vertical Energy Flux

In this section, we first document the characteristics of the mean energy flux associated with the interannual anomalies (i.e., $\langle p'w' \rangle$ over the period 1958–2008), and then we focus on ENSO and decadal time scales.

3.1. Mean Flux

As a benchmark for the rest of the paper, the total mean energy flux (i.e., $\langle p'w' \rangle$) is documented. The horizontal structure of the total vertical energy flux is displayed at different depths in Figures 3a–3c (sign convention throughout the paper is chosen so that downward energy flux is positive). This analysis reveals that the highest values are found near the equatorial region and along the coast, and that there is a decrease of the energy flux magnitude as depth increases, indicating that the energy tends to remain close to the coast as latitude increases. The vertical structure of the energy flux (Figures 3d–3g) is suggestive of its propagating nature: (1) the region of highest energy flux detaches from the coast as depth increases and (2) there is a decrease in the magnitude of the energy flux as latitude increases.

3.2. ENSO Time Scale

We now focus on the portion of energy flux due to El Niño events alone, using the formalism presented in the section 2.2.2 to distinguish the energy flux induced by each ENSO regime (cf. equation (4)). Figure 4 presents the vertical energy flux at different depths associated with the *E* and *C* regimes, which can be directly compared to Figures 3a–3c. The horizontal distribution of the energy flux associated with each El Niño regime first reveals that the ENSO energy flux is much more confined to the coastal region than the total energy flux, with an offshore extension of the amplitude that decreases southward. The comparison

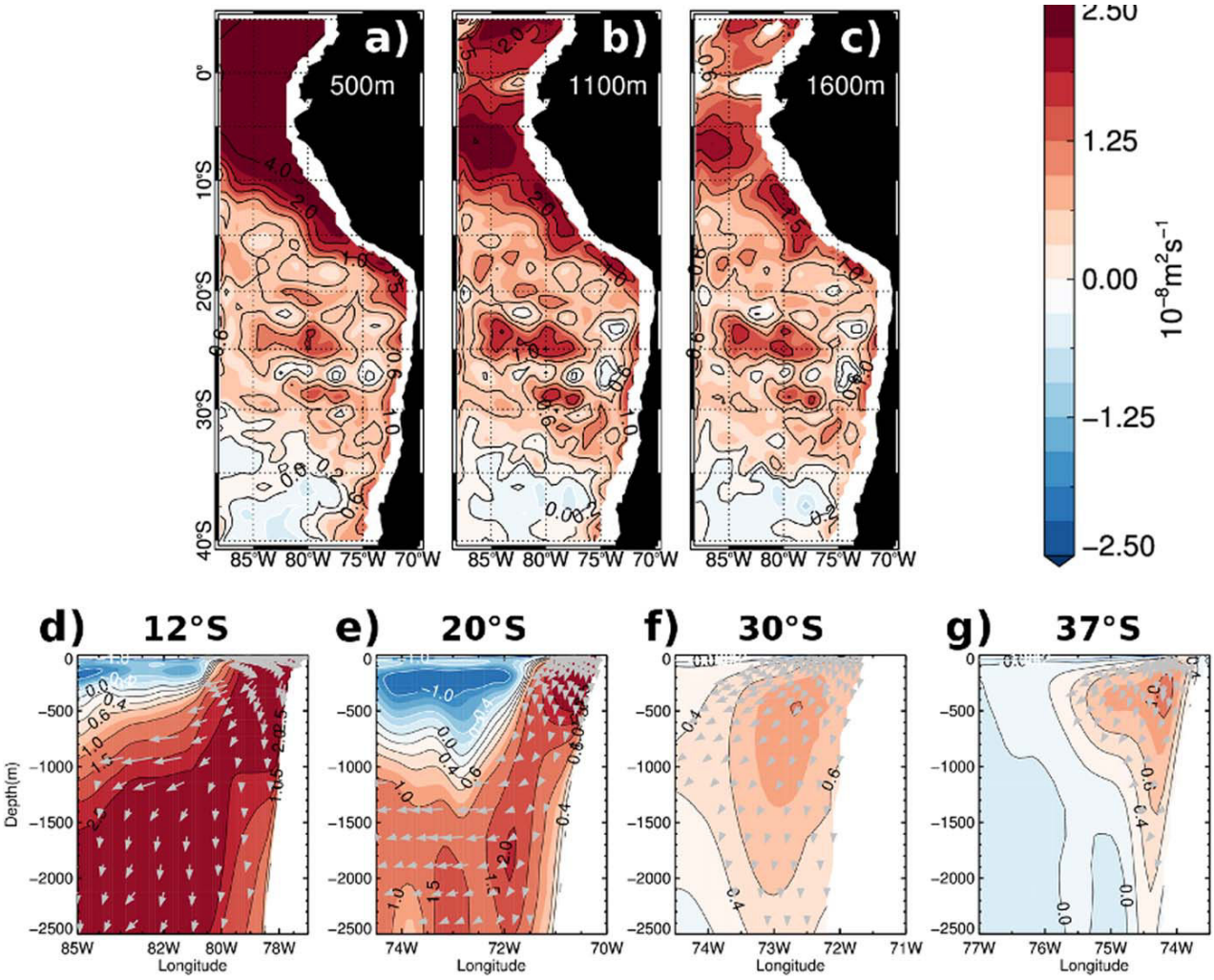

Figure 3. Mean interannual vertical energy flux ($\langle p'w' \rangle$) at (a) 500 m, (b) 1100 m, and (c) 1600 m. Cross-shore sections of mean interannual vertical energy flux at selected latitudes (d, e, f, and g). The arrows in Figures 3d–3g correspond to the scaled energy flux vector ($\langle p'u' \rangle$,$\langle p'w' \rangle$). The scaling consists in normalizing each component of the energy flux vector by the maximum value of the vector module, found in the displayed field. Arrows are only depicted for positive values of vertical energy flux, and scaled by 0.1 in the upper 500 m for better legibility. Units are in 10^{-8} m^2 s^{-1}.

between Figures 3 and 4 indicates in particular that there is a residual flux not explained by the two ENSO regimes in the offshore region (Figures 4g–4i). High values of this residual flux are located offshore around 25°S west of the Nazca ridge at almost all depths between 500 and 3000 m (not shown). This vertical energy flux may correspond to interannual variability associated with the interaction between the circulation and the topography, since it is located between high mounts (this offshore peak of vertical energy flux is also observed in the LIN experiment, although with weaker amplitude; see section 4.2 for a brief analysis of this experiment). Figure 4 also indicates that the contribution of the *E* regime to the vertical energy flux is much larger than the contribution of the *C* regime with for instance $p_E w_E \sim 4$ times larger than $p_C w_C$ on average between 5°S and 25°S near the slope (∼50 km from the slope) at 1100 m. Noteworthy the energy flux associated with the *C* regime is mostly related to La Niña events, as was verified by estimating the mean flux for the periods over which the C index of ENSO is either negative (La Niña) or positive (Central Pacific El Niño). The fact that $p_C w_C$ in the SEP is mostly related to La Niña events is consistent with Central Pacific El Niño events being dominantly associated with intraseasonal Kelvin wave activity (as opposed to interannual

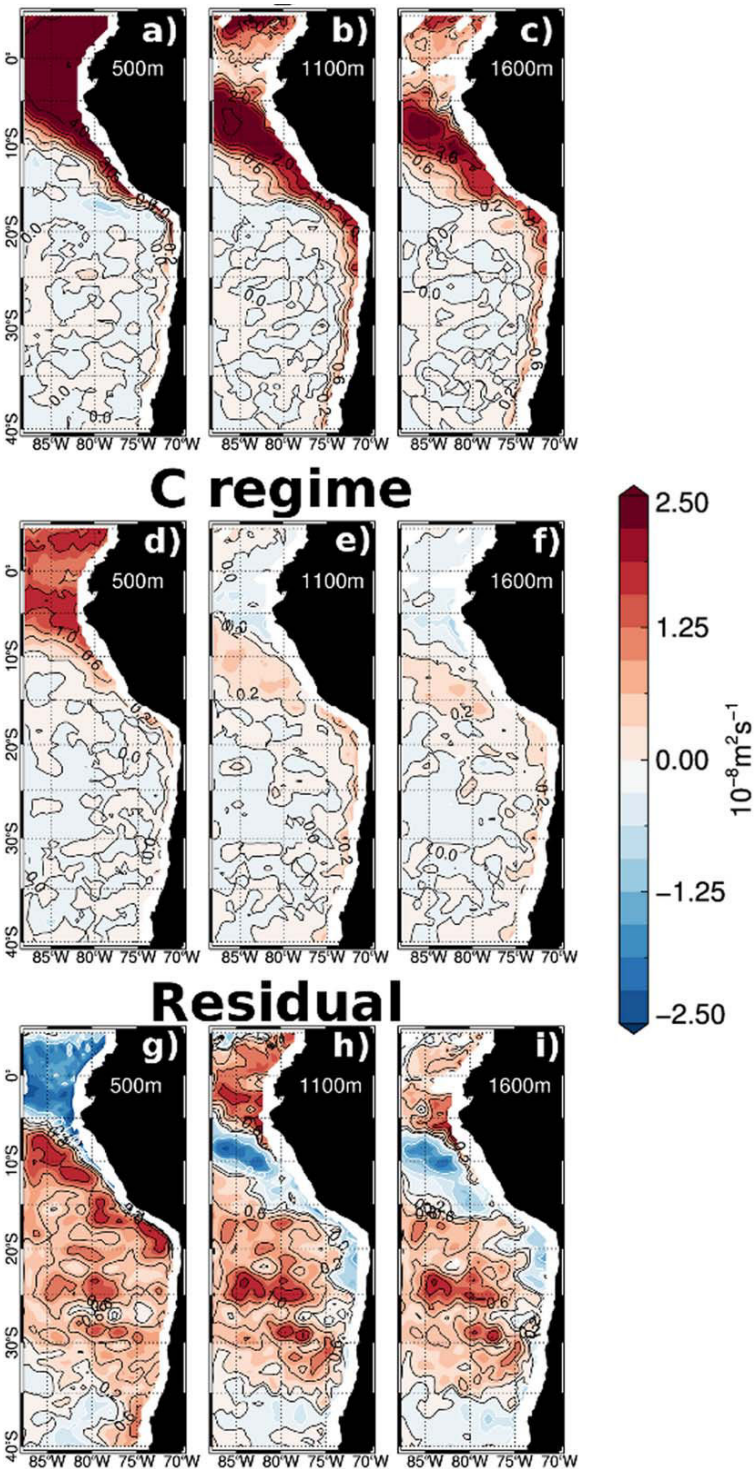

Figure 4. Same as Figures 3a–3c but for the components of the vertical energy flux associated with the (a–c) *E* and (d–f) *C* regimes, respectively (i.e., $p_E w_E$ and $p_C w_C$, respectively). (g–i) Residual term ($\langle p'w' \rangle - p'_{approx} w'_{approx}$) is also plotted. Units are in 10^{-8} m^2 s^{-1}.

The vertical structure of the energy flux associated with the ENSO regimes is further documented from cross-shore sections at different latitudes (Figure 5). Figure 5 reveals that the energy flux follows approximately the theoretical WKB raypaths associated with a phase speed value between that of the first and third baroclinic modes (see white and black plain thick lines in Figures 5a–5d and 5e–5h, respectively; trajectories have been calculated from equation (1)), with a slope that increases with latitude in consistency with theory. The portion of the vertical energy flux due to El Niño events thus concentrates closer to the coast as latitude increases, which at ∼500 m could appear as a coastal trapping of the energy from say ∼20°S (Figure 4a). Note that the energy flux related to the *C* regime tends to be associated with a slightly larger slope of the WKB raypaths, which is related to the fact that the spectrum of the *C* mode has a larger variance at decadal frequencies than the spectrum of the *E* mode [*Takahashi et al.*, 2011]. Given that raypath trajectories depend on the period of the surface-coastal forcing (equation (1)), the energy beams associated with a longer period of variability would have a smaller raypath slope. Overall, the results suggest the propagation of energy along the theoretical WKB trajectories at ENSO time scales. As this flux expands toward the deep ocean, it experiences a decrease in amplitude along its trajectory, which takes place around 1500–2000 m in the model. While the wave-induced flux is the result of an adiabatic process, its amplitude decrease suggests a dissipation process in the deep ocean. This will be discussed later in section 4.

3.3. Decadal Variability

Despite the simulation covering only five decades, it is interesting to investigate the extent to which the vertical energy flux in the regional model can also be interpreted as a decadal propagating energy flux. Figure 6 (top plots) presents the vertical energy flux at decadal time scales for the selected latitudes. First, it is interesting to note that the amplitude of the decadal energy flux has comparable amplitude than the energy flux related to the *E* regime, although weaker by an approximate factor of ∼2. Second, in a similar manner than for the energy flux associated with ENSO, the peak amplitude of the decadal flux follows approximately the theoretical WKB raypaths at 10 year period. The maximum amplitude is usually found offshore, which suggests a local forcing in addition to the equatorial source or a nonlinear amplification of the coastally induced flux. Thus, despite the much weaker amplitude of the decadal mode than the ENSO mode in the tropical Pacific, the pressure and vertical velocity anomalies covary in such a way that they form beams having comparable magnitude than the ENSO flux. Although the length of the simulation is a limitation for drawing firm conclusions, our analysis suggests that decadal variability in the SEP subthermocline can be to a large extent accounted for by linear wave dynamics.

Another indirect estimate of the decadal flux is provided by the residual flux (i.e., $p'w' - p'_{approx}w'_{approx}$) that shall grasp a share of the variability associated with decadal time scales (Figure 6, bottom plots). Interestingly the residual flux exhibits features reminiscent of a decadal vertical propagation although with clear differences with respect to the decadal flux. In particular the residual flux is in general much larger (by a factor of 2 to 3 near the coast and below the thermocline), which indicates that the residual flux grasps variability time scales other than just decadal. Nonetheless, the maximum amplitude is found in the near-coastal regions where the WKB raypaths at the 10 year period originate, and at some latitude (like 30°S) the residual flux follows approximately the theoretical trajectories far deep. This residual flux also accounts for mesoscale activity (and its low-frequency modulation), low-frequency modulation of coastal-trapped Kelvin wave activity (and its impact on thermocline) and (or) ENSO-induced Ekman transport and pumping.

4. Discussion

4.1. Baroclinic Mode Contributions

Given that, physically, the vertical propagation of energy results from the superposition of a certain number of baroclinic modes, the above result questions the extent to which the propagating characteristics of the ENSO energy flux arise from the contribution of the gravest modes that radiate off-shore the most, or from the higher-order modes which dissipate faster (because of the slower phase speed), but are also the conduit by which the flux should propagate deeper. In this section, we thus present the results of a vertical mode decomposition of the regional model, which provides material for the interpretation of the vertical energy flux pattern. Assuming that a large portion of the variance in the *w* and *p* fields is accounted for the

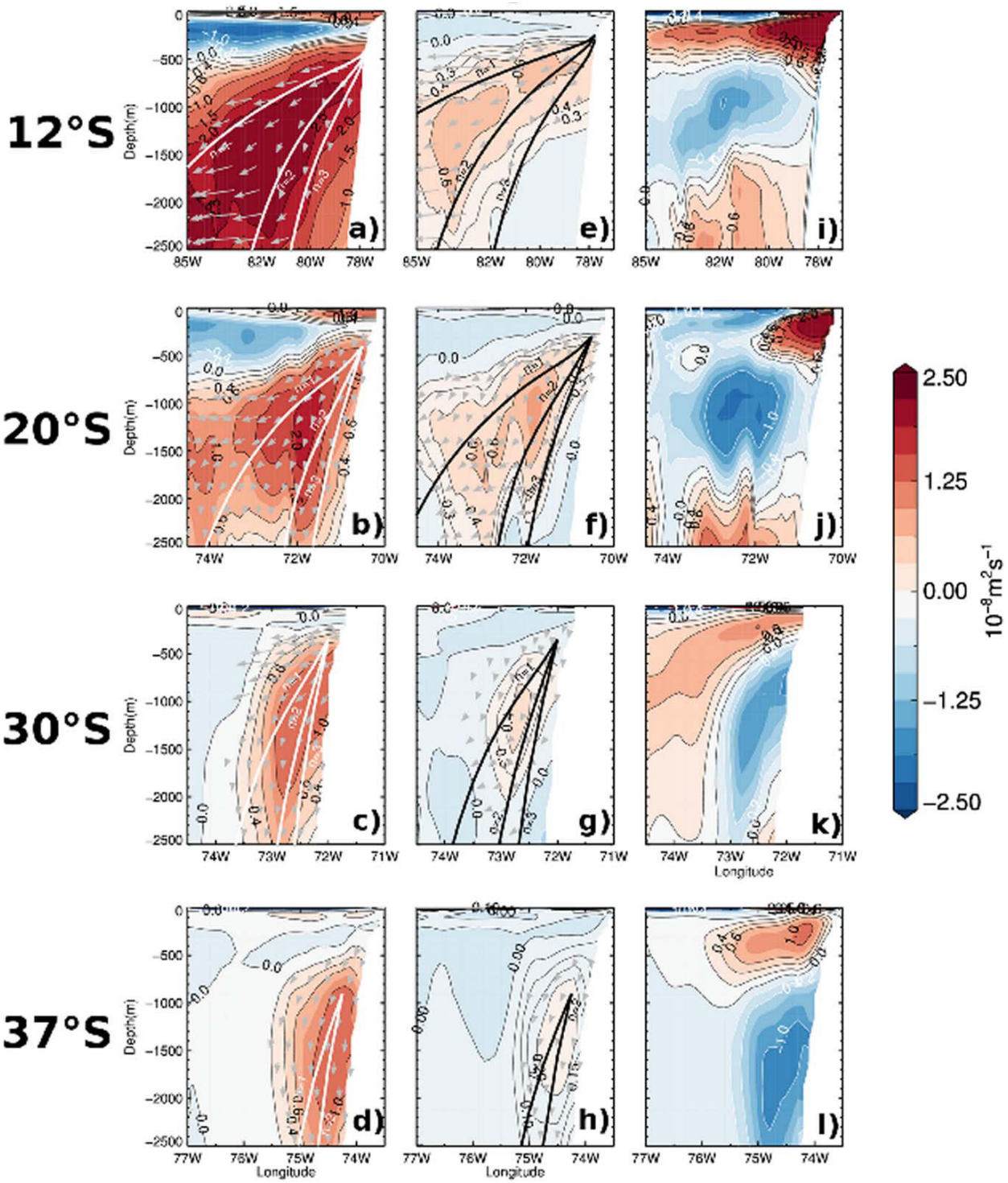

Figure 5. Cross-shore section of vertical energy flux associated with the (a–d) *E* and (e–h) *C* regimes at 12°S, 20°S, 30°S, and 37°S. Units are in 10^{-8} m^2 s^{-1} and contours in black are depicted every 0.2×10^{-8} m^2 s^{-1}. Gray arrows represent the scaled energy flux vector ($\langle p'u' \rangle$,$\langle p'w' \rangle$) related to each regime (scaling was performed as in Figure 2). Arrows are only depicted for positive values of vertical energy flux, below 200 m. Slanted white and black lines denote the theoretical WKB trajectories for phase speed values corresponding to the first three baroclinic modes (*n*), at periods of (a–d) 3.7 and (e–h) 4 years.

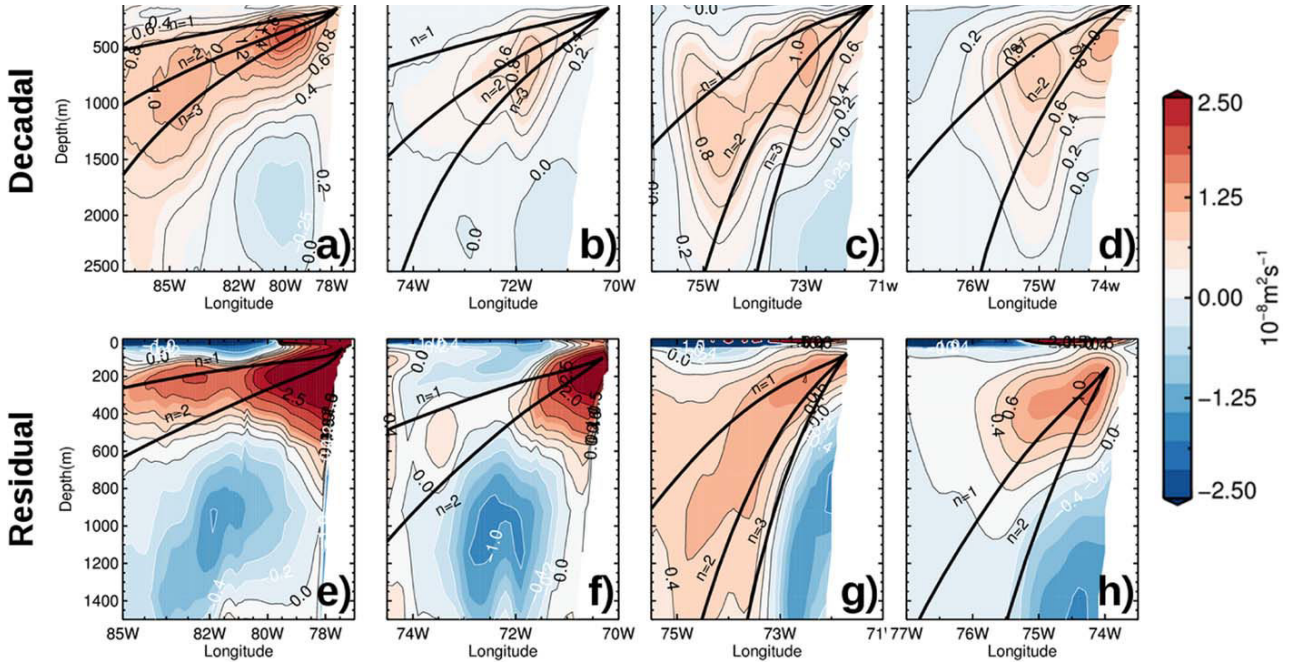

Figure 6. (a–d) Cross-shore sections of decadal energy flux ($\langle p_D w_D \rangle$) and (e–h) residual flux ($\langle p'w' \rangle - p'_{approx} w'_{approx}$) at selected latitudes. Slanted lines denote the theoretical WKB trajectories for phase speeds of the (a, b, c, and g) first three and the (d, e, f, and h) first two baroclinic modes with a period of 10 years.

contribution from the first three gravest modes (which is the case in the near-equatorial domain, cf. *Dewitte et al.* [1999]), the contribution of the gravest baroclinic modes to the vertical energy flux in the regional model is estimated as $\langle \sum_{n=1}^{3} p_n \cdot \sum_{n=1}^{3} (\partial \zeta_n / \partial t) \rangle$, where p_n and ζ_n are the nth baroclinic mode contribution to the pressure field and to the isotherm vertical displacements, respectively (see section 2.2.3). In order to focus on the ENSO vertical energy flux, the sum of the contributions of the gravest baroclinic modes to the pressure field and to the isotherm vertical displacements is first regressed against the E and C indices. The results are presented in Figure 7, which can be compared to Figure 5. The results indicate that the main characteristics of the energy beams close to the coast can be captured with only three modes, at least for the *E* regime. The amplitude of the vertical energy flux is in general lower than that for the estimates from equation (4) (i.e., $p_E w_E$ and $p_C w_C$), and the beams are more rapidly attenuated along their trajectory. High-order modes contribute to extend the energy flux deeper. As a consistency check, the multimode linear model tuned from the OGCM outputs (i.e., using P_n and c_n as derived from the vertical mode decomposition) is run using three modes. The model is initialized along the coast by the thermocline anomalies as derived from the vertical mode decomposition of the OGCM (see section 2.2.3). No local wind forcing is applied, which also tests the dominant role of the equatorial oceanic forcing. The results are presented in Figure 8, in a similar manner than above. The analysis indicates that the linear model can realistically reproduce the characteristics of the energy beams of the regional model with only three modes. As expected, the ENSO energy flux with three modes does not extend as far deep as the flux with all the modes. In particular, the vertical dissipation of the ENSO flux is prominent below 1000 m, which would correspond to the depth where higher-order modes contribute significantly to the variability. Considering that the wavelength of the wave increases with depth (because of the higher-order modes having a shorter vertical scales than the gravest modes and the weaker stratification), it is expected that mixing takes place in the region where the ENSO flux of Figure 8 dissipates the most (see section 4.2). Differences between the linear model solution and the OGCM modal decomposition are the largest south of 20°S, which may be due to the modal dispersion not accounted for by the linear model and or interaction between Rossby waves and mesoscale activity or the mean circulation. Overall our results support the interpretation of the vertical energy flux at ENSO time scales as resulting from the vertical propagation of extratropical Rossby waves originating from the remote equatorial forcing.

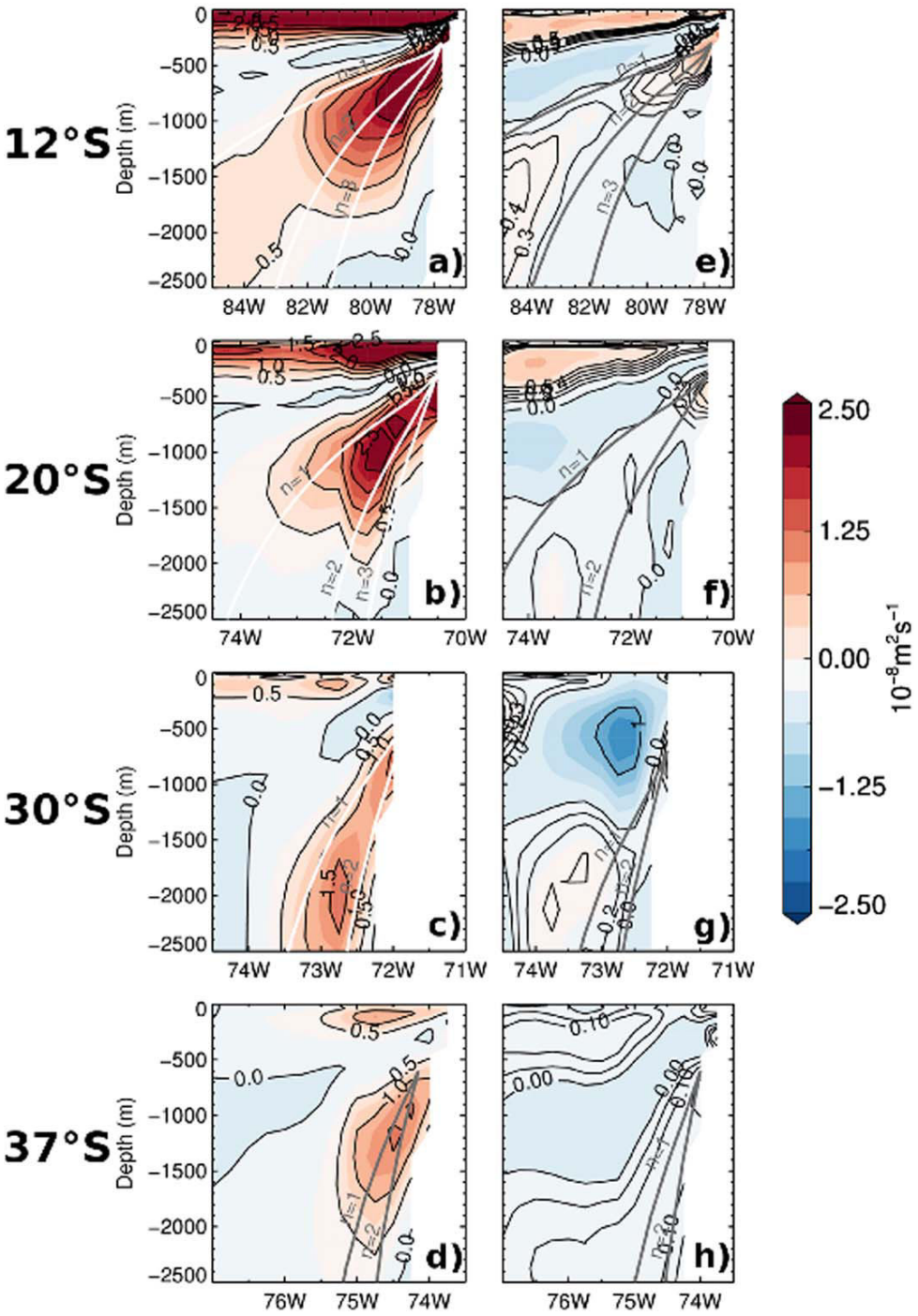

Figure 7. Vertical mode decomposition of the ENSO vertical energy flux: Summed-up contribution of the first three baroclinic modes to the vertical energy flux associated with the (a–d) *E* and *C* regimes at different latitudes. The white-gray lines represent the theoretical WKB raypaths, computed using the phase speeds of the baroclinic mode (*n*), at periods of (a–d) 3.7 and (e–h) 4.0 years. Units are in 10^{-8} m^2 s^{-1}.

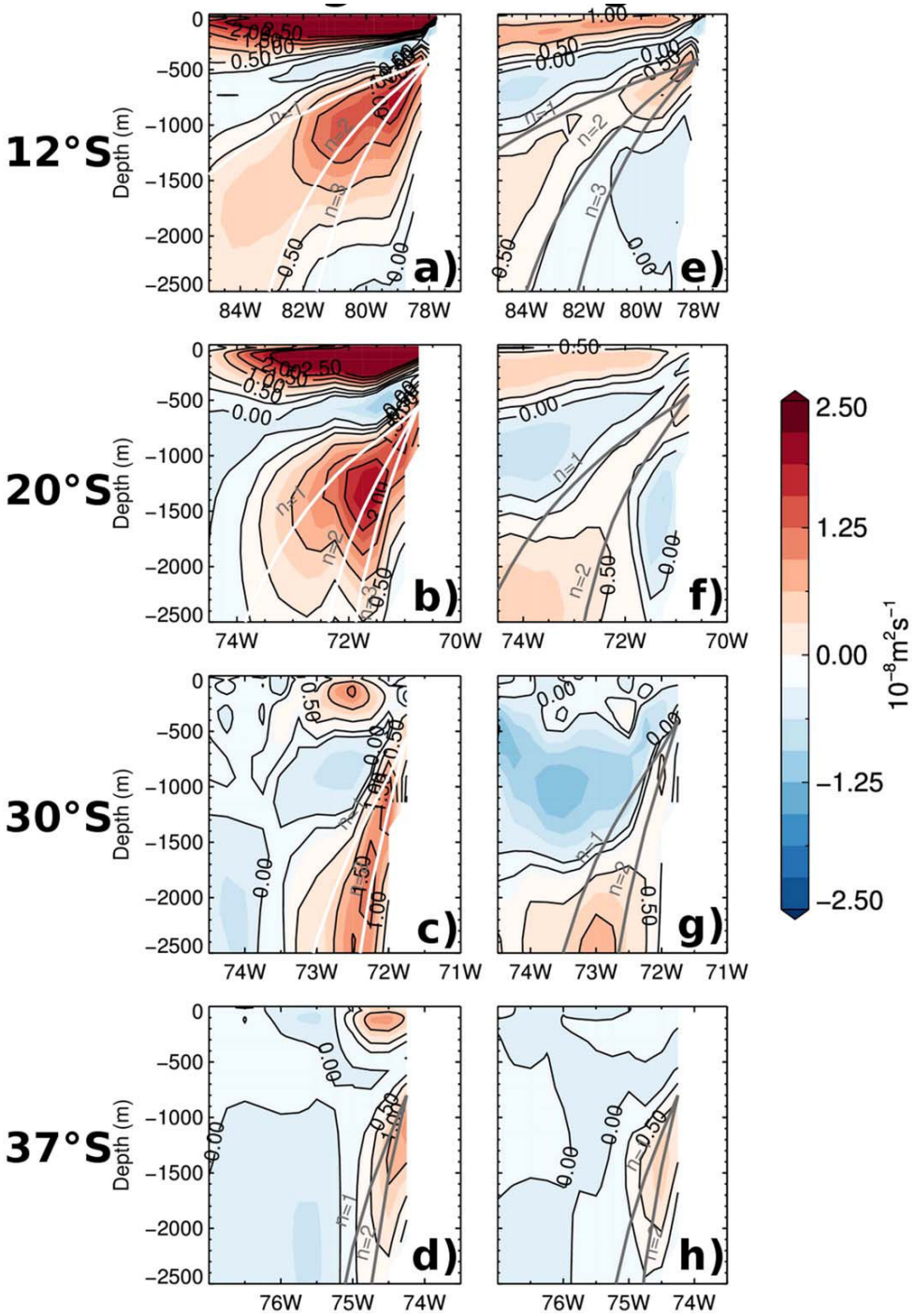

Figure 8. Linear model solution of the ENSO vertical energy flux: (a–d) *E* and (e–h) *C* regimes at 12°S, 20°S, 30°S, and 37°S. The white-gray lines represent the theoretical WKB ray paths, computed using the phase speeds of the baroclinic mode (*n*), at periods of (a–d) 3.7 and (e–h) 4.0 years. Units are in 10^{-8} m^2 s^{-1}. The boundary conditions used to initialize the model were low-pass filtered using a spectral filter with a cutoff period of 1 year.

deep mean circulation in the SEP. In particular, we are interested in the decrease of the ENSO energy flux observed along the propagation trajectory (section 3), given that dissipation can take place through a number of processes and might result in a transfer of heat toward the deep ocean (i.e., diabatic dissipation). Previous studies have documented several processes of wave dissipation which operate through nonlinearities in the momentum equations (e.g., baroclinic instability and subsequent breaking of the wave, *LaCasce and Pedlosky* [2004]), momentum diffusion toward the eddy field [*Qiu et al*., 1997], and wave triad instability [*Qiu et al*., 2013]. Other studies have focused on the effect of temperature-diapycnal diffusion on the wave amplitude attenuation [*Marchal*, 2009; *Furue et al*., 2015], which is more relevant for the interpretation of our results considering that the vertical flux in LIN (i.e., without nonlinearities in the momentum equations) yields comparable features than CR (see below). In particular, the theoretical study by *Marchal* [2009] indicates that vertical diffusion can critically damp the Rossby waves in the longwave limit, with the decay rate increasing linearly with the square root of vertical diffusivity. This indicates that the vertical attenuation of $\langle p'w' \rangle$ evidenced earlier can thus be related to a vertical heat flux. Under certain assumptions, it can be shown in particular that $\langle \frac{\partial (p'\ w')}{\partial z} \rangle$ is proportional to $\langle w'T' \rangle$ (see Appendix B for the derivation of this relationship) so that the regions of large vertical gradient in the energy flux should exhibit a peak vertical heat flux. As an attempt to verify this hypothesis, the vertical heat flux, $\langle w'T' \rangle$, is estimated from the regional model outputs, where w' and T' are the vertical velocity and temperature field, respectively, and the prime denotes the interannual anomaly (with respect to the mean seasonal cycle over the simulation period). The results are presented in Figure 9. This analysis indicates that the regions of maximum vertical heat flux below the thermocline are located within the trajectories of the WKB ray paths related to the *E* regime, with a peak amplitude in the vicinity of the region where the energy beams associated with the summed-up contribution of the first three baroclinic modes (white contours in Figures 9a–9h) decrease sharply. Our results therefore support the theoretical prediction of *Marchal* [2009] that diapycnal diffusion could significantly contribute to the observed attenuation of the ETRW. As a consistency check, the same diagnostic is performed for LIN, in which nonlinear advection of momentum is canceled out (Figures 9i–9l). LIN exhibits similar characteristics than CR, that is vertical dissipation of the ETRW taking place in the region where vertical diffusion is enhanced, which supports the above interpretation. Other possible processes include wave breaking at critical layers in a background mean flow. However, there is no evidence for any deep zonal flows in CR. There is also the possibility that the vertically propagating ETRW modulates the process of trapping of internal waves in the deep ocean, which can take place where N^2 is small [*Winters et al*., 2011]. This would deserve further study that is beyond the scope of the present paper. We discuss below implications of our results for the understanding of the processes that intervene in the ocean heat uptake, since they suggests that a portion of the low-frequency variability of the subthermocline heat content in the SEP could be associated with the rectification of Eastern Pacific El Niño events on the mean deep circulation. This process of energy propagation-dissipation would represent an energy pathway linking upper thermocline tropical dynamics with the deep offshore ocean at midlatitudes. As an attempt to evidence such a pathway, we calculated the dominant SVD (Singular Value Decomposition) mode between low-frequency change (11 year running mean) of heat content in the intermediate layer (1000–2500 m) and of the ENSO vertical energy flux ($\langle p_{approx} w_{approx} \rangle$) at two different depths, 1000 and 1500 m. The results are presented in Figure 10. It shows that there is a significant covariability (percentage of explained covariance is 70% and the correlation between the PC time series reaches -0.74) between heat content in the intermediate layer (where approximately, the dissipation of the energy flux is observed) and the ENSO energy originating from the coast of Peru. The mode patterns also explain a large amount of variance of the original field (see percentage in the plots). Positive energy flux is associated with negative heat content anomaly near 10°S and between 20°S and 30°S that extends offshore, meaning that the ENSO vertical energy flux tends to cool the intermediate layers. The PC time series suggests that the ENSO energy flux is in advance with respect to the change in heat content, although the length of the simulation is too short to establish the statistical significance of the phase lag. Note the contour in red dashed line in Figure 10b that represents the contour at 0.8 units for the ENSO flux mode pattern associated to the SVD analysis between the ENSO vertical energy at 1000 m (instead of 1500 m) and the heat content (1000–2500 m), which highlights the zonal propagation of the ENSO energy flux. It thus confirms the tight relationship between the heat content variability in the intermediate layers and the ENSO vertical energy flux in the model.

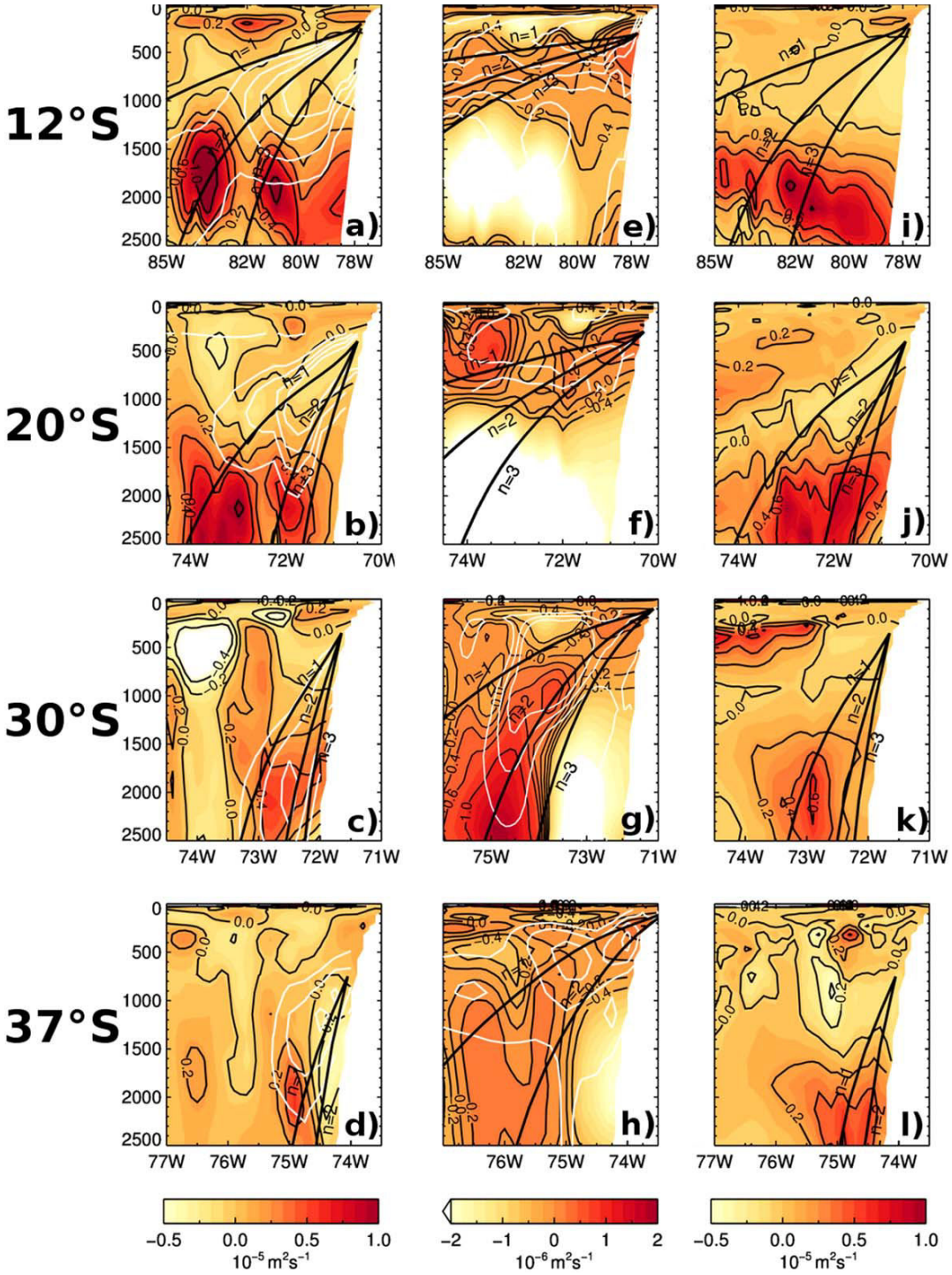

Figure 9. Zonal sections of the total vertical heat flux ($\langle w'T' \rangle$: (a–d) and the decadal heat flux ($\langle w_D T_D \rangle$: (e–h) from CR, and the total vertical heat flux from LIN ($\langle w'T' \rangle$: (i–l). Black slanted lines correspond to the theoretical WKB raypaths, computed using the phase speed values of the gravest baroclinic modes ($n = 1, 3$ for a, b, c, e, f, g, i, j, k and $n = 1, 2$ for d, h, l), at periods of (a–d, i–l) 3.7 and (e–h) 10 years. Temperature was scaled by the average vertical temperature gradient $d\overline{T}/dz$ in order to emphasize the vertically coherent patterns in the regions where the variability of T' is very low. This yields $m^2\ s^{-1}$ as the units of $\langle w'T' \rangle$. The energy flux (below 300 m depth) associated with the contribution of the first three baroclinic modes is plotted in plots Figures 9a–9h (white contours). The white contour values are the same ones as in Figure 6 for the Total CR heat flux (0.5–2.0, every 0.5) and every 0.2 in the 0.2–1.0 interval for the decadal heat flux.

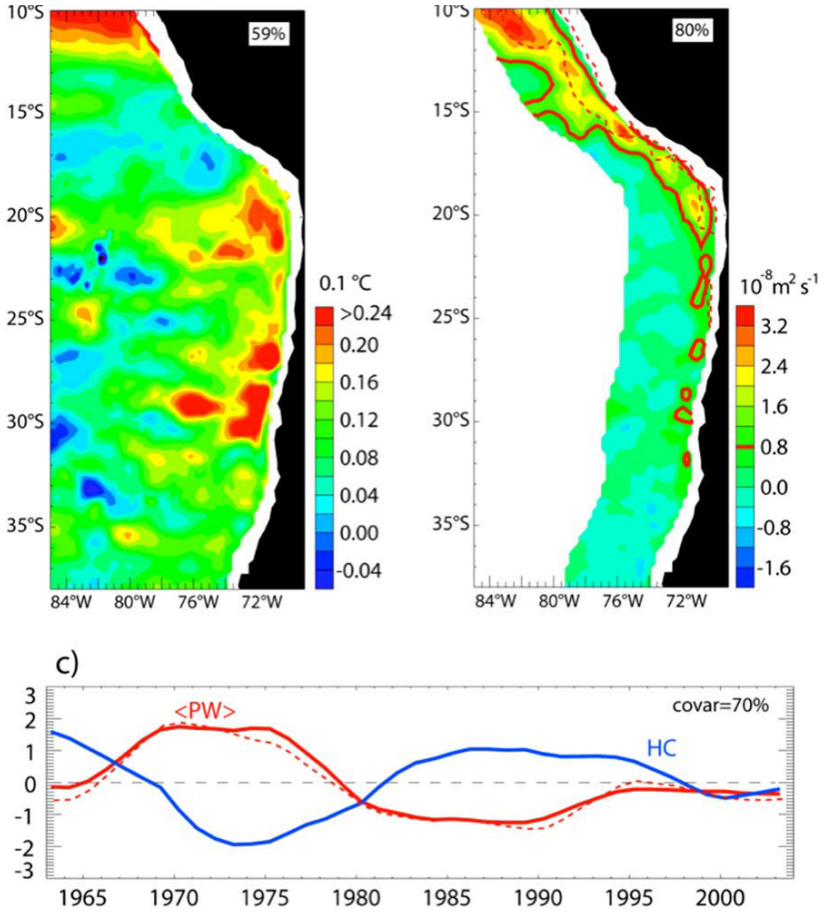

Figure 10. Dominant mode of the SVD analysis between the low-frequency changes (11 year running mean) of heat content (1000–2500) and of the ENSO vertical energy flux at 1500 m: (a) Mode pattern for heat content. (b) Mode pattern for the ENSO energy flux. The ENSO energy flux corresponds to the quantity $\langle p_{approx} w_{approx} \rangle$ where the mean is computed over 11 year running windows. (c) PC time series for heat content (blue) and vertical energy flux (red). The full line curve corresponds to the energy flux at 1500 m while the dashed line curve corresponds to the result of the SVD analysis between the heat content (1000–2500 m) and the vertical energy flux at 1000 m. The contour at 0.8 for the mode pattern for vertical flux at 1000 m is indicated in Figure 10b in dashed red line. The percentage of explained variance for both fields is indicated in Figures 10a and 10b, while the percentage of covariance is indicated in Figure 10c.

From a different perspective, our results could also have implications for understanding low-frequency changes in the SEP OMZ, since the vertical attenuation of the energy flux takes place below 1000 m, which corresponds to the vicinity of the lower boundary of the OMZ (at least in the range of latitude between 9°S and 21°S). There, mean vertical oxygen gradients are strong, which can result from a significant contribution of the eddy flux to shaping the OMZ limit [*Bettencourt et al.*, 2015; *Vergara et al.*, 2016]. Since the dissipation of the energy beams contributes to enhance diffusion in the vicinity of the lower OMZ boundary, we may hypothesize that an eddy oxygen flux is produced there, which can ventilate the OMZ. Interestingly, observations suggest a significant decadal variability of the lower limit of the OMZ in the eastern tropical Pacific (cf. Figure 2 in *Stramma et al.* [2008]). While this issue is difficult to tackle using observations, it could be addressed from the experimentation with the regional model used in this study coupled to a biogeochemical model. This is planned for future work.

5. Summary and Conclusions

The subthermocline vertical propagation of energy in the SEP is investigated using a high-resolution regional OGCM. The focus is on ENSO time scales, considering the efficient oceanic teleconnection linking

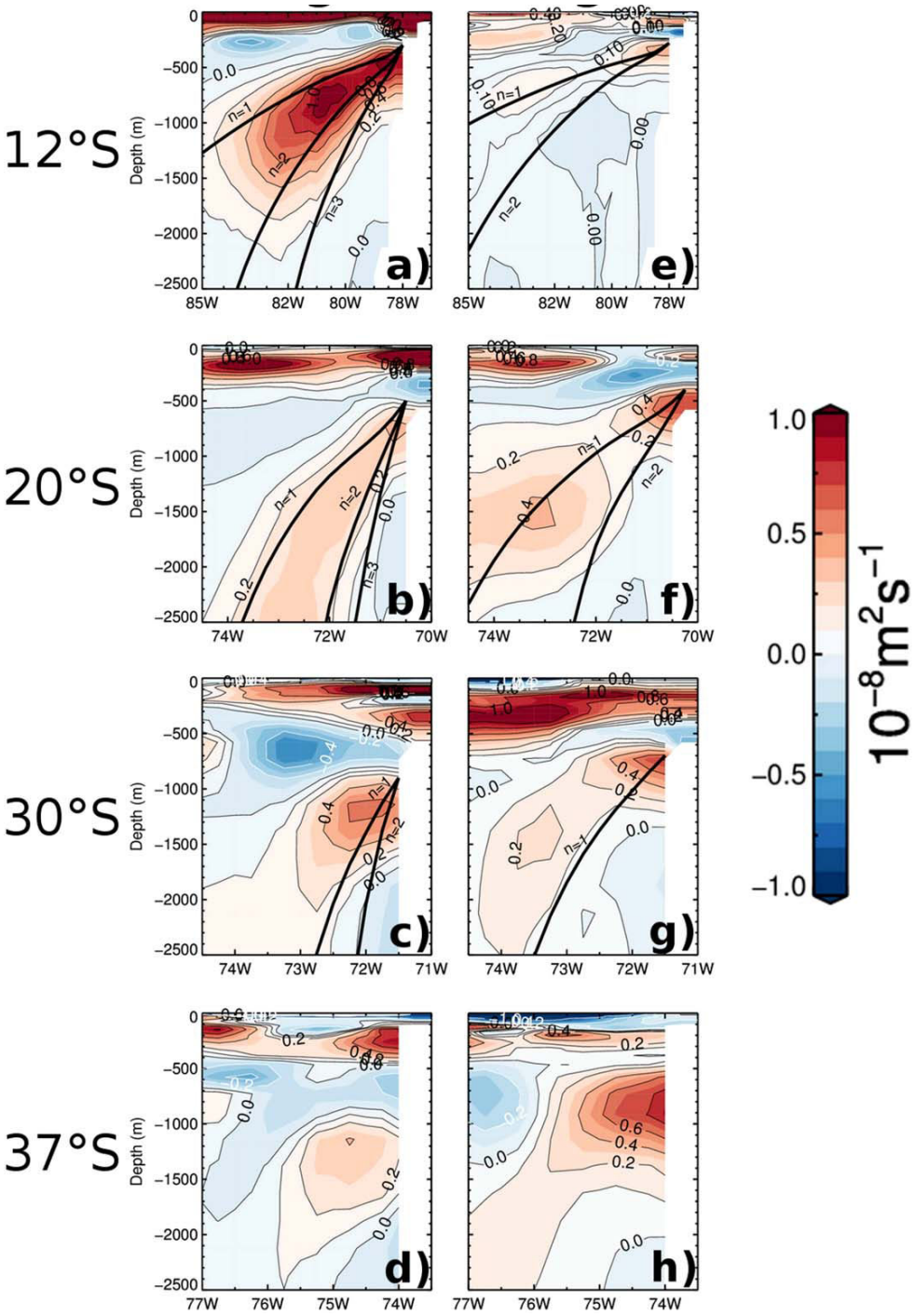

Figure 11. Cross-shore section of vertical energy flux associated with the (a–d) *E* and (e–h) *C* regimes at 12°S, 20°S, 30°S, and 37°S for SODA. Units in are in 10^{-8} m^2 s^{-1}. Slanted black lines denote the theoretical WKB trajectories for phase speeds of the first baroclinic modes (*n*), at periods of (a–d) 3.7 and (e–h) 4.0 years.

mately theoretical the WKB raypaths, having steeper slope poleward. The main contribution to the total energy flux is associated with the so-called tropical Pacific E regime, corresponding to the regime of interannual variability accounting for extreme Eastern Pacific El Niño events [*Takahashi et al*., 2011]. This somehow generalizes the findings of *Ramos et al*. [2008] that first documented the vertical propagation of ETRW energy in the SEP during the strong 1997–1998 El Niño event. The vertical energy flux associated with the *C* regime accounting for both Central Pacific El Niño and La Niña events is much weaker than that of the *E* regime, and is mostly due to La Niña events. The contrasting results between the estimates of $p_E w_E$ and $p_C w_C$ indicate a marked asymmetry of the oceanic ENSO teleconnection in the subthermocline of the SEP. The existence of the energy beams in the simulation questions the extent to which they can transfer heat to the deep ocean and thus rectify on the heat content of the deep layers. Consistently with theory [see *Marchal*, 2009, Appendix B], a sharp decrease of the vertical energy flux associated with ENSO is observed in the deep ocean (below 1000 m), which is in turn related to vertical temperature diffusion (i.e., vertical eddy heat flux). Consistent with the fact that eddy activity has a marginal impact on the energy beams (as revealed by the simulation where nonlinear advection of momentum is cancelled out), our result supports the notion that diapycnal diffusion is a major process leading to the attenuation of the low-frequency ETRW in this region. This has implications for the understanding of the heat content low-frequency variability in the deep-ocean [*Roemmich et al*., 2015], considering the current difficulties in closing the planetary energy budget [*Church et al*., 2011]. Our results suggest in particular a mechanism by which changes in tropical Pacific SST variability can influence the deep ocean heat content of the midlatitudes at long time scales.

Overall, our results suggest that a realistic representation of the interannual energy flux by ETRW and its dissipation might be important for climate models, considering its potentially important role on the heat budget of the deep ocean. Our case study for the SEP further suggests the critical role played by model physics (e.g., mixing scheme) and resolution on the simulation of the interannual vertical flux. As an illustration of the sensitivity of our results to these parameters, we present the estimate of the vertical energy flux as derived from the SODA outputs (Figure 11) that served as ocean boundary conditions of the regional model. Note that the comparison between SODA and the regional model is somewhat limited due to the use of a different atmospheric forcing in SODA compared to the regional model, and to the fact that SODA makes use of a data assimilation scheme, while there is no data assimilation in our simulation experiments. With these differences in mind, it is clear that while the SODA reanalysis is able to capture features comparable to the regional model, it also presents important differences, in particular a weaker amplitude of the vertical energy flux, suggesting a significant impact of resolution and model physics on the vertical propagation of energy at interannual time scales in this region. Considering the on-going challenge for quantifying natural and forced variability in oceanic models [*Penduff et al*., 2011], such impact may need to be evaluated. This could be achieved through the experimentation with a regional OGCM in an idealized framework (e.g., simplified coastline and continental slope, and periodic forcing) for which a heat budget in the deep ocean would be sought. This is planned for future work.

Appendix A: Comparison to Observations

This appendix provides material for assessing the realism of the regional model simulation, complementing the material presented in *Dewitte et al*. [2012].

A.1. Mean Stratification

The correct representation of the subsurface stratification in the simulation is evaluated contrasting the wind projection coefficients (P_n) for the first three baroclinic modes, defined as:

$$P_n(x,y) = \frac{\overline{H}(x,y)}{\int_{-H}^{0} \psi_n^2(x,y,z)dz} \tag{A1}$$

where $\overline{H}(x,y)$ is the mean thermocline depth, H is the bottom depth and $\psi_n(x,y,z)$ is the vertical structure of the baroclinic mode n, obtained from a vertical mode decomposition of the mean stratification [cf. *Dewitte and Reverdin*, 2000]. The first three P_n can depict the mean thermocline structure accounting for its depth, thickness and intensity [see *Dewitte et al*., 2008].

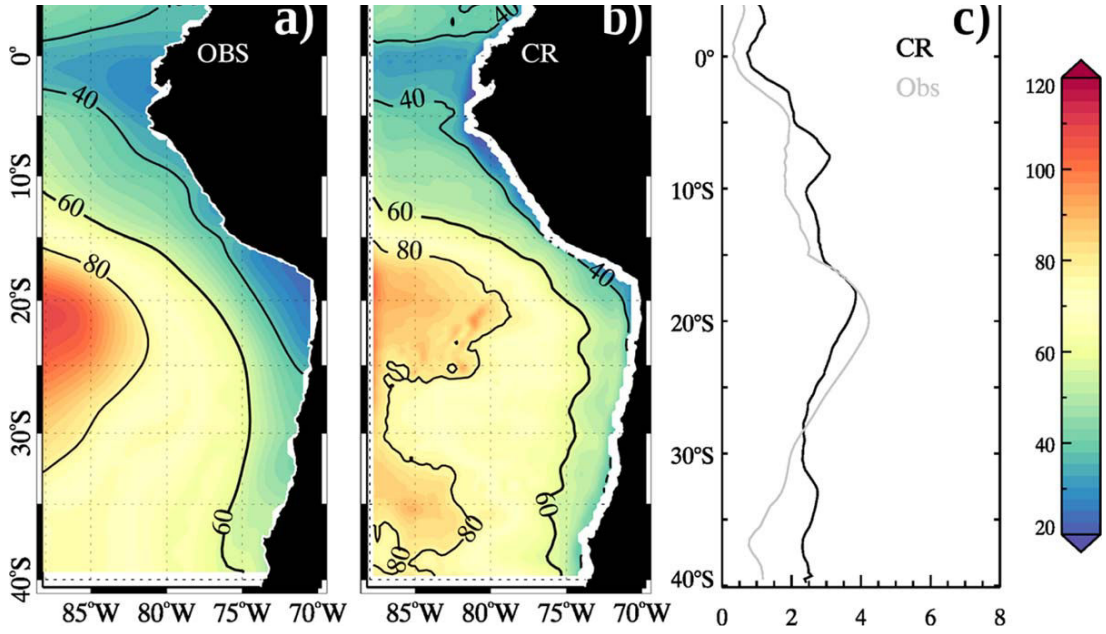

Figure A1. Mean thermocline depth (in m) computed from (a) the EN4 data set and (b) CR for the period 1958–2008. Black contours are depicted at 40, 60, and 80 m depth. (c) Mean (50 year average) thermocline gradient toward the coast (in cm km^{-1}).

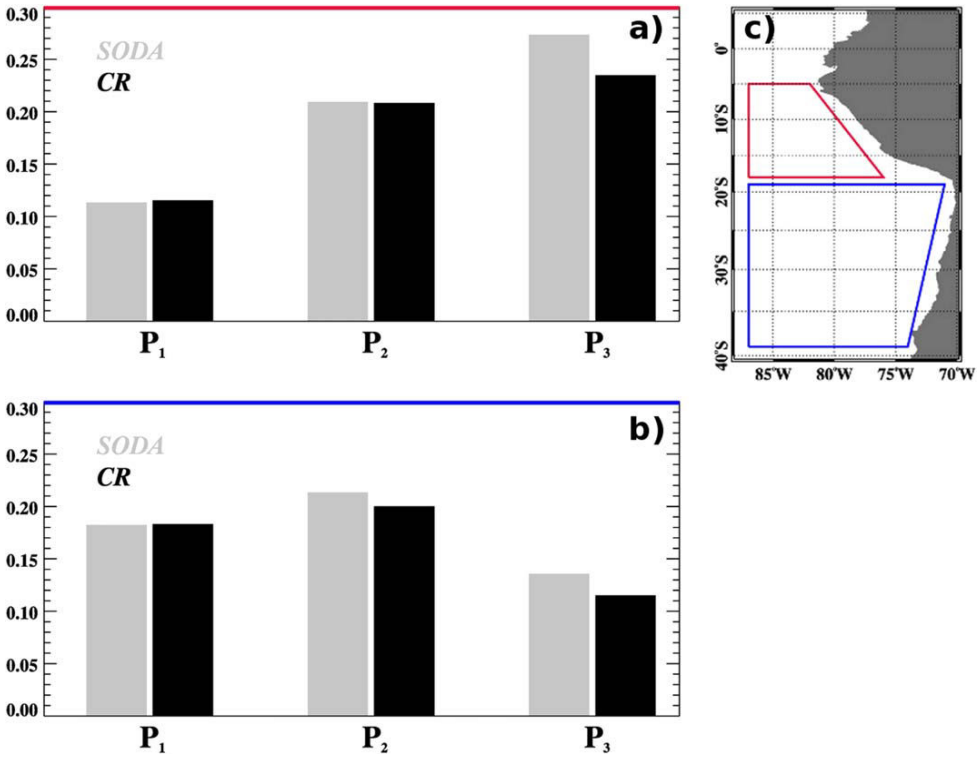

Figure A2. Mean value of the nondimensional wind projection coefficients for the first three baroclinic modes (P_i, $i = 1, 2, 3$) for the regions of (a) Peru and (b) Chile. The coefficients were computed following equation (A1), using the fields from SODA and CR.

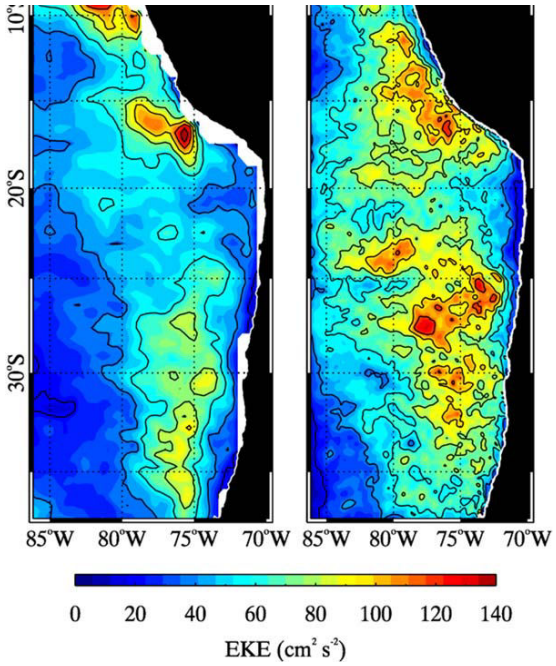

Figure A3. Mean surface eddy kinetic energy (EKE) for: (a) TOPEX-Jason1–2, (b) CR, over the period 1992–2008. Black contours are depicted every 20 $cm^2\ s^{-2}$, between 0 and 140 $cm^2\ s^{-2}$.

When contrasting SODA and CR (Figure A2), little difference is observed in the projection coefficients for the first two baroclinic modes (5% for the Chile region in P_2), which illustrates that the mean stratification in the regional simulation is comparable to the one from SODA. More important differences between SODA and the simulation are found for the projection coefficient of the third baroclinic mode (18% off Chile and 16% off Peru), related to the differences between the observations and the simulation near the coast. In this sense, deviations from the reanalysis product are expected near the coast given the higher spatial resolution of regional model and the realistic wind forcing used in CR [cf. *Goubanova et al*., 2011]. The latter in particular allows a more realistic representation of the coastal upwelling [*Cambon et al*., 2013].

A.1.1. Eddy Kinetic Energy

Sea surface height is used to compute the geostrophic currents field. The Eddy Kinetic Energy field (EKE) is then derived from the interannual anomalies of the geostrophic surface velocities (Figure A3). The EKE levels are well represented by the simulation (Figure A3b), although in general more intense than observations, consistent with other modeling studies in the region (see, e.g., Figure 5 in *Colas et al*. [2012]). Both the simulation and the observations display two regions of large EKE off Peru (10°S–18°S) and Chile (22°S–32°S) separated by a small region of low values centered at 20°S, with the model reproducing a slightly higher amplitude than the observations. Note that differences between model and observations are partly due the model setting not taking into account air-sea interactions at mesoscale [*Renault et al*., 2016]. Differences between the simulation and observations could also arise due to the smoothing inherent to the altimeter data.

A.1.2. Coastal Currents

As illustrated indirectly by the EKE levels, the simulation captures the main features of the coastal current system. In order to gain further insight in this matter, we contrast the simulation results against in situ currents (Figure A4). The mean profiles show a good agreement with the in situ data both in terms of values range and vertical trend (Figure A4d), although the simulation underestimates the meridional flow at the depth of the Peru Chile Under Current (PCUC). Cross-shore vertical sections (Figure A4ab) show a realistic pattern in agreement with the main currents described for the region [cf. *Strub et al*., 1998]. Near the coast, the *v* component exhibits a northward flow, representing the Chile Coastal Current (CCC). Over the slope,

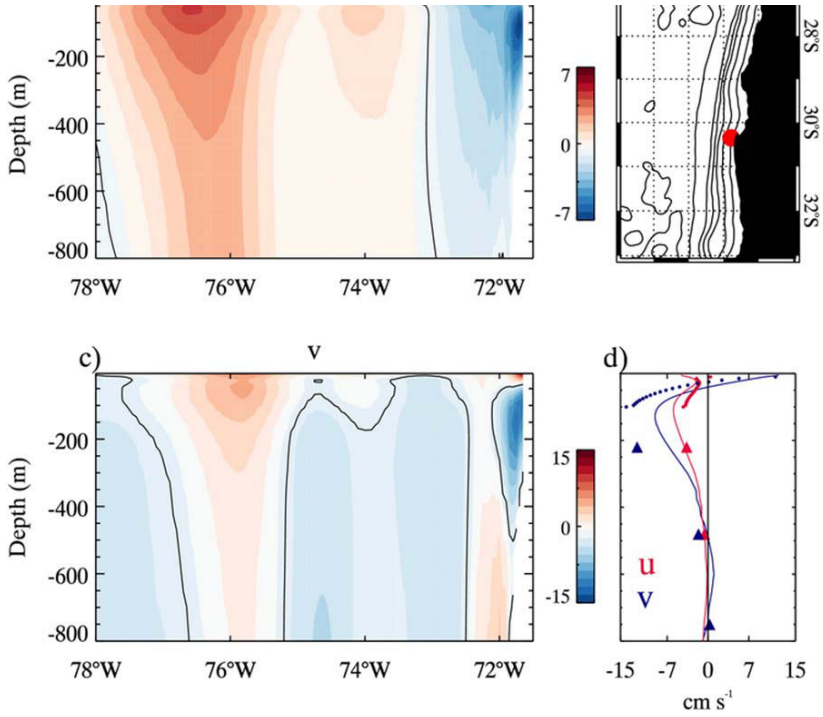

Figure A4. (a and c) Mean currents at 30°S from the simulation, and (d) mean profiles for both currents components at (b) the COSMOS mooring site. Black contours in Figures A4a and A4c denote the 0 cm s^{-1}. Depicted isobaths in Figure A4b correspond to 500, 1500, 3000, 4000, and 5000 m depth. Continuous lines in Figure A4d correspond to the currents from CR. ADCP (points) and RCMs (triangles) data from COSMOS mooring are also included in Figure A4d. All units are in cm s^{-1}. Average values are computed over the period November 1991 to September 2006.

an intense poleward flow extends down to around 600 m depth, corresponding to the PCUC. Offshore pattern shows another poleward flow around 200 km from the coast. This flow might be interpreted as the Peru Chile Counter Current (PCCC). Farther offshore, the model represents an equatorward flow, which corresponds to the Chile Peru Current.

A.1.3. Sea Level Anomalies

To assess the realism of the simulation along the coast, we contrast the simulated sea level against satellite data (TOPEX-Jason) and tide gauge data. The first EOF mode of the sea level anomalies at eight locations along the coast corresponding to the tide gauge locations is estimated for all products (Figure A5ab). The time period for this analysis corresponds to the years 1992–2008. A Pearson correlation analysis shows that the model is skillful in reproducing the low-frequency variability of the sea level along the coast, with in particular a good agreement in terms of spectral power, with a significant spectral peak in the period band between 2 and 4 years for all data sets.

In order to assess the realism in terms of sea level variability for the open ocean, the sea level anomalies were regressed against the E and C statistical modes for the model and observations and the resulting regression coefficient are presented in Figures A5c–A5f. The simulation exhibits an overall realistic pattern of the regression coefficients as compared to observations.

Appendix B: On the Relationship Between Vertical Energy Flux and Heat Flux

In conditions of stable stratification, the anomalous vertical mass flux is $m_z = \overline{\rho' w'}$ [*Monin and Ozmidov*, 1985], where the prime denotes the fluctuating density and vertical velocity. As the mass is displaced vertically, a potential energy per unit volume per second is associated with the change in height, which can be written as $\overline{g\rho' w'}$.

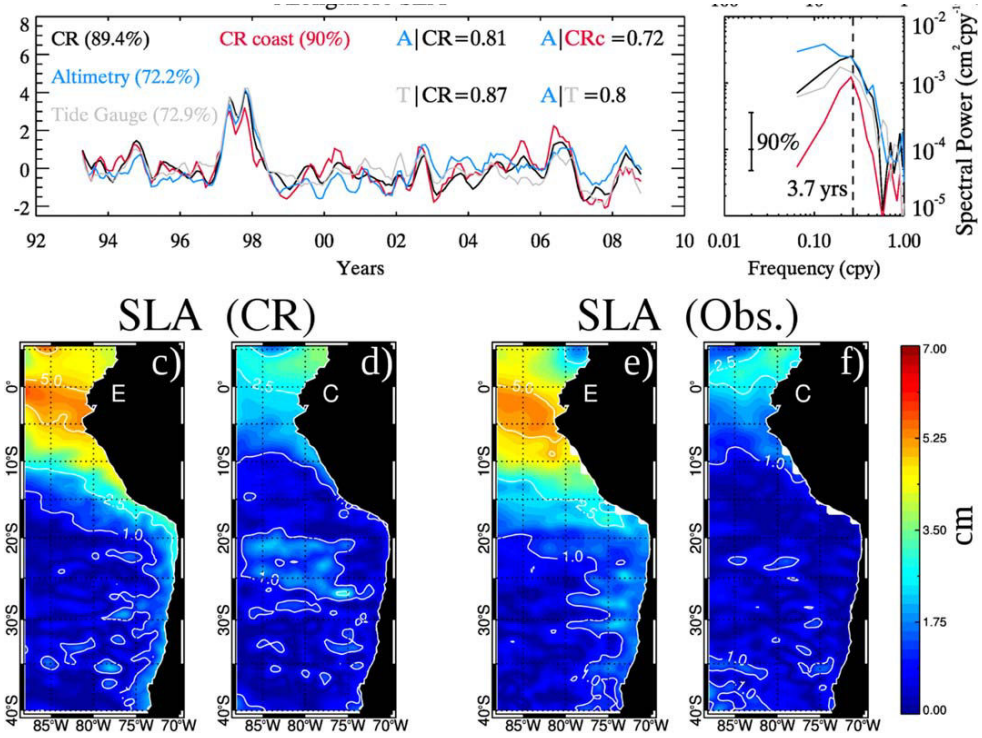

Figure A5. (a) First EOF mode of the coastal interannual sea level anomalies for CR, TOPEX-JASON 1–2, and Tide Gauge. Coastal points matching the positions of the sea level stations (gray) were chosen from CR (red). Otherwise, the CR sea level (black) was taken from the same position as the coastal altimetry (pale blue). Percentage of explained variance for each time series is indicated in parenthesis. Pearson correlation coefficients between the time series are also indicated. (b) Spectra of the sea level obtained by applying the Fast Fourier Transform to the time series depicted in Figure A5a. (c and d) Linear regression of SLA against the *E–C* indices for the CR simulation and (e and f) the TOPEX-JASON 1–2 data.

Assuming that the density fluctuations in the subthermocline are essentially controlled by variations in temperature (T'), we have

$$\rho' = -\alpha\rho_0 T' \tag{B1}$$

where α is the volume expansion coefficient of seawater and ρ_0 is the average density. The expression for the potential energy associated with m_z can then be written as

$$\overline{g\rho' w'} = -g\alpha\rho_0 \overline{w' T'} \tag{B2}$$

Before proceeding further, it is convenient to verify how the vertical gradients of w' scale in relationship to the vertical gradients of p', for the scales of interest. This condition will allow deriving a simplified expression involving $\overline{p' w'}$ from equation (B2).

From the relations that govern small perturbations in an incompressible stratified fluid, we can write the vertical velocities associated with those perturbations in terms of the time derivative of the density perturbations:

$$\frac{\partial \rho'}{\partial t} = w' \frac{\overline{\rho}}{g} N^2 \tag{B3}$$

where $\overline{\rho}$ is the time mean density, and N is the Brunt-Väisälä frequency. Using the hydrostatic relation, we can rearrange equation (B3) in the form:

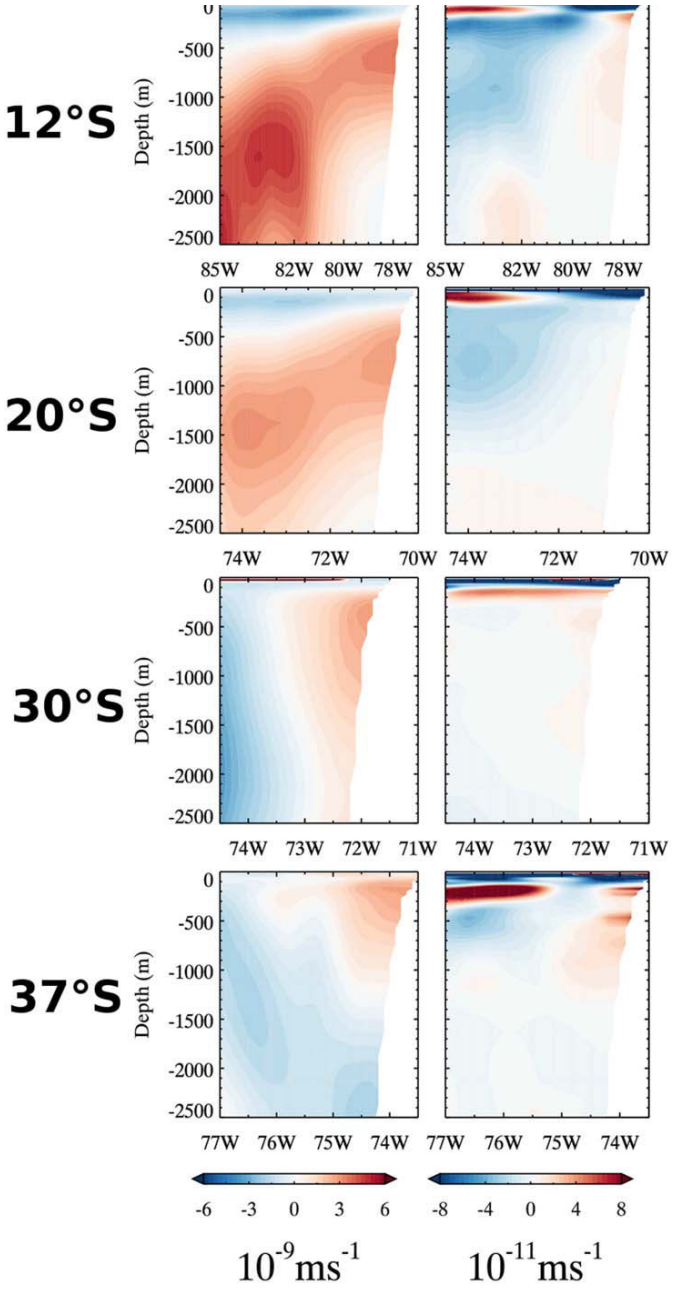

Figure B1. Cross shore sections of the terms $\langle w'\partial p'/\partial z\rangle$ and $\langle p'\partial w'/\partial z\rangle$ at 12°S, 20°S, 30°S, and 37°S. Please note that the color scales used to represent each term are different. p' is expressed in m and w' in m s^{-1}.

$$w' = -\frac{1}{\overline{\rho}N^2}\frac{\partial}{\partial t}\left[\frac{\partial p'}{\partial z}\right] \tag{B4}$$

For large-scale waves, the rate of change of pressure perturbations (and velocity) is proportional to the wave frequency ($\partial p'/\partial t \propto \omega$), which allows us to write the dimensional analysis of equation (B4) as $w' \sim \frac{\omega}{N^2}\frac{p'/\overline{\rho}}{H}$, and its vertical derivative ($\partial w'/\partial z$) as:

where ω is the frequency of interest and H is a vertical scale of variation for w' (which for the first three baroclinic modes is in the order of 10^3 to 10^2 m [see *Ramos et al.*, 2008]). Considering a period superior to 1 year (interannual), H as 10^3 m, a Brunt-Väisälä frequency of 0.2 cycles per hour (in the range of the lowest measured values in the abyssal Pacific; cf. *Wunsch* [2013] and *Levitus* [1982]) and a typical $\overline{\rho}$ value equal to 1027 kg m^{-3}, equation (B5) scales as:

$$\frac{\Delta w'}{\Delta z} \sim p' \times 10^{-9}$$

This suggests that over the same vertical scale, the term $\overline{p' \frac{\partial w'}{\partial z}}$ would tend to be smaller than the term $\overline{w' \frac{\partial p'}{\partial z}}$, which is corroborated by the results of Figure B1 that shows the estimates of these two terms from the model outputs. Note that the result of this dimensional analysis (i.e., $\overline{p' \frac{\partial w'}{\partial z}} \ll \overline{w' \frac{\partial p'}{\partial z}}$) also implies that the vertical gradient of the heat flux can be interpreted as anomalous nonlinear vertical advection of temperature since $\overline{w' \frac{\partial T'}{\partial z}} \approx \frac{\partial \overline{w'T'}}{\partial z}$ (assuming (B1)), which links the energy flux to the rate of temperature change in the deep ocean.

Using the hydrostatic approximation, (B2) can be rearranged as follows:

$$\frac{\partial \overline{p'w'}}{\partial z} = g\alpha\rho_0 \overline{w'T'} \tag{B6}$$

which implies that the vertical gradient of $\overline{p'w'}$ scale as $\overline{w'T'}$.

Introducing a heat flux Q, defined as:

$$Q = -C_p \rho \overline{w'T'}$$

where C_p is the specific heat of seawater at constant pressure, we can then rewritte (B6) in terms of Q as:

$$\frac{\partial \overline{p'w'}}{\partial z} = -\frac{g\alpha}{C_p} Q \tag{B7}$$

This expression relates the vertical gradients of the energy flux to a temperature flux, and can be interpreted as the rate of energy loss to turbulence, by working against the density gradients. Therefore, the dissipation or decreasing of the vertical wave energy flux results in a vertical heat flux. This formalism is used to interpret the results of Figure 9. Note that p' is used in the present appendix in Pa.

Acknowledgments

Oscar Vergara was supported by a doctoral scholarship from the National Chilean Research and Technology Council (CONICYT) through the program Becas Chile (scholarship 72130138). The authors are thankful for the financial support received from the Centre National d'Études Spatiales (CNES). Boris Dewitte acknowledges support from FONDECYT (project 1151185) and the LEFE-GMMC program (Mercator). Marcel Ramos acknowledges support from FONDECYT (project 1140845) and Chilean Millennium Initiative (NC120030). Oscar Pizarro acknowledges support from CONICYT (FONDECYT 1121041 and PIA PFB31 projects) and the Chilean Millennium Initiative (IC-120019). This work was granted access to the HPC resources of CALMIP supercomputing center, under the allocations 2016–1044 and 2017–1044. We are grateful to the National Center for Atmospheric Research (NCAR) for providing the SODA and NCEP data used in this paper (http://www.atmos.umd.edu/~ocean/). We thank National Oceanic and Atmospheric Administration Climate Diagnostics Center (NOAA/CDC) and the NCAR for making available the COADS data set used in the paper. Winds tress data were obtained from the Centre de Recherche et d'Exploitation Satellitaire (CERSAT), at IFREMER, Plouzané (France). Sea level altimetry data were obtained from Sea Level Research Group, University of Colorado. Tide gauge data were produced by the University of Hawaii Sea Level Center (http://uhslc.soest.hawaii.edu/), Manoa (Hawaii, United States of America). We are grateful to the MetOffice Hadley Centre for granting access to the EN4 data set (http://www.metoffice.gov.uk/hadobs/en4). The modeling data used throughout the paper are available upon request to B. Dewitte. The in situ current data are available upon request to O. Pizarro. The authors would like to thank the two anonymous reviewers for their constructive comments that helped improving the original manuscript.

References

Abraham, J. P., et al. (2013), A review of global ocean temperature observations: Implications for ocean heat content estimates and climate change, *Rev. Geophys.*, *51*, 450–483, doi:10.1002/rog.20022.

Belmadani, A., V. Echevin, B. Dewitte, and F. Colas (2012), Equatorially forced intraseasonal propagations along the Peru-Chile coast and their relation with the nearshore eddy activity in 1992–2000: A modeling study, *J. Geophys. Res.*, *117*, C04025, doi:10.1029/2011JC007848.

Bettencourt, J., C. López, E. Hernández-García, I. Montes, J. Sudre, B. Dewitte, A. Paulmier, and V. Garçon (2016), Boundaries of the Peruvian oxygen minimum zone shaped by coherent mesoscale dynamics, *Nat. Geosci.*, *8*, 937–940, doi:10.1038/ngeo2570.

Brandt, P., et al. (2015), On the role of circulation and mixing in the ventilation of oxygen minimum zones with a focus on the eastern tropical North Atlantic, *Biogeosciences*, *12*, 489–512, doi:10.5194/bg-12-489-2015.

Cambon G., K. Goubanova, P. Marchesiello, B. Dewitte, S. Illig, and V. Echevin (2013), Assessing the impact of downscaled winds on a regional ocean model simulation of the Humboldt system, *Ocean Modell.*, *65*, 11–24, doi:10.1016/j.ocemod.2013.01.007.

Capotondi, A., et al. (2015), Understanding ENSO diversity, *Bull. Am. Meteorol. Soc.*, *96*, 921–938, doi:10.1175/BAMS-D-13-00117.1.

Carton, J. A., and B. S. Giese (2008), A reanalysis of ocean climate using Simple Ocean Data Assimilation (SODA), *Mon. Weather Rev.*, *136*, 2999–3017, doi:10.1175/2007MWR1978.1.

Carton, J. A., G. Chepurin, X. Cao, and B. S. Giese (2000), A Simple Ocean Data Assimilation analysis of the global upper ocean 1950–1995, Part 1: Methodology, *J. Phys. Oceanogr.*, *30*, 294–309, doi:10.1175/1520-0485(2000)030 < 0294:ASODAA>2.0.CO;2.

Challenor, P. G., P. Cipollini, D. Cromwell, K. L. Hill, G. D. Quartly, and I. S. Robinson (2004), Characteristics of mid-latitude Rossby wave propagation from multiple satellite datasets, *Int. J. Remote Sens.*, *25*(7–8), 1297–1302, doi:10.1080/01431160310001592201.

Chelton, D., and M. Schlax (1996), Global observations of Oceanic Rossby Waves, *Science*, *272*, 234–238, doi:10.1126/science.2725259.234.

Church, J. A., N. J. White, L. F. Konikow, C. M. Domingues, J. G. Cogley, E. Rignot, J. M. Gregory, M. R. van den Broeke, A. J. Monaghan, and I. Velicogna (2011), Revisiting the Earth's sea-level and energy budgets from 1961 to 2008, *Geophys. Res. Lett.*, *38*, L18601, doi:10.1029/2011GL048794.

Centre ERS d'Archivage et de Traitement (CERSAT) (2002), Mean wind fields (MWF product) user manual volume 1: ERS-1, ERS-2 & NSCAT, Rep C2-MUT-W-05-IF, CERSAT-IFREMER, Brest, France.

329, doi:10.1007/s00382-011-1170-6.
daSilva A., A. C. Young, and S. Levitus (1994), Atlas of surface marine data 1994. Algorithms and procedures, *Tech. Rep. 6*, vol. 1, Natl. Oceanic and Atmos. Admin., Natl. Environ. Satell., Data, and Inform. Serv., U.S. Dep. of Comm., Washington, D. C.
Dewitte, B. (2000), Sensitivity of an intermediate ocean–atmosphere coupled model of the tropical pacific to its oceanic vertical structure, *J. Clim.*, *13*, 2363–2388, doi:10.1175/1520-0442(2000)013 < 2363:SOAIOA>2.0.CO;2.
Dewitte, B., and G. Reverdin (2000), Vertically propagating annual and interannual variability in an OGCM simulation of the tropical Pacific in 1985–1994, *J. Phys. Oceanogr.*, *30*, 1562–1581, doi:10.1175/1520-0485(2000)030 < 1562:VPAAIV>2.0.CO;2.
Dewitte, B., G. Reverdin, and C. Maes (1999), Vertical structure of an OGCM simulation of the equatorial Pacific Ocean in 1985–1994, *J. Phys. Oceanogr.*, *29*, 1542–1570.
Dewitte, B., M. Ramos, V. Echevin, O. Pizarro, and Y. duPenhoat (2008), Vertical structure variability in a seasonal simulation of a medium-resolution regional model simulation of the south eastern Pacific, *Prog. Oceanogr.*, *79*(2–4), 120–137, doi:10.1016/j.pocean.2008.10.014.
Dewitte, B., S. Illig, L. Renault, K. Goubanova, K. Takahashi, D. Gushchina, K. Mosquera, and S. Purca (2011), Modes of covariability between sea surface temperature and wind stress intraseasonal anomalies along the coast of Peru from satellite observations (2000–2008), *J. Geophys. Res.*, *116*, C04028, doi:10.1029/2010JC006495.
Dewitte, B., et al. (2012), Change in El Niño flavours over 1958–2008: Implications for the long-term trend of the upwelling off Peru, *Deep Sea Res., Part II*, *77–80*, 143–156, doi:10.1016/j.dsr2.2012.04.011.
Eliassen, A., and E. Palm (1960), On the transfer of energy in stationary mountain waves, *Geofys. Publ.*, *22*(3), 1–23.
Fjeldstad, J. E. (1933), Interne Wellen, *Geofys. Publ.*, *10*, 53 pp.
Furue, R., and M. Endoh (2005), Effects of the Pacific diapycnal mixing and wind stress on the global and Pacific meridional overturning, *J. Phys. Oceanogr.*, *35*, 1876–1890.
Furue, R., et al. (2015), Impacts of regional mixing on the temperature structure in the equatorial Pacific Ocean: Part 1: Vertically uniform vertical diffusion, *Ocean Modell.*, *91*, 9–11, doi:10.1016/j.ocemod.2014.10.002.
Gent, P., K. O'Neill, and M. A. Cane (1983), A model of the semiannual oscillation in the Equatorial Indian Ocean, *J. Phys. Oceanogr.*, *13*, 2148–2160, doi:10.1175/1520-0485(1983)013 < 2148:AMOTSO>2.0.CO;2.
Gill, A. E. (1982), *Atmosphere-Ocean Dynamics*, 2nd ed., 662 pp., Academic, London.
Gill, A. E., and A. J. Clarke (1974), Wind induced upwelling coastal currents and sea level changes, *Deep Sea Res. Oceanogr. Abstr.*, *21*, 325–345, doi:10.1016/0011-7471(74)90038-2.
Good, S. A., M. J. Martin, and N. A. Rayner (2013), EN4: Quality controlled ocean temperature and salinity profiles and monthly objective analyses with uncertainty estimates, *J. Geophys. Res.: Oceans*, *118*, 6704–6716, doi:10.1002/2013JC009067.
Goubanova, K., V. Echevin, B. Dewitte, F. Codron, K. Takahashi, P. Terray, and M. Vrac (2011), Statistical downscaling of sea-surface wind over the Peru–Chile upwelling region: diagnosing the impact of climate change from the IPSL-CM4 model, *Clim. Dyn.*, *36*(7–8), 1365–1378, doi:10.1007/s00382-010-0824-0.
Henley, B. J., J. Gergis, D. J. Karoly, S. B. Power, J. Kennedy, and C. K. Folland (2015), A tripole index for the interdecadal Pacific oscillation, *Clim. Dyn.*, *45*, 3077–3090, doi:10.1007/s00382-015-2525-1.
Kalnay, E., et al. (1996), The NCEP/NCAR 40-year reanalysis project, *Bull. Am. Meteorol. Soc.*, *77*, 437–471, doi:10.1175/1520-0477(1996)077 < 0437:TNYRP>2.0.CO;2.
Kessler, W. S. (1990), Observations of long Rossby waves in the northern tropical Pacific, *J. Geophys. Res.*, *95*, 5183–5217, doi:10.1029/JC095iC04p05183.
Kessler, W., and J. P. McCreary (1993), The Annual Wind-driven Rossby Wave in the Subthermocline Equatorial Pacific, *J. Phys. Oceanogr.*, *23*, 1192–1207, doi:10.1175/1520-0485(1993)023 < 1192:TAWDRW>2.0.CO;2.
Kuhlbrodt, T., and J. M. Gregory (2012), Ocean heat uptake and its consequences for the magnitude of sea level rise and climate change, *Geophys. Res. Lett.*, *39*, L18608, doi:10.1029/2012GL052952.
LaCasce, J., and J. Pedlosky (2004), The instability of Rossby basin modes and oceanic eddy field, *J. Phys. Oceanogr.*, *34*, 2027–2041, doi:10.1175/1520-0485(2004)034 < 2027:TIORBM>2.0.CO;2.
Large, W., J. C. McWilliams, and S. Doney (1994), Oceanic vertical mixing: A review and model with a nonlocal boundary layer parameterization, *Rev. Geophys.*, *32*, 363–403, doi:10.1029/94RG01872.
Lee, T., and M. J. McPhaden (2010), Increasing intensity of El Niño in the central-equatorial Pacific, *Geophys. Res. Lett.*, *37*, L14603, doi:10.1029/2010GL044007.
Levitus, S. (1982), Climatological Atlas of the World Ocean, *NOAA Prof. Pap. 13*, 173 pp., U.S. Gov. Print. Off., Washington, D. C.
Luyten, J. R., J. Pedlosky, and H. Stommel (1983), The Ventilated Thermocline, *J. Phys. Oceanogr.*, *13*, 292–309, doi:10.1175/1520-0485(1983)013 < 0292:TVT>2.0.CO;2.
Marchal, O. (2009), Extratropical Rossby waves in the presence of buoyancy mixing. *J. Phys. Oceanogr.*, *39*, 2910–2924, doi:10.1175/2009JPO4139.1.
Marshall, D. P., and L. Zanna (2014), A conceptual model of ocean heat uptake under climate change, *J. Clim.*, *27*(22), 8444–8465, doi:10.1175/JCLI-D-13-00344.1.
McCreary, J. (1984), Equatorial beams, *J. Mar. Res.*, *42*, 395–430, doi:10.1357/002224084788502792.
Meyers, G. (1979), On the annual Rossby wave in the tropical North Pacific Ocean, *J. Phys. Oceanogr.*, *9*, 664–673, doi:10.1175/1520-0485(1979)009 < 0663:OTARWI>2.0.CO;2.
Monin, A. S., and R. V. Ozmidov (1985), *Turbulence in the Ocean*, 248 pp., D. Reidel Publ. Co., Dordrecht, Netherlands, doi:10.1007/978-94-009-5217-1.
Montecinos, A., and O. Pizarro (2005), Interdecadal sea surface temperature–sea level pressure coupled variability in the South Pacific Ocean, *J. Geophys. Res.*, *110*, C08005, doi:10.1029/2004JC002743.
Montecinos, A., O. Leth, and O. Pizarro (2007), Wind-driven interdecadal variability in the eastern South Pacific, *J. Geophys. Res.*, *112*, C04019, doi:10.1029/2006JC003571.
Mosquera-Vasquez, K., B. Dewitte, and S. Illig (2014), The Central Pacific El Niño intraseasonal Kelvin wave, *J. Geophys. Res. Oceans*, *119*, 6605–6621, doi:10.1002/2014JC010044.
Nerem, R.S., D. P. Chambers, C. Choe, and G. T. Mitchum (2010), Estimating mean sea level change from the TOPEX and Jason altimeter missions, *Mar. Geod.*, *33*, suppl. 1, 435–446, doi:10.1080/01490419.2010.491031.
Paulmier, A., and D. Ruiz-Pino (2009), Oxygen Minimum Zones (OMZs) in the modern ocean, *Progr. Oceanogr.*, *80*(3–4), 113–128, doi:10.1016/j.pocean.2008.05.001.

Penduff, T., M. Juza, B. Barnier, J. Zika, W. K. Dewar, A.-M. Treguier, J.-M. Molines, and N. Audiffren (2011), Sea-level expression of intrinsic and forced ocean variabilities at interannual time scales, *J. Clim.*, *24*, 5652–5670, doi:10.1175/JCLI-D-11-00077.1.

Penven, P., V. Echevin, J. Pasapera, F. Colas, and J. Tam (2005), Average circulation, seasonal cycle, and mesoscale dynamics of the Peru Current System: A modeling approach, *J. Geophys. Res.*, *110*, C10021, doi:10.1029/2005JC002945.

Pizarro, O., and A. Montecinos (2004), Interdecadal variability of the thermocline along the west coast of South America, *Geophys. Res. Lett.*, *31*, L20307, doi:10.1029/2004GL020998.

Pizarro, O., G. Shaffer, B. Dewitte, and M. Ramos (2002), Dynamics of seasonal and interannual variability of the Peru-Chile Undercurrent, *Geophys. Res. Lett.*, *29*(12), 1581, doi:10.1029/2002GL014790.

Power, S., T. Casey, C. Folland, A. Colman, and V. Mehta (1999), Inter-decadal modulation of the impact of ENSO on Australia, *Clim. Dyn.*, *15*(5), 319–324, doi:10.1007/s003820050284.

Qiu, B., W. Miao, and P. Muller (1997), Propagation and decay of forced and free baroclinic Rossby waves in off-equatorial oceans, *J. Phys. Oceanogr.*, *27*, 2405–2417, doi:10.1175/1520-0485(1997)027 < 2405:PADOFA>2.0.CO;2.

Qiu, B., S. Chen, and H. Sasaki (2013), Generation of the north equatorial undercurrent jets by triad baroclinic Rossby wave interactions, *J. Phys. Oceanogr.*, *43*, 2682–2698, doi:10.1175/JPO-D-13-099.1.

Ramos, M., O. Pizarro, L. Bravo, and B. Dewitte (2006), Seasonal variability of the permanent thermocline off northern Chile, *Geophys. Res. Lett.*, *33*, L09608, doi:10.1029/2006GL025882.

Ramos, M., B. Dewitte, O. Pizarro, and G. Garric (2008), Vertical propagation of extratropical Rossby waves during the 1997–1998 El Niño off the west coast of South America in a medium-resolution OGCM simulation, *J. Geophys. Res.*, *113*, C08041, doi:10.1029/2007JC004681.

Renault, L., M. Molemaker, J. McWilliams, A. Shchepetkin, F. Lemarié, D. Chelton, S. Illig, and A. Hall (2016), Modulation of wind work by oceanic current interaction with the atmosphere, *J. Phys. Oceanogr.*, *i*, 1685–1704, doi:10.1175/JPO-D-15-0232.1.

Roemmich D., J. Church, J. Gilson, D. Monselesan, P. Sutton, and S. Wijffels (2015), Unabated planetary warming and its ocean structure since 2006, *Nat. Clim. Change*, *5*(3), 240–245, doi:10.1038/nclimate2513.

Shchepetkin, A. F., and J. C. McWilliams (2005), The regional oceanic modeling system: A split-explicit, free-surface, topography-following-coordinate ocean model, *Ocean Modell.*, *9*, 347–404, doi:10.1016/j.ocemod.2004.08.002.

Shaffer, G., O. Pizarro, L. Djurfeldt, S. Salinas, and J. Rutllant (1997), Circulation and low frequency variability near the Chile coast: Remotely-forced fluctuations during the 1991–1992 El Niño, *J. Phys. Oceanogr.*, *27*, 217–235, doi:10.1175/1520-0485(1997)027 < 0217:CALFVN>2.0.CO;2.

Shaffer, G., S. Hormazabal, O. Pizarro, and M. Ramos (2004), Circulation and variability in the Chile Basin, *Deep Sea Res., Part I*, *51*, 1367–1386, doi:10.1016/j.dsr.2004.05.006.

Stramma, L., G. C. Johnson, J. Sprintall, and V. Mohrholz (2008), Expanding oxygen-minimum zones in the tropical oceans, *Science*, *320*(5876), 655–658, doi:10.1126/science.1153847.

Stramma, L., A. Oschlies, and S. Schmidtko (2012), Mismatch between observed and modeled trends in dissolved upper-ocean oxygen over the last 50 years, *Biogeosciences*, *9*, 4045–4057, doi:10.5194/bg-9-4045-2012.

Strub, P. T., J. Mesías, V. Montecino, J. Rutllant, and S. Salinas (1998), Coastal ocean circulation off western South America, in *The Sea*, vol. 11, edited by A. R. Robinson and K. H. Brink, pp. 273–313, John Wiley, Hoboken, N. J.

Tailleux, R. (2004), A WKB analysis of surface signature and vertical structure of long extratropical baroclinic Rossby waves over topography, *Ocean Modell.*, *6*, 191 – 219, doi:10.1016/S1463-5003(02)00065-3.

Tailleux, R., and J. C. McWilliams (2002), The effect of bottom pressure decoupling on the speed of extratropical baroclinic Rossby waves, *J. Phys. Oceanogr.*, *31*, 1461–1476, doi:10.1175/1520-0485(2001)031 < 1461:TEOBPD>2.0.-CO;2.

Takahashi, K., A. Montecinos, K. Goubanova, and B. Dewitte (2011), ENSO regimes: reinterpreting the canonical and Modoki El Niño, *Geophys. Res. Lett.*, *38*, L10704, doi:10.1029/2011GL047364.

Thierry, V., A. Treguier, and H. Mercier (2004), Numerical study of the annual and semi-annual fluctuations in the deep equatorial Atlantic Ocean, *Ocean Modell.*, *6*(1), 1–30, doi:10.1016/S1463-5003(02)00054-9

Vargas, G., S. Pantoja, J. A. Rutllant, C. B. Lange, and L. Ortlieb (2007), Enhancement of coastal upwelling and interdecadal ENSO-like variability in the Peru-Chile Current since late 19th century, *Geophys. Res. Lett.*, *34*, L13607, doi:10.1029/2006GL028812.

Vega, A., Y. duPenhoat, B. Dewitte, and O. Pizarro (2003), Equatorial forcing of interannual Rossby waves in the eastern South Pacific, *Geophys. Res. Lett.*, *30*(5), 1197, doi:10.1029/2002GL015886.

Vergara, O., B. Dewitte, I. Montes, V. Garçon, M. Ramos, A. Paulmier, and O. Pizarro (2016), Seasonal variability of the oxygen minimum zone off Peru in a high-resolution regional coupled model, *Biogeosciences*, *13*, 4389–4410, doi:10.5194/bg-13-4389-2016.

von Schuckmann, K., J.-B. Sallée, D. Chambers, P.-Y. Le Traon, C. Cabanes, F. Gaillard, S. Speich, and M. Hamon (2014), Consistency of the current global ocean observing systems from an Argo perspective, *Ocean Sci.*, *10*, 547–557, doi:10.5194/os-10-547-2014.

Winters, K. B., P. N. Lombard, J. J. Riley, and E. A. D'Assaro (1995), Available potential energy and mixing in density-stratified fluids, *J. Fluid Mech.*, *299*, 115–128, doi:10.1017/S002211209500125X.

Winters, K. B., P. Bouruet-Aubertot, and T. Gerkema (2011), Critical reflection and abyssal trapping of near-inertial waves on a β-plane, *J. Fluid Mech.*, *684*, 111–136, doi:10.1017/jfm.2011.280.

Wunsch, C. (2013), Baroclinic motions and energetics as measured by altimeters, *J. Atmos. Oceanic Technol.*, *30*, 140–150, doi:10.1175/JTECH-D-12-00035.1.

Yeager, S. G., and W. G. Large (2007), Observational Evidence of Winter Spice Injection, *J. Phys. Oceanogr.*, *37*, 2895–2919, doi:10.1175/2007JPO3629.1.

Yeh, S.-W., J.-S. Kug, B. Dewitte, M.-H. Kwon, B. Kirtman, and F.-F. Jin (2009), El Niño in a changing climate, *Nature*, *461*, 511–514, doi:10.1038/nature08316.

Résumé de l'article *Vertical energy flux at ENSO timescales in the sub-thermocline of the Southeastern Pacific*

La variabilité basse fréquence de la circulation de subsurface dans l'océan Pacifique Sud-Est reste très peu étudiée, dû principalement au manque d'observations sur une durée suffisante. Ce bassin océanique est néanmoins considéré comme l'une des régions clés dans la compréhension de la variabilité du climat, grâce à sa contribution au bilan thermique planétaire. La variabilité dans le Pacifique Sud-Est est connectée à celle du Pacifique équatorial à travers la dynamique d'ondes (i.e. l'onde de Kelvin côtière et l'onde de Rossby extratropicale) se propageant à différentes échelles de temps, et qui rendent ce système particulièrement sensible à la variabilité climatique des tropiques. Dans ce travail, une simulation régionale de haute-résolution sur la période 1958-2008 est utilisée pour documenter la variabilité sous la thermocline dans l'océan Pacifique Sud-Est aux échelles de temps interannuelle et décennale. Dans ce travail, l'accent est mis sur le flux vertical d'énergie induit par la propagation verticale/vers l'ouest de l'onde de Rossby extratropicale (ETRW), liée au forçage de type lointain de la part du Pacifique équatorial. Le formalisme WKB est utilisé comme outil de diagnostique pour interpréter le flux vertical d'énergie le long de la côte Sud-Américaine. En particulier, nous montrons que $\sim$80% du flux d'énergie vertical/vers le large à l'échelle interannuelle est associé aux évènements El Niño du Pacifique Est. Une décomposition en modes verticaux montre que les schémas de flux verticaux d'énergie associés aux évènements El Niño se projettent sur la structure verticale des trois premiers modes baroclines, ce qui confirme l'interprétation du flux d'énergie comme étant associé à la propagation de l'onde de Rossby. Des tests de sensibilité effectués avec un modèle linéaire ajusté aux conditions de la simulation régionale, révèlent que les modes baroclines supérieurs contribuent à la propagation du flux d'énergie pendant les évènements El Niño. Le sort de l'énergie associé à la propagation verticale de l'onde de Rossby extratropicale est discuté, du point de vue des incertitudes dans le bilan d'énergie de la région.

3.4 Synthesis

In this chapter we addressed the subsurface variability of the circulation in the SEP, in connection with the equatorial forcing.

In the first part of the present chapter, we tested the possibility of studying the subthermocline low-frequency variability in the SEP using the available *in situ* observations. First, we contrasted our results against previous works in the equatorial Pacific, where it was shown that it is possible to document the subsurface variability associated with the long Rossby waves at seasonal to interannual timescales using the currently available ARGO observations. However, the results were not satisfying when reproducing the analyses in the extra-tropical region. These apparently conflicting results are interpreted in consideration of (i) the lower phase speed of the long Rossby wave off the equatorial Pacific, in combination with (ii) the sparse coverage of the ARGO floats in the SEP.

The second part of this chapter studied the low frequency variability of the SEP subthermocline circulation, in terms of the energy discharge associated with the different ENSO regimes.

Using the statistical formalism presented in *Chapter 2*, we distinguish between the contributions of the E and C ENSO regimes to the vertical energy flux that propagates into the SEP subthermocline. We find that the magnitude of the energy flux associated with the E regime (related to the extraordinary eastern Pacific El Niño events) corresponds to 80% of the interannual vertical energy flux in the SEP. On the other hand, the energy flux due to the C regime is far less significant than the energy flux related to the E regime. This energy flux is in fact mostly related to La Niña events, as verified by computing the C regime energy flux for $C > 0$ (Central Pacific El Niño events) and for $C < 0$ (La Niña events).

We observe a decadal modulation of the interannual vertical energy flux (which is on average, less than half of the energy flux related to the EP El Niño events), and the interpretation using the WKB theory reveals that the dominant period of this modulation of the energy flux is ~10 years. We interpret this result in the light of the decadal modulation of the climatic variability in the equatorial Pacific, that echoes on the SEP subthermocline circulation.

The use of a multimode-linear model verified our interpretation of the propagating variability in terms of the vertical/westward propagation of long Rossby waves, resulting from the constructive contribution of several baroclinic modes that form the energy "beams" through which the energy propagates. The energy beams agree with the ray-path slopes predicted by the WKB theory, with a slope that increases with latitude.

Our diagnosis of the interannual vertical energy flux also reveals a decrease of the ETRW amplitude along the propagation trajectory, which is shown to be related to a vertical temperature diffusion for the E regime and the decadal fluctuations of the energy flux. This indicates that (i) diapycnal diffusion significantly contributes to the attenuation of the ETRW in this region and (ii) the discharge of the tropical Pacific onto the intermediate–deep SEP at interannual and decadal timescales entails a vertical heat flux into the SEP subthermocline. This process can be seen as an energy transfer from the large-scale wave field to the smaller scale turbulent field.

Chapter 4

Ventilation of the South Pacific oxygen minimum zone: the role of the ETRW and mesoscale

4.1 Overview

In the previous chapter we investigated the low-frequency variability of the SEP circulation, in relation with remote forcing. The load of the interannual tropical Pacific variability on the subthermocline circulation was analyzed from the perspective of the vertical long Rossby wave propagation. In the present chapter, this mechanism is transposed to study the variability of the subthermocline circulation in the SEP at seasonal timescale. In particular, we focus on the influence of the seasonal fluctuations of the circulation on the ventilation of the OMZ found in the SEP, which is a focus of increasing concern for the scientific community due to its implications at different levels, such as interactions with the local ecosystem and the highly-productive upwelling system in the SEP (e.g. Prince and Goodyear (2006); Stramma et al. (2010); Gilly et al. (2013)), and climatic feedbacks through its involving in the global nitrogen and carbon cycles (Kock et al., 2016; Paulmier et al., 2011).

Although a comprehensive understanding of the OMZ dynamics is still incomplete, recent efforts have pointed out a close relationship with the circulation features in the SEP (cf. Bettencourt et al. (2015) and Montes et al. (2014)), which strongly suggests that the OMZ variability may be also sensitive to the circulation fluctuations. In this sense, the present chapter responds to the current knowledge gap on the OMZ variability at seasonal timescale and its relation with the circulation variability. The main objective of this chapter is thus to document the processes that are influential for the seasonality of the OMZ. In particular, we analyze to which extent the seasonal variability of the OMZ can be interpreted in terms of the vertical propagation of long Rossby

waves, which, as exposed in the previous chapter, contributes significantly to the low-frequency variability of the intermediate and deep circulation in the SEP.

Recent evidence indicates that the mesoscale structures play a decisive role in shaping the OMZ (Bettencourt et al., 2015). In this sense, we also evaluate the contribution of the circulation fluctuations in the form of mesoscale structures to the seasonal OMZ variability.

4.2 Seasonal variability of the oxygen minimum zone

The body of this subsection corresponds to the article "Seasonal variability of the oxygen minimum zone off Peru in a high-resolution coupled model", published in "Biogeosciences", in August 2016.

Citation: Vergara, O., Dewitte, B., Montes, I., Garçon, V., Ramos, M., Paulmier, A., and Pizarro, O., (2016), Seasonal variability of the oxygen minimum zone off Peru in a high-resolution regional coupled model, Biogeosciences, 13, 4389-4410, doi:10.5194/bg-13-4389-2016.

Seasonal variability of the oxygen minimum zone off Peru in a high-resolution regional coupled model

Oscar Vergara[1], Boris Dewitte[1,3,4,5], Ivonne Montes[2], Veronique Garçon[1], Marcel Ramos[3,4,5], Aurélien Paulmier[1], and Oscar Pizarro[6,7]

[1]Laboratoire d'Études en Géophysique et Océanographie Spatiales, CNRS/IRD/CNES/UPS, UMR5566, Toulouse, France
[2]Instituto Geofísico del Perú (IGP), Lima, Perú
[3]Departamento de Biología, Facultad de Ciencias del Mar, Universidad Católica del Norte, Coquimbo, Chile
[4]Millennium Nucleus for Ecology and Sustainable Management of Oceanic Islands (ESMOI), Coquimbo, Chile
[5]Centro de Estudios Avanzado en Zonas Áridas (CEAZA), Coquimbo, Chile
[6]Department of Geophysics, University of Concepción, Concepción, Chile
[7]Millennium Institute of Oceanography, University of Concepción, Concepción, Chile

Correspondence to: Oscar Vergara (oscar.vergara@legos.obs-mip.fr)

Received: 8 December 2015 – Published in Biogeosciences Discuss.: 18 January 2016
Revised: 16 June 2016 – Accepted: 17 June 2016 – Published: 8 August 2016

Abstract. In addition to being one of the most productive upwelling systems, the oceanic region off Peru is embedded in one of the most extensive oxygen minimum zones (OMZs) of the world ocean. The dynamics of the OMZ off Peru remain uncertain, partly due to the scarcity of data and to the ubiquitous role of mesoscale activity on the circulation and biogeochemistry. Here we use a high-resolution coupled physical/biogeochemical model simulation to investigate the seasonal variability of the OMZ off Peru. The focus is on characterizing the seasonal cycle in dissolved O_2 (DO) eddy flux at the OMZ boundaries, including the coastal domain, viewed here as the eastern boundary of the OMZ, considering that the mean DO eddy flux in these zones has a significant contribution to the total DO flux. The results indicate that the seasonal variations of the OMZ can be interpreted as resulting from the seasonal modulation of the mesoscale activity. Along the coast, despite the increased seasonal low DO water upwelling, the DO peaks homogeneously over the water column and within the Peru Undercurrent (PUC) in austral winter, which results from mixing associated with the increase in both the intraseasonal wind variability and baroclinic instability of the PUC. The coastal ocean acts therefore as a source of DO in austral winter for the OMZ core, through eddy-induced offshore transport that is also shown to peak in austral winter. In the open ocean, the OMZ can be divided vertically into two zones: an upper zone above 400 m, where the mean DO eddy flux is larger on average than the mean seasonal DO flux and varies seasonally, and a lower part, where the mean seasonal DO flux exhibits vertical–zonal propagating features that share similar characteristics than those of the energy flux associated with the annual extratropical Rossby waves. At the OMZ meridional boundaries where the mean DO eddy flux is large, the DO eddy flux has also a marked seasonal cycle that peaks in austral winter (spring) at the northern (southern) boundary. In the model, the amplitude of the seasonal cycle is 70 % larger at the southern boundary than at the northern boundary. Our results suggest the existence of distinct seasonal regimes for the ventilation of the OMZ by eddies at its boundaries. Implications for understanding the OMZ variability at longer timescales are discussed.

1 Introduction

In addition to hosting one of the most productive upwelling systems, the South Eastern Pacific (SEP) is home to one of the most extensive oxygen minimum zones (OMZs) of the world ocean (Fuenzalida et al., 2009; Paulmier and Ruiz-Pino, 2009). These oxygen-deficient regions are key to understanding the role of the ocean in the greenhouse gas budget, in climate and in the presently unbalanced nitrogen cy-

cle (Gruber, 2008). The OMZs represent a net nitrogen loss to the atmosphere in the form of N_2O (particularly the SEP OMZ; Farías et al., 2007; Arévalo-Martínez et al., 2015) in addition with other toxic or climatically active gases, such as H_2S and CH_4, respectively, in extremely low dissolved oxygen (DO) concentrations (Libes, 1992; Law et al., 2013). They might even limit the ocean carbon sequestration and act as CO_2 sources for the atmosphere (Paulmier et al., 2008, 2011). Furthermore, the OMZs contribute to the habitat compression of marine organisms, in a zone that sustains 10 % of the world fish catch (Prince and Goodyear, 2006; Chavez et al., 2008). Therefore, understanding the dynamics behind the OMZ becomes not just a matter of scientific interest but also a major societal concern.

In general, these low-oxygen regions are considered to result from the interaction of biogeochemical and physical processes (Karstensen et al., 2008). The SEP presents high biological productivity, inducing a significant DO consumption mainly through the remineralization associated with a complex nutrient cycle supported by the intense upwelling. In addition, the SEP encompasses a so-called "shadow zone", a near stagnant/sluggish circulation region next to the eastern basin boundary, not ventilated by the basin-scale wind-driven circulation (Luyten et al., 1983). Assuming a steady state, lateral oxygen fluxes from subtropical water masses and diapycnal mixing are expected to balance the oxygen consumption (Brandt et al., 2015). However, the diversity of environmental forcings in the SEP and the variety of timescales at which they operate (Pizarro et al., 2002; Dewitte et al., 2011, 2012) have eluded a proper understanding of the processes controlling the OMZ structure and variability. On the one hand, the scarcity of data and rare surveys have only permitted the documentation of the DO temporal variability at a few locations (e.g., Morales et al., 1999; Cornejo et al., 2006; Gutiérrez et al., 2008; Llanillo et al., 2013). On the other hand, the highly complex interaction between physical and biogeochemical mechanisms makes modeling and prediction of OMZ location, intensity and its temporal variability a challenging task (Karstensen et al., 2008; Cabré et al., 2015). Low-resolution CMIP class coupled models still have severe biases of physical and biogeochemical origins, particularly in eastern boundary current systems (Richter, 2015), which has eluded the interpretation of long-term trends in OMZ (Stramma et al., 2008, 2012; Cabré et al., 2015). Regional coupled biogeochemical modeling nonetheless has provided a complementary approach to gain insight in the dynamics of OMZ and its relationship with climate (Resplandy et al., 2012; Gutknecht et al., 2013a). One recent modeling effort to understand the dynamics behind the OMZ in the eastern tropical Pacific comes from Montes et al. (2014). This study provided a first regional simulation of the OMZ in the SEP and summarized the elements involved in maintaining the OMZ found off the coast of Peru as the result of a delicate balance of (i) the equatorial current system dynamics – the relatively oxygen-rich waters carried by the Equatorial Undercurrent (EUC), the relatively oxygen-poor and nutrient-rich waters carried by the primary and secondary Tsuchiya Jets (primary and secondary southern subsurface countercurrents) – and (ii) the high surface productivity rates induced by the coastal upwelling, which in turn triggers an intense oxygen consumption in the subsurface. Their model experiments also showed that different eddy kinetic energy (EKE) levels, induced by different representations of the mean vertical structure of the coastal current, may contribute to the expansion or erosion of the upper boundary of the OMZ.

The study by Montes et al. (2014) established a benchmark in terms of numerical modeling of the OMZ in the SEP, focusing on its permanent regime and connection with the equatorial current dynamics. In the present study, we also take advantage of the regional modeling approach in order to investigate the mechanisms associated with the seasonal cycle of DO within the OMZ. The motivation for focusing on seasonal variability is threefold: (1) a better knowledge of the processes acting on the OMZ at seasonal timescale is viewed as a prerequisite for interpreting longer timescales of variability (ENSO, decadal); (2) the scarcity of quality long-term subsurface biogeochemical data in the SEP is a limitation for tackling the investigation of OMZ variability at low frequency; (3) to the authors' knowledge, this issue has not been addressed in the literature for the eastern tropical Pacific, although it has been a concern for other tropical oceans (Resplandy et al., 2012; Gutknecht et al., 2013a; Duteil et al., 2014).

Here, besides investigating to what extent the seasonal OMZ variability can relate to the variability of the environmental forcing in the SEP (local wind, equatorial Kelvin and extratropical Rossby waves, hereby referred to as ETRW), our interest is on examining the DO budget (i.e., the balance between oxygen sources and sinks) and relating it to the physical DO flux. In particular, since the Peruvian region is the location of relatively intense eddy activity (Chaigneau et al., 2009), the question of whether or not eddy activity is involved in the seasonal variability of the OMZ arises and calls for assessing its contribution to the DO flux. There is growing evidence that the mesoscale activity plays a key role in the biogeochemical cycles and the OMZ structure in eastern boundary upwelling systems (Duteil and Oschlies, 2011; Nagai et al., 2015). Most studies addressing the role of mesoscale processes in the OMZs have focused on the ventilation from the coastal domain, where the primary production bloom provides nutrients and DO anomalies that are in turn transported offshore (Stramma et al., 2013; Czeschel et al., 2015; Thomsen et al., 2016). Gruber et al. (2011) showed that mesoscale activity is prone to reducing the biological production and offshore carbon export in upwelling systems by both rectifying on the mean circulation (i.e., eddy-induced mixing tends to flatten the isotherms nearshore and reduce the upwelling) and changing its nutrient transport capacity. This process has been to some extent supported by observations in the Peruvian OMZ (Stramma et al., 2013). In this sense,

the mesoscale activity represents a ventilation pathway for the OMZ, through the offshore transport of oxygen-enriched waters. The ventilation of the OMZ could also take place at its meridional boundaries where strong mean DO gradients are found along with eddy activity. Recently, Bettencourt et al. (2015) proposed that mesoscale eddies shape the Peruvian OMZ by controlling the diffusion of DO into the OMZ at the meridional boundaries. Although it is likely that both processes are important for understanding the OMZ structure, it has not been clarified to which extent the variability of the OMZ could be understood in terms of the changes in the DO eddy flux into the OMZ through these different pathways. The mesoscale activity also exhibits a significant meridional variability off Peru (Chaigneau et al., 2009), which questions whether the offshore ventilation process can operate effectively for modulating the whole OMZ. Another related open question is at which timescales the ventilation process through eddies-induced mixing can operate effectively. In this paper we will tackle these issues from a regional modeling approach, focusing on the seasonal timescale.

The paper is organized as follows. After the introduction (Sect. 1), we detail the observations and model configuration used in the study, as well as the methodology employed in the treatment of the information (Sect. 2). We also evaluate the realism of the simulation against the available observations in reproducing the main characteristics of the OMZ. The subsequent section (Sect. 3) characterizes the DO annual cycle inside the OMZ. Section 4 opens with the analysis of the seasonal variability of the coastal OMZ and the contribution of the DO budget terms associated with it. This analysis is followed by the results of DO flux directed offshore and completed by the analysis of DO flux across the OMZ meridional boundaries. Section 5 presents a discussion of the main results and Sect. 6 presents a summary and the concluding remarks.

2 Data description and methods

2.1 Data

2.1.1 Dissolved oxygen concentration from the CSIRO Atlas of Regional Seas (CARS)

CARS is a climatological product derived from a quality-controlled archive of historical subsurface ocean measurements, most of which were collected during the past 50 years (additional information might be found on the website of the project: http://www.marine.csiro.au/~dunn/cars2009/). For the present study, we use the CARS2009 version of the CARS product (Ridgway et al., 2002), which has an horizontal resolution of $0.5° \times 0.5°$ and 79 vertical levels, with a 10 m resolution near the surface layer. We use CARS to assess the model's skills in simulating the OMZ mean state and variability. One advantage of this product is its refined interpolation treatment near steep topography in comparison to other products such as the World Ocean Atlas (Dunn and Ridgway, 2002). Also, it includes the annual and semiannual oxygen cycles, although the semiannual cycle is available only for the first 375 m over the region of interest due to the scarcity of data.

2.1.2 Chlorophyll *a* concentration from SeaWiFS

Eight-day composites at $0.5° \times 0.5°$ resolution of the SeaWiFS chlorophyll product (version 4), between January 2000 and December 2008, are used to compute the surface chlorophyll seasonal cycle (McClain et al., 1998; O'Reilly et al., 2000).

2.1.3 Sea surface temperature (SST)

The NOAA Optimum Interpolation SST (OISST V2) product is contrasted against the simulation SST. This product is an analysis constructed by combining observations from different platforms (satellites, ships, buoys) on a regular global grid. More information about the methodology used to construct this data set may be found in Reynolds et al. (2007) and the product website (https://www.ncdc.noaa.gov/oisst). The version used in this study corresponds to daily SST maps with a spatial resolution of $0.25° \times 0.25°$, spanning the period 2000–2008.

2.1.4 Sea level height (SLH)

The TOPEX/JASON1–2 merged SLH data set, distributed by the Sea Level Research Group, University of Colorado (http://sealevel.colorado.edu/), is used to derive the geostrophic velocity field and the mean EKE field. This data set corresponds to a globally gridded $0.25° \times 0.25°$ weekly product. The information used corresponds to the period 1993–2008. Further details on this product may be found in Nerem et al. (2010).

2.2 Model simulation

We use a high-resolution simulation of the southeastern Pacific, based on the hydrodynamic Regional Ocean Modeling System (ROMS) circulation model (see Shchepetkin and McWilliams, 2005, 2009, for a complete description of the model) coupled with a nitrogen-based biogeochemical model developed for the eastern boundary upwelling systems (BioEBUS; Gutknecht et al., 2013a, b), hereby referred as CR BIO.

The model is used at an eddy-resolving resolution ($1/12°$ at the Equator) for a region extending from 12° N to 40° S and from the coast to 95° W – although this study only focuses on the domain spanning the latitudes of Peru and Ecuador (Fig. 1) – with lateral open boundaries at its northern, southern and western frontiers. The physical model resolves the hydrostatic primitive equations with a free-surface

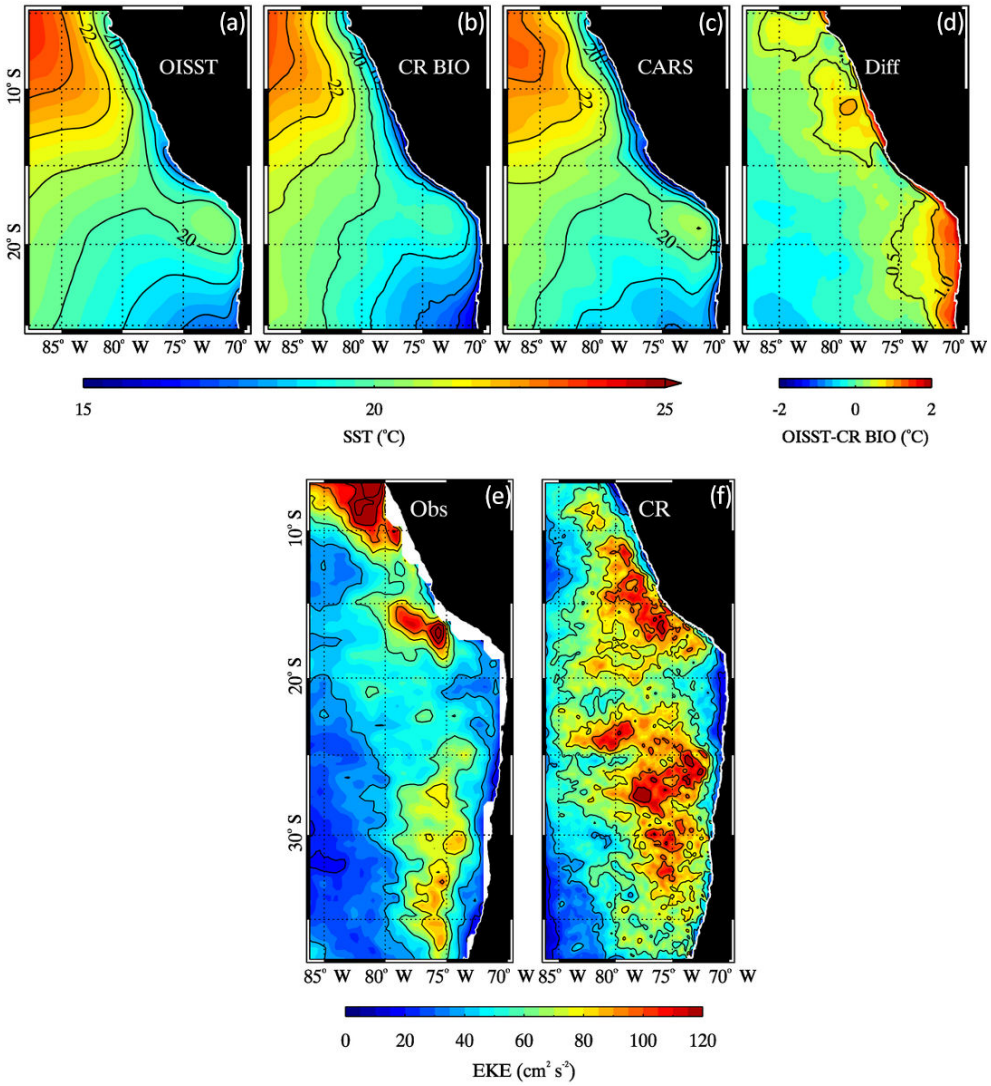

Figure 1. Mean sea surface temperature (SST) between 2000 and 2008 for **(a)** OISST product (0.25° × 0.25°), **(b)** the simulation (1/12°) and **(c)** CARS data set (0.5° × 0.5°). **(d)** Difference between the OISST product and the simulation. Mean eddy kinetic energy (EKE) between 1993 and 2008, for **(e)** TOPEX/Poseidon Jason 1–2 merged product (0.25° × 0.25°), and **(f)** simulation (1/12°). EKE was derived from the interannual anomalies of the geostrophic velocity field.

explicit scheme and a stretched terrain-following sigma coordinates on 37 vertical levels. The configuration is similar to Dewitte et al. (2012), that is the open boundary conditions are provided by 5-day mean oceanic outputs from SODA (Version 2.1.6) for temperature, salinity, horizontal velocity and sea level for the period 1958–2008, while wind stress and speed forcing at the air/sea interface come from the NCEP/NCAR reanalysis. The atmospheric fields have been statistically downscaled following the method by Goubanova et al. (2011) in order to correct for the unrealistic wind stress curl near the coast of the NCEP Reanalysis (see Cambon et al., 2013, for a validation of the method for oceanic applications). Atmospheric fluxes were derived from the bulk formula using the temperature from COADS 1° × 1° monthly climatology (daSilva et al., 1994). Relative humidity and shortwave and long-wave radiations are also from COADS. Bottom topography is from the GEBCO 30 arcsec grid data set, interpolated to the model grid and smoothed as in Penven et al. (2005) in order to minimize the pressure gradient errors and modified at the boundaries to match the SODA bottom topography. This model configuration has been validated from satellite and in situ observations in Dewitte et al. (2012) with a focus on mean state interannual variability. In general the model is skillful in simulating the mean SST field (Fig. 1a, c) as well as other main aspects of the mean circulation (e.g., Peru/Chile Undercurrent, EKE; see Fig. 3 in Dewitte et al., 2012), although with a slight cold

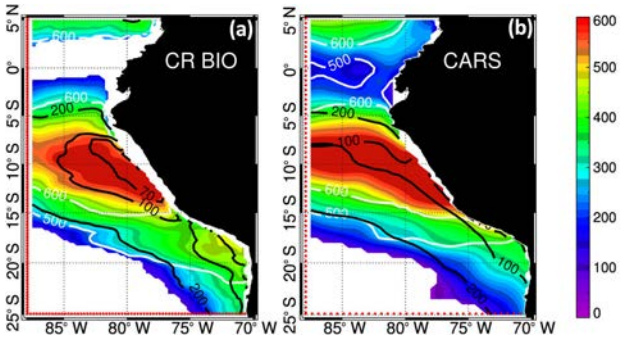

Figure 2. Mean oxygen minimum zone core thickness (color scale in meters) for **(a)** the simulation and **(b)** CARS. Depths of the lower (white) and upper (black) limits of the OMZ core are also depicted. The OMZ core is defined as [DO] < 20 µM. The red dots denote the horizontal resolution of the DO field.

bias ($\sim 1\,^{\circ}$C) that could be partly attributed to the use of climatological heat flux forcing (Fig. 1d).

The mesoscale activity diagnosed from the mean EKE, has a comparable pattern than altimetry, although with a larger amplitude (Fig. 1e, f). Similar levels of mesoscale activity have been obtained by previous modeling studies in the Peruvian region (e.g., Echevin et al., 2011; Colas et al., 2012).

The ocean model within this configuration is coupled to the BioEBUS model following similar methodology than Montes et al. (2014). BioEBUS uses two compartments of phytoplankton and zooplankton, small (flagellates and ciliates, respectively) and large (diatoms and copepods, respectively), detritus, dissolved organic nitrogen and the inorganic nitrogen forms nitrate, nitrite and ammonium, as well as nitrous oxide (see Gutknecht et al., 2013a, b, for a description of the model). The open-boundary conditions for the biogeochemical model are provided by the climatological CARS data set (nitrate and oxygen concentrations) and by SeaWiFS archive (chlorophyll *a* concentration). Additional biogeochemical tracers are computed following Gutknecht et al. (2013a, b). Initial phytoplankton concentration is defined as a function of vertically extrapolated satellite Chl *a* following Morel and Berthon (1989). An offshore decreasing cross-shore profile, following in situ observations, is applied for zooplankton, and a vertical constant (exponential) profile is used for detritus (nitrite, ammonium and dissolved organic nitrogen). In order to get a realistic solution for the region, the model parameters were tuned to simultaneously fit modeled oxygen and nitrate fields to observations (see Table A1 of Montes et al. (2014) for parameter values). These changes were motivated by the need to adjust the microbiological rates to values observed in the SEP. Within this parameter configuration, BioEBUS has been shown to be skillful for simulating the OMZ off Peru (Montes et al., 2014). In particular the pattern correlations between the model and observations for both the annual mean and the seasonal cycle inside the OMZ present comparable scores (> 0.85, cf. Montes et al., 2014) as well as low standard deviations (i.e., in the order of the observed values). The model was run over the period 1958–2008 with a 10-year spin-up obtained by repeating the year 1958. Although, after the spin-up, the simulation has reached stable conditions and the OMZ volume does not drift, we focus in the present study only on the period 2000–2008.

The reason for focusing on the last 10 years of our simulation is also motivated by the fact that the atmospheric momentum forcing is close to the satellite QuickSCAT winds by construction (see Goubanova et al., 2011, for details) so that this period of the simulation is the one when the model is the most constrained by observations. Most previous modeling studies for this region (Penven, et al. 2005; Montes et al., 2010, 2014; Echevin et al., 2011; Colas et al., 2012) have also used a wind forcing from the QuickSCAT scatterometer, which provides a benchmark for assessing our simulation.

A monthly-mean climatology is calculated for all variables over this period from the 3-day mean outputs of the model, which can be compared to the CARS data.

Consistently with Montes et al. (2014), the coupled simulation is skillful in simulating the mean characteristics of the OMZ off the Peruvian coast (Figs. 2 and 3). In particular the thickness and location of the model OMZ core limits are realistic, and in good agreement with previous studies (Fig. 2; e.g., Paulmier et al., 2006; Cornejo and Farías, 2012; Montes et al., 2014). Note that the simulation reproduces a thinner OMZ around 10° S in comparison to CARS, which agrees with the results obtained by Montes et al. (2014) (see Fig. 2 in that study). Close to the western boundary of our model domain, the simulated OMZ also exhibits a realistic vertical structure (Fig. 3) with comparable concentration in DO than observations in the vicinity of the Equatorial Undercurrent (~ 100 m; Equator). Furthermore, the simulation is consistent in reproducing the oxygen-consuming processes, as supported by the apparent oxygen utilization (AOU; Fig. 4), also in good agreement with previous studies (cf. Fig. 8 in Cabré et al., 2015). AOU was computed as the difference between the DO concentration and the saturated oxygen (O_2sat) concentration (AOU = O_2sat–O_2) with O_2sat computed following the methodology of García and Gordon (1992). The realistic representation of the oxygen-consuming processes is reflected by the particulate organic carbon flux as well (Fig. 5a), whose values at 100 m fall within the observed range for the region (30–60 gC m^{-2} yr^{-1} in the shelf area; Dunne et al., 2005; Henson et al., 2012). In addition, the low transfer efficiency of carbon (10–15 % or lower over and next to the shelf; Henson et al., 2012), from the euphotic zone to greater depths (Fig. 5b), implies that the remineralization processes take place at realistic depths and therefore allow for a correct vertical representation of the OMZ (cf. Fig. S2 in Cabré et al., 2015, for comparison).

The core of the OMZ, defined with a suboxic concentration ([DO] < 20 µM; µM will be used to refer to µmol L^{-1} in all the text and figures), occupies nearly 23 % of the

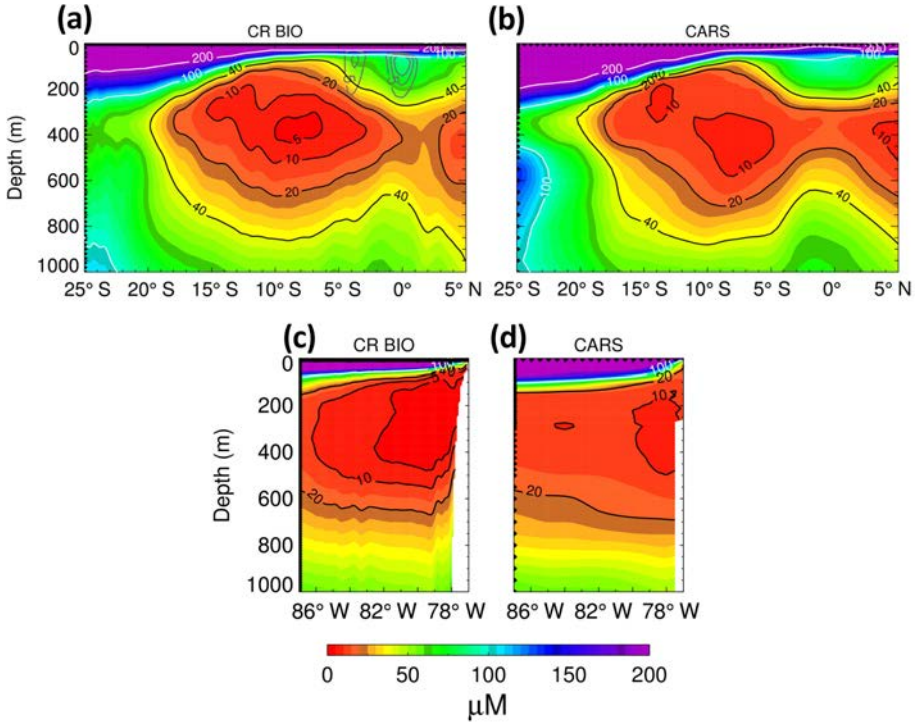

Figure 3. Mean oxygen concentration for a meridional section at 85° W **(a, b)** and a cross-shore section at 12° S **(c, d)**, for both the simulation and CARS. Gray contours in **(a)** show mean zonal speed of 5, 10 and 15 cm s^{-1}, respectively. The black dots denote the horizontal and vertical resolution of the DO field.

domain volume (Fig. 6a), with the less oxygenated layers comprised between 5 and 15° S, and 100 and 600 m depth (Fig. 3). As expected, the simulation presents more details than the climatological product (Fig. 3). Moreover, we computed a geographical OMZ overlapping metric following Cabré et al. (2015), which quantifies the spatial agreement of the OMZ volume distribution between the simulation and CARS, varying between 0 (no agreement) and 1 (perfect collocation). We obtained a value of 0.79, which is ∼ 58 % above the best CMIP5 models used in Cabré et al. (2015).

Despite the overall good agreement between the model and observations, the simulation overestimates the oxygen content in certain regions of the domain as compared to CARS, particularly southwards of 20° S (Fig. 3a) and close to the coast (Fig. 3d). The simulation also underestimates by 6 % the volume of suboxic water (Fig. 6a), which is comparable to the differences obtained by Montes et al. (2014) using the same model within a different configuration and boundary forcing.

The modeled DO distribution is also characterized by finer spatial scales of variability inside the OMZ compared to observations (Fig. 3c and d). In particular, the model oxycline is shallower and with a more intense DO gradient than the observations, which has been also observed in a regional simulation of the Arabian Sea OMZ (Resplandy et al., 2012). While this could be partly due to CARS underestimating the DO gradient, as a result of its relatively low vertical resolution, it could also be that the model underestimates the vertical diffusivity in the vicinity of the oxycline. Also, it must be kept in mind that CARS is built using all the available data from the second half of the twentieth century (1940–2009), whereas we focus on the period 2000–2008 for the simulation, which is known to be a colder period than the previous decades in the eastern tropical Pacific (Henley et al., 2015). Other limitations for the comparison between model and data include the errors associated with the scarcity of data in some regions (Bianchi et al., 2012) and biases in model parametrizations. Nonetheless, the simulation is in overall good agreement with CARS in terms of mean characteristics of the OMZ (Figs. 4, 6a).

In order to evaluate the realism of the seasonal cycle, we estimate the seasonal variability of the volume of water within the suboxic DO concentration range 0–20 µM in both the model and data (Fig. 6b). The results indicate that, despite a weaker amplitude (by 15 % on average), the seasonal cycle of the OMZ core is relatively well simulated by the model. For hypoxic DO volume in the range 40–50 µM, the agreement is as good as inside the OMZ core, with a Pearson correlation value of 0.9 and a volume root mean square (RMS) difference of 16 %, between the simulation and the observations.

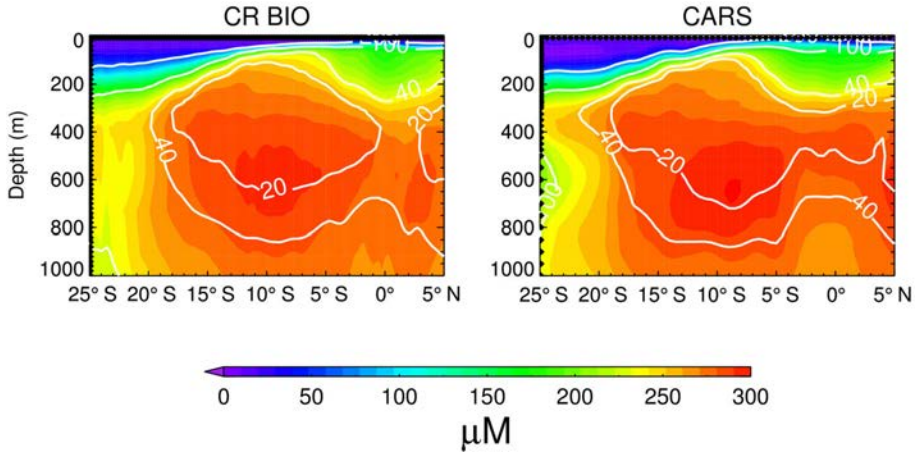

Figure 4. Mean apparent oxygen utilization (AOU) at 85° W for both CR BIO and CARS. White contours denote the mean oxygen concentration isopleths (in µM). The black dots denote the horizontal and vertical resolution of the DO field.

In order to summarize the model validation, we present a Taylor diagram showing the statistics of the comparison between the model and observations for a depth range encompassing the OMZ (Fig. 7). This analysis indicates that within the present model configuration, we reach a skill comparable to the model configuration of Montes et al. (2014) (their Fig. 1). The good agreement of the seasonal cycle between CARS and the simulation, in addition to the consistency of our results with those of Montes et al. (2014), provides confidence in using the model outputs for investigating the processes associated with the seasonal variability of the OMZ.

2.3 Methods

In this work, our approach is twofold: First, the biogeochemical processes for DO are investigated explicitly through the online oxygen budget. Although this methodology can provide a direct estimate of the seasonal variability in advection and mixing, it does not allow for a direct estimate of the eddy contribution to DO change that can also vary seasonally. The DO flux associated with different timescales of variability is therefore estimated. This consists in computing the temporal average of the cross-products between DO and velocity anomalies. Anomalies can refer either to seasonal anomalies (in that case, this provides the mean seasonal DO flux: $\langle \widetilde{u} \times \widetilde{\mathrm{O}_2} \rangle$, where $\sim$ refers to the seasonal anomalies) or to the intraseasonal anomalies, calculated here as the departure from the monthly mean (in that case, this provides an estimate of the mean DO eddy flux: $\langle u' \times \mathrm{O}_2' \rangle$, where the apostrophe refers to the intraseasonal anomalies). In this paper we are also interested in the seasonality of the DO eddy flux. This is estimated from the monthly-mean seasonal cycle of the mean DO eddy flux calculated over a 3-month running window and is now referred to as $\overline{\langle u' \times \mathrm{O}_2' \rangle}$. The climatological EKE activity is estimated similarly.

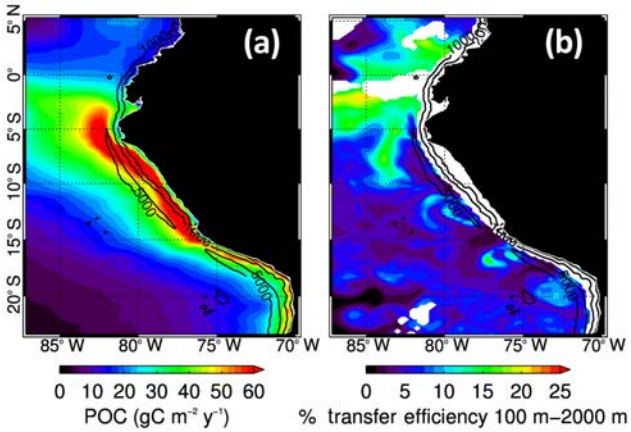

Figure 5. **(a)** Particulate organic carbon (POC) flux at 100 m and **(b)** POC transfer efficiency between 100 and 2000 m (POC flux at 2000 m divided by POC flux at 100 m), computed from the simulation. Integrated carbon flux at the depth of 100 m is 0.8 Pg C yr^{-1}. Black contours correspond to the 200, 1000 and 5000 m isobaths.

The DO budget consists in the following equation:

$$\frac{\partial \mathrm{O}_2}{\partial t} = -\boldsymbol{u} \cdot (\nabla \mathrm{O}_2) + K_h \cdot \nabla^2 \mathrm{O}_2 + \frac{\partial}{\partial z}\left(K_Z \frac{\partial \mathrm{O}_2}{\partial z}\right) + \mathrm{SMS}(\mathrm{O}_2). \quad (1)$$

The first three terms on the right-hand side represent the physical processes involved in the changes in oxygen concentration. The first term stands for the advection of oxygen, where $\boldsymbol{u}$ is the velocity vector (note that the model determines the vertical velocity component from the continuity equation). The second term corresponds to the horizontal subgrid-scale diffusivity (with K_h the eddy diffusion coefficient equal to 100 $\mathrm{m}^2\ \mathrm{s}^{-1}$ in this version of the model), and the third term corresponds to the vertical mixing (with turbulent diffusion coefficient K_z calculated based on the K-profile parameterization mixing scheme; Large et al., 1994). Note that the

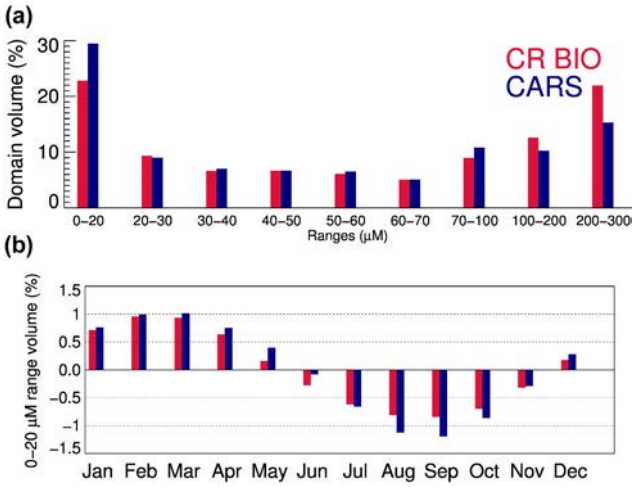

Figure 6. (a) Domain volume distribution (25° S–5° N, 88–70° W) as a function of the oxygen concentration and **(b)** annual cycle, relative to the mean, of the volume distribution inside the OMZ core (DO value range corresponding to 0–20 µmol L^{-1}), for both CARS and the simulation.

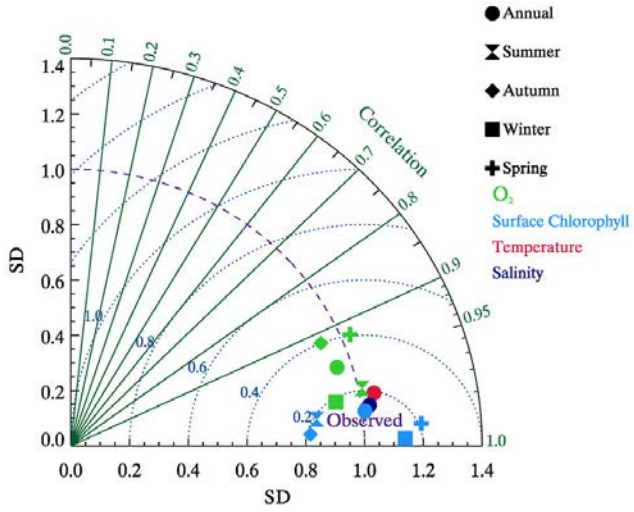

Figure 7. Taylor diagram of the seasonal mean (hourglass, diamond, square and cross) and annual mean (circle) pattern of DO and surface chlorophyll (25° S–5° N, 88–70° W). Only annual mean pattern comparisons are shown for temperature and salinity (same spatial domain). DO, temperature and salinity were vertically averaged between 100 and 600 m depth (focus on the OMZ core). Only the surface chlorophyll values within 250 km next to the coast were considered. The comparisons are made between the simulation and CARS (for DO, temperature and salinity) and SeaWiFS (for surface chlorophyll). Ordinate and abscissa axes represent the standard deviation normalized by the observations standard deviation. Blue dotted radial lines indicate the RMS difference between the observations and the simulation.

model also has numerical diffusion associated with inherent spurious diapycnal mixing of the numerical scheme, so that K_h is empirically adjusted.

The fourth term represents the "source-minus-sink" contribution to the oxygen changes, directly due to biogeochemical activity. Biogeochemical processes correspond to the sum of oxygen sources and sinks, namely the photosynthetic production, and the aerobic processes (oxic decomposition, excretion and nitrification). In this study, for simplicity, those will be considered as a summed-up contribution to the DO rate of change, whereas physical processes will be divided into advection and mixing terms. Each term of this oxygen budget is determined online at each time integration. While horizontal diffusion and vertical diffusivity are explicit sources of mixing, they are not the only terms contributing to mixing. Later on in the paper, unless stated otherwise, the term mixing will refer to the integrated effect of all processes contributing to mixing directly or indirectly. Besides the horizontal diffusion ($K_h \times \nabla^2 O_2$) and vertical mixing $\left(\frac{\partial}{\partial z}\left(K_Z \frac{\partial O_2}{\partial z}\right)\right)$, mixing can be also induced by nonlinear advection. The latter corresponds to $\left(u'\partial u'/\partial x\right)+\left(v'\partial v'/\partial y\right)+\left(w'\partial w'/\partial z\right)$, assuming the Reynolds decomposition for the velocity field, i.e., $\bar{\boldsymbol{u}}+\boldsymbol{u'}$, where $\boldsymbol{u'}$ accounts for the intraseasonal variability (periods shorter than ~ 3 months).

In the SEP, the subthermocline seasonal variability can be interpreted as resulting from the propagation of ETRW. ETRW radiate from the coast and propagate vertically, inducing a vertical energy flux whose trajectory follows the theoretical Wentzel–Kramers–Brillouin (WKB) ray paths (Dewitte et al., 2008; Ramos et al., 2008). The energy flux results from the phase relationship between vertical velocity associated with the vertical displacement of the isotherms, and the pressure fluctuations associated with them. In the regions sufficiently below the thermocline for DO consumption to become weak (that is DO can be considered a passive tracer), it is expected that changes in DO relate to the anomalous velocity field and that the DO flux shares comparable characteristics than the Eliassen–Palm flux (Eliassen and Palm, 1960). The trajectories of the WKB ray paths are a function of latitude, local stratification and the phase speed of the Rossby wave (see Ramos et al., 2008). The latter consists in the superposition of a certain number of baroclinic modes, in order to propagate vertically, so the phase speed can range from c_1 to c_n, where c_n is the theoretical phase speed of a nth baroclinic mode, obtained from the vertical mode decomposition of the local density profile.

3 Characteristics of the DO annual cycle

While the annual signal is a conspicuous feature inside the region (Fig. 6b), it could manifest differently across the OMZ. As a first step towards investigating processes driving the rate of DO change, it appears important to document the vertical structure variability of the DO annual cycle within the OMZ. The amplitude and phase of the annual harmonic of the model DO climatology are presented along a zonal section

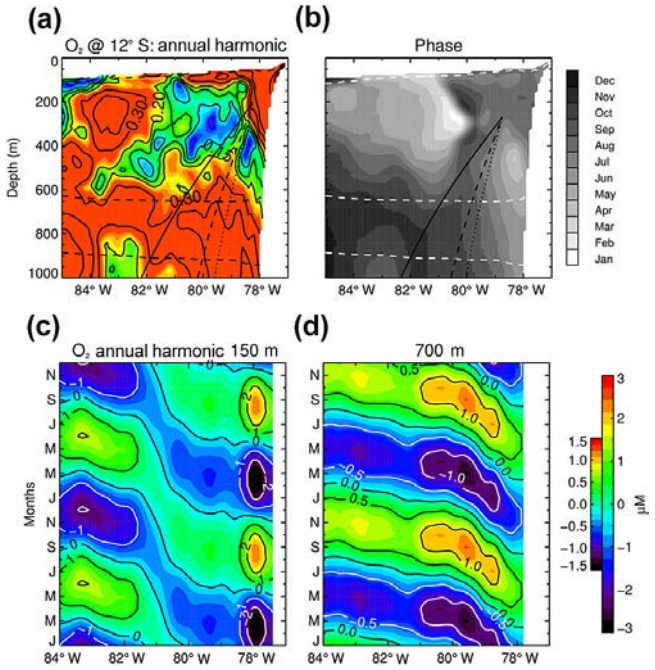

Figure 8. **(a)** Amplitude and **(b)** phase of the annual maximum (in months) of the annual harmonic of the normalized DO concentration at 12° S. The slanted vertical lines indicate the theoretical WKB ray paths at a frequency of $\omega = 2\pi \times 1\,\mathrm{yr}^{-1}$, for different values of phase speed. The theoretical trajectories were computed using the phase speed of the first (full), second (dashed) and third (dotted) baroclinic modes of a long Rossby wave. Dashed contours in **(a)** and **(b)** depict the 45 and 20 µM mean DO values. Land and the region outside the 45 µM mean DO isopleth are masked in white. **(c)** Annual harmonic of the DO concentration at 12° S, at 150 m and **(d)** 700 m depth. Small color scale corresponds to 700 m and the large color scale denotes the levels used in **(c)**.

off central Peru (12° S, Fig. 8a, b), where the OMZ core is extensive (Fig. 2). The DO climatology has been normalized by its RMS in order to emphasize the regions where the amplitude in DO changes (and mean DO) is weak. The amplitude reveals a complex pattern with three regions of large relative variability: (1) near the coast (i.e., fringe of ~ 150 km) between the oxycline and 400 m, (2) offshore between 82 and 84° W in the upper 400 m and (3) below 500 m. The phase lines over these three regions suggest distinct propagating characteristics: whereas in the coastal region there is no propagation, in the offshore and deep region there is indication of a westward propagation. In the region below 500 m, the phase lines tend also to be parallel and slope downward, suggestive of westward–downward propagation (estimated phase speed of $\sim 2.5\,\mathrm{cm\,s}^{-1}$). These propagating characteristics can be evidenced in the Hovmöller diagrams of the recomposed annual cycle at the depth of 150 m (Fig. 8c) and 700 m (Fig. 8d). While at 150 m the annual signal does not clearly propagate and only shows two domains of high amplitude, separated by low amplitude values (Fig. 8c) there is a clear westward propagation of the DO anomalies at 700 m, with the phase speed increasing westward. At 400 m, the propagation is only observed west of 81° W (Fig. 8b). In addition to the large vertical structure variability of the annual cycle, the OMZ annual cycle is also characterized by a large horizontal variability in particular at its northern and southern boundaries. This is illustrated in Fig. 9, which displays the amplitude of the annual cycle of the DO climatology at 400 m and evidences amplitude peaks at the OMZ meridional boundaries (between the 20 and 45 µM isopleths).

The annual variability pattern evidenced above results from a delicate balance between the physical processes (namely advection and mixing, cf. Eq. 1) and the biogeochemical processes (consumption versus production). As a first step towards investigating each term of the DO budget, it is interesting to evaluate the relative contribution of the physical and biogeochemical fluxes to the DO variability at seasonal scale. The RMS of the climatological fluxes along a section at 12° S indicates that the maximum amplitude of the seasonal fluxes takes place near the oxycline and along the coast over the whole water column (Fig. 10). The relative importance of the physical processes against the biogeochemical processes varies across the OMZ. At the coast and near the oxycline, the annual variability of the biogeochemical processes reaches values almost half those of the variability in physical processes (Fig. 10c), as a consequence of the proximity to both the well-lit and highly productive part of the water column, and the high remineralization activity that occurs near the oxycline. Towards offshore and at depth, the relative importance of the variability of the biogeochemical processes reduces gradually. Near ~ 300 m the variability of the biogeochemical processes is nearly one-fifth of the physical processes variability. Below ~ 300 m, and towards the lower part of the OMZ core and below, the physical processes variability is 1 order of magnitude larger. Consequently, the distribution of DO in the lower part of the OMZ is rather a function of advection/diffusion than a consequence of the biogeochemical processes, although DO consumption even at very low levels has the potential to generate local gradients and therefore induce advection. The spatial heterogeneity in the seasonal DO changes induced by the biogeochemistry and dynamics, as described above, appears as an ubiquitous feature in the OMZ. To illustrate this, we estimate the proportion of explained variance of the seasonal DO rate of change by the physical fluxes as

$$R^2_{\mathrm{Phys.}} = (1 - \mathrm{RMS(biogeochemical\ fluxes)}/ \mathrm{RMS(total\ fluxes)}) \cdot 100. \quad (2)$$

Figure 11a and b present the results of $R^2_{\mathrm{Phys.}}$ at 100 and 450 m depth, which evidences that the relative importance of the physical fluxes versus the biogeochemical fluxes in the seasonal DO variability increases with depth and is enhanced at the OMZ boundaries. However, the biogeochemical fluxes explain more than 50 % of the variance in seasonal

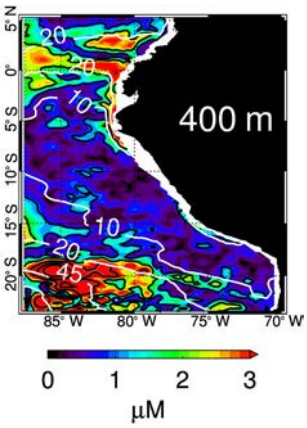

Figure 9. Annual DO harmonic amplitude at 400 m depth. White contours denote the 10, 20 and 45 µM mean oxygen isolines. Black contours denote the 1, 2, 4, 6 and 8 µM levels.

DO change rate in a narrow (∼ 200 km width) coastal fringe that extends more offshore to the north of the domain (around 8° S; Fig. 11a) and vertically down to 300 m (Fig. 11c).

Based on the above analysis, it is clear that the coastal region (first 200–300 km from the coast) below the oxycline corresponds to a territory where the seasonal variability of biogeochemical and physical fluxes have a comparable magnitude, whereas outside this region, notably in the lower part of the OMZ core, the physical fluxes variability dominates over the biogeochemical fluxes variability at seasonal timescale. Hereafter we examine the possibility of two distinct regimes of OMZ dynamics at seasonal timescale: one associated with the upper OMZ (including coastal domain and meridional boundaries), and one associated with the deep OMZ. In the following we investigate the processes responsible for the DO flux.

4 Seasonality of the OMZ ventilation

It has been shown for the SEP that the DO content near the coast is set to a large extent from the transport of oxygen-deficient waters from the equatorial current system, particularly the oxygen-depleted secondary southern subsurface countercurrent (Montes et al., 2014). Therefore, the seasonal variability of DO is likely to result in part from the seasonal variability of the different branches of the EUC in the far eastern Pacific. Local wind stress forcing (and its intraseasonal activity) has also a marked seasonal cycle off Peru (Dewitte et al., 2011) which may impact both the upwelling dynamics – through Ekman pumping/transport – and mixing. Some studies also argue that the DO exchange between the coastal domain and the OMZ takes place through the offshore transport of DO-poor waters by eddies (Czeschel et al., 2011), implying that the variability of such processes is set up by coastal processes that determine the nature of the DO source. As a first step, we investigate the mechanisms responsible for the seasonal variability in DO along the coast, which can be considered as the eastern boundary of the OMZ. This is aimed at providing material for the interpretation of the offshore DO flux variability.

4.1 The coastal domain as the eastern boundary of the OMZ: variability and mechanisms

We analyze the seasonal variability along the coast, at a section at 12° S. Similar results are obtained for latitudes between 7 and 14° S (not shown), which corresponds to the latitude range where the Peru Undercurrent (PUC) is well defined. The results are also presented in terms of the first empirical orthogonal function (EOF) mode, in order to ease the interpretation of the variability, reduced as a spatial pattern modulated by a seasonal time series. It was verified in particular that the consideration of the first EOF mode of each term leads to an almost perfect closure of the DO budget (see below, Table 1). Figure 12 displays the first EOF mode of various climatological fields in a section at 12° S near the coast and from the oxycline (45 µM isoline) to the depth of 300 m. Figure 13 shows the principal components associated with the first EOF-mode patterns. The seasonal DO cycle is dominated by an annual component, with a peak centered in August (Fig. 13a), and the largest variability at the coast below the oxycline that extends offshore and downward, resulting in an elongated tongue below 100 m near ∼ 78° W (Fig. 12a). During the first quarter of the year, oxygen anomalies remain relatively stable (oxygen rate nearly zero, Fig. 13b) and negative due to a high production of organic matter in austral summer (cf. Fig. 1c of Gutiérrez et al., 2011) that stimulates a subsurface oxygen consumption associated with the degradation of this organic matter. DO anomalies start to increase during the second quarter, become positive in June and reach their maximum in August (Fig. 13a). The peak anomaly in austral winter could be understood in terms of the increased mixing (see Fig. 13a showing EKE peaking in July) associated with the increase in baroclinic instability due to the seasonal intensification of the PUC from June. Note that the pattern of the first EOF mode of the alongshore current coincides with the mean position of the PUC (see Fig. 12b), so that seasonal variations of the PUC can be interpreted in terms of the variations in the vertical shear of the coastal current system. Other processes that may explain the peak DO anomaly in austral winter include the reduced productivity and downwelling that peaks in June (Fig. 13c), associated with seasonal equatorial downwelling Kelvin wave.

The following investigates the tendency terms of the DO budget in order to quantitatively interpret the DO seasonal cycle near the coast. Given that the analysis is performed inside the 45 µM isopleth, the biogeochemical flux term is largely dominated by the "sinks" terms (aerobic processes; 1 order of magnitude larger than "sources"), driven by organic matter remineralization and zooplankton respiratory

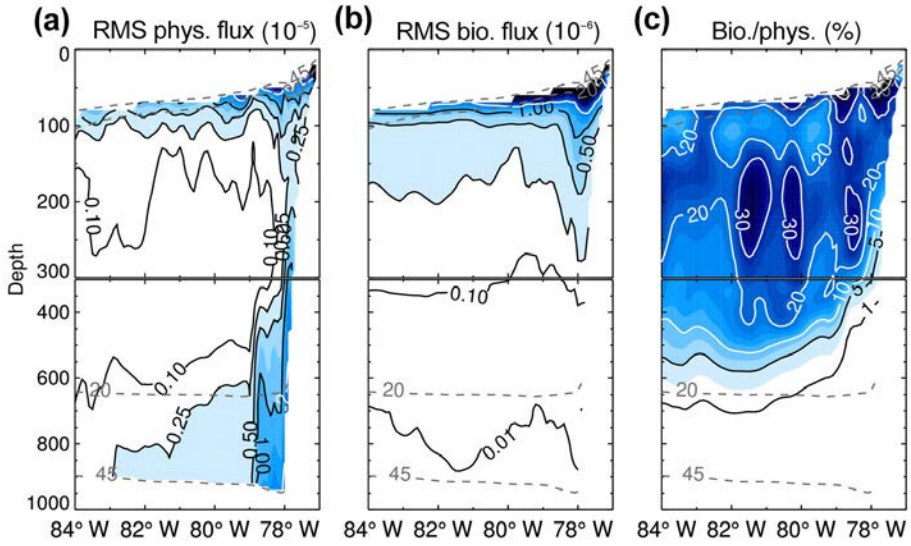

Figure 10. Root mean square of the seasonal cycle of **(a)** physical and **(b)** biogeochemical oxygen fluxes (in 10^{-5} and 10^{-6} µM s^{-1}, respectively) for CR BIO at 12° S. **(c)** Ratio between the RMS of the biogeochemical fluxes and the physical fluxes, expressed as percentage. Dashed contours depict the 45 and 20 µM mean oxygen values. Note the vertical scale change at 300 m depth. Land and the region outside the 45 µM mean DO isopleth are masked in white.

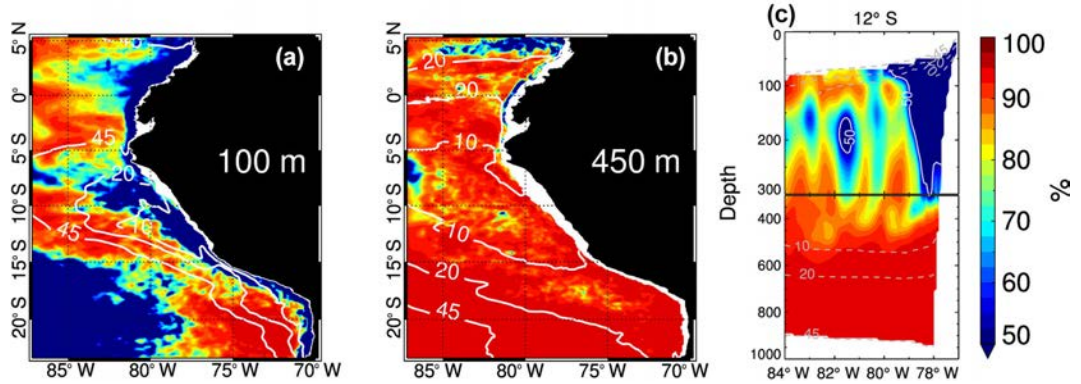

Figure 11. Percentage of the seasonal DO rate variance explained by the physical fluxes, at **(a)** 100 and **(b)** 450 m depth, and along a cross-shore section at 12° S. Solid white lines **(a, b)** and dashed gray lines **(c)** denote the 10, 20 and 45 µM mean DO isopleths. Land and the region outside the 45 µM mean DO isopleth are masked in white in **(c)**.

metabolic terms (not shown). For clarity, the seasonal DO budget is presented synthetically, from the first EOF mode of the climatological advection, mixing (horizontal and vertical diffusion) and biogeochemical fluxes terms. Although this does not warranty a perfect closure, it eases the interpretation. Note that the residual resulting from the difference between the first EOF mode of the rate of DO changes and the summed-up contribution of all the other terms in Fig. 13b is rather weak, validating to some extent our approach (see also Table 1). First of all, we find that the largest amplitude of the mode patterns is found near the coast and inside the mean PUC core (Fig. 12d to g). During the first part of the year (January to May), positive advection anomalies are compensated by mixing (horizontal and vertical diffusion), and they maintain the rate of DO change relatively low (Fig. 13b; Table 1). Biogeochemical fluxes anomalies are positive during that period, associated with a positive anomaly of primary production in the well lit surface layers, implied by the high chlorophyll *a* values (Fig. 13c). A positive oxygen anomaly is sustained by the advection terms and the biogeochemical terms and is balanced out by the mean advection of low DO waters carried by the PUC (Montes et al. 2010, 2014), generating the relatively stable oxygen values (oxygen rate nearly 0).

From May, the rate of DO changes increases concomitantly with EKE (Fig. 13a, b), followed 1 month later by mixing (horizontal and vertical diffusion), whereas advection and biogeochemical fluxes decrease. By June–July, the inten-

Table 1. Austral summer (DJF mean) and winter (JJA mean) seasonal anomalies of the DO budget, averaged over the core of the Peru Undercurrent at 12° S (as depicted by the red contour in Fig. 12). The values for the seasonal cycle and the reconstructed first EOF mode (Figs. 12 and 13) are presented along with the difference between climatology and EOF. All values are in 10^{-6} µM s^{-1}. Mixing here consists in the summed-up contribution of horizontal diffusion ($K_h \times \nabla^2 O_2$) and vertical diffusivity $\left(\frac{\partial}{\partial z}\left(K_Z \frac{\partial O_2}{\partial z}\right)\right)$.

	Climatology		EOF		Difference	
	Summer	Winter	Summer	Winter	Summer	Winter
$\partial O_2/\partial t$	1.10	−2.74	1.30	−2.67	−0.20	−0.07
Adv	0.61	−9.38	0.85	−9.30	−0.24	−0.08
Mixing	−0.42	7.99	−0.35	7.99	−0.07	0.00
Biogeochemical flux	0.91	−1.35	1.00	−1.35	−0.09	0.00

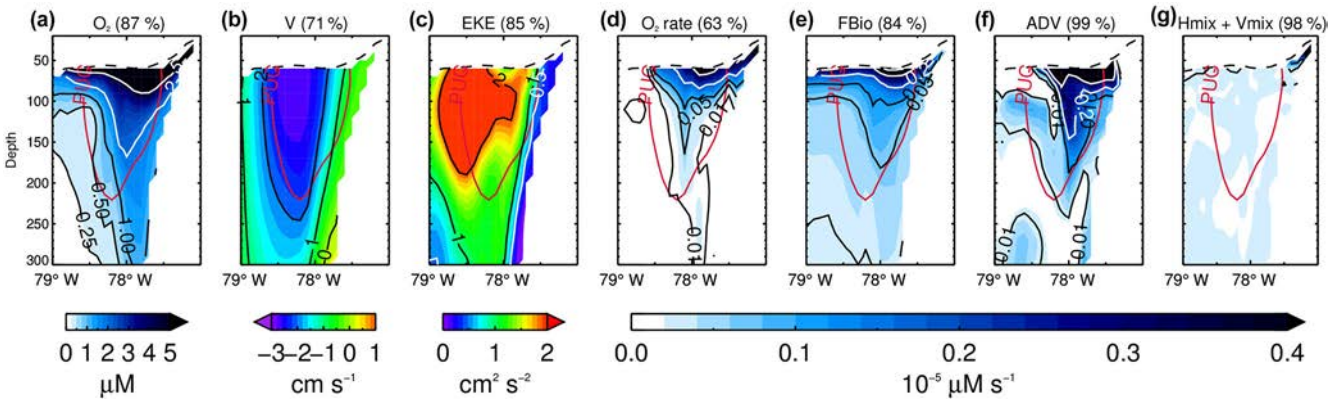

Figure 12. First EOF-mode pattern of **(a)** DO, **(b)** alongshore currents component, **(c)** eddy kinetic energy, **(d)** oxygen rate, **(e)** biogeochemical flux, **(f)** advective terms (sum of horizontal and vertical components) and **(g)** mixing terms (sum of horizontal and vertical components). Percentage of explained variance by each EOF-mode pattern is indicated in parentheses on top of each panel. The red contour denotes the mean position of the Peru Undercurrent core, defined here as alongshore southward current exceeding 4 cm s^{-1}. The black dashed contour denotes the mean DO 45 µM isopleth. Land and the region outside the 45 µM mean DO isopleth are masked in white. The EOF-mode patterns were multiplied by the RMS of the principal component (PC) time series. Multiplying the EOF pattern by the PC time series plotted in Fig. 13 yields the contribution of the first EOF mode to the original field, in dimensionalized units (i.e., µM s^{-1} for the tendency terms).

sification in alongshore winds (Fig. 13c) starts to propel the coastal upwelling, which has two compensating effects: on one hand, it triggers photosynthesis in the lit surface layers (DO rate turns to positive values); on the other hand, it uplifts low-oxygen waters from the OMZ. The intraseasonal wind activity also starts to increase at that time (cf. Fig. 13c; see also Dewitte et al., 2011), which favors mixing and the downward intrusion of positive DO anomalies (note the deepening of the mixed layer in Fig. 13c). The overall effect is an increase in DO, which leads to a peak anomaly in August. At that time, the DO rate drops sharply due to the strong subsurface DO consumption (Table 1) associated with aerobic remineralization of organic matter produced earlier in the season (DO rate moves sharply to negative values) and the high mixing that brings DO-depleted waters from the subsurface into the deepened mixed layer. Note that this is consistent with the decrease in surface chlorophyll *a* (Fig. 13c) and the interpretation proposed by Echevin et al. (2008) to explain the austral summer minimum in surface chlorophyll *a* observed off central Peru.

This change to oxygen-poor conditions combines with the natural decrease in oxygen production towards the end of the upwelling season and coincides with a restratification of the water column, which restricts the oxygenated waters near the surface (Echevin et al., 2008). This altogether contributes to maintain a negative DO rate inside the coastal OMZ, despite the increase in anomalous DO flux from the advective terms and (later on) biogeochemical processes towards the end of the year. As a result, oxygen returns to low values towards the end of the year.

4.2 Offshore flux

While the coastal OMZ variability is heavily constrained by the environmental forcings – coastal upwelling, coastal current system and local wind – due to the shallow oxycline there, the offshore OMZ, as embedded in the shadow zone of the thermohaline circulation, is somewhat insensitive

to direct local forcing and rather experiences remote influence in the form of westward-propagating mesoscale eddies (Chaigneau et al., 2009) and ETRW (Ramos et al., 2008; Dewitte et al., 2008). The influence of westward-propagating mesoscale eddies on the OMZ translates as the transfer of coastal water properties towards the open ocean (DO included), while these properties are altered during transport due to physical/biogeochemical interactions (Stramma et al., 2014; Karstensen et al., 2015). Towards the end of their lifetime, hydrographic and biogeochemical anomalies carried by eddies are redistributed in the ocean (Brandt et al., 2015), linking the coast and the open ocean. Although most eddy genesis takes place near the coast and seasonal ETRW have a coastally forced component, we expect different characteristics of the seasonal variability in DO between the coast and the open ocean, given that oxygen demand will change from one region to the other. We also distinguish the mean DO flux associated with the annual component of the circulation that represents the transport in DO associated with seasonal changes in the large-scale circulation and the annual variability of the DO eddy flux that corresponds to the annual changes in the transport due to eddies. These two quantities are diagnosed at 12° S (Figs. 14 and 15). The DO has been normalized by its climatological variability in order to emphasize variability patterns where DO is low.

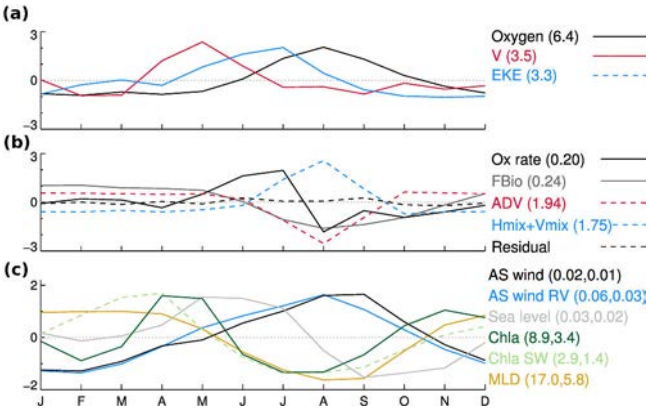

Figure 13. (a, b) Non-dimensional principal components (PCs) associated with the EOF patterns in Fig. 12. Multiplying the principal component by the associated EOF pattern (from Fig. 12) yields a first EOF-mode reconstruction of the original field. RMS values of the principal components are indicated in parenthesis (corresponding units as in Fig. 12). The residual corresponds to the difference between the rate of DO change and the sum of all the terms of the right-hand side of Eq. (1) in terms of the normalized PC time series. The weak residual indicates that the seasonal DO budget can be interpreted from the EOF decomposition. The EOF decomposition was performed over the climatological (mean seasonal cycle) fields. **(c)** Normalized seasonal cycle of coastal alongshore wind (AS wind) and coastal alongshore wind running variance (variance over a 30-day running window) at 12° S, sea level at the coast at 12° S, surface chlorophyll *a* from CR BIO (Chl *a*) and from SeaWiFS (Chl *a* SW) averaged over a coastal band of 2° width at 12° S, and mixed layer depth (MLD) at the coast at 12° S. Mean and RMS used to normalize each time series, are indicated in parenthesis. Original seasonal cycle is found by multiplying the normalized series by its RMS and then adding the mean. Original units are $\mathrm{N\,m^{-2}}$, m, $\mathrm{mg\,m^{-3}}$ and m, respectively.

4.2.1 Mean seasonal flux

We first document the mean DO flux associated with the annual component of the circulation. It consists in the mean of the cross-product of the annual harmonics of the climatological velocity and DO (Fig. 14a). The results indicate that the amplitude of the annual DO flux is maximum near the coast and below ∼400 m and it tends to be orientated westward–downward, following approximately the trajectories of theoretical WKB paths for the annual period Rossby wave. Note that this is consistent with the westward-propagating pattern of DO below 400 m evidenced earlier (Fig. 8). As a consistency check, we also estimated the annual energy flux vector in the (x, z) plane associated with a long extratropical Rossby wave; that is $\left(\langle p^{1\mathrm{yr}} \times u^{1\mathrm{yr}} \rangle, \langle p^{1\mathrm{yr}} \times w^{1\mathrm{yr}} \rangle\right)$ where the superscript denotes the annual harmonics and the bracket the temporal average (Fig. 14b). The flux vector indicates vertical propagation of energy at the annual period and the pattern of maximum flux coincides approximately with the region of maximum amplitude of the mean seasonal DO flux. This suggests that the annual ETRW are influential on the DO flux below ∼400 m. This is interpreted as resulting from the advection of DO by the ETRW since biogeochemical fluxes have much less influence on the DO rate of change below 400 m (Fig. 10c) and the amplitude of the annual cycle of climatological DO eddy flux has a much reduced amplitude below that depth (Fig. 15a), suggesting a small contribution of horizontal and vertical diffusion to the DO budget. Note that the DO (Fig. 15a) was normalized prior to compute the DO eddy flux, so it is possible to compare to Fig. 14a, and therefore contrast the flux associated with the annual ETRW against the annual DO eddy flux. It was verified that the vertical structure variability of the annual DO flux described above for the section of 12° S is comparable at other latitudes within the OMZ. In particular, the annual DO flux tends to remain homogeneous along trajectories mimicking the energy paths of the ETRW at the annual period when the slope becomes steeper to the south (not shown).

4.2.2 Seasonal eddy flux

As previously described, the annual amplitude of the climatological DO eddy flux is the largest in the upper 400 m near the coast at 12° S consistently with the high EKE in this region. Since EKE is large along the coast of Peru, exchange of DO induced by eddies could be expected at all latitudes, with a direction that depends on the sign of the DO gradient at the coast. Figure 16 presents the annual harmonic of the climatological DO eddy flux along the coast and averaged in

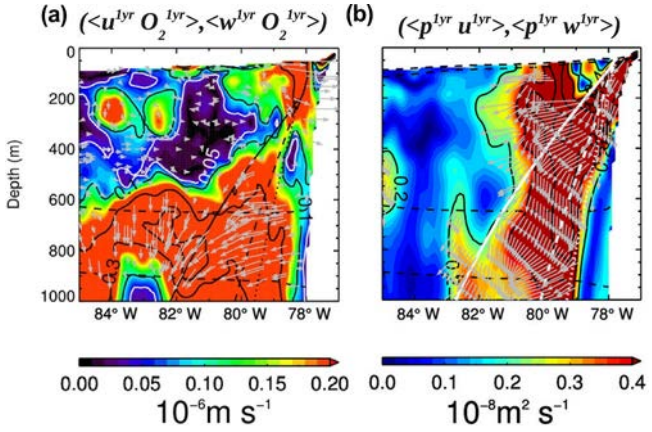

Figure 14. **(a)** Norm of the annual DO flux vector (i.e., $\sqrt{\left(\langle u^{1\mathrm{yr}} \times \mathrm{O}_2^{1\mathrm{yr}} \rangle\right)^2 + \left(\langle w^{1\mathrm{yr}} \times \mathrm{O}_2^{1\mathrm{yr}} \rangle\right)^2}$) for a cross-shore section at 12° S. Arrows indicate the vector direction $\left(\text{i.e., } \left[\langle u^{1\mathrm{yr}} \times \mathrm{O}_2^{1\mathrm{yr}} \rangle, \langle w^{1\mathrm{yr}} \times \mathrm{O}_2^{1\mathrm{yr}} \rangle\right]\right)$. The DO signal was normalized by its root mean square value before computing the annual harmonic in order to emphasize the flux patterns where DO concentration is very low. **(b)** Norm of the annual energy flux vector (i.e., $\sqrt{\left(\langle p^{1\mathrm{yr}} \times u^{1\mathrm{yr}} \rangle\right)^2 + \left(\langle p^{1\mathrm{yr}} \times w^{1\mathrm{yr}} \rangle\right)^2}$). Arrows inside the 0.2 contour indicate the vector direction $\left(\text{i.e., } \left[\langle p^{1\mathrm{yr}} \times u^{1\mathrm{yr}} \rangle, \langle p^{1\mathrm{yr}} \times w^{1\mathrm{yr}} \rangle\right]\right)$. Some theoretical WKB trajectories (1-year period) originating from near the coast at the surface are drawn for phase speed values of a first (full), second (dashed) and third (dotted) baroclinic modes. The range of phase speed values (modes 1–3) is obtained from a vertical mode decomposition of the mean model stratification. Dashed black contours indicate the 45 and 20 µM mean DO isopleths. Land and the region outside the 45 µM mean DO isopleth are masked in white.

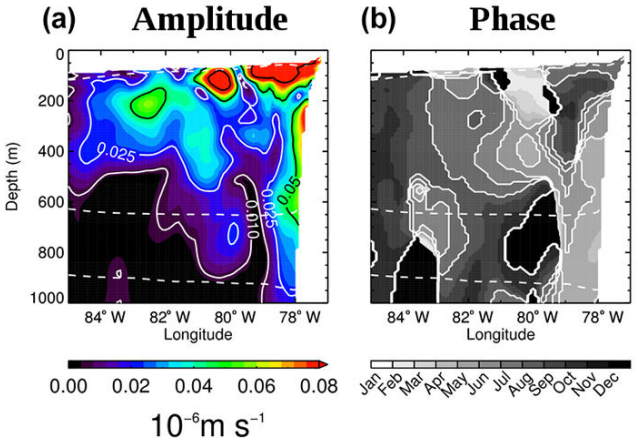

Figure 15. Zonal section of the annual harmonic of the module of the seasonal DO eddy-flux vector $\left(\overline{\langle u' \times \mathrm{O}_2' \rangle}, \overline{\langle w' \times \mathrm{O}_2' \rangle}\right)$ at 12° S. **(a)** Amplitude of the harmonic and **(b)** phase of the annual maximum (in months). Dashed white contours indicate the 45 and 20 µM mean DO isopleths. DO was normalized by its RMS prior to carrying out analysis. Land and the region outside the 45 µM mean DO isopleth are masked in white.

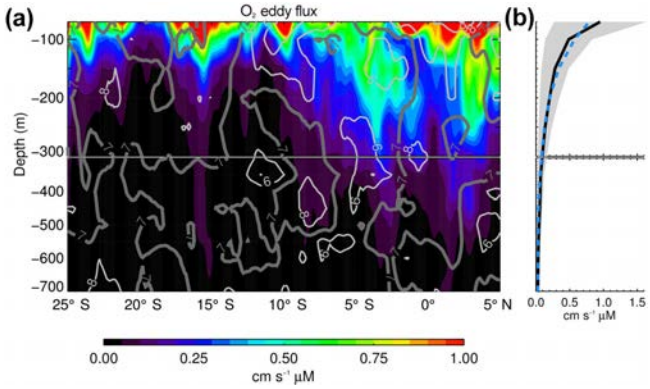

Figure 16. **(a)** Amplitude (color shading) and phase (months, gray contours) of the annual harmonic of the climatological DO eddy flux along the coast. The climatology of DO eddy flux was averaged over a coastal fringe of 2° width, starting from 1° from the coast. **(b)** Meridional average vertical profile (black line), ±RMS (gray shading). An exponential model fitted to the average vertical profile (dashed blue line) yields a vertical decay scale of ∼ 90 m.

a coastal fringe distant 1° from the coast and 2° width. The maximum amplitude – reaching $\sim 1\,\mathrm{cm\,s^{-1}}$ µM – is concentrated in the upper oxycline (Fig. 16a) with a peak during austral winter. The peak season is also confirmed by the EOF analysis of the climatological DO eddy flux (not shown). Despite the relative large meridional variability in the amplitude, the mean vertical structure of the DO eddy flux consists in an approximate exponentially decaying profile with depth, with a decay scale of ∼ 90 m (Fig. 16b) so that at 300 m the seasonal DO eddy flux is on average only 19 % of that at 100 m along the coast. Figure 16a also reveals that the annual DO eddy flux is larger towards the northern rim of the domain and extends deeper than towards the south. The high values are increasingly confined close to the surface towards the southern part of the domain, in comparison to the northern part, although the vertical attenuation displays a similar scale.

4.3 Meridional boundaries

Here, our objective is to document the seasonality of the DO eddy flux. As a first step, we estimate the distribution of mean DO eddy flux in order to identify the regions where its magnitude is large and thus where it is likely to vary seasonally with a significant amplitude.

4.3.1 Mean seasonal flux

The horizontal distribution of mean DO eddy flux displays the highest values at the boundaries of the OMZ core (Fig. 17) and adjacent to the 45 µM isopleth. Towards the inner OMZ, the mean DO eddy-flux values decrease notoriously, with a factor of nearly 10 between the interior and

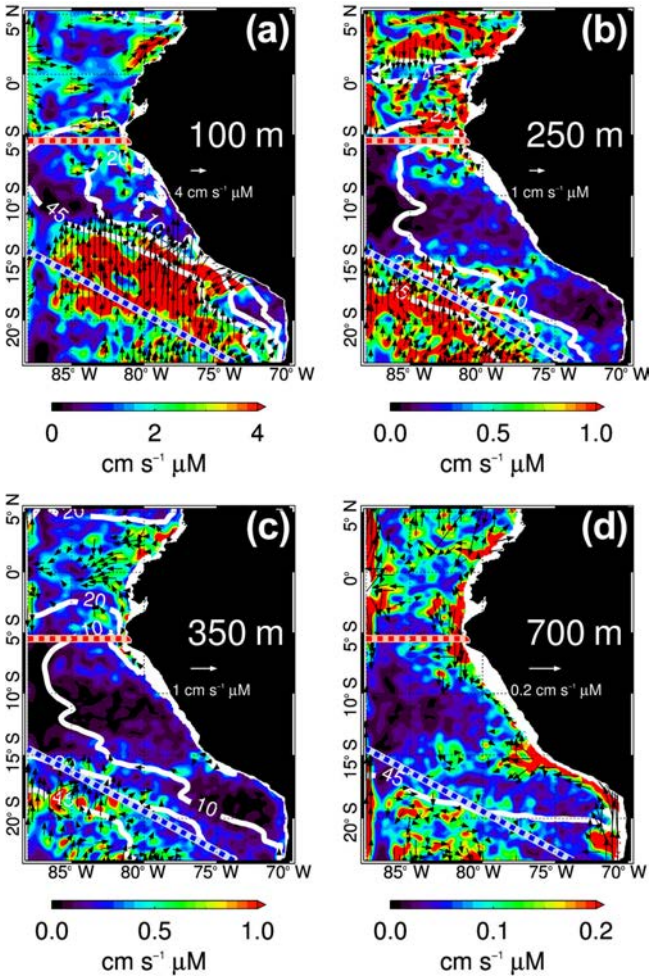

Figure 17. Module of the mean DO eddy-flux vector $\left(\langle u' \times O_2' \rangle, \langle v' \times O_2' \rangle\right)$ at **(a)** 100 m, **(b)** 250 m, **(c)** 350 m and **(d)** 700 m depth. Arrows displayed only for values above the central value in each color bar denote the vector direction and strength. White contours correspond to the 45, 20 and 10 µM mean DO values. Red and blue lines denote the position of vertical sections.

exterior of the 10 µM contour. In agreement with the observations reported in the previous section, the mean DO eddy flux decreases sharply with depth (approximately 1 order of magnitude between 100 and 700 m), with the highest values concentrated near the oxycline, as expected from the increasing oxygen concentration in this part of the OMZ. In this sense, the pattern of DO eddy flux around the depth of the oxycline encloses a region of high variability (not shown).

To gain further insight with respect to the vertical structure of the DO eddy flux and at the same time diagnose the role of the mesoscale activity at the boundaries of the OMZ, we compute the mean DO eddy flux across the two sections that correspond to the northern and southern limits of the OMZ (depicted in Fig. 18). These limits are defined based on Fig. 17 and are located in the provinces of high amplitude of the mean DO eddy flux.

The DO eddy flux across each of the northern and southern boundaries was computed by averaging the product of the fluctuating velocity component normal to the boundary in the horizontal directions and the fluctuating DO concentration component, thereby obtaining horizontal eddy fluxes.

As observed in Fig. 17, the highest values for both northern and southern boundary sections are found between the oxycline and the lower OMZ core limit (Fig. 18), being almost 1 order of magnitude smaller at greater depths (Fig. 18c). These high values, located between $\sim$100 and 300 m, are followed by a sharp decrease (average decrease of 1.5 cm s^{-1} µM in 100 m). At the range of depths between 100 and 300 m, the DO eddy flux displays higher values at the southern boundary (nearly twice as large) when compared with the northern boundary. This relationship is less clear when analyzing the lower part of the OMZ. At both meridional boundaries, the mean DO eddy flux in the upper part of the OMZ is nearly 1 order of magnitude larger than in the lower part.

4.3.2 Seasonal eddy flux

We now document the seasonal variability of the DO eddy flux across the OMZ boundaries analyzed above (Fig. 18). An EOF analysis of the mean seasonal cycle of the DO eddy flux is performed at the boundary sections previously defined. Figure 19 presents the first EOF-mode patterns along with the associated time series. In order to estimate the uncertainty associated with the location of the OMZ boundaries, we repeated this analysis for 12 nearby sections parallel to the boundaries and spaced by $\sim$20 km. This leads to an estimated error (standard deviation across the different sections) of the DO eddy flux. The error is represented as a colored shading in Fig. 19b, d, e. At both locations, the first EOF accounts for a well-defined seasonal cycle. At the northern boundary (Fig. 19a), the seasonal cycle of the DO eddy flux peaks in austral winter, in phase with the DO changes along the coast (Fig. 16). Note that the seasonal cycle is in phase with that of the intraseasonal activity of the horizontal currents normal to the section, which was estimated the same way as the climatological eddy flux (see red line in Fig. 19b), supporting the idea that the climatological DO eddy flux results from anomalous advection. The amplitude of the mode pattern is maximum at the oxycline with DO between 20 and 45 µM and presents a sharp decrease below the OMZ core depth (Fig. 19a). This sharp decrease is evidenced by the mean vertical profile of the DO eddy-flux seasonal variability estimated as the RMS across the section of the EOF-mode pattern (Fig. 19e). The vertical structure of the DO eddy-flux variability indicates that there is a difference of nearly 1 order of magnitude between 100 and 300 m depth. From that depth on, the DO eddy-flux variability decreases linearly.

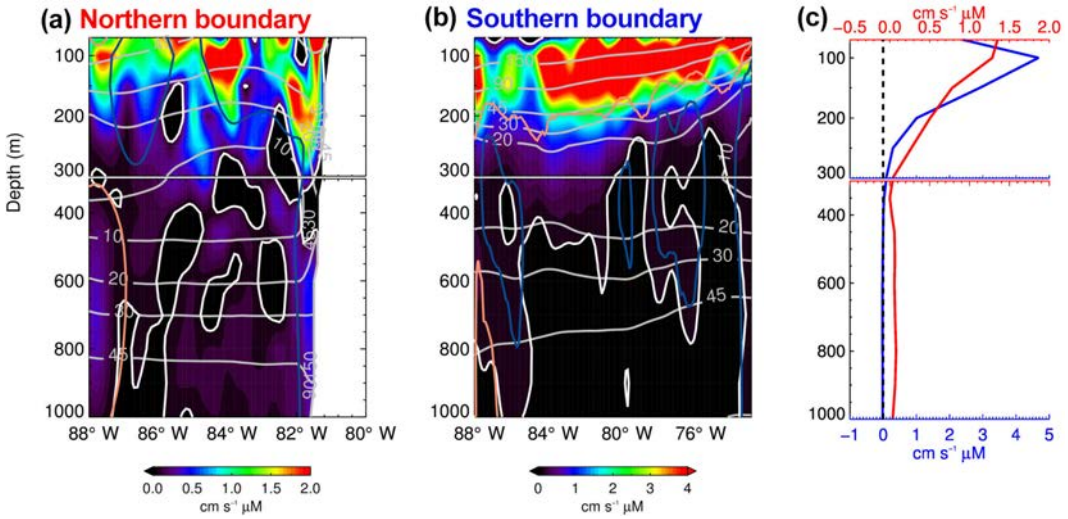

Figure 18. **(a)** Mean DO eddy flux normal to the section denoted by the red line in Fig. 17. **(b)** Mean DO eddy flux normal to the section denoted by the blue line in Fig. 17. **(c)** Horizontal mean of **(a)** and **(b)** (red and blue lines, respectively). Gray contours denote mean DO concentrations, and light red/blue contours correspond to positive/negative values of mean currents normal to the section ($1.0/-1.0\,\mathrm{cm\,s^{-1}}$ in **a** and $0.4/-0.2\,\mathrm{cm\,s^{-1}}$ in **b**). White contour denotes the 0 value. The sign convention was chosen so that a positive horizontal flux indicates transport towards the interior of the OMZ.

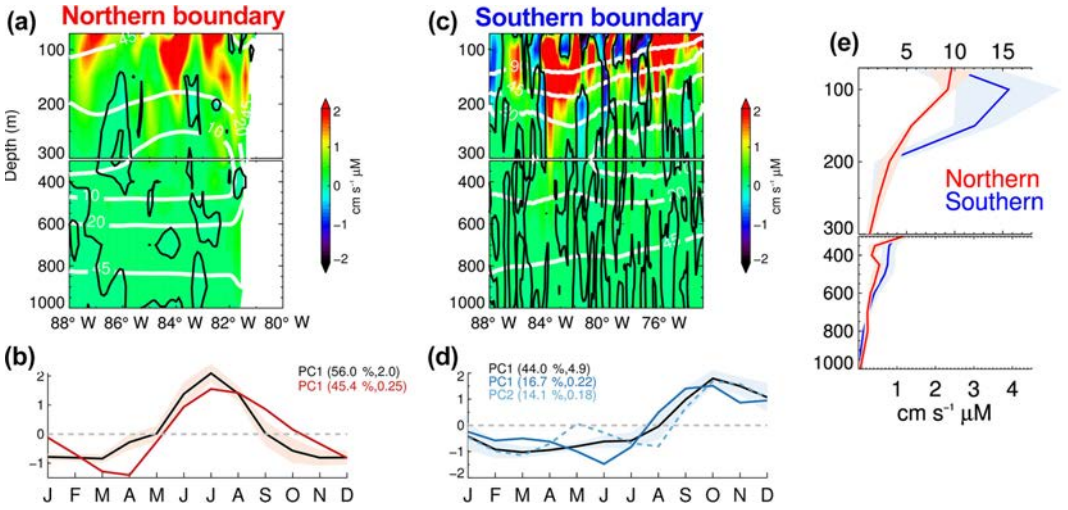

Figure 19. **(a)** First EOF mode of the seasonal cycle of the DO eddy flux normal to the section depicted in Fig. 17 by the dashed red line (northern boundary). **(b)** Principal component (PC) time series associated with the first EOF mode (black line). The red line in **(b)** corresponds to the PC time series associated with the first EOF mode of the seasonal cycle of the 30-day running variance of intraseasonal currents normal to the section. **(c)** First EOF mode of the seasonal cycle of the DO eddy flux normal to the oblique section depicted in Fig. 17 by the dashed blue line (southern boundary). **(d)** PC time series associated with the first EOF mode (black line). The blue curves (full and dashed lines) in **(d)** correspond to the PC time series associated with the first and second EOF modes of the seasonal cycle of the 30-day running variance of the intraseasonal currents normal to the section (computed as in **b**). Percentage of explained variance and RMS value are indicated in parentheses in the panels **(b)** and **(d)** (in $\mathrm{cm\,s^{-1}}$ μM and $\mathrm{cm\,s^{-1}}$ for DO eddy flux and currents, respectively). White contours in **(a)** and **(c)** denote mean DO concentration values in μM. **(e)** RMS of the spatial patterns **(a)** and **(c)**, computed along the horizontal direction. Note the scale leap at 300 m. Red/blue shading in **(b)**, **(d)** and **(e)** represents an estimate of the error associated with slight changes in the location of the boundaries, i.e., when the EOF is performed over a section that is located at a distance from the original section (cf. Fig. 17) compromised between ±120 km (see text). The error corresponds to the standard deviation among 12 PC time series (for **b** and **d**) and EOF patterns (for **e**).

In contrast with the northern boundary, the seasonal variability at the southern boundary peaks during austral spring (Fig. 19d), in phase with the intraseasonal activity of the horizontal currents normal to the section. The amplitude of the seasonal cycle is the largest around the depth of the oxycline and remains high down to the vicinity of the OMZ core upper limit (Fig. 19c). Below the depth of the OMZ core, the amplitude of the EOF mode decreases sharply (~ 1 order of magnitude in 100 m; Fig. 19c). This is evidenced by the profile of the DO eddy-flux seasonal variability, estimated in the same manner as for the northern boundary (Fig. 19e). This profile shares some characteristics with its counterpart at the northern boundary, meaning a sharp decrease between the oxycline and the OMZ core depths, suffering a reduction of nearly 90 % (Fig. 19e). In contrast, the variability along the southern boundary is ~ 70 % larger than along the northern boundary. At both boundaries, the zonal wavelength of the seasonal DO eddy-flux variability along the boundary is estimated to be in the order of $\sim 10^2$ km, a scale that falls within the range of observed eddies diameter (Chaigneau and Pizarro, 2005), which indicates that locally there can be an injection or removal of DO across the boundary on average over a season. The mean DO eddy flux across the boundaries is nevertheless positive.

5 Discussion

We now discuss some limitations and implications of our results. While the model realistically simulates the main characteristics of the OMZ (position, intensity, average volume and seasonal variations), it still presents biases that could be influential on our results. In particular, and since the coastal domain is viewed here as a boundary of the OMZ, it is important to have a realistic mean DO concentration there. Compared to CARS, the simulated suboxic volume is, however, underestimated by ~ 6 %, and 85 % of this error can be attributed to the coastal domain (fringe of 3° from the coast). This bias could be due to several factors. Montes et al. (2014) observed variations of the suboxic volume in the order of 5 % when contrasting two simulations that used different oceanic open boundary conditions, which indicates a sensibility of the simulated OMZ to the physical parameters and to the representation of the equatorial current system. This bias could also be partly due to coastal sediments processes (DO demanding processes) that are not represented in our simulation. Using a similar configuration to the one used in the present study on the Namibian OMZ, Gutknecht et al. (2013a) observed that the differences between the simulated OMZ volume and CARS increased towards the shelf, which could be related to the exclusion of the DO demand from the sediments in the model. The role of benthic processes in constraining the DO demand has been studied in the northern California current system (Bianucci et al., 2012; Siedlecki et al., 2015), indicating that locally such processes might be essential to explain the hypoxic conditions. The inclusion of a sediment module in the current model setting is planned for future work to address this issue.

Another process that could contribute to the underestimation of the suboxic volume in the simulation is the higher mesoscale activity in the model compared to the observations (Fig. 1), which could in turn induce a higher ventilation of the OMZ in the simulation.

Besides other likely sources of biases related to an imperfect model setting (e.g., use of relatively low-resolution atmospheric forcings near the coast, absence of air/sea coupling at mesoscale, absence of coupling with benthic oxygen demand or consideration of N_2 fixation), another inherent limitation of our study is related with the difficulty in validating some aspects of the eddy field, in particular its vertical structure. This might be overcome in the future as the Argo coverage increases (cf. TPOS2020).

With the limitations of our regional modeling approach in mind, it is worthwhile to discuss some implications of our results. While previous studies have mostly focused on the role of the mean DO eddy flux in shaping the OMZ (Resplandy et al., 2012; Brandt et al., 2015; Bettencourt et al., 2015), we have documented here how the seasonal DO changes inside the OMZ are essentially controlled by the DO eddy flux at the OMZ limits, which means that the seasonality of the OMZ can be interpreted as resulting from a modulation of the mesoscale activity at seasonal timescales. We infer that the seasonality of the DO eddy flux is regulated by different physical processes depending on the region. At the coast, there is a constructive coupling between eddies resulting from the instability of the PUC peaking in austral winter and the enhanced DO along the coast resulting from an increased horizontal and vertical diffusion at the same season.

At the northern part of the OMZ, the DO eddy flux is related to the strong EKE around 5° S that peaks in austral winter. Despite the fact that the northern OMZ is embedded in the equatorial wave guide, it can be ruled out that the seasonal cycle in DO eddy flux is strongly linked to the intraseasonal long equatorial waves since the intraseasonal Kelvin wave activity tends to peak in austral summer (Illig et al., 2014). The boundary forcing sensitivity model experiments of Echevin et al. (2011) also suggest that the enhanced mesoscale activity observed off northern Peru during winter would be related to internal variability or local wind stress rather than being connected to the equatorial Kelvin wave activity. Whether or not the strong EKE found there results from the instability of the coastal currents system or of the EUC and the South Equatorial Current would need to be explored.

Regarding the southern boundary, it is interesting to note that the DO eddy-flux peaks in austral spring, 3 months later than at the northern boundary. A possible mechanism driving the local variability observed at the southern section is the generation of local baroclinic instability and vorticity input from wind stress curl as observed for the Califor-

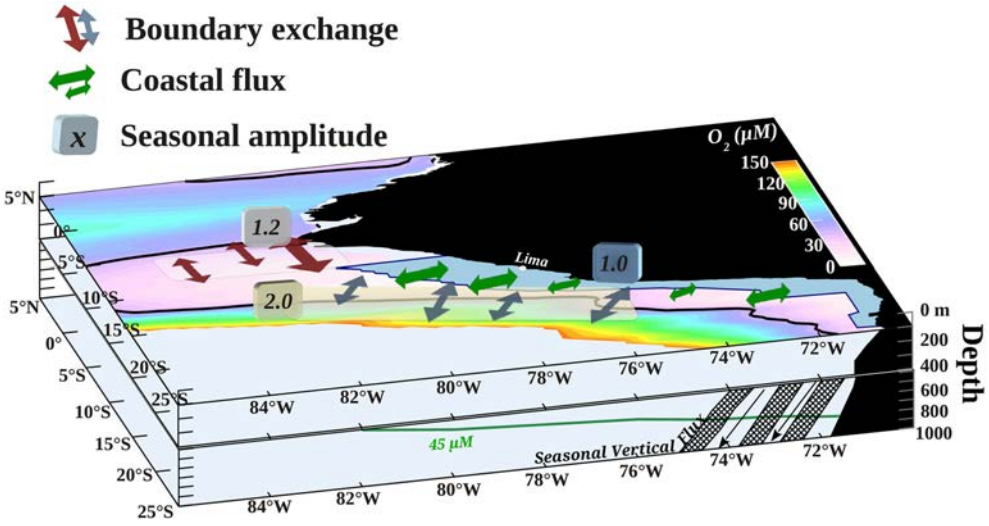

Figure 20. Schematic of the main processes driving the seasonal variability in the SEP OMZ: the DO eddy flux through the north–south boundaries and the DO flux that takes place at the coastal boundary of the OMZ. The coastal band limits are defined by the light blue shading adjacent to the coast. A scale of the seasonal amplitude of the eddy-driven DO flux at each OMZ boundary is indicated (units in cm s^{-1} μM). The mean DO concentration (color shading) and the position of the 45 μM isopleth (thick black contour) at 100 m depth are also represented. The vertical/offshore DO flux induced by the propagation of the annual ETRW across the 45 μM isopleth at 25° S is represented in the bottom panel.

nia system (Kelly et al., 1998). The southern section lies within the northeastern rim of the southeast Pacific anticyclone, and the peak in the seasonal DO eddy flux coincides with the reported intensity peak of the seasonal cycle of the Anticyclone, towards the end of the year (Rahn et al., 2015; Ancapichún and Garcés-Vargas, 2015). Therefore, the mesoscale activity in this region could be directly modulated by the winds. An additional source of intraseasonal (internal) variability in the currents field could be the interaction between the annual extratropical Rossby wave and the mean circulation (Dewitte et al., 2008; Qiu et al., 2013). The actual source of the eddy activity in this region would also deserve further investigation.

Our study also reveals that the most prominent propagating features in DO inside the OMZ at annual frequency is below ~ 300 m, where the seasonal DO flux follows approximately the theoretical WKB ray paths of the annual ETRW. From that depth, the seasonal variability in physical fluxes becomes 1 order of magnitude larger than that of the biogeochemical fluxes (Fig. 10c). This supports the observation that DO tends to behave as a passive tracer so that vertical displacements of the DO isopleths mimic those of the isotherms, inducing a seasonal DO flux that resembles the energy flux path of the ETRW. This mechanism adds a dimension to the understanding of the OMZ variability, considering that the vertical propagation of ETRW can take place at frequencies ranging from annual (Dewitte et al., 2008) to interannual (Ramos et al., 2008).

We now discuss some implications of our results with regards to current concerns around OMZ variability at long timescales. A recent study has suggested a trend in the OMZ towards expansion and intensification (Stramma et al., 2008), the forcing mechanism of which remains unclear (Stramma et al., 2010). Observations in the Pacific Ocean also suggest that the OMZ characteristics vary decadally (Stramma et al., 2008, 2010). Since decadal variability can manifest as a low-frequency modulation of the seasonal cycle, our study may provide guidance for investigating OMZ variability at long timescales. In particular, we show that the variability of the OMZ is not only related to the fluctuations of the equatorial currents system but also impacted by the subtropical variability. This view would link the OMZ low-frequency fluctuations to changes in the midlatitude circulation, in addition to variations in the equatorial Pacific (Stramma et al., 2010). Although we observe a larger amplitude of the seasonal cycle in the subtropics compared to the equatorial region, which could denote a preferential OMZ ventilation through the south, this result should be interpreted in light of a possible overestimation of the ventilation at that boundary in our simulation. We also note that the relative contribution of the mean DO flux and the DO eddy flux exhibit significant interannual fluctuations at the OMZ boundaries (not shown), which suggests that eddy-induced DO flux may not be the only key player for understanding long-term trend in the OMZ. It is interesting to note that, so far, it has been difficult to reconcile the observed trend in the OMZ with the trend simulated by the current generation of coupled models (Stramma et al., 2012), which has been attributed to biases in the mean circulation and inadequate remineralization representation (Cocco et al., 2013; Cabré et al., 2015). Our results

support the view that such discrepancy may partly originate from the inability of the low-resolution models to account for the DO eddy flux and its modulation. Regional modeling experiments also showed that eddy activity can be modulated at ENSO and decadal timescales (Combes et al., 2015; Dewitte et al., 2012). This issue would certainly require further investigation and could benefit from the experimentation with our coupled model platform. This is planned for future work.

Lastly, the seasonal changes in the OMZ evidenced in this work are associated with a seasonal change of the oxycline depth (and an oxycline intensity change; not shown), which can be considered a proxy for the production of greenhouse gases (CO_2 and N_2O) inside the OMZ (e.g., Paulmier et al., 2011; Kock et al., 2016). Our results suggest that the impact of the OMZ on the atmosphere through the production of climatically active gases, such as CO_2 and N_2O, would be seasonally damped during austral winter due to a deepening of the oxycline and a weakening of its intensity.

6 Summary and conclusions

A high-resolution coupled physical/biogeochemical model experiment is used to document the seasonal variability of the OMZ off Peru. The annual harmonic of DO reveals three main regions with enhanced amplitude or specific propagation characteristics, suggesting distinct dynamical regimes: (1) the coastal domain, (2) the offshore ocean below 400 m and (3) at the southern and northern boundaries. In the coastal portion of the OMZ, the seasonal variability is related to the local wind forcing and therefore follows to a large extent the paradigm of upwelling triggered productivity, followed by remineralization. It is shown in particular that DO peaks in austral winter, which is associated with horizontal and vertical diffusion induced by both the increase in baroclinic instability and intraseasonal wind activity. This is counterintuitive with regards to the seasonality of the alongshore upwelling favorable winds also peaking in austral winter, which would tend to favor the intrusion of deoxygenated waters from the open-ocean OMZ to the shelf. Instead, the coastal domain can be viewed as a source of DO in austral winter for the OMZ through offshore transport. The latter is induced by eddies that are triggered by the instabilities of the PUC. In the model, the offshore DO eddy flux has a marked seasonal cycle that is in phase with the seasonal cycle of the DO along the coast, implying that the coastal domain, viewed here as the eastern boundary of the OMZ, is a source of seasonal variability for the OMZ. This appears to operate effectively in the upper 300 m. Below that depth, the DO eddy flux is much reduced due to both a much weaker eddy activity and a very low DO concentration. In contrast, a mean seasonal DO flux is observed and exhibits propagating features reminiscent of the vertical propagation of energy associated with the annual ETRW.

In the upper 300 m, the OMZ seasonal variability is also associated with the DO eddy flux at the OMZ meridional boundaries where it is the most intense. We find that the seasonal cycle in DO eddy flux peaks in austral winter at the northern boundary, while it peaks a season later at the southern boundary. Additionally, the amplitude of the seasonal cycle in DO eddy flux is larger at the southern boundary than at the northern boundary. The schematic of Fig. 20 summarizes the main processes documented in this paper to explain the seasonality of the OMZ.

Acknowledgements. Oscar Vergara was supported by a doctoral scholarship from the National Chilean Research and Technology Council (CONICYT) through the program Becas Chile (scholarship 72130138). The authors are thankful for the financial support received from the Centre National d'Etudes Spatiales (CNES). Boris Dewitte acknowledges support from FONDECYT (project 1151185). Marcel Ramos acknowledges support from FONDECYT (project 1140845) and Chilean Millennium Initiative (NC120030). Oscar Pizarro acknowledges support from the FONDECYT 1121041 project and the Chilean Millennium Initiative (IC-120019). The authors thank the two anonymous reviewers for their constructive comments that helped improving the manuscript.

Edited by: K. Fennel
Reviewed by: two anonymous referees

References

Ancapichún, S. and Garcés-Vargas, J.: Variability of the Southeast Pacific Subtropical Anticyclone and its impact on sea surface temperature off north-central Chile, Cienc. Mar., 41, 1–20, doi:10.7773/cm.v41i1.2338, 2015.

Arévalo-Martínez, D., Kock, L. A., Löscher, C. R., Schmitz, R. A., and Bange, R. A.: Massive nitrous oxide emissions from the tropical South Pacific Ocean, Nat. Geosci., 8, 530–533, doi:10.1038/NGEO2469, 2015.

Bettencourt, J. H., López, C., Hernández-García, E., Montes, I., Sudre, J., Dewitte, B., Paulmier A., and Garçon, V.: Boundaries of the Peruvian Oxygen Minimum Zone shaped by coherent mesoscale dynamics, Nat. Geosci., 8, 937–940,, doi:10.1038/ngeo2570, 2015.

Bianchi, D., Dunne, J. P., Sarmiento, J. L., and Galbraith, E. D.: Data-based estimates of suboxia, denitrification, and N_2O production in the ocean and their sensitivities to dissolved O_2, Global Biogeochem. Cy., 26, GB2009, doi:10.1029/2011GB004209, 2012.

Bianucci, L., Fennel, K., and Denman, K. L.: Role of sediment denitrification in water column oxygen dynamics: comparison of the North American East and West Coasts, Biogeosciences, 9, 2673–2682, doi:10.5194/bg-9-2673-2012, 2012.

Brandt, P., Bange, H. W., Banyte, D., Dengler, M., Didwischus, S.-H., Fischer, T., Greatbatch, R. J., Hahn, J., Kanzow, T., Karstensen, J., Körtzinger, A., Krahmann, G., Schmidtko, S., Stramma, L., Tanhua, T., and Visbeck, M.: On the role of circulation and mixing in the ventilation of oxygen minimum zones with

a focus on the eastern tropical North Atlantic, Biogeosciences, 12, 489–512, doi:10.5194/bg-12-489-2015, 2015.

Cabré, A., Marinov, I., Bernardello, R., and Bianchi, D.: Oxygen minimum zones in the tropical Pacific across CMIP5 models: mean state differences and climate change trends, Biogeosciences, 12, 5429–5454, doi:10.5194/bg-12-5429-2015, 2015.

Cambon G., Goubanova, K., Marchesiello, P., Dewitte, B., Illig, S., and Echevin, V.: Assessing the impact of downscaled winds on a regional ocean model simulation of the Humboldt system, Ocean Model., 65, 11–24, 2013.

Chavez, F. P., Bertrand, A., Guevara-Carrasco, R., Soler, P., and Csirke, J.: The northern Humboldt Current System: Brief history, present status and a view towards the future, Prog. Oceanogr., 79, 95–105, 2008.

Chaigneau, A. and Pizarro, O.: Eddy characteristics in the eastern South Pacific, J. Geophys. Res., 110, C06005, doi:10.1029/2004JC002815, 2005.

Chaigneau, A., Eldin G., and Dewitte, B.: Eddy activity in the four major upwelling systems from satellite altimetry (1992–2007), Prog. Oceanogr., 83, 117–123, doi:10.1016/j.pocean.2009.07.012, 2009.

Cocco, V., Joos, F., Steinacher, M., Frölicher, T. L., Bopp, L., Dunne, J., Gehlen, M., Heinze, C., Orr, J., Oschlies, A., Schneider, B., Segschneider, J., and Tjiputra, J.: Oxygen and indicators of stress for marine life in multi-model global warming projections, Biogeosciences, 10, 1849–1868, doi:10.5194/bg-10-1849-2013, 2013.

Colas, F., McWillimas, J. C., Capet, X., and Kurian, J.: Heat balance and eddies in the Peru-Chile current system, Clim. Dynam., 39, 509–529, doi:10.1007/s00382-011-1170-6, 2012.

Combes, V., Hormazabal, S., and Di Lorenzo, E.: Interannual variability of the subsurface eddy field in the Southeast Pacific, J. Gephys. Res., 120, 4907–4924, doi:10.1002/2014JC010265, 2015.

Cornejo, M. and Farías, L.: Following the N_2O consumption in the oxygen minimum zone of the eastern South Pacific, Biogeosciences, 9, 3205–3212, doi:10.5194/bg-9-3205-2012, 2012.

Cornejo, M., Farías, L., and Paulmier, A.: Temporal variability in N_2O water content and its air-sea exchange in an upwelling area off central Chile (36° S), Mar. Chem., 101, 85–94, doi:10.1016/j.marchem.2006.01.004, 2006.

Czeschel, R., Stramma, L., Schwarzkopf, F. U., Giese, B. S., Funk, A., and Karstensen, J.: Middepth circulation of the eastern tropical South Pacific and its link to the oxygen minimum zone, J. Geophys. Res., 116, C01015, doi:10.1029/2010JC006565, 2011.

Czeschel, R., Stramma, L., Weller, R. A., and Fischer, T.: Circulation, eddies, oxygen, and nutrient changes in the eastern tropical South Pacific Ocean, Ocean Sci., 11, 455–470, doi:10.5194/os-11-455-2015, 2015.

daSilva A., Young, A. C., and Levitus, S.: Atlas of surface marine data 1994. Algorithms and procedures. vol. 1 Technical Report 6, US Department of Commerce, NOAA, NESDIS, 1994.

Dewitte B., Ramos, M., Echevin, V., Pizarro, O., and duPenhoat, Y.: Vertical structure variability in a seasonal simulation of a medium-resolution regional model simulation of the South Eastern Pacific, Prog. Oceanogr., 79, 120–137, 2008.

Dewitte, B., Illig, S.,Renault, L., Goubanova, K., Takahashi, K., Gushchina, D., Mosquera, K., and Purca, S.: Modes of covariability between sea surface temperature and wind stress intraseasonal anomalies along the coast of Peru from satellite observations (2000–2008), J. Geophys. Res., 116, C04028, doi:10.1029/2010JC006495, 2011.

Dewitte, B., Vazquez-Cuervo, J., Goubanova, K., Illig, S., Takahashi, K., Cambon, G., Purca, S., Correa, D., Gutiérrez, D., Sifeddine, A., and Ortlieb, L.: Change in El Nino flavours over 1958–2008: Implications for the long-term trend of the upwelling off Peru, Deep-Sea Res. Pt. II, 77–80, 143–156, doi:10.1016/j.dsr2.2012.04.011, 2012.

Dunn J. R. and Ridgway, K. R.: Mapping ocean properties in regions of complex topography, Deep-Sea Res. Pt. I, 49, 591–604, 2002.

Dunne, J. P., Armstrong, R. A., Gnanadesikan, A., and Sarmiento, J. L.: Empirical and mechanistic models for the particle export ratio, Global Biogeochem. Cy., 19, GB4026, doi:10.1029/2004gb002390, 2005.

Duteil, O. and Oschlies, A.: Sensitivity of simulated extent and future evolution of marine suboxia to mixing intensity, Geophys. Res. Lett., 38, L06607, doi:10.1029/2011GL046877, 2011.

Duteil, O., Schwarzkopf, F. U., Böning, C. W., and Oschlies, A.: Major role of the equatorial current system in setting oxygen levels in the eastern tropical Atlantic Ocean: A high-resolution model study, Geophys. Res. Lett., 41, 2033–2040, doi:10.1002/2013GL058888, 2014.

Echevin, V., Aumont, O., Ledesma, J., and Flores, G.: The seasonal cycle of surface chlorophyll in the Peruvian upwelling system: A modelling study, Progr. Oceanogr., 79, 2–4, 167–176, 2008.

Echevin, V., Colas, F., Chaigneau, A., and Penven, P.: Sensitivity of the Northern Humboldt Current System nearshore modeled circulation to initial and boundary conditions, J. Geophys. Res., 116, C07002, doi:10.1029/2010JC006684, 2011.

Eliassen, A. and Palm, E.: On the transfer of energy in stationary mountain waves, Geofys. Publ., 22, 1–23, 1960.

Farías, L., Paulmier, A., and Gallegos, M.: Nitrous oxide and N-nutrient cycling in the oxygen minimum zone off northern Chile, Deep-Sea Res. Pt. I, 54, 164–180, doi:10.1016/j.dsr.2006.11.003, 2007.

Fuenzalida, R., Schneider, W., Garces-Vargas, J., Bravo, L., and Lange, C.: Vertical and horizontal extension of the oxygen minimum zone in the eastern South Pacific Ocean, Deep-Sea Res. Pt. II, 56, 992–1003, doi:10.1016/j.dsr2.2008.11.001, 2009.

García, H. E. and Gordon, L. I.: Oxygen solubility in seawater – better fitting equations, Limnol. Oceanogr., 37, 1307–1312, 1992.

Goubanova, K., Echevin, V., Dewitte, B., Codron, F., Takahashi, K., Terray, P., and Vrac, M.: Statistical downscaling of sea-surface wind over the Peru–Chile upwelling region: diagnosing the impact of climate change from the IPSL-CM4 model, Clim. Dynam., 36, 1365, doi:10.1007/s00382-010-0824-0, 2011.

Gruber, N.: The marine nitrogen cycle: Overview of distributions and processes, in: Nitrogen in the marine environment, second Edn., edited by: Capone, D. G., Bronk, D. A., Mulholland, M. R., and Carpenter, E. J., Elsevier, Amsterdam, 1–50, 2008.

Gruber, N., Lachkar, Z., Frenzel, H., Marchesiello, P., Münnich, M., McWilliams, J. C., Nagai, T., and Plattner, G. K.: Eddy-induced reduction of biological production in eastern boundary upwelling systems, Nat. Geosci., 4, 787–792, doi:10.1038/ngeo1273, 2011.

Gutiérrez, D., Enriquez, E., Purca, S., Quipuzcoa, L., Marquina, R., Flores, G., and Graco, M.: Oxygenation episodes on the conti-

nental shelf of central Peru: remote forcing and benthic ecosystem response, Prog. Oceanogr., 79, 177–189, 2008.

Gutiérrez, D., Bouloubassi, I., Sifeddine, A., Purca, S., Goubanova, K., Graco, M., Field, D., Mejanelle, L., Velazco, F., Lorre, A., Salvatteci, R., Quispe, D., Vargas, G., Dewitte, B., and Ortlieb, L.: Coastal cooling and increased productivity in the main upwelling zone off Peru since the mid-twentieth century, Geophys. Res. Lett., 38, L07603, doi:10.1029/2010GL046324, 2011.

Gutknecht, E., Dadou, I., Le Vu, B., Cambon, G., Sudre, J., Garçon, V., Machu, E., Rixen, T., Kock, A., Flohr, A., Paulmier, A., and Lavik, G.: Coupled physical/biogeochemical modeling including O_2-dependent processes in the Eastern Boundary Upwelling Systems: application in the Benguela, Biogeosciences, 10, 3559–3591, doi:10.5194/bg-10-3559-2013, 2013a.

Gutknecht, E., Dadou, I., Marchesiello, P., Cambon, G., Le Vu, B., Sudre, J., Garçon, V., Machu, E., Rixen, T., Kock, A., Flohr, A., Paulmier, A., and Lavik, G.: Nitrogen transfers off Walvis Bay: a 3-D coupled physical/biogeochemical modeling approach in the Namibian upwelling system, Biogeosciences, 10, 4117–4135, doi:10.5194/bg-10-4117-2013, 2013b.

Henley, B. J., Gergis, J., Karoly, D. J., Power, S. B., Kennedy, J., and Folland, C. K.: A Tripole Index for the Interdecadal Pacific Oscillation, Clim. Dynam., 45, 3077–3090, doi:10.1007/s00382-015-2525-1, 2015.

Henson, S. A., Sanders, R., and Madsen, E.: Global patterns in efficiency of particulate organic carbon export and transfer to the deep ocean, Global Biogeochem. Cy., 26, GB1028, doi:10.1029/2011gb004099, 2012.

Illig, S., Dewitte, B., Goubanova, K., Cambon, G., Boucharel, J., Monetti, F., Romero, C., Purca, S., and Flores, R.: Forcing mechanisms of intraseasonal SST variability off central Peru in 2000–2008, J. Geophys. Res., 119, 3548–3573, doi:10.1002/2013JC009779, 2014.

Karstensen, J., Stramma, L., and Visbeck, M.: Oxygen minimum zones in the eastern tropical Atlantic and Pacific oceans, Progr. Oceanogr., 77, 331–350, 2008.

Karstensen, J., Fiedler, B., Schütte, F., Brandt, P., Körtzinger, A., Fischer, G., Zantopp, R., Hahn, J., Visbeck, M., and Wallace, D.: Open ocean dead zones in the tropical North Atlantic Ocean, Biogeosciences, 12, 2597–2605, doi:10.5194/bg-12-2597-2015, 2015.

Kelly, K., Beardsley, R., Limeburner, R., and Brink, K.: Variability of the near-surface eddy kinetic energy in the California Current based on altimetric, drifter and moored data, J. Geophys. Res., 103, 13067–13083, 1998.

Kock, A., Arévalo-Martínez, D. L., Löscher, C. R., and Bange, H. W.: Extreme N_2O accumulation in the coastal oxygen minimum zone off Peru, Biogeosciences, 13, 827–840, doi:10.5194/bg-13-827-2016, 2016.

Large, W. G., McWilliams, J. C., and Doney, S. C.: Oceanic vertical mixing: A review and a model with a nonlocal boundary layer parameterization, Rev. Geophys., 32, 363–403, doi:10.1029/94RG01872, 1994.

Law, C. S., Brévière, E., de Leeuw, G., Garçon, V., Guieu, C., Kieber, D. J., Kontradowitz, S., Paulmier, A., Quinn, P. K., Saltzman, E. S., Stefels, J., and von Glasow, R.: Evolving research directions in Surface Ocean – Lower Atmosphere (SOLAS) science, Environ. Chem., 10, 1–16, doi:10.1071/EN12159, 2013.

Libes, S. M.: An Introduction to Marine Biogeochemistry, John Wiley and Sons, New York, 734 pp., 1992.

Llanillo, P. J., Karstensen, J., Pelegrí, J. L., and Stramma, L.: Physical and biogeochemical forcing of oxygen and nitrate changes during El Niño/El Viejo and La Niña/La Vieja upper-ocean phases in the tropical eastern South Pacific along 86° W, Biogeosciences, 10, 6339–6355, doi:10.5194/bg-10-6339-2013, 2013.

Luyten, J. R., Pedlosky, J., and Stommel, H.: The ventilated thermocline, J. Phys. Oceanogr., 13, 292–309, 1983.

McClain, C. R., Cleave, M. L., Feldman, G. C., Gregg, W. W., Hooker, S. B., and Kuring, N.: Science quality SeaWiFS data for global biosphere research, Sea Technol., 39, 10–16, 1998.

Montes, I., Colas, F., Capet, X., and Schneider, W.: On the pathways of the equatorial subsurface currents in the Eastern Equatorial Pacific and their contributions to the Peru-Chile Undercurrent, J. Geophys. Res., 115, C09003, doi:10.1029/2009JC005710, 2010.

Montes, I., Dewitte, B., Gutknecht, E., Paulmier, A., Dadou, I., Oschlies, A., and Garçon, V.: High-resolution modeling of the Eastern Tropical Pacific oxygen minimum zone: Sensitivity to the tropical oceanic circulation, J. Geophys. Res.-Oceans, 119, 5515–5532, doi:10.1002/2014JC009858, 2014.

Morales, C. E., Hormazabal, S. E., and Blanco, J.: Interannual variability in the mesoscale distribution of the depth of the upper boundary of the oxygen minimum layer off northern Chile (18–24S): Implications for the pelagic system and biogeochemical cycling, J. Mar. Res., 57, 909–932, doi:10.1357/002224099321514097, 1999.

Morel, A. and Berthon, J. F.: Surface pigments, algal biomass profiles, and potential production of euphotic layer: Relationship reinvestigated in view of remote-sensing applications, Limnol. Oceanogr., 34, 1545–1562, 1989.

Nagai, T., Gruber, N., Frenzel, H., Lachkar, Z., McWilliams, J. C., and Plattner, G.-K.: Dominant role of eddies and filaments in the offshore transport of carbon and nutrients in the California Current System, J. Geophys. Res.-Oceans, 120, 5318–5341, doi:10.1002/2015JC010889, 2015.

Nerem, R. S., Chambers, D. P., Choe, C., and Mitchum, G. T.: Estimating mean sea level change from the TOPEX and Jason altimeter missions, Mar. Geod., 33, Supplement 1, 435–446, 2010.

O'Reilly, J. E., Maritorena, S., Siegel, D., O'Brien, M. O., Toole, D., Mitchell, B. G., Kahru, M., Chavez, F., Strutton, P. G., Cota, G. F., Hooker, S. B., McClain, C., Carder, K., Muller-Karger, F., Harding, L., Magnuson, A., Phinney, D., Moore, G., Aiken, J., Arrigo, K. R., Letelier, R. M., and Culver, M.: Ocean chlorophyll a algorithms for SeaWiFS, OC2, and OC4: Version 4, in: SeaWiFS Postlaunch Calibration and Validation Analyses, Part 3, NASA Tech. Memo 2000–206892, vol. 11, edited by: Hooker, B., and Firestone, E. R., NASA, Goddard Space Flight Center, Greenbelt, Maryland, 9–19, 2000.

Paulmier, A. and Ruiz-Pino, D.: Oxygen minimum zones (OMZs) in the modern ocean, Prog. Oceanogr., 80, 3–4, 113–128, doi:10.1016/j.pocean.2008.08.001, 2009.

Paulmier, A., Ruiz-Pino, D., Garçon, V., and Farías, L.: Maintaining of the East South Pacific Oxygen Minimum Zone (OMZ) off Chile, Geophys. Res. Lett., 33, L20601, doi:10.1029/2006GL026801, 2006.

Paulmier, A., Ruiz-Pino, D., and Garçon, V.: The Oxygen Minimum Zone (OMZ) off Chile as intense source of CO_2 and N_2O, Cont. Shelf Res., 28, 2746–2756, 2008.

Paulmier, A., Ruiz-Pino, D., and Garçon, V.: CO_2 maximum in the oxygen minimum zone (OMZ), Biogeosciences, 8, 239–252, doi:10.5194/bg-8-239-2011, 2011.

Penven, P., Echevin, V., Pasapera, J., Colas, F., and Tam, J.: Average circulation, seasonal cycle, and mesoscale dynamics of the Peru Current System: a modeling approach, J. Geophys. Res., 110, C10021, doi:10.1029/2005JC002945, 2005.

Pizarro, O., Shaffer, G., Dewitte, B., and Ramos, M.: Dynamics of seasonal and interannual variability of the Peru-Chile Undercurrent, Geophys. Res. Lett., 29, 1581, doi:10.1029/2002GL014790, 2002.

Prince, E. D. and Goodyear, C. P.: Hypoxia-based habitat compression of tropical pelagic fishes, Fish. Oceanogr., 15, 451–464, doi:10.1111/j.1365-2419.2005.00393.x, 2006.

Qiu, B., Chen, S., and Sasaki, H.: Generation of the North Equatorial Undercurrent jets by triad baroclinic Rossby wave interactions, J. Phys. Oceanogr., 43, 2682–2698, doi:10.1175/JPO-D-13-099.1, 2013.

Rahn, D., Rosenblüth, B., and Rutllant, J.: Detecting Subtle Seasonal Transitions of Upwelling in North-Central Chile, J. Phys. Oceanogr., 45, 854–867, 2015.

Ramos, M., Dewitte, B., Pizarro, O., and Garric, G.: Vertical propagation of extratropical Rossby waves during the 1997–1998 El Niño off the west coast of South America in a medium-resolution OGCM simulation, J. Geophys. Res., 113, C08041, doi:10.1029/2007JC004681, 2008.

Resplandy, L., Lévy, M., Bopp, L., Echevin, V., Pous, S., Sarma, V. V. S. S., and Kumar, D.: Controlling factors of the oxygen balance in the Arabian Sea's OMZ, Biogeosciences, 9, 5095–5109, doi:10.5194/bg-9-5095-2012, 2012.

Reynolds, R. W., Smith, T. M., Liu, C., Chelton, D. B., Casey, K. S., and Schlax, M. G.: Daily high-resolution blended analyses for sea surface temperature, J. Climate, 20, 5473–5496, 2007.

Richter, I.: Climate model biases in the eastern tropical oceans: causes, impacts and ways forward, WIREs Clim. Change, 6, 345–358, doi:10.1002/wcc.338, 2015.

Ridgway K. R., Dunn, J. R., and Wilkin, J. L.: Ocean interpolation by four-dimensional least squares – Application to the waters around Australia, J. Atmos. Ocean. Tech., 19, 1357–1375, 2002.

Shchepetkin, A. F. and McWilliams, J. C.: The regional oceanic modeling system: a split-explicit, free-surface, topography-following-coordinate ocean model, Ocean Model., 9, 347–404, 2005.

Shchepetkin, A. F. and McWilliams, J. C.: Correction and commentary for "Ocean forecasting in terrain-following coordinates: Formulation and skill assessment of the regional ocean modeling system" by Haidvogel et al., J. Comp. Phys., 227, 3595–3624, 2009.

Siedlecki, S. A., Banas, N. S., Davis, K. A., Giddings, S., Hickey, B. M., MacCready, P., Connolly, T., and Geier, S.: Seasonal and interannual oxygen variability on the Washington and Oregon continental shelves, J. Geophys. Res.-Oceans, 120, 608–633, doi:10.1002/2014JC010254, 2015.

Stramma, L., Johnson, G. C., Sprintall, J., and Mohrholz, V.: Expanding oxygen-minimum zones in the tropical oceans, Science, 320, 655–658, 2008.

Stramma, L., Johnson, G. C., Firing, E., and Schmidtko, S.: Eastern Pacific oxygen minimum zones: Supply paths and multidecadal changes, J. Geophys. Res., 115, C09011, doi:10.1029/2009JC005976, 2010.

Stramma, L., Oschlies, A., and Schmidtko, S.: Mismatch between observed and modeled trends in dissolved upper-ocean oxygen over the last 50 yr, Biogeosciences, 9, 4045–4057, doi:10.5194/bg-9-4045-2012, 2012.

Stramma, L., Bange, H. W., Czeschel, R., Lorenzo, A., and Frank, M.: On the role of mesoscale eddies for the biological productivity and biogeochemistry in the eastern tropical Pacific Ocean off Peru, Biogeosciences, 10, 7293–7306, doi:10.5194/bg-10-7293-2013, 2013.

Stramma, L., Weller, R. A., Czeschel, R., and Bigorre, S.: Eddies and an extreme water mass anomaly observed in the eastern south Pacific at the Stratus mooring, J. Geophys. Res.-Oceans, 119, 1068–1083, 2014.

Thomsen, S., Kanzow, T., Krahmann, G., Greatbatch, R. J., Dengler, M., and Lavik, G.: The formation of a subsurface anticyclonic eddy in the Peru-Chile Undercurrent and its impact on the near-coastal salinity, oxygen, and nutrients distributions, J. Geophys. Res.-Oceans, 121, 476–501, doi:10.1002/2015JC010878, 2016. Thomsen, S., Kanzow, T., Krahmann, G., Greatbatch, R. J., Dengler, M., and Lavik, G.: The formation of a subsurface anticyclonic eddy in the Peru-Chile Undercurrent and its impact on the near-coastal salinity, oxygen, and nutrients distributions, J. Geophys. Res.-Oceans, 121, 1, 476–501, doi:10.1002/2015JC010878, 2016.

Résumé de l'article *Seasonal variability of the oxygen minimum zone off Peru in a high-resolution coupled model*

Le Pacifique Sud-Est est reconnu comme l'une des régions les plus productives au monde en terme de production primaire dans la couche euphotique. Sous la surface, la région au large du Pérou abrite l'une des zones de minimum d'oxygène (OMZ[1]) la plus étendue au monde, qui a fait l'objet d'importants programmes de recherche depuis la dernière décennie. Malgré ces efforts, le volume de données acquis dans cette région reste insuffisant pour bien comprendre la dynamique qui contrôle les variations de l'OMZ. De plus, les interactions biogéochimiques complexes qui ont lieu dans cette zone et la présence de forts gradient biogéochimiques et d'une dynamique océanique non-linéraire rendent l'étude de la variabilité de l'OMZ difficile. Dans cette étude, nous utilisons un modèle couplé physique/biogéo-chimique de haute résolution pour étudier les variations saisonnières de l'OMZ. En se focalisant sur la caractérisation du cycle saisonnier de l'oxygène dissout (DO[2]) induit par les structures de mésoéchelle (flux turbulents d'oxygène), à travers les différentes frontières de l'OMZ. Du à son impact significatif sur le flux total d'oxygène, nous prenons aussi en compte les variations saisonnières de la région côtière, que nous considérons comme la frontière Est de l'OMZ. Les résultats indiquent que les variations saisonnières de l'OMZ peuvent s'interpréter à travers la modulation saisonnière de l'activité mésoéchelle. Malgré la remontée des eaux suboxiques ayant lieu pendant le pic de la saison d'upwelling, les concentrations de DO sur la plate-forme continentale sont maximales durant cette période le long des côtes Péruviennes. Le maximum saisonnier de DO a principalement lieu dans le coeur du sous-courant de Pérou-Chili (PUC[3]) pendant l'hiver austral, résultant du mélange associé à l'augmentation de l'activité intra-saisonnière du vent de surface et aux instabilités baroclines du PUC. Cette variabilité montre que l'océan côtier se comporte comme une source d'oxygène pour l'intérieur de l'OMZ pendant l'hiver austral, lié aux flux d'oxygène vers l'Ouest qui sont induits par l'activité mésoéchelle. Au large des cotes Péruviennes, l'OMZ peut être divisée verticalement en deux zones. La première s'étend entre la limite supérieure de l'OMZ et 400 m de profondeur, où les flux turbulents d'oxygène associés à l'activité de mésoéchelle sont plus importants que le flux advectif total d'oxygène. Dès 400 m de profondeur, le flux saisonnier d'oxygène montre des caractéristiques de propagation verticale/vers l'Ouest rappelant les trajectoires théoriques du flux d'énergie associé à l'onde de Rossby extratropicale à l'échelle

[1] De l'anglais *Oxygen Minimum Zone*.
[2] De l'anglais *Dissolved Oxygen*.
[3] De l'anglais *Peru Undercurrent*.

annuelle. Aux frontières océaniques de l'OMZ, le maximum saisonnier du flux turbulent d'oxygène à lieu pendant l'hiver (printemps) austral à travers la frontière Nord (Sud) de l'OMZ. Dans le modèle, l'amplitude du cycle saisonnier du flux d'oxygène à travers la frontière Sud est 70% plus important qu'à travers la frontière Nord. Nos résultats suggèrent l'existence de différents régimes de ventilation à l'échelle saisonnière, liés à chacune des frontières de l'OMZ. La discussion de nos résultats se fait dans un contexte d'étude de la variabilité de l'OMZ à long-terme.

4.3 Synthesis

The purpose of this chapter was to document how the fluctuations of the subthermocline circulation at seasonal timescale relate to the seasonal ventilation of the OMZ.

The OMZ results from complex physical-biogeochemical interactions (Karstensen et al., 2008), which reflects in the different mechanisms that contribute to its seasonality. Our analyses first evidenced that two regimes define the phenology of the OMZ. Over the shelf, along the coast, the seasonal variability of the OMZ results from the combined effect of the fluctuations in the coastal circulation system, and the annual cycle of organic matter production/degradation. On the other hand, the seasonality of the offshore OMZ is essentially controlled by the fluctuations of the circulation. This dichotomy motivated us to address the two regions separately.

Our results indicate that the seasonality of the coastal OMZ emerges from the response of the coastal circulation system to the seasonal cycle of the upwelling-favorable alongshore wind, that triggers a primary production bloom and subsequent remineralization. We evidenced that the seasonal peak in austral winter is related to an increase in vertical/horizontal diffusion, that involves an offshore transport of oxygen during this period. We interpret this result as a mechanism that allows for the seasonal ventilation of the OMZ from the coast during austral winter.

In the meridional boundaries of the OMZ, we observe that the OMZ seasonality is controlled by the fluctuations of the circulation, with eddies driving a seasonal ventilation of the OMZ in the upper $300m$. Below this depth, the seasonal variations of the OMZ (amplitude and phase) show offshore/vertical propagating features, with a very similar pattern than the annual extra-tropical Rossby wave.

Chapter 5

Conclusions and Perspectives

In the present thesis work, we investigated the variability of the intermediate to deep circulation of the Southeastern Pacific (SEP) at different timescales, focusing on the circulation fluctuations associated with the propagation of the extra-tropical Rossby wave (ETRW) and the mesoscale activity. To this extent, we adopted a modeling approach that allowed us to document the circulation variability from the coast to the abyssal offshore region.

The oceanic variability in the SEP results from a large number of forcing mechanisms, both local and remote, which interplay to shape and modulate the circulation. On the one hand, the local influence of the alongshore wind stress influences the coastal circulation in the shallow layers, while the coastal waveguide links the different climatic modes of variability of the equatorial Pacific with the coastal and offshore components of the SEP circulation. These characteristics motivated the choice of approaching the study of the SEP circulation through the analysis of the variability related to each forcing mechanism. Within this general framework, we first addressed the problem of the circulation variability related to the ENSO events, which correspond to the most prominent climatic mode of variability in the equatorial Pacific. The surface variability related to these events is fairly well documented along the South American coast, although at the same time this region corresponds to one of the ocean basins with the lowest number subsurface observations, which greatly difficults documenting and analyzing the vertical structure of the circulation variability. Using a medium-resolution OGCM, Ramos et al. (2008) first evidenced that the circulation anomalies observed in the SEP during the 1997/98 El Niño event propagated vertically as ETRW. In this regard, our results with respect to the subthermocline interannual variability can be seen as a generalization of the results of Ramos et al. (2008), which considered only one event (although it corresponds to the strongest ENSO event in the modern observations). The time range of our study encompasses 2 events that have been characterized as extraordinary El Niño events (EP events; Takahashi et al.,

2011), which account for more than 80% of the interannual energy flux into the subthermocline circulation in the SEP (along the theoretical WKB ray-paths). This highlights the profound implications that the climatic variability in the tropical Pacific has for the circulation in the SEP, whose effects are not restricted to the coastal circulation but propagate efficiently toward the abyssal ocean through wave dynamics.

The tropical Pacific also experiences significant variability at decadal timescale, which partly reflects as a modulation of the climatic variability at shorter timescale, and in particular the modulation of the ENSO modes (Ogata et al., 2013). Our results indicate that the decadal variability of the tropical Pacific also propagates into the SEP subthermocline, following the theoretical trajectories defined by the WKB ray-paths. For a given latitude, the energy beams related to the decadal energy flux extend farther off-shore in comparison to the interannual energy flux.

In principle, the vertical energy flux induced by the propagation of ETRW corresponds to an adiabatic process, given that it only acts to conservatively rearrange the energy field. However, there could be energy losses along the propagation trajectory, that would traduce in a diffusion/dissipation of energy. Our results indicate that the amplitude of the energy flux does not remain constant but that instead decreases along the wave propagation trajectory, and that this energy dissipation is associated with a vertical diffusion of heat into the deep ocean. In particular, there is a vertical heat diffusion associated with the strong El Niño events and with the decadal modulation of the interannual variability, that follows the theoretical WKB trajectories. This indicates that the energy discharge of the tropical Pacific onto the SEP subthermocline at interannual and decadal timescales entails a vertical heat diffusion.

Contrasting the results presented in *Chapter 3* against the previous estimations of vertical energy flux evidences the sensitivity of this process to the spatial resolution of the model used to document it. In particular, our work contrasts against the energy flux results obtained by Ramos et al. (2008), which were limited by the use of a medium-resolution OGCM. Although that work clearly evidences the westward/vertical energy flux induced by the propagation of the ETRW (supported by the interpretation using linear wave theory), the vertical structure of the energy beams is poorly resolved, which prevents performing a diagnosis of its dissipation. In addition, the simulation used in that study only spans 10 years and encompasses only one El Niño event (even though is the strongest event in modern records). This could result detrimental for the interannual energy flux estimations as hinted by the magnitude differences in energy flux estimations between Ramos et al. (2008) and our study (nearly one order of magnitude). The use of a high-resolution simulation spanning the second half of the XXth century allowed us not only to document the vertical structure of the energy flux and

its magnitude, but also its vertical dissipation toward the deep ocean and thus the potential influence of this process on the abyssal accumulation of heat in the mid-latitudes of the SEP, which could in turn take part in the planetary energy balance.

In the second part of the present thesis work, we concentrated our efforts on documenting the circulation variability in the SEP at seasonal timescales, from the perspective of the interactions between the circulation fluctuations and the OMZ, with a particular focus on the processes that are influential for its ventilation at this timescale. Although the role of the OMZ in the climate system and in the habitat compression of one of the most exploited ecosystems in the ocean are well identified (Kock et al., 2016; Paulmier et al., 2011; Prince and Goodyear, 2006), significant advances with respect to the understanding of its dynamics have been only achieved recently. In this context, the second part of the present thesis work is motivated by the current knowledge gaps on the OMZ dynamics and variability at different timescales. In this sense, a comprehensive understanding of the processes that drive the seasonal OMZ variability is considered a prerequisite for interpreting longer timescales of variability.

While the subsurface circulation variability at interannual to decadal timescales in the SEP is largely influenced by the variability that takes place in the tropical Pacific, the seasonal fluctuations of the circulation in the SEP are determined by both local ocean-atmosphere interactions and the remote influence of the tropical Pacific (Aguirre et al., 2012; Penven et al., 2005; Pizarro et al., 2002).

Previous studies evidenced that mesoscale eddies play an important role in shaping the OMZ (cf. Bettencourt et al., 2015), which leads to think that these structures may also intervene in the OMZ variability. Our results show that in fact the OMZ variability results from a joint contribution between the biogeochemical processes (reduced in our study to a production and consumption of oxygen) and the circulation variability. However, we notice that the degree of importance attached to each process varies across the OMZ. Along the coast, the seasonality of the OMZ results from the response of the coastal circulation system to the seasonal variations of the local alongshore wind stress, which triggers a primary production bloom in the euphotic zone and the associated organic matter remineralization in the subsurface. Our results indicate that the seasonal peak in the coastal OMZ ventilation that takes place in austral winter relates to a seasonal increase in the oxygen eddy transport. This oxygen transport is directed toward the less oxygenated region of the OMZ located offshore, meaning that the coastal region behaves as an oxygen source for the OMZ at seasonal timescales.

Our results evidence that the seasonality of the offshore OMZ, where the oxygen production is rather weak (Pennington et al., 2006), is essentially controlled by the fluctuations of the circulation. In particular, we observe that the seasonal oxygen changes

are induced by an eddy flux over the upper 300 m, that drives a seasonal ventilation through the OMZ boundaries. The vertical structure of the oxygen eddy flux is consistent with the vertical structure of the mesoscale structures observed in the region (Chaigneau et al., 2011), with the highest amplitude in the upper 300 m. Below that depth, the amplitude of the eddy-induced oxygen flux is low, and the annual variations of the OMZ (amplitude and phase of the annual harmonic) evidence a vertical/offshore propagating pattern that matches the structure of the energy beams associated with the annual extra-tropical Rossby wave.

The results presented here also suggest that the processes involved in the seasonal variations of the OMZ could influence its ventilation at lower frequencies of variability, and in this sense the critical importance of the eddy fluxes evidenced in *Chapter 4* would need to be addressed for longer timescales. It has been recently suggested that the eddy field in the SEP undergoes a significant modulation at interannual timescales, in relationship with the strong ENSO events in the tropical Pacific (Combes et al., 2015). In particular, a decrease of the water volume transported offshore by subsurface eddies has been observed during strong El Niño events (e.g. 1982-1983, 1997-1998; Combes et al., 2015), which is related to a relaxation of the isopycnals along the coast and a weakened baroclinic instability during those periods. The relevance that the interannual variability of the SEP circulation has for the ventilation processes evidenced here would be a potential next step for research on the OMZ dynamics.

Although the simulation used to characterize the seasonality of the OMZ ventilation in *Chapter 4* only spans 8 years, the eddy oxygen flux at the OMZ boundaries presents a marked interannual variability (Fig. 5.1). This calls for assessing the sensitivity of the OMZ ventilation mechanisms to the interannual variability of the circulation, and in this sense a possible direction for future research could be to investigate the impact of the different types of El Niño events on the OMZ ventilation, considering that each type of event is associated with a different modulation of the SEP circulation characteristics (e.g. during CP events the coastal thermocline in the SEP is very close to its climatological mean, but it deepens several tens of meters during the EP events; Dewitte et al., 2012). This question acquires further relevance in the context of the currently long-term expansion of the OMZ, which mechanisms are not yet elucidated. Recently, Dewitte et al. (2012) suggested that the increased occurrence of the CP El Niño events rectifies on the mean circulation off Peru, impacting on the vertical structure of the coastal currents system and reducing the baroclinic instability, which in turn leads to a reduction of the mean eddy kinetic energy field. In the light of the mechanisms evidenced in *Chapter 4*, this rectification of the mean state could also reflect on the long-term ventilation of the OMZ. In this regard, a possible work hypothesis would be that

the long-term decrease in the eddy activity (indirectly reflected by the EKE decrease reported by Dewitte et al. (2012)), would translate as a reduction of the OMZ ventilation rates. This scenario would then favor an accumulation of oxygen depleted waters and eventually, an expansion of the OMZ. To verify the validity of this hypothesis, a long-term coupled physical/biogeochemical simulation should be used. It should then be verified that the ventilation mechanisms observed for the seasonal periods are also significant for the OMZ ventilation at longer timescales, before looking to document their long-term trend.

The mean oxygen flux also evidences an interannual modulation below 300m (Fig. 5.1) which suggests that there is a response of the lower OMZ related to the ETRW at this timescale. The magnitude of the energy flux associated with the ETRW at interannual timescale is higher than the one related to the annual ETRW (*Chapters 3 and 4*). In this sense, the interannual modulation of the OMZ by this mechanism could significantly influence the oxygen flux from the coast towards the OMZ core, and therefore modulate the oxygenation of the inner and lower parts of the OMZ. Whether or not this process is influential for the OMZ at interannual timescale could be addressed using a long-term coupled simulation as mentioned above, conducting analyses of the oxygen fluxes similar to the ones performed in *Chapter 4*. In this context, addressing the variability of the lower part of the OMZ for longer timescales could be an additional objective of such a study, given that the ETRW also induces an energy flux at decadal timescale that propagates in region below 300m (*Chapter 3*). Future work on the OMZ using similar coupled simulations as the one used here should also include a sediments module, in order to account for its contribution to the oxygen budget. In general, biogeochemical processes that take place at the water column/sediments interface can be considered as a net sink for the oxygen budget (associated with the remineralization of organic matter), so adding such a module to our coupled platform should in principle increase the OMZ volume. This improvement has the potential to solve, at least in part, the slight bias in the OMZ volume observed during our experiment (*Chapter 4*).

The results obtained during the present thesis work also evidenced the methodological challenges in the observation of the physical mechanisms related to the variability of the intermediate to deep circulation in the SEP. In particular, the sparse vertical/temporal resolution of the observational data sets presently available prevent documenting the vertical structure of the circulation variability induced by the propagation of the ETRW. Despite that the spatial subsurface coverage in the SEP is still insufficient to appropriately study the characteristics of the vertical ETRW propagation (which also prevented the validation of the vertical propagation diagnosed from the simulations), long-term products derived from ARGO observations at the floats'

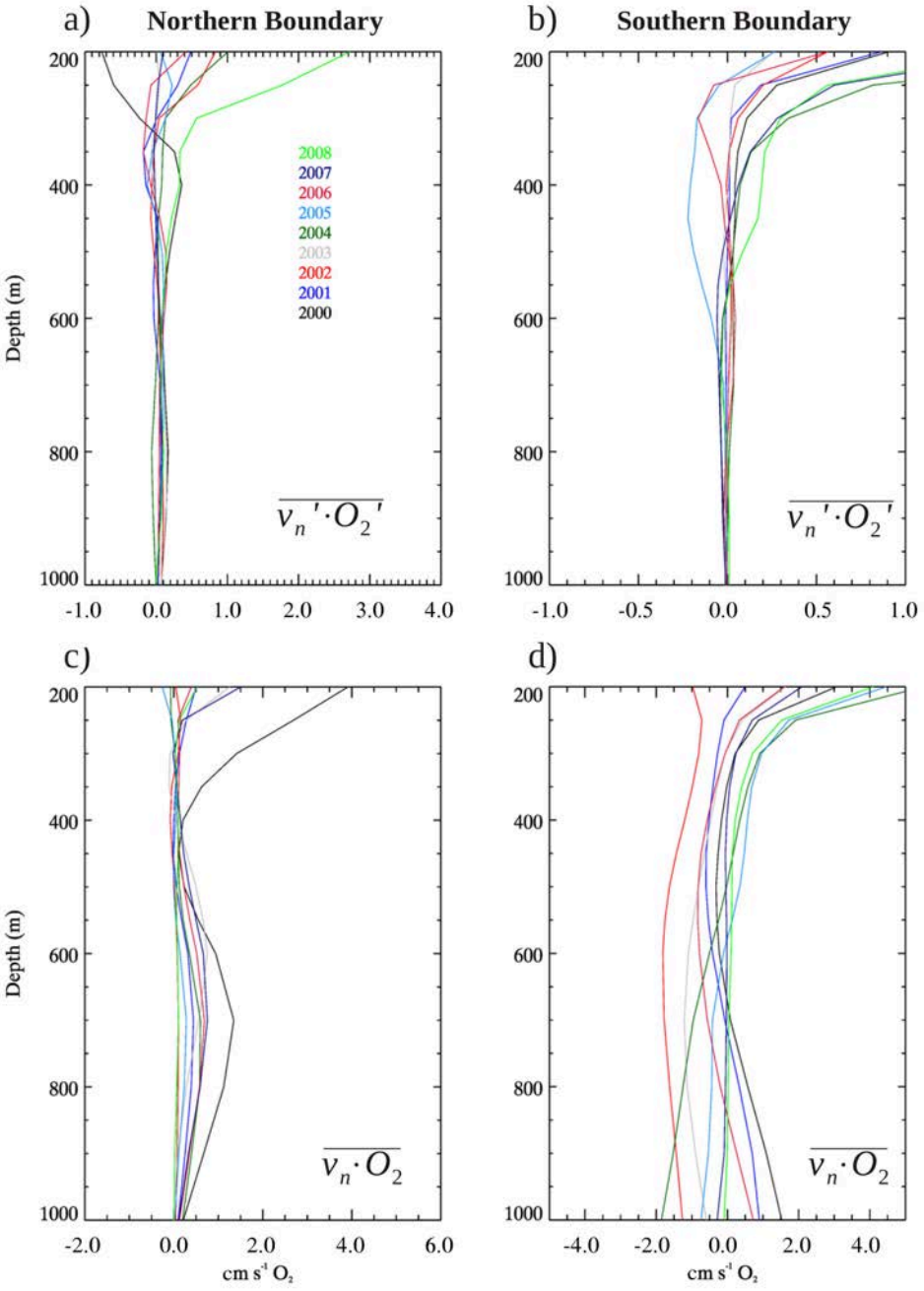

Figure 5.1: *Yearly averages of (a,b) oxygen eddy flux and (c, d) oxygen flux (computed using the monthly terms), averaged along the northern and southern boundaries. Subscript n denotes the velocity component normal to the boundary, and the apostrophe denotes the intraseasonal fluctuations (as defined in* Chapter 4*).*

parking depth evidence the offshore propagation of ETRW at annual timescale (Fig. 5.2). Considering that international efforts are being carried out towards increasing the spatial coverage of the ARGO floats in the Pacific[1] and the extension of the depth range currently measured[2], diagnosing the vertical propagation of ETRW at different timescales in the SEP from observations will be a possibility in the near future.

The increase of *in situ* measurements in the SEP will be also beneficial for constraining the current oceanic simulations, and will contribute to elucidate the questions remaining on the deep circulation off South America. Several studies have suggested that the abyssal flow around 2500 m in the SEP participates in the meridional overturning circulation and would link the equatorial Pacific to the Southern Ocean (e.g. Reid (1997), Tsuchiya and Talley (1998), Sloyan et al. (2001), Shaffer et al. (2004)). Documenting the mean characteristics and variability of the deep branches of the MOC in the South Pacific could benefit from the use of a modeling platform as the one used in the present study. In addition, it would be interesting to investigate the modulation of the deep flow associated with the vertical propagation of ETRW at the different timescales, considering that the propagation trajectory of the ETRW spans several hundred km off the coast in the abyssal SEP. As we documented in the present study, although most of the interannual energy flux that propagates into the deep SEP is related to the extreme EP El Niño events, there is a fraction that appears to be unrelated to these events. In this context it would be interesting to evaluate the different contributions to the "residual" energy flux; is it locally forced by the surface wind? or is it intrinsically forced by multi-scale interactions? Dewitte et al. (2008b) suggested that a significant share of the residual annual variability of the circulation (i.e. that is not related the coastal boundary forcing) arises from the interaction between the mean circulation and the ETRW. Is this also the case for the interannual timescale? These questions could be answered through the use of a simulation experiment that only takes into account the boundary forcing at the equatorial Pacific, and compare the results against a "full" simulation (which includes both local and remote forcing).

Increasing the observations in the deep ocean is also viewed as an essential step for elucidating the mechanisms that participate in the planetary energy budget. Currently, the earth's climate system experiences a state of positive radiative energy imbalance, which results from the decrease of the outgoing longwave radiation at the top of the atmosphere. Consequently, there is a heat trapping in the atmosphere and a global increase in temperature. Given its higher heat capacity compared to the atmosphere, the ocean absorbs around 93% of the heat excess, which is then redistributed and translates as a generalized rise in ocean temperature. Although the energy fluxes between

[1]TPOS2020 program (http://tpos2020.org/)
[2]Deep ARGO implementation (http://www.argo.ucsd.edu/)

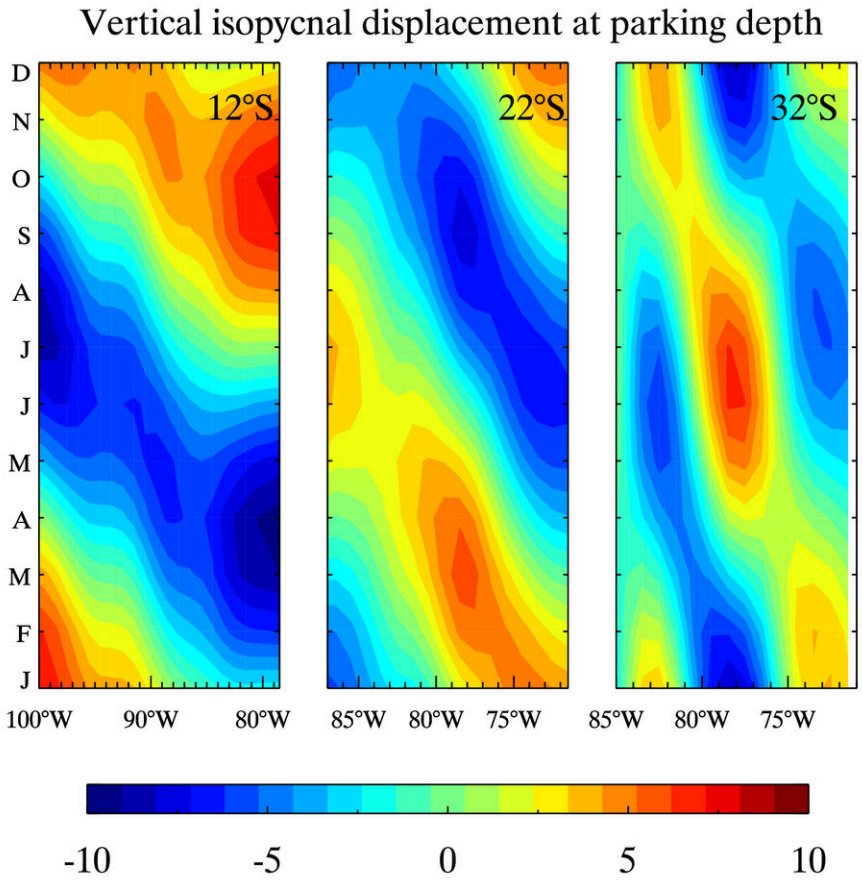

Figure 5.2: *Hövmöller diagrams of the annual harmonic of the vertical isopycnal displacements at the ARGO floats parking depth (~1000db), at several latitudes in the SEP. Vertical isopycnal displacements were computed using 1 degree monthly temperature and salinity data (http://sio-argo.ucsd.edu/) over the period 2004-2016.*

the ocean and the atmosphere occur at the interface, observations indicate that as much as 25% of the ocean heat increase takes place below 700m depth (see Abraham et al. (2013) for a review), and despite several hypotheses on the mechanisms that participate in the ocean's energy redistribution (see Banks and Gregory (2006) and P. Xie and Vallis (2012)), the subsurface ocean warming and its associated mechanisms remain at the center of a heated debate in the climatic community (Balmaseda et al., 2013; Llovel et al., 2014), partly due to insufficient measurements to accurately estimate the deep ocean contribution to the planetary energy imbalance.

This thesis work focuses on a mechanism that drives an energy discharge from the tropical Pacific onto the deep Southeastern Pacific, which has the potential to participate in the modulation of the deep ocean heat uptake. The results indicate that the dissipation of the energy flux induced by the passage of the ETRW at interannual to interdecadal timescales can be interpreted in terms of a vertical heat diffusion toward the deep ocean (*Chapter 3*). While we did not provide a comprehensive heat

budget of the deep ocean, our model results suggest a mechanism that could participate in the energy redistribution over the intermediate to deep ocean layers. Moreover, the timescales evidenced in the present study (interannual to interdecadal) are much shorter than the turning times of the deep Pacific MOC (age of the circulation below 1500m ranges from 600 to 900 years in the SEP; Matsumoto, 2007), which leads to think that this mechanism could also play a role in the deep ocean's response to the surface heat changes observed over the last 50 years (Balmaseda et al., 2013). Overall, these results call for a thorough documentation of the energy and heat fluxes in the abyssal SEP, and for assessing the role of the ETRW in the context of the deep ocean energy uptake. In the light of the sparse *in situ* observations in the deep SEP, this task would benefit from the use of regional ocean modeling tools, such as the platform used here.

In this task, a first step in closing the heat budget in the bathypelagic zone and assessing the role of the MOC in the SEP would be to validate the mean heat flux trends observed with the most recent ARGO products (e.g. Roemmich et al., 2015). From there, an attempt to perform a closed box-like heat budget for the SEP could be made, and the different contributions to the heat fluxes in the region could be assessed in an analogous manner as was done for the oxygen budget in *Chapter 4*. In this context, the use of a long-term simulation should be sought, given that it would also allow for an unprecedented documentation of the deep ocean's response during the negative phase of Interdecadal Pacific Oscillation (IPO) and its associated mechanisms. It has been suggested that the current hiatus in the surface warming trends is associated with the negative IPO phase (Meehl et al., 2011, 2013), that reinforces the trades and in turn enhances the upwelling of cold water in the SEP (see Whitmarsh et al. (2015) for a review). In parallel, observations indicate that the heat burial rate in the deep Pacific ocean has accelerated during the last 15 years (Gleckler et al., 2016), although the mechanisms driving this deep warming are uncertain (Liu et al., 2016). Considering the preponderant role of the ocean as a buffer for the earth's energy imbalance (Rhein et al., 2013), such a work (and the present thesis work) embeds in the current efforts of the scientific community towards a better understanding of the physical mechanisms involved in the decadal and longer timescale trends of the earth climate system, its response to anthropogenic forcing, and future evolution.

Conclusions et Perspectives (français)

Dans ce travail, nous avons étudié la variabilité de la circulation intermédiaire et profonde dans l'océan Pacifique Sud-Est (SEP : South-Eastern Pacific) à différentes échelles de temps, allant de l'échelle saisonnière à l'échelle décennale. Nous nous sommes concentrés en particulier sur les fluctuations de la circulation associées à la variabilité de méso-échelle et à la propagation de l'onde de Rossby extratropicale (ETRW : Extra Tropical Rossby Wave). Pour mener ce travail, nous avons adopté une approche basée sur la modélisation à l'échelle régionale, ce qui nous a permis d'étudier la variabilité depuis la région côtière vers le large, et depuis la subsurface vers la région abyssale.

Les fluctuations de la circulation dans le SEP sont le résultat des multiples forçages, d'origine locale comme lointaine, qui interagissent pour moduler les caractéristiques de la circulation. D'une part l'influence du vent parallèle à la côte impacte la circulation côtière sur le plateau et module l'intensité de l'upwelling côtier, et d'une autre le guide d'onde côtier qui fait le lien entre la variabilité équatoriale aux différentes bandes de fréquence, impacte les fluctuations de la circulation à la côte et au large dans le SEP. Cette diversité a motivé le choix d'approcher séparément les différentes échelles temporelles impliquées dans la variabilité de la circulation. Dans ce cadre, nous nous sommes intéressés dans un premier temps à l'effet des événements El Niño sur la circulation (échelle interannuelle), et plus précisément au flux vertical d'énergie induit par la propagation de l'onde de Rossby extratropicale associé à ce type d'évènements dans le SEP. En particulier, nous avons pu constater que 80% du flux d'énergie qui se propage verticalement sous la thermocline vers l'océan profond (le long des trajectoires théoriques WKB) dans le SEP est lié aux évènements El Niño extraordinaires (régime "E" dans notre approche), qui ont lieu dans la partie Est du basin équatorial. Ce résultat met en évidence les profondes implications que la variabilité équatoriale a sur la circulation dans le SEP, mais également que cette influence ne se limite pas à la région côtière. L'interprétation de ce flux d'énergie à travers la théorie WKB (adaptée pour les latitudes moyennes) montre que la propagation verticale d'énergie à l'échelle interannuelle est le résultat de la contribution des modes baroclines les plus bas.

En plus de l'importante variabilité d'échelle interannuelle, le Pacifique tropical présente également une variabilité significative à l'échelle décennale, qui s'exprime en partie comme une modulation des fluctuations d'échelles plus courte, en particulier de l'échelle interannuelle. Nous constatons l'existence d'un flux d'énergie qui se propage en suivant les rayons WKB associé aux fluctuations décennales.

En principe, le flux d'énergie induit par la propagation de ETRW dans le SEP correspond à un processus de type adiabatique, et agirait pour réorganiser le champ

d'énergie de manière conservative (sans dissipation d'énergie). Néanmoins, nous observons que l'amplitude du flux d'énergie diminue le long de la trajectoire de propagation, ce qui met en évidence un processus de dissipation dans l'océan profond. Nos résultats montrent que cette dissipation est associée à une diffusion de chaleur vers l'océan profond. En particulier, nous observons un flux de chaleur lié à la dissipation d'énergie le long des rayons théoriques WKB associé aux évènements El Niño extraordinaires et aux fluctuations décennales. Ces résultats indiquent que la décharge d'énergie en provenance du Pacifique tropical sous la thermocline du Pacifique Sud-Est, aux échelles interannuelle et décennale, comporte une diffusion verticale de chaleur.

Ce dernier résultat s'insère dans les perspectives générales de la communauté climatique. L'océan agit comme un régulateur du climat global, en absorbant l'excès d'énergie accumulé dans l'atmosphère (plus de 90% du surplus d'énergie radiative dans l'atmosphère est absorbé par l'océan) et en faisant la redistribution de cette énergie. Bien que l'objet de ce travail ne soit pas d'étudier le sort final du flux d'énergie sous la thermocline, nous proposons un mécanisme qui pourrait être impliqué dans la redistribution d'énergie au sein des couches intermédiaires et profondes de l'océan Pacifique Sud-Est, et qui pourrait donc jouer un rôle dans la dynamique du climat. Une perspective de travail futur sur cette thématique serait de quantifier la contribution du mécanisme de propagation d'énergie lié à l'onde de Rossby, dans le contexte de l'absorption d'énergie de la part de l'océan profond, et sa réponse au différents de régimes d'ENSO. Un tel travail pourrait bénéficier de l'usage des outils de modélisation régionale, comme cela était le cas pour cette thèse.

La deuxième partie de ce travail est consacrée à l'étude des fluctuations de la circulation à l'échelle saisonnière, du point de vue de la ventilation de la Zone de Minimum d'Oxygène (OMZ : Oxygen Minimum Zone) du Pacifique Sud-Est, et les processus associés à cette ventilation. Nos résultats montrent que la ventilation de l'OMZ sur les premiers 300 m de la colonne d'eau est essentiellement définie par la modulation saisonnière de l'activité de méso-échelle, induisant un flux turbulent d'oxygène à travers les frontières méridiennes de l'OMZ, et depuis la région côtière, plus oxygénée, vers l'intérieur de l'OMZ. La structure verticale de ce flux turbulent d'oxygène correspond à la structure verticale des tourbillons dans la région, et montre une forte décroissance à partir de 300 m de profondeur, où les flux turbulents d'oxygène sont très faibles. En revanche, à partir de cette profondeur, les fluctuations saisonnières d'oxygène ont des caractéristiques de propagation qui ressemblent à celles du flux d'énergie induit par l'onde de Rossby annuelle.

Ces résultats suggèrent aussi que les processus impliqués dans la ventilation de l'OMZ à l'échelle saisonnière pourraient aussi l'être dans sa variabilité basse fréquence.

Par exemple, des études récentes montrent que le volume d'eaux transporté par les tourbillons depuis la côte dans le SEP diminuerait fortement lors des évènements ENSO, et ce dû à une diminution de l'instabilité barocline, ce qui pourrait impacter le mécanisme de ventilation de l'OMZ lié au transport d'oxygène par la mésoéchelle. La contribution de la modulation interannuelle du système des courants à la ventilation de l'OMZ mériterait donc d'être évaluée. En lien avec la sensibilité de l'OMZ aux fluctuations interannuelles, une perspective de travail serait de quantifier l'effet des régimes ENSO sur la ventilation de l'OMZ, sachant que chaque régime a des impacts très contrastés sur la circulation du SEP. Par exemple, certains travaux montrent que les niveaux d'activité de mésoéchelle dans la région se réduisent drastiquement pendant les évènements El Niño du Pacifique Central. Ceci permettrait une accumulation des eaux pauvres en oxygène à l'intérieur de l'OMZ, liée à une baisse de la ventilation par la méso-échelle, dans le cas où ce type d'évènements ENSO deviennent plus fréquents, ce qui est suggéré par certains auteurs.

Enfin, la perspective d'évaluer la sensibilité des mécanismes de ventilation l'OMZ aux échelles interannuelles pourrait aussi être abordée du point de vue de l'ETRW. Comme il a été montré dans les *Chapitres 3 et 4*, les niveaux d'énergie associés à l'onde de Rossby pendant les évènements ENSO sont plus hauts que l'onde de Rossby annuelle, ce qui pourrait impliquer que la rectification de la circulation intermédiaire soit plus importante pour les fluctuations interannuelles que pour le cycle saisonnier.

References

Abraham, J. P. et al. (2013). "A review of global ocean temperature observations: Implications for ocean heat content estimates and climate change". In: *Reviews of Geophysics* 51.3, pp. 450–483. DOI: 10.1002/rog.20022.

Aguirre, C., O. Pizarro, P. T. Strub, R. Garreaud, and J. A. Barth (2012). "Seasonal dynamics of the near-surface alongshore flow off central Chile". In: *Journal of Geophysical Research: Oceans* 117.C1, n/a–n/a. DOI: 10.1029/2011JC007379.

Allen, J. S. (1975). "Coastal Trapped Waves in a Stratified Ocean". In: *Journal of Physical Oceanography* 5.2, pp. 300–325. DOI: 10.1175/1520-0485(1975)005<0300:CTWIAS>2.0.CO;2.

Ancapichún, S. and J. Garcés-Vargas (2015). "Variability of the Southeast Pacific Subtropical Anticyclone and its impact on sea surface temperature off north-central Chile". In: *Ciencias Marinas* 41.1, pp. 1–20. DOI: 10.7773/cm.v41i1.2338.

Arakawa, A. and V. R. Lamb (1977). "Computational Design of the Basic Dynamical Processes of the UCLA General Circulation Model". In: *General circulation models of the atmosphere*. Ed. by Julius Chang. Vol. 17. New York: Academic Press, pp. 173–265. DOI: 10.1016/B978-0-12-460817-7.50009-4.

Aravena, G., B. Broitman, and N. C. Stenseth (2014). "Twelve Years of Change in Coastal Upwelling along the Central-Northern Coast of Chile: Spatially Heterogeneous Responses to Climatic Variability". In: *PLoS ONE* 9.2. Ed. by M. Gomez-Gesteira, e90276. DOI: 10.1371/journal.pone.0090276.

Ashok, K., S. K. Behera, S. A. Rao, H. Weng, and T. Yamagata (2007). "El Niño Modoki and its possible teleconnection". In: *Journal of Geophysical Research* 112.C11, p. C11007. DOI: 10.1029/2006JC003798.

Ashok, K. and T. Yamagata (2009). "Climate change: The El Niño with a difference". In: *Nature* 461.7263, pp. 481–484. DOI: 10.1038/461481a.

Astudillo, O., B. Dewitte, M. Mallet, F. Frappart, J. Ruttlant, M. Ramos, L. Bravos, K. Goubanova, and S. Illig (2016). "Near-shore surface winds along the coast of Peru/Chile as derived from altimetry". In: *Journal of Remote Sensing of Environment*.

Bakun, A. and C. S. Nelson (1991). "The Seasonal Cycle of Wind-Stress Curl in Subtropical Eastern Boundary Current Regions". In: *Journal of Physical Oceanography* 21.12,

pp. 1815–1834. DOI: 10.1175/1520-0485(1991)021<1815:TSCOWS>2.0.CO;2.

Balmaseda, M. A., K. E. Trenberth, and E. Källén (2013). "Distinctive climate signals in reanalysis of global ocean heat content". In: *Geophysical Research Letters* 40.9, pp. 1754–1759. DOI: 10.1002/grl.50382.

Banks, H. T. and J. M. Gregory (2006). "Mechanisms of ocean heat uptake in a coupled climate model and the implications for tracer based predictions of ocean heat uptake". In: *Geophysical Research Letters* 33.7, p. L07608. DOI: 10.1029/2005GL025352.

Barber, R. T. and F. P. Chávez (1986). "Ocean variability in relation to living resources during the 1982-83 El Niño". In: *Nature* 319.6051, pp. 279–285. DOI: 10.1038/319279a0.

Benestad, R. E., R. T. Sutton, and D. L. Anderson (2002). "The effect of El Niño on intraseasonal Kelvin waves". In: *Quarterly Journal of the Royal Meteorological Society* 128.582, pp. 1277–1291. DOI: 10.1256/003590002320373292.

Bettencourt, J. H., C. López, E. Hernández-García, I. Montes, J. Sudre, B. Dewitte, A. Paulmier, and V. Garçon (2015). "Boundaries of the Peruvian oxygen minimum zone shaped by coherent mesoscale dynamics". In: *Nature Geoscience* 8.12, pp. 937–940. DOI: 10.1038/ngeo2570.

Blanco, J. L., M.-e. Carr, A. C. Thomas, and P. T. Strub (2002). "Hydrographic conditions off northern Chile during the 1996-1998 La Niña and El Niño events". In: *Journal of Geophysical Research* 107.C3, pp. 173–185. DOI: 10.1029/2001JC001002.

Brink, K. H. (1980). "Propagation of Barotropic Continental Shelf Waves over Irregular Bottom Topography". In: *Journal of Physical Oceanography*. DOI: 10.1175/1520-0485(1980)010.

Brink, K. H. (1982). "A Comparison of Long Coastal Trapped Wave Theory with Observations off Peru". In: *Journal of Physical Oceanography* 12.8, pp. 897–913. DOI: 10.1175/1520-0485(1982)012.

Brodeau, L., B. Barnier, A.-M. Treguier, T. Penduff, and S. Gulev (2010). "An ERA40-based atmospheric forcing for global ocean circulation models". In: *Ocean Modelling* 31.3, pp. 88–104. DOI: 10.1016/j.ocemod.2009.10.005.

Brown, J. N. and A. V. Fedorov (2010). "How Much Energy Is Transferred from the Winds to the Thermocline on ENSO Time Scales?" In: *Journal of Climate* 23.6, pp. 1563–1580. DOI: 10.1175/2009JCLI2914.1.

Cane, M. A. and E. S. Sarachik (1977). "Forced baroclinic Ocean motions. II. The linear equatorial bounded case". In: 35.4.

Capet, X., P. Marchesiello, and J. C. McWilliams (2004). "Upwelling response to coastal wind profiles". In: *Geophysical Research Letters* 31.13, p. L13311. DOI: 10.1029/2004GL020123.

Capone, D. G. and D. A. Hutchins (2013). "Microbial biogeochemistry of coastal upwelling regimes in a changing ocean". In: *Nature Geoscience* 6.9, pp. 711–717. DOI: 10.1038/ngeo1916.

Carton, J. A., G. Chepurin, and X. Cao (2000a). "A Simple Ocean Data Assimilation Analysis of the Global Upper Ocean 1950–95. Part II: Results". In: *Journal of Physical Oceanography* 30.2, pp. 311–326. DOI: 10.1175/1520-0485(2000)030<0311:ASODAA>2.0.CO;2.

Carton, J. A., G. Chepurin, X. Cao, and B. Giese (2000b). "A Simple Ocean Data Assimilation Analysis of the Global Upper Ocean 1950–95. Part I: Methodology". In: *Journal of Physical Oceanography* 30.2, pp. 294–309. DOI: 10.1175/1520-0485(2000)030<0294:ASODAA>2.0.CO;2.

Cashin, P., K. Mohaddes, and M. Raissi (2014). "Fair Weather or Foul? The Macroeconomic Effects of El Niño". In: *Cambridge Working Papers in Economics* cwpe, p. 1418. DOI: 10.2139/ssrn.2643965.

Chaigneau, A., A. Gizolme, and C. Grados (2008). "Mesoscale eddies off Peru in altimeter records: Identification algorithms and eddy spatio-temporal patterns". In: *Progress in Oceanography* 79.2-4, pp. 106–119. DOI: 10.1016/j.pocean.2008.10.013.

Chaigneau, A., M. Le Texier, G. Eldin, C. Grados, and O. Pizarro (2011). "Vertical structure of mesoscale eddies in the eastern South Pacific Ocean: A composite analysis from altimetry and Argo profiling floats". In: *Journal of Geophysical Research* 116.C11, p. C11025. DOI: 10.1029/2011JC007134.

Chaigneau, A. and O. Pizarro (2005a). "Eddy characteristics in the eastern South Pacific". In: *Journal of Geophysical Research: Oceans* 110.6, pp. 1–12. DOI: 10.1029/2004JC002815.

Chaigneau, A. and O. Pizarro (2005b). "Mean surface circulation and mesoscale turbulent flow characteristics in the eastern South Pacific from satellite tracked drifters". In: *Journal of Geophysical Research* 110.5, pp. 1–17. DOI: 10.1029/2004JC002628.

Chaudhuri, A. H., R. M. Ponte, G. Forget, and P. Heimbach (2013). "A Comparison of Atmospheric Reanalysis Surface Products over the Ocean and Implications for Uncertainties in Air–Sea Boundary Forcing". In: *Journal of Climate* 26.1, pp. 153–170. DOI: 10.1175/JCLI-D-12-00090.1.

Chelton, D. B. and M. G. Schlax (1996). "Global Observations of Oceanic Rossby Waves". In: *Science* 272.5259, pp. 234–238. DOI: 10.1126/science.272.5259.234.

Church, J. A. et al. (2011). "Revisiting the Earth's sea-level and energy budgets from 1961 to 2008". In: *Geophysical Research Letters* 38.18, n/a–n/a. DOI: 10.1029/2011GL048794.

Clarke, A. J. (1983). "The Reflection of Equatorial Waves from Oceanic Boundaries". In: *Journal of Physical Oceanography* 13.7, pp. 1193–1207. DOI: 10.1175/1520-0485(1983)013.

Clarke, A. J. and R. Ahmed (1999). "Dynamics of Remotely Forced Intraseasonal Oscillations off the Western Coast of South America". In: *Journal of Physical Oceanography* 29.2, pp. 240–258. DOI: 10.1175/1520-0485(1999)029<0240:DORFIO>2.0.CO;2.

Clarke, A. J. and C. Shi (1991). "Critical frequencies at ocean boundaries". In: *Journal of Geophysical Research* 96.C6, p. 10731. DOI: 10.1029/91JC00933.

Colas, F., X. Capet, J. C. McWilliams, and A. F. Shchepetkin (2008). "1997-1998 El Niño off Peru: A numerical study". In: DOI: 10.1016/j.pocean.2008.10.015.

Colas, F., J. C. McWilliams, X. Capet, and J. Kurian (2012). "Heat balance and eddies in the Peru-Chile current system". In: *Climate Dynamics* 39.1-2, pp. 509–529. DOI: 10.1007/s00382-011-1170-6.

Combes, V., S. Hormazabal, and E. Di Lorenzo (2015). "Interannual variability of the subsurface eddy field in the Southeast Pacific". In: *Journal of Geophysical Research: Oceans* 120.7, pp. 4907–4924. DOI: 10.1002/2014JC010265.

Condie, S. and J. R. Dunn (2006). "Seasonal characteristics of the surface mixed layer in the Australasian region: implications for primary production regimes and biogeography". In: *Marine and Freshwater Research* 57.6, p. 569. DOI: 10.1071/MF06009.

Cornejo-Rodriguez, M. D. P. and D. B. Enfield (1987). "Propagation and forcing of high-frequency sea level variability along the west coast of South America". In: *Journal of Geophysical Research* 92.C13, p. 14323. DOI: 10.1029/JC092iC13p14323.

Correa-Ramirez, M. A., S. Hormazábal, and C. Morales (2012). "Spatial patterns of annual and interannual surface chlorophyll-a variability in the Peru–Chile Current System". In: *Progress in Oceanography* 92, pp. 8–17. DOI: 10.1016/j.pocean.2011.07.008.

Correa-Ramirez, M. A., S. Hormazábal, and G. Yuras (2007). "Mesoscale eddies and high chlorophyll concentrations off central Chile (29°-39°S)". In: *Geophysical Research Letters* 34.12, p. L12604. DOI: 10.1029/2007GL029541.

DeSzoeke, R. A. and D. B. Chelton (1999). "The Modification of Long Planetary Waves by Homogeneous Potential Vorticity Layers". In: *Journal of Physical Oceanography* 29.3, pp. 500–511. DOI: 10.1175/1520-0485(1999)029<0500:TMOLPW>2.0.CO;2.

DeSzoeke, S. P., S. Yuter, D. Mechem, C. W. Fairall, C. D. Burleyson, and P. Zuidema (2012). "Observations of Stratocumulus Clouds and Their Effect on the Eastern Pacific Surface Heat Budget along 20°S". In: *Journal of Climate* 25.24, pp. 8542–8567. DOI: 10.1175/JCLI-D-11-00618.1.

Dewitte, B., S. Illig, L. Renault, K. Goubanova, K. Takahashi, D. Gushchina, K. Mosquera, and S. Purca (2011). "Modes of covariability between sea surface temperature and wind stress intraseasonal anomalies along the coast of Peru from satellite observations (2000–2008)". In: *Journal of Geophysical Research* 116.C4, p. C04028. DOI: 10.1029/2010JC006495.

Dewitte, B., S. Illig, L. Parent, Y. DuPenhoat, L. Gourdeau, and J. Verron (2003). "Tropical Pacific baroclinic mode contribution and associated long waves for the 1994-1999 period from an assimilation experiment with altimetric data". In: *Journal of Geophysical Research* 108.C4, p. 3121. DOI: 10.1029/2002JC001362.

Dewitte, B., S. Purca, S. Illig, L. Renault, and B. S. Giese (2008a). "Low-Frequency Modulation of Intraseasonal Equatorial Kelvin Wave Activity in the Pacific from SODA: 1958–2001". In: *Journal of Climate* 21.22, pp. 6060–6069. DOI: 10.1175/2008JCLI2277.1.

Dewitte, B., M. Ramos, V. Echevin, O. Pizarro, and Y. Dupenhoat (2008b). "Vertical structure variability in a seasonal simulation of a medium-resolution regional model of the Eastern South Pacific". In: *Progress in Oceanography* 79, pp. 120–137. DOI: 10.1016/j.pocean.2008.10.014.

Dewitte, B. and G. Reverdin (2000). "Vertically Propagating Annual and Interannual Variability in an OGCM Simulation of the Tropical Pacific Ocean in 1985-94". In: *Journal of Physical Oceanography*. DOI: 10.1175/1520-0485(2000)030<1562:VPAAIV>2.0.CO;2.

Dewitte, B., G. Reverdin, and C. Maes (1999). "Vertical Structure of an OGCM Simulation of the Equatorial Pacific Ocean in 1985–94". In: *Journal of Physical Oceanography* 29.7, pp. 1542–1570. DOI: 10.1175/1520-0485(1999)029<1542:VSOAOS>2.0.CO;2.

Dewitte, B. et al. (2012). "Change in El Niño flavours over 1958–2008: Implications for the long-term trend of the upwelling off Peru". In: *Deep Sea Research Part II: Topical Studies in Oceanography* 77, pp. 143–156. DOI: 10.1016/j.dsr2.2012.04.011.

Dool, H. M. van den, S. Saha, and A. Johansson (2000). "Empirical Orthogonal Teleconnections". In: *Journal of Climate* 13.8, pp. 1421–1435. DOI: 10.1175/1520-0442(2000)013<1421:EOT>2.0.CO;2.

Dunn, J. R. and K. R. Ridgway (2002). "Mapping ocean properties in regions of complex topography". In: *Deep Sea Research Part I: Oceanographic Research Papers* 49.3, pp. 591–604. DOI: 10.1016/S0967-0637(01)00069-3.

Durack, P. J. and S. E. Wijffels (2010). "Fifty-Year Trends in Global Ocean Salinities and Their Relationship to Broad-Scale Warming". In: *Journal of Climate* 23.16, pp. 4342–4362. DOI: 10.1175/2010JCLI3377.1.

Ekman, V. W. (1902). "Om jordrotationens inverkan pa vindstrommar i lafvet". In: *Nyt Magazin f. Naturvidenskab* 40.27.

Eliassen, A. and E. Palm (1960). "On the transfer of energy in the stationary mountain waves". In: *Geofysike Publikasjoner* 12.3, p. 23.

Enfield, D. B., M. D. P. Cornejo-Rodriguez, R. L. Smith, and P. A. Newberger (1987). "The equatorial source of propagating variability along the Peru coast During the 1982-1983 El Niño". In: *Journal of Geophysical Research* 92.C13, p. 14335. DOI: 10.1029/JC092iC13p14335.

Fu, L.-L. and A. Cazenave (2001). *Satellite altimetry and earth sciences : a handbook of techniques and applications*. 1st Editio. Academic Press, p. 463.

Fu, L.-L. and D. B. Chelton (2001). "Chapter 2 Large-Scale Ocean Circulation". In: *International Geophysics* 69, pp. 133–viii. DOI: 10.1016/S0074-6142(01)80147-9.

Fuente, M. de la, L. Skinner, E. Calvo, C. Pelejero, and I. Cacho (2015). "Increased reservoir ages and poorly ventilated deep waters inferred in the glacial Eastern Equatorial Pacific". In: *Nature Communications* 6, p. 7420. DOI: 10.1038/ncomms8420.

Furue, R. et al. (2015). "Impacts of regional mixing on the temperature structure of the equatorial Pacific Ocean. Part 1: Vertically uniform vertical diffusion". In: *Ocean Modelling* 91, pp. 91–111. DOI: 10.1016/j.ocemod.2014.10.002.

Gaillard, F. (2012). *ISAS-Tool Version 6 : Method and configuration*. Tech. rep. Brest: Ifremer, p. 18. DOI: 10.13155/22583.

Garreaud, R. and R. C. Muñoz (2005). "The Low-Level Jet off the West Coast of Subtropical South America: Structure and Variability". In: *Monthly Weather Review* 133.8, pp. 2246–2261. DOI: 10.1175/MWR2972.1.

Garreaud, R., J. Rutllant, and H. Fuenzalida (2002). "Coastal Lows along the Subtropical West Coast of South America: Mean Structure and Evolution". In: *Monthly Weather Review* 130.1, pp. 75–88. DOI: 10.1175/1520-0493(2002)130.

Gent, P. R. and J. R. Luyten (1985). "How Much Energy Propagates Vertically in the Equatorial Oceans?" In: *Journal of Physical Oceanography* 15.7, pp. 997–1007. DOI: 10.1175/1520-0485(1985)015<0997:HMEPVI>2.0.CO;2.

Gill, A. E. (1982). *Atmosphere-ocean dynamics*. 2nd Editio. London: Academic Press, p. 662.

Gilly, W. F., J. M. Beman, S. Y. Litvin, and B. H. Robison (2013). "Oceanographic and Biological Effects of Shoaling of the Oxygen Minimum Zone". In: *Annual Review of Marine Science* 5.1, pp. 393–420. DOI: 10.1146/annurev-marine-120710-100849.

Gleckler, P. J., P. J. Durack, R. J. Stouffer, G. C. Johnson, and C. E. Forest (2016). "Industrial-era global ocean heat uptake doubles in recent decades". In: *Nature Climate Change* 6.4, pp. 394–398. DOI: 10.1038/nclimate2915.

Good, S. A., M. J. Martin, and N. A. Rayner (2013). "EN4: Quality controlled ocean temperature and salinity profiles and monthly objective analyses with uncertainty estimates". In: *Journal of Geophysical Research: Oceans* 118.12, pp. 6704–6716. DOI: 10.1002/2013JC009067.

Gray, A. R. and S. C. Riser (2014). "A Global Analysis of Sverdrup Balance Using Absolute Geostrophic Velocities from Argo". In: *Journal of Physical Oceanography* 44.4, pp. 1213–1229. DOI: 10.1175/JPO-D-12-0206.1.

Gruber, N., Z. Lachkar, H. Frenzel, P. Marchesiello, M. Münnich, J. C. McWilliams, T. Nagai, and G.-K. Plattner (2011). "Eddy-induced reduction of biological production in eastern boundary upwelling systems". In: *Nature Geoscience* 4.11, pp. 787–792. DOI: 10.1038/ngeo1273.

Gushchina, D. and B. Dewitte (2012). "Intraseasonal Tropical Atmospheric Variability Associated with the Two Flavors of El Niño". In: *Monthly Weather Review* 140.11, pp. 3669–3681. DOI: 10.1175/MWR-D-11-00267.1.

Gutiérrez, D., E. Enríquez, S. Purca, L. Quipúzcoa, R. Marquina, G. Flores, and M. Graco (2008). "Oxygenation episodes on the continental shelf of central Peru: Remote forcing and benthic ecosystem response". In: *Progress in Oceanography* 79.2, pp. 177–189. DOI: 10.1016/j.pocean.2008.10.025.

Haidvogel, D. B., J. L. Wilkin, and R. Young (1991). "A semi-spectral primitive equation ocean circulation model using vertical sigma and orthogonal curvilinear horizontal coordinates". In: *Journal of Computational Physics* 94.1, pp. 151–185. DOI: 10.1016/0021-9991(91)90141-7.

Hansen, J., M. Sato, P. Kharecha, and K. von Schuckmann (2011). "Earth's energy imbalance and implications". In: *Atmospheric Chemistry and Physics* 11.24, pp. 13421–13449. DOI: 10.5194/acp-11-13421-2011.

Hedström, K. S. (1997). *(DRAFT) User's manual for an S-Coordinate Primitive Equation Ocean Circulation Model (SCRUM) Version 3.0.* Tech. rep. Institute of Marine and Coastal Sciences, Rutgers University Contribution 97-10, p. 116.

Hodur, R., X. Hong, J. Doyle, J. Pullen, J. Cummings, P. Martin, and M. A. Rennick (2002). "The Coupled Ocean/Atmosphere Mesoscale Prediction System (COAMPS)". In: *Oceanography* 15.1, pp. 88–98. DOI: 10.5670/oceanog.2002.39.

Holte, J., F. Straneo, C. Moffat, R. Weller, and J. T. Farrar (2013). "Structure and surface properties of eddies in the southeast Pacific Ocean". In: *Journal of Geophysical Research: Oceans* 118.5, pp. 2295–2309. DOI: 10.1002/jgrc.20175.

Hooker, S. B., G. Lazin, G. Zibordi, and S. McLean (2002). "An Evaluation of Above- and In-Water Methods for Determining Water-Leaving Radiances". In: *Journal of Atmospheric and Oceanic Technology* 19.4, pp. 486–515. DOI: 10.1175/1520-0426(2002)019<0486:AEOAAI>2.0.CO;2.

Hormazábal, S., G. Shaffer, and O. Pizarro (2002). "Tropical Pacific control of intraseasonal oscillations off Chile by way of oceanic and atmospheric pathways". In: *Geophysical Research Letters* 29.6. DOI: 10.1029/2001GL013481.

Hosoda, S., T. Suga, N. Shikama, and K. Mizuno (2009). "Global surface layer salinity change detected by Argo and its implication for hydrological cycle intensification". In: *Journal of Oceanography* 65.4, pp. 579–586. DOI: 10.1007/s10872-009-0049-1.

Huyer, A., R. L. Smith, and T. Paluszkiewicz (1987). "Coastal upwelling off Peru during normal and El Ni{ñ}o times, 1981-1984". In: *Journal of Geophysical Research* 92.C13, p. 14297. DOI: 10.1029/JC092iC13p14297.

Illig, S., B. Dewitte, K. Goubanova, G. Cambon, J. Boucharel, F. Monetti, C. Romero, S. Purca, and R. Flores (2014). "Forcing mechanisms of intraseasonal SST variability off central Peru in 2000-2008". In: *Journal of Geophysical Research: Oceans* 119.6, pp. 3548–3573. DOI: 10.1002/2013JC009779.

Ingleby, B. and M. Huddleston (2007). "Quality control of ocean temperature and salinity profiles — Historical and real-time data". In: *Journal of Marine Systems* 65.1-4, pp. 158–175. DOI: 10.1016/j.jmarsys.2005.11.019.

IOC (2012). *Global Sea Level Observing System (GLOSS) Implementation Plan – 2012*. Tech. rep. Paris: UNESCO/IOC (IOC Technical Series No.100), p. 41.

Kao, H.-Y. and J.-Y. Yu (2009). "Contrasting Eastern-Pacific and Central-Pacific Types of ENSO". In: *Journal of Climate* 22.3, pp. 615–632. DOI: 10.1175/2008JCLI2309.1.

Karoly, D. J., D. G. Vincent, D. J. Karoly, and D. G. Vincent (1998). *Meteorology of the Southern Hemisphere*. Vol. 27. 49. American Meteorological Society, p. 410. DOI: 10.1175/0065-9401-27.49.1.

Karstensen, J., L. Stramma, and M. Visbeck (2008). "Oxygen minimum zones in the eastern tropical Atlantic and Pacific oceans". In: *Progress in Oceanography* 77.4, pp. 331–350. DOI: 10.1016/j.pocean.2007.05.009.

Kelly, R. and J. L. Blanco (1984). "Estudio oceanografico de las aguas del norte de chile durante febrero y marzo de 1983". In: *Revista de la Comisión Permanente del Pacífico Sur* 15, pp. 179–201.

Kessler, W. S. (1990). "Observations of long Rossby waves in the northern tropical Pacific". In: *Journal of Geophysical Research* 95.C4, p. 5183. DOI: 10.1029/JC095iC04p05183.

Kessler, W. S. (2006). "The circulation of the eastern tropical Pacific: A review". In: *Progress in Oceanography* 69.2-4, pp. 181–217. DOI: 10.1016/j.pocean.2006.03.009.

Kessler, W. S. and J. P. McCreary (1993). "The Annual Wind-driven Rossby Wave in the Subthermocline Equatorial Pacific". In: *Journal of Physical Oceanography* 23.6, pp. 1192–1207. DOI: 10.1175/1520-0485(1993)023<1192:TAWDRW>2.0.CO;2.

Kessler, W. S., M. J. McPhaden, and K. M. Weickmann (1995). "Forcing of intraseasonal Kelvin waves in the equatorial Pacific". In: *Journal of Geophysical Research* 100.C6, p. 10613. DOI: 10.1029/95JC00382.

Kiladis, G. N., H. von Storch, and H. Loon (1989). "Origin of the South Pacific Convergence Zone". In: *Journal of Climate* 2, pp. 1185–1195. DOI: 10.1175/1520-0442(1989)002<1185:OOTSPC>2.0.CO;2.

Killworth, P. D. and J. R. Blundell (1999). "The Effect of Bottom Topography on the Speed of Long Extratropical Planetary Waves". In: *Journal of Physical Oceanography* 29.10, pp. 2689–2710. DOI: 10.1175/1520-0485(1999)029<2689:TEOBTO>2.0.CO;2.

Killworth, P. D. and J. R. Blundell (2003a). "Long Extratropical Planetary Wave Propagation in the Presence of Slowly Varying Mean Flow and Bottom Topography. Part I: The Local Problem". In: *Journal of Physical Oceanography* 33.4, pp. 784–801. DOI: 10.1175/1520-0485(2003)33<784:LEPWPI>2.0.CO;2.

Killworth, P. D. and J. R. Blundell (2003b). "Long Extratropical Planetary Wave Propagation in the Presence of Slowly Varying Mean Flow and Bottom Topography. Part II: Ray Propagation and Comparison with Observations". In: *Journal of Physical Oceanography* 33.4, pp. 802–821. DOI: 10.1175/1520-0485(2003)33<802:LEPWPI>2.0.CO;2.

Killworth, P. D. and J. R. Blundell (2004). "The Dispersion Relation for Planetary Waves in the Presence of Mean Flow and Topography. Part I: Analytical Theory and One-Dimensional Examples". In: *Journal of Physical Oceanography* 34.12, pp. 2692–2711. DOI: 10.1175/JPO2635.1.

Killworth, P. D. and J. R. Blundell (2005). "The Dispersion Relation for Planetary Waves in the Presence of Mean Flow and Topography. Part II: Two-Dimensional Examples

and Global Results". In: *Journal of Physical Oceanography* 35.11, pp. 2110–2133. DOI: 10.1175/JPO2817.1.

Kim, S. T. and J.-Y. Yu (2012). "The two types of ENSO in CMIP5 models". In: *Geophysical Research Letters* 39.11. DOI: 10.1029/2012GL052006.

Kock, A., D. L. Arévalo-Martínez, C. R. Loscher, and H. W. Bange (2016). "Extreme N2O accumulation in the coastal oxygen minimum zone off Peru". In: *Biogeosciences* 13.3, pp. 827–840. DOI: 10.5194/bg-13-827-2016.

Kug, J.-S., J. Choi, S.-I. An, F.-F. Jin, and A. T. Wittenberg (2010). "Warm Pool and Cold Tongue El Niño Events as Simulated by the GFDL 2.1 Coupled GCM". In: *Journal of Climate* 23.5, pp. 1226–1239. DOI: 10.1175/2009JCLI3293.1.

Lacasce, J. H. and J. Pedlosky (2004). "The Instability of Rossby Basin Modes and the Oceanic Eddy Field". In:

Large, W. G. and G. Danabasoglu (2006). "Attribution and Impacts of Upper-Ocean Biases in CCSM3". In: *Journal of Climate* 19.11, pp. 2325–2346. DOI: 10.1175/JCLI3740.1.

Large, W. G., J. C. McWilliams, and S. Doney (1994). "Oceanic vertical mixing: A review and a model with a nonlocal boundary-layer parameterization". In: *Reviews of Geophysics* 32.4, p. 363. DOI: http://dx.doi.org/10.1029/94rg01872.

Larkin, N. K. and D. E. Harrison (2005). "On the definition of El Ni{ñ}o and associated seasonal average U.S. weather anomalies". In: *Geophysical Research Letters* 32.13, p. L13705. DOI: 10.1029/2005GL022738.

Lee, T. and M. J. McPhaden (2010). "Increasing intensity of El Niño in the central-equatorial Pacific". In: *Geophysical Research Letters* 37.14. DOI: 10.1029/2010GL044007.

Leth, O. and G. Shaffer (2001). "A numerical study of the seasonal variability in the circulation off central Chile". In: *J. Geophys. Res.* 106.C10, pp. 22229–22248. DOI: 10.1029/2000JC000627.

Levitus, S. (1982). *Climatological Atlas of the World Ocean*. Tech. rep. NOAA Prof. Paper No. 13, U.S. Govt. Printing Office, p. 173.

Levitus, S. et al. (2012). "World ocean heat content and thermosteric sea level change (0–2000 m), 1955–2010". In: *Geophysical Research Letters* 39.10. DOI: 10.1029/2012GL051106.

Liu, W. et al. (2016). "Tracking ocean heat uptake during the surface warming hiatus". In: *Nature Communications* 7, p. 10926. DOI: 10.1038/ncomms10926.

Llovel, W., J. K. Willis, F. W. Landerer, and I. Fukumori (2014). "Deep-ocean contribution to sea level and energy budget not detectable over the past decade". In: *Nature Climate Change* 4.11, pp. 1031–1035. DOI: 10.1038/nclimate2387.

Lorenc, A. C., R. S. Bell, and B. Macpherson (1991). "The Meteorological Office analysis correction data assimilation scheme". In: *Quarterly Journal of the Royal Meteorological Society* 117.497, pp. 59–89. DOI: 10.1002/qj.49711749704.

Lozier, M. S. and S. C. Riser (1989). "Potential Vorticity Dynamics of Boundary Currents in a Quasi-geostrophic Ocean". In: *Journal of Physical Oceanography* 19.9, pp. 1373–1396. DOI: 10.1175/1520-0485(1989)019<1373:PVDOBC>2.0.CO;2.

Lukas, R. and E. Firing (1985). "The Annual Rossby Wave in the Central Equatorial Pacific Ocean". In: *Journal of Physical Oceanography* 15.1, pp. 55–67. DOI: 10.1175/1520-0485(1985)015<0055:TARWIT>2.0.CO;2.

Luyten, J. R., J. Pedlosky, and H. Stommel (1983). "The Ventilated Thermocline". In: *Journal of Physical Oceanography* 13.2, pp. 292–309. DOI: 10.1175/1520-0485(1983)013.

Maharaj, A. M., P. Cipollini, N. J. Holbrook, P. D. Killworth, and J. R. Blundell (2007). "An evaluation of the classical and extended Rossby wave theories in explaining spectral estimates of the first few baroclinic modes in the South Pacific Ocean". In: *Ocean Dynamics* 57.3, pp. 173–187. DOI: 10.1007/s10236-006-0099-5.

Marchal, O. (2009). "Extratropical Rossby Waves in the Presence of Buoyancy Mixing". In: *Journal of Physical Oceanography* 39.11, pp. 2910–2925. DOI: 10.1175/2009JPO4139.1.

Marchesiello, P., J. C. McWilliams, and A. F. Shchepetkin (2003). "Equilibrium Structure and Dynamics of the California Current System". In: *Journal of Physical Oceanography* 33.4, pp. 753–783. DOI: 10.1175/1520-0485(2003)33<753:ESADOT>2.0.CO;2.

Matsumoto, K. (2007). "Radiocarbon-based circulation age of the world oceans". In: *Journal of Geophysical Research* 112.C9, p. C09004. DOI: 10.1029/2007JC004095.

McCreary, J. P. (1984). "Equatorial beams". In: *Journal of Marine Research* 42.2, pp. 395–430. DOI: 10.1357/002224084788502792.

McGillicuddy, D. J. et al. (1998). "Influence of Mesoscale Eddies on New Production in the Sargasso Sea". In: *Nature* 394.1977, pp. 263–266. DOI: 10.1038/28367.

Mechoso, C. R. et al. (2014). "Ocean–Cloud–Atmosphere–Land Interactions in the Southeastern Pacific: The VOCALS Program". In: *Bulletin of the American Meteorological Society* 95.3, pp. 357–375. DOI: 10.1175/BAMS-D-11-00246.1.

Meehl, G. A., J. M. Arblaster, J. T. Fasullo, A. Hu, and K. E. Trenberth (2011). "Model-based evidence of deep-ocean heat uptake during surface-temperature hiatus periods". In: *Nature Climate Change* 1.7, pp. 360–364. DOI: 10.1038/nclimate1229.

Meehl, G. A. et al. (2013). "Externally Forced and Internally Generated Decadal Climate Variability Associated with the Interdecadal Pacific Oscillation". In: *Journal of Climate* 26.18, pp. 7298–7310. DOI: 10.1175/JCLI-D-12-00548.1.

Mitchum, G. T. (2000). "An Improved Calibration of Satellite Altimetric Heights Using Tide Gauge Sea Levels with Adjustment for Land Motion". In: *Marine Geodesy* 23.3, pp. 145–166. DOI: 10.1080/01490410050128591.

Moffitt, S. E., R. A. Moffitt, W. Sauthoff, C. V. Davis, K. Hewett, and T. M. Hill (2015). "Paleoceanographic Insights on Recent Oxygen Minimum Zone Expansion: Lessons for Modern Oceanography". In: *PLOS ONE* 10.1. DOI: 10.1371/journal.pone.0115246.

Monin, A. S. and R. V. Ozmidov (1985). *Turbulence in the Ocean*. Dordrecht: Springer Netherlands, p. 248. DOI: 10.1007/978-94-009-5217-1.

Montecino, V. and C. B. Lange (2009). "The Humboldt Current System: Ecosystem components and processes, fisheries, and sediment studies". In: *Progress in Oceanography* 83.1-4, pp. 65–79. DOI: 10.1016/j.pocean.2009.07.041.

Montecinos, A., O. Leth, and O. Pizarro (2007). "Wind-driven interdecadal variability in the eastern tropical and South Pacific". In: *Journal of Geophysical Research* 112.C4, p. C04019. DOI: 10.1029/2006JC003571.

Montes, I., F. Colas, X. Capet, and W. Schneider (2010a). "On the pathways of the equatorial subsurface currents in the eastern equatorial Pacific and their contributions to the Peru-Chile Undercurrent". In: *Journal of Geophysical Research* 115.C9, p. C09003. DOI: 10.1029/2009JC005710.

Montes, I., F. Colas, X. Capet, and W. Schneider (2010b). "On the pathways of the equatorial subsurface currents in the eastern equatorial Pacific and their contributions to the Peru-Chile Undercurrent". In: *Journal of Geophysical Research: Oceans* 115.9, p. C09003. DOI: 10.1029/2009JC005710.

Montes, I., B. Dewitte, E. Gutknecht, A. Paulmier, I. Dadou, A. Oschlies, and V. Garçon (2014). "High-resolution modeling of the Eastern Tropical Pacific oxygen minimum zone: Sensitivity to the tropical oceanic circulation". In: *Journal of Geophysical Research: Oceans* 119.8, pp. 5515–5532. DOI: 10.1002/2014JC009858.

Montes, I., W. Schneider, F. Colas, B. Blanke, and V. Echevin (2011). "Subsurface connections in the eastern tropical Pacific during La Nina 1999–2001 and El Nino 2002–2003". In: *Journal of Geophysical Research* 116.C12, p. C12022. DOI: 10.1029/2011JC007624.

Moore, D. W. and S. G. H. Philander (1977). "Modeling of the tropical oceanic circulation". In: *The Sea Vol. VI*. Wiley Intescience, pp. 319–361.

Morales, C., S. Hormazábal, I. Andrade, and M. Correa-Ramirez (2013). "Time-Space Variability of Chlorophyll-a and Associated Physical Variables within the Region

off Central-Southern Chile". In: *Remote Sensing* 5.11, pp. 5550–5571. DOI: 10.3390/rs5115550.

Mosquera-Vásquez, K., B. Dewitte, and S. Illig (2014). "The Central Pacific El Niño intraseasonal Kelvin wave". In: *Journal of Geophysical Research: Oceans* 119.10, pp. 6605–6621. DOI: 10.1002/2014JC010044.

Munk, W. H. (1950). "On the Wind-driven Ocean Circulation". In: *Journal of Meteorology* 7.2, pp. 80–93. DOI: 10.1175/1520-0469(1950)007<0080:OTWDOC>2.0.CO;2.

Muñoz, R. C. and R. Garreaud (2005). "Dynamics of the Low-Level Jet off the West Coast of Subtropical South America". In: *Monthly Weather Review* 133.12, pp. 3661–3677. DOI: 10.1175/MWR3074.1.

Nansen, F. (1898). *Farthest North (The Norwegian Polar Expedition 1893-1896)*. ARCHIBALD CONSTABLE and COMPANY, p. 544.

Narayan, N., A. Paul, S. Mulitza, and M. Schulz (2010). "Trends in coastal upwelling intensity during the late 20th century". In: *Ocean Sci* 6, pp. 815–823. DOI: 10.5194/os-6-815-2010.

Newman, M., S.-I. Shin, and M. A. Alexander (2011). "Natural variation in ENSO flavors". In: *Geophysical Research Letters* 38.14. DOI: 10.1029/2011GL047658.

Ogata, T., S.-P. Xie, A. Wittenberg, D.-Z. Sun, T. Ogata, S.-P. Xie, A. Wittenberg, and D.-Z. Sun (2013). "Interdecadal Amplitude Modulation of El Niño–Southern Oscillation and Its Impact on Tropical Pacific Decadal Variability*". In: *Journal of Climate* 26.18, pp. 7280–7297. DOI: 10.1175/JCLI-D-12-00415.1.

O'Reilly, J. E., S. Maritorena, B. G. Mitchell, D. A. Siegel, K. L. Carder, S. A. Garver, M. Kahru, and C. McClain (1998). "Ocean color chlorophyll algorithms for SeaWiFS". In: *Journal of Geophysical Research: Oceans* 103.C11, pp. 24937–24953. DOI: 10.1029/98JC02160.

Paulmier, A. and D. Ruiz-Pino (2009). "Oxygen minimum zones (OMZs) in the modern ocean". In: *Progress in Oceanography* 80.3, pp. 113–128. DOI: 10.1016/j.pocean.2008.08.001.

Paulmier, A., D. Ruiz-Pino, and V. Garçon (2011). "CO2 maximum in the oxygen minimum zone (OMZ)". In: *Biogeosciences* 8.2, pp. 239–252. DOI: 10.5194/bg-8-239-2011.

Pedlosky, J. (1987). *Geophysical fluid dynamics*. Springer-Verlag, p. 710.

Pennington, J. T., K. L. Mahoney, V. S. Kuwahara, D. D. Kolber, R. Calienes, and F. P. Chavez (2006). "Primary production in the eastern tropical Pacific: A review". In: *Progress in Oceanography* 69.2, pp. 285–317. DOI: 10.1016/j.pocean.2006.03.012.

Penven, P., V. Echevin, J. Pasapera, F. Colas, and J. Tam (2005). "Average circulation, seasonal cycle, and mesoscale dynamics of the Peru current system : a modeling approach - art. no. C10021". In: *Journal of Geophysical Research Oceans* 110.C10.

Penven, P., C. Roy, G. B. Brundrit, A. Colin De Verdière, P. Fréon, A. S. Johnson, J. R. E. Lutjeharms, and F. A. Shillington (2001). "A regional hydrodynamic model of upwelling in the Southern Benguela". In: *South African Journal of Science* 97.11, pp. 472–475.

Pizarro, O., A. J. Clarke, and S. Van Gorder (2001). "El Niño Sea Level and Currents along the South American Coast: Comparison of Observations with Theory". In: *Journal of Physical Oceanography* 31.7, pp. 1891–1903. DOI: 10.1175/1520-0485(2001)031<1891:ENOSLA>2.0.CO;2.

Pizarro, O. and A. Montecinos (2004). "Interdecadal variability of the thermocline along the west coast of South America". In: *Geophysical Research Letters* 31.20, p. L20307. DOI: 10.1029/2004GL020998.

Pizarro, O., G. Shaffer, B. Dewitte, and M. Ramos (2002). "Dynamics of seasonal and interannual variability of the Peru-Chile Undercurrent". In: *Geophysical Research Letters* 29.12, p. 1581. DOI: 10.1029/2002GL014790.

Pond, S. and G. L. Pickard (1983). *Introductory dynamical oceanography*. 2nd Ed. Butterworth-Heinemann, p. 329.

Prince, E. D. and C. P. Goodyear (2006). "Hypoxia-based habitat compression of tropical pelagic fishes". In: *Fisheries Oceanography* 15.6, pp. 451–464. DOI: 10.1111/j.1365-2419.2005.00393.x.

Purkey, S. G. and G. C. Johnson (2010). "Warming of Global Abyssal and Deep Southern Ocean Waters between the 1990s and 2000s: Contributions to Global Heat and Sea Level Rise Budgets*". In: *Journal of Climate* 23.23, pp. 6336–6351. DOI: 10.1175/2010JCLI3682.1.

Qiu, B. (2002). "Large-Scale Variability in the Midlatitude Subtropical and Subpolar North Pacific Ocean: Observations and Causes". In: *Journal of Physical Oceanography* 32.1, pp. 353–375. DOI: 10.1175/1520-0485(2002)032<0353:LSVITM>2.0.CO;2.

Qiu, B., S. Chen, H. Sasaki, B. Qiu, S. Chen, and H. Sasaki (2013). "Generation of the North Equatorial Undercurrent Jets by Triad Baroclinic Rossby Wave Interactions". In: *Journal of Physical Oceanography* 43.12, pp. 2682–2698. DOI: 10.1175/JPO-D-13-099.1.

Qiu, B., W. Miao, and P. Muller (1997). "Propagation and Decay of Forced and Free Baroclinic Rossby Waves in Off-Equatorial Oceans". In: *Journal of Physical Oceanography* 27.11, pp. 2405–2417. DOI: 10.1175/1520-0485(1997)027<2405:PADOFA>2.0.CO;2.

Ramos, M., B. Dewitte, O. Pizarro, and G. Garric (2008). "Vertical propagation of extratropical Rossby waves during the 1997–1998 El Niño off the west coast of South America in a medium-resolution OGCM simulation". In: *Journal of Geophysical Research* 113.C8, p. C08041. DOI: 10.1029/2007JC004681.

Reid, J. L. (1997). "On the total geostrophic circulation of the pacific ocean: flow patterns, tracers, and transports". In: *Progress in Oceanography* 39.4, pp. 263–352. DOI: 10.1016/S0079-6611(97)00012-8.

Renault, L., B. Dewitte, M. Falvey, R. Garreaud, V. Echevin, and F. Bonjean (2009). "Impact of atmospheric coastal jet off central Chile on sea surface temperature from satellite observations (2000–2007)". In: *Journal of Geophysical Research* 114.C8, p. C08006. DOI: 10.1029/2008JC005083.

Reynolds, R. W. and T. M. Smith (1994). "Improved Global Sea Surface Temperature Analyses Using Optimum Interpolation". In: *Journal of Climate* 7.6, pp. 929–948. DOI: 10.1175/1520-0442(1994)007<0929:IGSSTA>2.0.CO;2.

Reynolds, R. W., T. M. Smith, C. Liu, D. B. Chelton, K. S. Casey, and M. G. Schlax (2007). "Daily High-Resolution-Blended Analyses for Sea Surface Temperature". In: *Journal of Climate* 20.22, pp. 5473–5496. DOI: 10.1175/2007JCLI1824.1.

Rhein, M. et al. (2013). "Climate Change 2013: The Physical Science Basis". In: *IPCC, 2013: Climate Change 2013: The Physical Science Basis.* Ed. by T. Stocker et al. Cambridge University Press, Cambridge, United Kingdom and New York, NY, USA. Chap. 3, pp. 255–316. DOI: 10.1017/CBO9781107415324.010..

Rhines, P. (1986). "Vorticity Dynamics of the Oceanic General Circulation". In: *Annual Review of Fluid Mechanics* 18.1, pp. 433–497. DOI: 10.1146/annurev.fluid.18.1.433.

Richter, I. (2015). "Climate model biases in the eastern tropical oceans: causes, impacts and ways forward". In: *Wiley Interdisciplinary Reviews: Climate Change* 6.3, pp. 345–358. DOI: 10.1002/wcc.338.

Ridgway, K. R., J. R. Dunn, and J. L. Wilkin (2002). "Ocean Interpolation by Four-Dimensional Weighted Least Squares—Application to the Waters around Australasia". In: *Journal of Atmospheric and Oceanic Technology* 19.9, pp. 1357–1375. DOI: 10.1175/1520-0426(2002)019<1357:OIBFDW>2.0.CO;2.

Roemmich, D., J. Church, J. Gilson, D. Monselesan, P. Sutton, and S. Wijffels (2015). "Unabated planetary warming and its ocean structure since 2006". In: *Nature Climate Change* 5.3, pp. 240–245. DOI: 10.1038/nclimate2513.

Roemmich, D. and B. Owens (2000). "The Argo Project: Global Ocean Observations for Understanding and Prediction of Climate Variability". In: *Oceanography* 13.2, pp. 45–50. DOI: 10.5670/oceanog.2000.33.

Romea, R. D. and R. L. Smith (1983). "Further Evidence for Coastal Trapped Waves along the Peru Coast". In: *Journal of Physical Oceanography* 13.8, pp. 1341–1356. DOI: 10.1175/1520-0485(1983)013.

Rutllant, J., I. Masotti, J. Calderón, and S. A. Vega (2004). "A comparison of spring coastal upwelling off central Chile at the extremes of the 1996-1997 ENSO cycle". In: *Continental Shelf Research* 24.7-8, pp. 773–787. DOI: 10.1016/j.csr.2004.02.005.

Schopf, P. S., D. L. Anderson, and R. Smith (1981). "Beta-dispersion of low-frequency Rossby waves". In: *Dynamics of Atmospheres and Oceans* 5.3, pp. 187–214. DOI: 10.1016/0377-0265(81)90011-7.

Shaffer, G., S. Hormazábal, O. Pizarro, and M. Ramos (2004). "Circulation and variability in the Chile Basin". In: *Deep Sea Research Part I: Oceanographic Research Papers* 51.10, pp. 1367–1386. DOI: 10.1016/j.dsr.2004.05.006.

Shaffer, G., S. Hormazábal, O. Pizarro, and S. Salinas (1999). "Seasonal and interannual variability of currents and temperature off central Chile". In: *Journal of Geophysical Research: Oceans* 104.C12, pp. 29951–29961. DOI: 10.1029/1999JC900253.

Shaffer, G., O. Pizarro, L. Djurfeldt, S. Salinas, and J. Rutllant (1997). "Circulation and Low-Frequency Variability near the Chilean Coast: Remotely Forced Fluctuations during the 1991-92 El Niño". In: *Journal of Physical Oceanography* 27.2, pp. 217–235. DOI: 10.1175/1520-0485(1997)027<0217:CALFVN>2.0.CO;2.

Shchepetkin, A. F. and J. C. McWilliams (1998). "Quasi-Monotone Advection Schemes Based on Explicit Locally Adaptive Dissipation". In: *Monthly Weather Review* 126.6, pp. 1541–1580. DOI: 10.1175/1520-0493(1998)126<1541:QMASBO>2.0.CO;2.

Shchepetkin, A. F. and J. C. McWilliams (2005). "The regional oceanic modeling system (ROMS): a split-explicit, free-surface, topography-following-coordinate oceanic model". In: *Ocean Modelling* 9.4, pp. 347–404. DOI: 10.1016/j.ocemod.2004.08.002.

Silva, N. and S. Neshyba (1979). "On the southernmost extension of the Peru-Chile undercurrent". In: *Deep Sea Research Part A, Oceanographic Research Papers* 26.12, pp. 1387–1393. DOI: 10.1016/0198-0149(79)90006-2.

Skliris, N., R. Marsh, S. A. Josey, S. A. Good, C. Liu, and R. P. Allan (2014). "Salinity changes in the World Ocean since 1950 in relation to changing surface freshwater fluxes". In: *Climate Dynamics* 43.3-4, pp. 709–736. DOI: 10.1007/s00382-014-2131-7.

Sloyan, B. M., S. R. Rintoul, B. M. Sloyan, and S. R. Rintoul (2001). "The Southern Ocean Limb of the Global Deep Overturning Circulation*". In: *Journal of Physical Oceanography* 31.1, pp. 143–173. DOI: 10.1175/1520-0485(2001)031<0143:TSOLOT>2.0.CO;2.

Slutz, R. J., S. J. Lubker, J. D. Hiscox, S. D. Woodruff, R. L. Jenne, D. H. Joseph, P. M. Steurer, and J. D. Elms (1985). *Comprehensive Ocean-Atmosphere Data Set; Release 1*. Tech. rep. Boulder, Colorado: NOAA Environmental Research Laboratories, Climate Research Program, p. 268.

Smith, R. L. (1978). "Poleward propagating perturbations in currents and sea levels along the Peru Coast". In: *Journal of Geophysical Research* 83.C12, p. 6083. DOI: 10.1029/JC083iC12p06083.

Song, Y. T. (1998). "A General Pressure Gradient Formulation for Ocean Models. Part I: Scheme Design and Diagnostic Analysis". In: *Monthly Weather Review* 126.12, pp. 3213–3230. DOI: 10.1175/1520-0493(1998)126<3213:AGPGFF>2.0.CO;2.

Spillane, M. C., D. B. Enfield, and J. S. Allen (1987). "Intraseasonal Oscillations in Sea Level along the West Coast of the Americas". In: *Journal of Physical Oceanography* 17.3, pp. 313–325. DOI: 10.1175/1520-0485(1987)017<0313:IOISLA>2.0.CO;2.

Stommel, H. (1948). "The westward intensification of wind driven ocean currents". In: *Transactions, American Geophysical Union* 29.2, p. 202. DOI: 10.1029/TR029i002p00202.

Stramma, L., S. Schmidtko, L. A. Levin, and G. C. Johnson (2010). "Ocean oxygen minima expansions and their biological impacts". In: *Deep Sea Research Part I: Oceanographic Research Papers* 57.4, pp. 587–595. DOI: 10.1016/j.dsr.2010.01.005.

Strub, P. T., J. M. J. Mesías, V. Montecino, J. Rutllant, S. Salinas, A. R. Robinson, and K. H. Brink (1998). "Coastal ocean circulation off western South America". In: *The Sea*. Vol. 11. Robinson, A. R., and K. H. Brink, pp. 273–313.

Sverdrup, H. U. (1947). "Wind-Driven Currents in a Baroclinic Ocean; with Application to the Equatorial Currents of the Eastern Pacific". In: *Proceedings of the National Academy of Sciences of the United States of America* 33.11, pp. 318–26.

Tailleux, R. (2012). "On the Generalized Eigenvalue Problem for the Rossby Wave Vertical Velocity in the Presence of Mean Flow and Topography". In: *Journal of Physical Oceanography* 42.6, pp. 1045–1050. DOI: 10.1175/JPO-D-12-010.1.

Takahashi, K. (2005). "The Annual Cycle of Heat Content in the Peru Current Region*". In: *Journal of Climate* 18.23, pp. 4937–4954. DOI: 10.1175/JCLI3572.1.

Takahashi, K. and D. S. Battisti (2007a). "Processes controlling the mean tropical pacific precipitation pattern. Part I: The Andes and the eastern Pacific ITCZ". In: *Journal of Climate* 20.14, pp. 3434–3451. DOI: 10.1175/JCLI4198.1.

Takahashi, K. and D. S. Battisti (2007b). "Processes controlling the mean tropical Pacific precipitation pattern. Part II: The SPCZ and the Southeast Pacific dry zone". In: *Journal of Climate* 20.23, pp. 5696–5706. DOI: 10.1175/2007JCLI1656.1.

Takahashi, K., A. Montecinos, K. Goubanova, and B. Dewitte (2011). "ENSO regimes: Reinterpreting the canonical and Modoki El Niño". In: *Geophysical Research Letters* 38.10, n/a–n/a. DOI: 10.1029/2011GL047364.

Trenberth, K. E. (1997). "The Definition of El Niño". In: *Bulletin of the American Meteorological Society* 78.12, pp. 2771–2777. DOI: 10.1175/1520-0477(1997)078<2771:TDOENO>2.0.CO;2.

Trenberth, K. E. and D. P. Stepaniak (2001). "Indices of El Niño Evolution". In: *Journal of Climate* 14.8, pp. 1697–1701. DOI: 10.1175/1520-0442(2001)014<1697:LIOENO>2.0.CO;2.

Trenberth, K. E. and D. P. Stepaniak (2004). "The flow of energy through the earth's climate system". In: *Quarterly Journal of the Royal Meteorological Society* 130.603, pp. 2677–2701. DOI: 10.1256/qj.04.83.

Tsuchiya, M. and L. D. Talley (1998). "A Pacific hydrographic section at 88°W: Water-property distribution". In: *Journal of Geophysical Research: Oceans* 103.C6, pp. 12899–12918. DOI: 10.1029/97JC03415.

Vargas, G., S. Pantoja, J. Rutllant, C. B. Lange, and L. Ortlieb (2007). "Enhancement of coastal upwelling and interdecadal ENSO-like variability in the Peru-Chile Current since late 19th century". In: *Geophysical Research Letters* 34.13, n/a–n/a. DOI: 10.1029/2006GL028812.

Vecchi, G. A., B. J. Soden, A. T. Wittenberg, I. M. Held, A. Leetmaa, and M. J. Harrison (2006). "Weakening of tropical Pacific atmospheric circulation due to anthropogenic forcing". In: *Nature* 441.7089, pp. 73–76. DOI: 10.1038/nature04744.

Vega, A., Y. DuPenhoat, B. Dewitte, and O. Pizarro (2003). "Equatorial forcing of interannual Rossby waves in the eastern South Pacific". In: *Geophysical Research Letters* 30.5. DOI: 10.1029/2002GL015886.

Verkley, W. T. M. (1990). "On the Beta Plane Approximation". In: *Journal of the Atmospheric Sciences* 47.20, pp. 2453–2460. DOI: 10.1175/1520-0469(1990)047<2453:OTBPA>2.0.CO;2.

Veronis, G. (1963). "On inertially-controlled flow patterns in a β-plane ocean". In: *Tellus* 15.1, pp. 59–66. DOI: 10.1111/j.2153-3490.1963.tb01363.x.

Veronis, G. (1981). "Dynamics of large-scale ocean circulation". In: *Evolution of Physical Oceanography*. Ed. by B. A. Warren and C. Wunsch. Cambridge, Massachusetts: MIT Press. Chap. 6.

Wang, L., C. Koblinsky, S. Howden, and BekleyB. (1998). "Large scale Rossby wave in the mid latitude South Pacific from altimetry data". In: *Geophysical Research Letters* 25.2, pp. 179–182. DOI: 10.1029/97GL03567.

Weng, H., S. K. Behera, and T. Yamagata (2009). "Anomalous winter climate conditions in the Pacific rim during recent El Ni{ñ}o Modoki and El Ni{ñ}o events". In: *Climate Dynamics* 32.5, pp. 663–674. DOI: 10.1007/s00382-008-0394-6.

White, W. B. and J. F. T. Saur (1983). "Sources of Interannual Baroclinic Waves in the Eastern Subtropical North Pacific". In: *Journal of Physical Oceanography* 13.3, pp. 531–544. DOI: 10.1175/1520-0485(1983)013.

Whitmarsh, F., J. Zika, and A. Czaja (2015). *Ocean heat uptake and the global surface temperature record*. London.

Wittenberg, A. T., A. Rosati, T. L. Delworth, G. A. Vecchi, and F. Zeng (2014). "ENSO Modulation: Is It Decadally Predictable?" In: *Journal of Climate* 27.7, pp. 2667–2681. DOI: 10.1175/JCLI-D-13-00577.1.

Wolter, K. and M. Timlin (1993). "Monitoring ENSO in COADS with a seasonally adjusted principal component index". In: *17th Climate Diagnostics Workshop*. Norman, Oklahoma: NOAA/NMC/CAC, NSSL, Oklahoma Clim. Survey, CIMMS and the School of Meteor., Univ. of Oklahoma, pp. 52–57.

Woodruff, S. D., R. J. Slutz, R. L. Jenne, and P. M. Steurer (1987). "A Comprehensive Ocean-Atmosphere Data Set". In: *Bulletin of the American Meteorological Society* 68.10, pp. 1239–1250. DOI: 10.1175/1520-0477(1987)068<1239:ACOADS>2.0.CO;2.

Woodward, R. H. and W. W. Gregg (1998). *An Assessment of SeaWiFS and MODIS Ocean Coverage*. Tech. rep. Greenbelt, Maryland: NASA Goddard Space Flight Center, p. 44.

Worley, S. J., S. D. Woodruff, R. W. Reynolds, S. J. Lubker, and N. Lott (2005). "ICOADS release 2.1 data and products". In: *International Journal of Climatology* 25.7, pp. 823–842. DOI: 10.1002/joc.1166.

Wunsch, C. (2013). "Baroclinic Motions and Energetics as Measured by Altimeters". In: *Journal of Atmospheric and Oceanic Technology* 30.1, pp. 140–150. DOI: 10.1175/JTECH-D-12-00035.1.

Wyrtki, K. (1963). *The horizontal and vertical field of motion in the Peru Current*. Vol. 8. University of California Press, pp. 313–345.

Wyrtki, K. (1966). "Oceanography of the Eastern Equatorial Pacific Ocean". In: *Oceanography and Marine Biology Annual Revue* 4, pp. 33–68.

Xie, P. and G. K. Vallis (2012). "The passive and active nature of ocean heat uptake in idealized climate change experiments". In: *Climate Dynamics* 38.3-4, pp. 667–684. DOI: 10.1007/s00382-011-1063-8.

Xie, S.-P., C. Deser, G. A. Vecchi, J. Ma, H. Teng, and A. T. Wittenberg (2010). "Global Warming Pattern Formation: Sea Surface Temperature and Rainfall". In: *Journal of Climate* 23.4, pp. 966–986. DOI: 10.1175/2009JCLI3329.1.

Xu, Z., P. Chang, I. Richter, W. Kim, and G. Tang (2014). "Diagnosing southeast tropical Atlantic SST and ocean circulation biases in the CMIP5 ensemble". In: *Climate Dynamics* 43.11, pp. 3123–3145. DOI: 10.1007/s00382-014-2247-9.

Yañez, E., M. Barbieri, C. Silva, K. Nieto, and F. Espindola (2001). "Climate variability and pelagic fisheries in northern Chile". In: *Progress in Oceanography* 49.1, pp. 581–596. DOI: 10.1016/S0079-6611(01)00042-8.

Yeh, S.-W., J.-S. Kug, and S.-I. An (2014). "Recent progress on two types of El Niño: Observations, dynamics, and future changes". In: *Asia-Pacific Journal of Atmospheric Sciences* 50.1, pp. 69–81. DOI: 10.1007/s13143-014-0028-3.

Yeh, S.-W., J.-S. Kug, B. Dewitte, M.-H. Kwon, B. P. Kirtman, and F.-F. Jin (2009). "El Niño in a changing climate". In: *Nature* 461.7263, pp. 511–514. DOI: 10.1038/nature08316.

Zheng, X. et al. (2011). "Observations of the boundary layer, cloud, and aerosol variability in the southeast Pacific near-coastal marine stratocumulus during VOCALS-REx". In: *Atmospheric Chemistry and Physics* 11.18, pp. 9943–9959. DOI: 10.5194/acp-11-9943-2011.

Abstract

The oceanic circulation in the subthermocline of the South Eastern Pacific remains poorly documented although this region is thought to play a key role in the climate variability owed to, in particular, the presence of an extended oxygen minimum zone (OMZ) that intervenes in the carbon and nitrogen cycle. The subthermocline in this region is also largely unmonitored and historical estimates of ocean heat content are mostly limited to the upper 500 m. In this thesis we document various oceanic processes at work in the subthermocline based on a regional modeling approach that is designed to take in account the efficient oceanic teleconnection from the equatorial region to the mid-latitudes, in particular at ENSO (El Niño Southern Oscillation) timescales. The focus is on two aspects: (1) the seasonality of the turbulent flow and its role in modulating the OMZ volume off Peru, and (2) the planetary wave fluxes associated with interannual to decadal timescales. It is first shown that the vertical energy flux at interannual timescales can be interpreted as resulting from the vertical propagation of extra-tropical Rossby waves remotely forced from the equatorial region. This flux primarily results from extreme Eastern Pacific El Niño events, despite that a significant fraction of interannual Sea Surface Temperature (SST) variability in the tropical Pacific is also associated with Central Pacific El Niño events and La Niña events. Vertically propagating energy flux at decadal timescales is also evidenced in the model, which, like for the interannual flux, is marginally impacted by mesoscale activity. On the other hand, the wave energy beams experience a marked dissipation in the deep-ocean (2000 m) which is interpreted as resulting from vertical diffusivity. While the oxygen field within the OMZ appears to be influenced by the vertical propagation of isopycnals height anomalies, induced by the seasonal Rossby waves, the seasonality of the OMZ is shown to be dominantly associated with the seasonal change in the eddy flux at its boundaries. Implications of the results for the study of both the low-frequency variability of the OMZ and the Earth's energy budget are discussed.

Résumé

L'objectif principal de cette thèse est l'étude de la connexion entre la variabilité dans l'océan Pacifique équatorial et la circulation de subsurface le long des côtes du Pérou et du Chili, à des échelles de temps interannuelles à décennales. Les diagnostiques menés dans ce travail se basent sur un modèle régional océanique. L'accent est mis sur l'interprétation de la propagation verticale de la variabilité dans les couches intermédiaires de l'océan, où l'on trouve une intense zone de minimum d'oxygène (OMZ[1]), et la relation de cette propagation verticale avec les processus advectifs et diffusifs. La propagation verticale est diagnostiquée à travers le flux vertical d'énergie associé à la propagation verticale de l'onde de Rossby extratropicale (ETRW[2]).

Aux échelles de temps interannuelles, les résultats montrent que 80% du flux vertical d'énergie dans l'océan Pacifique Sud-Est (SEP[3]) est associé aux événements El Niño extraordinaires. Ce flux d'énergie s'étend vers l'Ouest en suivant les rayons théoriques WKB, avec une pente plus prononcée au fur et à mesure que la latitude augmente. Les analyses du flux d'énergie mettent aussi en évidence l'existence d'une modulation du flux d'énergie interannuel à l'échelle décennale, qui serait liée aux fluctuations décennales et inter-décennales dans le Pacifique équatorial. Une décomposition de la stratification en modes verticaux montre que le flux d'énergie associé à El Niño et aux fluctuations décennales se projette sur les trois premiers modes baroclines, ce qui confirme l'interprétation du flux d'énergie comme la propagation de l'onde de Rossby. Des tests de sensibilité menés avec un modèle linéaire ajusté aux conditions de la simulation montrent que la propagation d'énergie verticale pendant les événements El Niño est aussi impactée par la contribution des modes baroclines supérieurs. La variabilité méridienne/verticale du flux d'énergie vertical met en évidence une atténuation de l'amplitude le long de la trajectoire de l'onde, ce qui est interprété comme un flux diffusif de chaleur induit par la dissipation de l'onde.

La variabilité de subsurface de la circulation à l'échelle saisonnière est aussi étudiée

[1]De l'anglais *Oxygen Minimum Zone*.
[2]De l'anglais *Extra-Tropical Rossby Wave*.
[3]De l'anglais *South-Eastern Pacific*.

dans cette région à travers la ventilation de l'OMZ. Les résultats montrent que la variabilité saisonnière de l'OMZ en dessous de 400 m de profondeur possède des caractéristiques de propagation similaires à celles du flux d'énergie associé à l'ETRW annuelle, ce qui indique que l'ETRW pourrait influencer la variabilité de l'OMZ profonde, du moins à l'échelle saisonnière. Au-dessus de 400 m de profondeur, le processus dominant qui influence la ventilation de l'OMZ à l'échelle saisonnière est le transport d'oxygène par les tourbillons de méso-échelle.

Dans ce travail, nous mettons en évidence la nature complexe de la variabilité de la circulation de subsurface dans le SEP. Nous montrons en particulier la connexion entre la circulation sous la thermocline extratropicale et les modes climatiques de variabilité du Pacifique équatorial.